SOLID-STATE PHYSICAL FORM DETECTION AND QUANTITATION OF PHARMACEUTICALS IN FORMULATIONS

BY

Eric Matthew Gorman

B.S., Drake University, 2004
M.S., University of Kansas, 2007

Submitted to the graduate degree program in Pharmaceutical Chemistry and the Graduate Faculty of the University of Kansas in partial fulfillment of the requirements for the degree of Doctor of Philosophy.

Dissertation Committee:

_____
Valentino J. Stella, Chairperson

_____
Eric J. Munson

_____
Jennifer S. Laurence

_____
Cory Berkland

_____
Robert C. Dunn

Date defended: March 17, 2011

The Dissertation Committee for Eric M. Gorman certifies that this is the approved version of the following dissertation:

SOLID-STATE PHYSICAL FORM DETECTION AND QUANTITATION OF PHARMACEUTICALS IN FORMULATIONS

_____

Valentino J. Stella, Chairperson

Date approved: March 17, 2011

Abstract

The majority of pharmaceutical dosage forms are marketed as solids, and the active pharmaceutical ingredient (API) can exist in various physical forms. These physical forms can be either crystalline or amorphous, and will have different physical properties. The physical form of the API is selected to provide the appropriate solubility, stability, and bioavailability for the formulation. However, processing steps involved in the production of the formulation can induce changes in the physical form of the API and thus impact the performance of the formulation. Therefore, it is critical to characterize the physical form of the API in the formulation, and to monitor it for any changes in the physical form during storage.

Multiple solid-state characterization techniques are typically employed in order to identify and quantitate physical forms of APIs. However, most of these techniques suffer from significant issues related to the interference of excipient signals with API signals when analyzing formulations. Additionally, in order to perform quantitative measurements pure standards are needed and calibration curves must be generated for most of these characterization techniques.

This dissertation demonstrates the superior ability of solid-state nuclear magnetic resonance (SSNMR) spectroscopy to both detect and quantitate physical forms of APIs within formulations, relative to other solid-state characterization techniques. Specifically, SSNMR has been used to understand the dehydration of levofloxacin hemihydrate, including the discovery of a previously unreported anhydrous polymorph. Three formulations for pulmonary delivery have been characterized by both differential scanning

calorimetry (DSC) and SSNMR. DSC could not clearly identify the physical form of the APIs in the formulations, but SSNMR was able to unambiguously determine the physical forms of the APIs in all cases.

The work presented in the dissertation also demonstrates that SSNMR can be used to quantitate the relative amounts of physical forms of APIs within formulations without pure standards or calibration curves. Finally, the relative ability of SSNMR and other solid-state characterization techniques were compared and clearly illustrate that SSNMR is considerably more powerful in the relative quantitation of API physical form in both pure materials and formulations.

Dedicated to:

My parents, Rod and Mindy, for all of their love and support in each and every one my endeavors

Acknowledgements

I must begin by thanking my graduate advisor, Dr. Eric Munson. Without his support none of this work would have been possible. Additionally, there are very few professors that would not only allow but also encourage their graduate students to perform three different industrial internships during the course of their graduate school careers. I also greatly appreciate the many opportunities that he has given me to attend conferences and present my research over the course of my graduate education, including the opportunity to spend an entire week in Germany.

Many thanks to Dr. Valentino Stella for stepping in as an advisor for these last few months. Also, I greatly appreciate all of the guidance and valuable feedback that have been provided by Dr. Stella and Dr. Jennifer Laurence throughout the writing of this dissertation. In addition, I would like to thank the other members of my dissertation committee, Dr. Cory Berkland and Dr. Robert Dunn, for their time in reviewing the dissertation and attending my defense.

Had it not been for my interactions with Dr. Colin Cairns and Dr. Nita Pandit during my time at Drake University I might never have ventured down the path of scientific research. It was Dr. Cairns who gave me my first opportunity to perform research and introduced me to Dr. Pandit. Dr. Pandit served as both my academic and research advisor for most of my time at Drake and to this day is an important mentor and friend in my scientific career. However, ultimately it was my undergraduate research experiences with Dr. Robin Bogner of the University of Connecticut and Dr. Ronald Borchardt of the

University of Kansas who helped me to solidify my interest in research and decide to attend graduate school.

Thanks to the support of Dr. Munson I have also had the opportunity to participate in three industrial internships during my time at the University of Kansas. My first internship was at Bristol-Myers Squibb under the mentorship of Dr. Mandar Dali and Dr. Venkatramana Rao, who taught me a great deal about conducting research in a corporate environment. The second internship was at Schering Plough where I had the opportunity to work closely with Dr. Niran Nugara, Dr. Saly Romero-Torres, Dr. Lin Xie, and Dr. Charlie "Andy" Evans. It was this internship at which I learned the importance of embracing change and ultimately provided the inspiration for some of the research presented in this dissertation.

My third and final internship was with Pfizer under the direction of Dr. Mark Zell. I would like to thank Dr. Zell for all of his help in extending my experience at Pfizer with a co-op with the materials science group and his mentorship and friendship through our many interactions both in and out of the lab, especially our lunch time runs. My co-op in the materials science group would not have been possible had it not been for the work of Dr. Linda Lohr and Dr. Heather Frericks-Schmidt, and this opportunity has provided me with invaluable experience with serving as a worldwide expert within a large multinational pharmaceutical corporation. I am also indebted to the materials science group, especially Dr. Briana Samas, Dr. Peter Larkin, Shawn Mehrens, and Melissa Casteel for all of their help and allowing me to use their various instruments for some of the research that is presented in this dissertation.

Additionally, I would like to thank both the structure elucidation and material science groups for providing such a fun and dynamic working environment.

Thanks to the Munson Research Group: Dr. Dewey Barich, Dr. Joe Lubach, Dr. Loren Schieber, Dr. Diana Sperger, Dr. Bob Berendt, Ben Nelson, Sarah Pyszczynski, Elodie Dempah, and Bo Ponputtapitak. We have had many great experiences together both inside and outside the lab and you have taught me a great deal about working in a professional environment. Special thanks to Ben for all of your efforts to help keep the lab running on a day-to-day basis, none of us could have gotten all of our work accomplished without your help.

I would also like to thank the faculty, staff, and students of the Department of Pharmaceutical Chemistry at the University of Kansas. You help provide a great learning and working environment. I am especially grateful of the hard work of Nancy Helm, Ann Heptig, Nicole Brooks, and Karen Hall to help ensure that the department runs smoothly and to help in any way that they could.

I am deeply indebted to Dr. Dewey Barich and Teresa Pepper for all of their help and friendship over the course of my time at the University of Kansas. Whether we were trying to comprehend a new episode of Lost or just needing to take a mental break, you were willing to be there to help me out. I am especially grateful for your willingness to adopt Buddy when I went to Pfizer for an extended period and to open your home to me when I returned to write this dissertation. Also, thank you to Teresa and her co-workers for putting up with Dr. Barich and I when, on countless occasions, we turned to "shop talk" at lunch.

Last, but certainly not least, I cannot thank my family enough for all of their love and support my whole life. You taught me the value of hard work and

the importance of being a good and honest person. While you may not have always understood the work that I do, you have always been there to support me in all of my endeavors. I may be moving half-way across the country to start a new life, but I know that we will remain just as close as when we crammed ourselves into my tiny one bedroom apartment for the entire Thanksgiving weekend just to spend time near one another.

Table of Contents

Index of Tables

Index of Figures

List of Abbreviations

API = active pharmaceutical ingredient

CI = confidence interval

CortA = cortisone 21-acetate

CP = cross polarization

DMF = N,N-dimethyl formamide

DP = direct polarization

DSC = differential scanning calorimetry

FID = free induction decay

HMB = hexamethyl benzene

LOD = limit-of-detection

LOQ = limit-of-quantification

MAS = magic angle spinning

MDSC = modulated differential scanning calorimetry

MGA = 3-methylglutaric acid

MLR = multiple linear regression

MSC = multiplicative scatter correction

NMR = nuclear magnetic resonance

PLGA = poly(D,L-lactide-co-glycolide)

PLS = partial least squares

PXRD = powder X-ray diffraction

RF = radio frequency

RMSEC = root mean square error of calibration

RMSEV = root mean square error of validation

RSD = relative standard deviation

S/N = signal-to-noise ratio

SD = standard deviation

SG = Savitzky-Golay

SNV = standard normal variate

SSNMR = solid-state nuclear magnetic resonance

T_g = glass-transition temperature

TGA = thermogravimetric analysis

TOSS = total suppression of spinning sideband

Chapter 1

Introduction to Pharmaceutical Solids

1.1 Objectives

The primary objective of this dissertation is to determine the capability of solid-state characterization techniques to detect and quantitate physical forms of drugs within pharmaceutical formulations. The first section of this dissertation will focus on the ability of various techniques to identify physical forms of a drug and to detect the physical forms within formulations. Later sections will focus on the development of methods using solid-state nuclear magnetic resonance (SSNMR) spectroscopy to quantitate physical forms of drugs within formulations and compare the performance of those methods with other solid-state characterization techniques that are commonly used for physical form quantitation.

The following sections will provide a general introduction to pharmaceutical solids. The first section will cover crystalline and amorphous materials. In addition, a variety of solid form classifications will be introduced, including polymorphs, salts, solvates, and cocrystals. Attention will also be given to the selection of a physical form for use in a solid pharmaceutical formulation. And finally, the potential impacts of manufacturing processes on the physical form of the drug within the formulation will also be presented.

1.2 Introduction

More than 80% of all pharmaceutical dosage forms are solids.[1,2] They can utilize various routes of drug administration including: injection, inhalation, topical application, and oral ingestion. They are more difficult to develop and

manufacture than liquid formulations. Nonetheless, patients generally prefer solid pharmaceuticals, which are typically more stable than liquid formulations, resulting in longer shelf lives.

A single dose of a drug will typically be in the range of a few milligrams to hundreds of milligrams depending upon the potency of the drug. For most drugs, if the needed dose was simply compressed into a tablet, it would be too small for the majority of patients to handle without difficulty. Therefore a drug, often referred to as the active pharmaceutical ingredient (API), is typically mixed with various excipients to produce a formulation. Some excipients help to make handling of the API easier by improving the flow properties of the powders so that they do not clog the manufacturing equipment. Other excipients aid in the dissolution of the tablets once they are ingested by a patient or make the tablets physically stronger so that they do not crumble before reaching the patient. Individual excipients are classified based on the roles that they play within a formulation, such as binders, disintegrants, lubricants, wetting agents, coatings, and flavoring agents, but oftentimes an excipient plays more than one role.

Unfortunately, an API cannot simply be mixed with a set of excipients, compressed into a tablet and then given to a patient without further characterization. There are a variety of physical states in which the API can exist, and different physical forms of a material will have distinct properties that can affect things like dissolution rate and chemical stability. Therefore it is important to identify the physical forms of an API and carefully choose the one with the most appropriate physical properties for use in the formulation. The following sections will introduce the concept of physical forms as they relate to pharmaceuticals and discuss the selection of a physical form for use in a solid

formulation.

1.3 Physical Forms of Pharmaceuticals

Generally speaking, a pharmaceutical solid will exist in either a crystalline or an amorphous state. A crystalline solid is characterized by highly ordered packing of the molecules within the material. Conversely, amorphous solids are defined as lacking any long-range molecular order. The choice of using a crystalline or amorphous solid can dramatically affect the development of a solid formulation. The following sections will describe both crystalline and amorphous solids along with their advantages and disadvantages for use in pharmaceutical solids.

1.3.1 Crystalline Solids

A solid material where the molecules are packed in a repetitive order over long distances in three dimensions is said to be crystalline. In a crystal, the smallest repeating unit is called the unit cell. It contains one or more molecules that have a specific conformation and arrangement in the unit cell. The unit cell then repeats in three dimensions to produce a crystal lattice that is held together by the presence of various non-covalent bonding interactions, including intra- and intermolecular hydrogen bonding and van der Waals forces.[3] In many cases a material may have different crystal structures made by adopting different conformations or packing arrangements of the molecules, resulting from changing the bonding interactions. The different crystal structures are termed polymorphs, and the phenomenon of polymorphism is very common within

pharmaceuticals.[4]

Polymorphs will have different thermodynamic and physical properties due to the differences in their non-covalent bonding interactions. While multiple polymorphs can exist at a given temperature and pressure, they will each have a different free energy. The one with the lowest free energy is the most thermodynamically stable form at that temperature and pressure, and all the other polymorphs are said to be metastable compared to the most stable form. Given a sufficient amount of time at the given temperature and pressure, all of the metastable forms would eventually convert to the most stable form. However, it may take anywhere from seconds to years for the conversion to occur, and the kinetics of interconversion will be different for each form.

The relative thermodynamic stability of polymorphic forms may change at different temperatures.[5,6] When one polymorph has a lower free energy than another polymorph at all temperatures below the melting point of the forms, then the pair of forms are said to be monotropically related. A pair of polymorphs are enantiotropically related if at some temperature, called the transition temperature, there is a change in which form has the lower free energy. Figure 1 illustrates a polymorphic system that consists of three forms (Forms A, B, and C). In this example Form A and Form B are enantiotropically related to each other while Forms A and B are each monotropically related to Form C. Form A is the thermodynamically stable form while B and C are metastable at all temperatures below the transition temperature. Above the transition temperature Form B is the thermodynamically stable form while A and C are metastable.

While polymorphic systems are defined by their thermodynamic

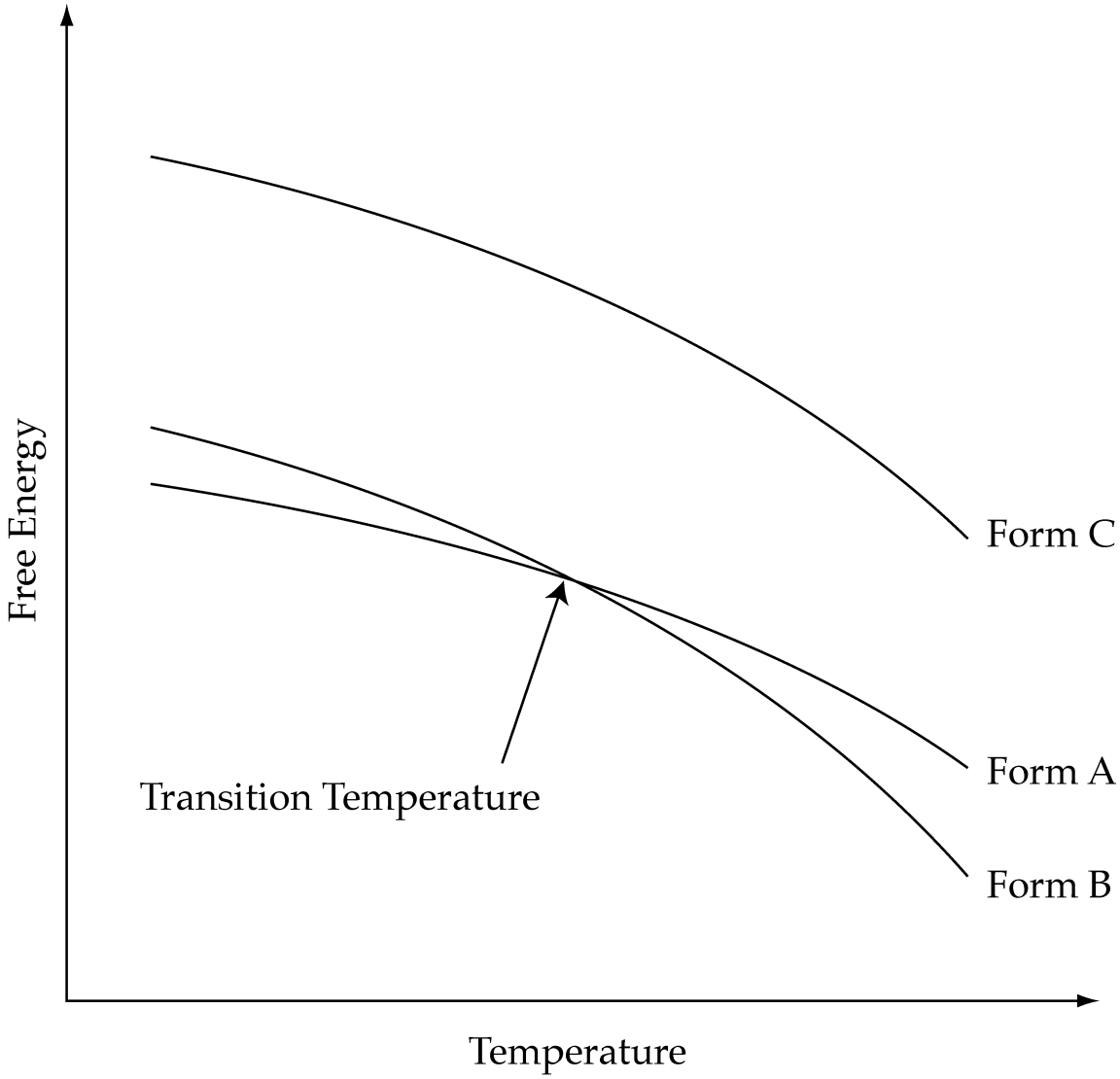

Figure 1.1 Theoretical phase diagram of a polymorphic system that consists of three forms (A, B, and C). Form A and B are enantiotropically related with their transition temperature indicated on the phase diagram. Both Form A and B are monotropically related to Form C.

relationships, it is really their physical properties that are of greatest interest when developing a pharmaceutical formulation. Chief among these properties is solubility, because an API that does not dissolve cannot be absorbed by the patient and have the desired physiological effects. The thermodynamically stable form will have the lowest solubility (the equilibrium solubility of the API) and often be the most chemically stable of the polymorphs. Therefore the stable form is often the first choice when picking the polymorph that will be used in a formulation.[7]

One potential complication when choosing the most stable polymorph is when that form is enantiotropically related to another polymorph. The API will typically experience a variety of conditions, including a range of temperatures, from the time that it is made until it is included into the formulation and ultimately used by the patient. Some of these conditions may be controlled, such as drying steps used in the manufacturing process, while others may be outside the control of the manufacturer, such as a patient leaving their bottle of tablets in their car on a hot summer day. While every possible situation cannot be anticipated, it is still important to consider these factors when picking the polymorph that will be formulated. As an example, consider the system shown in Figure 1 and assume that the transition temperature of the forms is 50 °C. Form A could be a good choice because it is the most stable form at temperatures the product would experience under normal storage.[8] However, assume that drying steps will probably be needed during manufacturing, and will be done at 80 – 100 °C. In a typical enantiotropic system, the actual polymorph conversion from Form A to B could occur at a temperature significantly higher than the point at which the relative free energies invert, and if cooled back down there

may not be any observed conversion of Form B back to A.[9-12] Therefore, significantly more information would be needed about the kinetics of transformation between Form A and B at a variety of temperatures before making a final decision on which form to include in the formulation, but in many cases Form B would be chosen to avoid unintended conversions during manufacture and because it would likely remain unchanged over the shelf life of the product.[9]

It is becoming increasingly common that the most stable form is not sufficiently soluble to achieve the necessary bioavailability from the formulation. If the polymorphs are ranked in order of increasing free energy the order will also represent the rank ordering of the forms from the least to most soluble in terms of apparent solubility. Therefore, a metastable form will have an apparent solubility that is higher than the equilibrium solubility of the API, and may provide the necessary increase in solubility to produce a viable formulation. However, formulation of metastable polymorphs must be approached with great caution because conversion to the stable polymorph within a formulation can have devastating effects.[13,14] Unfortunately, if significant increases in solubility are required, the least stable polymorph may be needed but it will also be the most prone to convert to the stable form. In situations where no metastable polymorph can provide sufficient solubility and physical stability other physical forms must be explored. The amorphous state can be particularly useful in these situations and will be discussed in the following section.

1.3.2 Amorphous Solids

When the molecules of a solid lack any long-range order the material is

said to be amorphous. Amorphous materials have also been described as frozen liquids and are thought to contain a distribution of conformations and molecular orientations. A key characteristic of amorphous systems is the lack of a melting point and the presence of a glass transition temperature (T_g). The T_g designates a change in the heat capacity of the material. At temperatures below the T_g the material is in what is referred to as the glassy state, in which the molecules are relatively static with few modes of motion. In the rubbery state, above T_g, the material is able to flow and the molecules have much greater mobility.[3]

A major issue with amorphous materials is that molecules have higher mobility and thus are metastable and significantly more susceptible to chemical degradation than crystalline forms of the same material. However, they often have apparent solubilities that are dramatically higher than their stable crystalline counterparts.[15,16] It has been observed that if amorphous materials are stored at a temperature that is significantly below their T_g that they typically do not crystallize or undergo significant chemical degradation. Thus a rule of thumb has developed which states that if an amorphous material is stored at least 50 °C below its T_g the material will be stable.[17] Therefore, a material stored at room temperature (approximately 25 – 30 °C) should be stable if its T_g is greater than about 75 – 80 °C.

The most stable crystalline form is typically the first choice when choosing the solid form that will be used in a formulation, but as noted previously, in some cases solubility is a limitation. A metastable crystalline form may be chosen to provide moderate increases in the solubility of the API. However, metastable polymorphs cannot always achieve the needed bioavailability or may be physically unstable. An amorphous solid can be used to resolve these

situations, provided that it does not have physical and chemical stability issues. When the T_g is too low to prevent changes at room temperature, one option is to store the material at lower temperatures. While this choice is sometimes used, it makes handling of the final product more difficult and expensive due to the need for special handling.

An alternative to special storage conditions is the preparation of an amorphous dispersion. When the API is molecularly dispersed into another material, typically a polymer, the resulting amorphous material will in theory have a T_g that is the weighted average of the T_g's of the individual components in their pure form.[18,19] If the polymer that is used to produce the amorphous dispersion has a higher T_g than the API, it may be possible to prepare an amorphous material that would offer the enhanced solubility that is needed and the resulting increase in the T_g may by sufficient to allow the product to be stored under ambient conditions. Apart from amorphous dispersions, only physical forms that involve different packing arrangements of the same chemical compound have been considered. The next section will explore crystalline forms where other molecules, in addition to the API, are incorporated into the crystal structure.

1.3.3 Solvates, Salts, and Cocrystals

The previous section on crystalline solids focused on polymorphism, which is defined as different forms having the same chemical composition but differ in their crystal structures. In some cases it is also possible for a compound to pack into a crystalline lattice that incorporates other molecules into the crystal structure. They are not polymorphs, since these additional crystal structures

have a different chemical composition than the original compound, but they are related physical forms. These physical forms are classified as solvates, salts, or cocrystals, depending upon the ionization state of the molecules and the physical properties of the components when in their pure forms.

Solvates, salts, and cocrystals will contain at least two chemical entities that are usually present in stoichiometric amounts, but also may be non-stoichiometric.[20-22] The material is classified as a solvate if one of the chemical entities is a liquid in its pure form at room temperature. The remaining materials can be categorized as a salt if a proton has been transferred between the components, or a cocrystal if no proton transfer has occurred between the components. These physical forms can offer alternatives to the formulation of polymorphs or amorphous forms when the physical properties (i.e., solubility, stability, etc.) of the known polymorphs or amorphous form are not sufficient for formulation.

Considerable time, effort, and resources are spent to identify and characterize all of the potential physical forms of API's. Once the desired physical form is identified, the final step in the synthetic route to make the API is typically designed to produce the desired form. The API is then mixed with the other formulation components to produce the final product that is to be used by the patient. Ideally, the physical form of the API is unaltered during processing. Unfortunately, this is not always the case. The following sections will describe some of the processing steps that are commonly involved in the manufacture of a pharmaceutical formulation and the effects that they can have on the physical form of the API.

1.4 Processing Induced Physical Form Changes

The practice of converting a powder of pure API into a tablet involves the use of numerous processing steps, or unit operations, that can expose the API to various thermal and physical stresses. These stresses can induce partial or full conversions of the API into an undesirable physical form. In the event of an unidentified physical form change the API may undergo accelerated chemical degradation or fail to fully dissolve and deliver a full dose to the patient. The subsequent sections will give an overview of some of the more common unit operations that are used in the production of pharmaceutical formulations and some of the physical form changes that they can induce.

1.4.1 Crystallization

The final step in the synthesis of an API is typically crystallization to yield the desired physical form for the formulation. The crystallization is typically carried out under specific conditions (solvent, temperature, etc.) in order to control the physical form that is obtained. In some cases seed crystals of the desired form are added to the mixture to help drive the crystallization to the desired form.[23] However, in some cases the desired form is still not obtained or the product may be a mixture of forms. This may be caused by a variety of factors, including the presence of impurities in the crystallization medium and the presence or lack of scratches in the vessel in which the crystallization is performed.[7,24,25] Unlike most unit operations, issues during crystallization can often be fixed so that the desired physical form is still obtained. This is typically done by repeating the crystallization several times to remove an impurity,

changing to another vessel, or somehow modifying the procedure to overcome the cause of the initial issue.

1.4.2 Wet Granulation

An important property in the manufacture of pharmaceutical solids is the flowability of the powders that are used. If a powder does not flow well it will tend to clog the manufacturing equipment and result in tablets that are not of a uniform size and do not contain a uniform dose of the API. One method of improving the flowability of a powder is through a process called wet granulation. This process involves mixing the powder with a small amount of a liquid (typically water) in order to agglomerate the particles followed by drying and sieving. These larger agglomerates will have better flow properties and yield tablets that are more uniform in size and dose.

The presence of liquid during the wet granulation can cause a variety of changes in the physical form of the API. For formulations of a metastable polymorph, the liquid may provide a medium in which the API can dissolve and crystallize in the stable form. A formulation containing an anhydrous form of the API may crystallize as a solvate by incorporating some of the liquid into its crystal structure. Other physical forms, such as salts, may undergo disproportionation and crystallize in their individual components.[26-28] However, the liquid that is added is only intended to facilitate the formation of agglomerates and needs to be removed before proceeding to additional unit operations.

1.4.3 Drying

Several unit operations involve the use of solvents but if not removed they can cause issues with both the chemical and physical stability of the API. Therefore, at least one drying step will often be used during the manufacture of a pharmaceutical solid, and will simply involve heating the material to a particular temperature for a certain amount of time.

While drying is one of the simplest unit operations it can have multiple effects on the physical form of the API in a formulation. The addition of heat and solvent molecules (liquid or vapor) can induce many of the polymorph conversion and disproprtionation issues that were discussed previously. However, without careful control and monitoring it can also result in either under or over drying of the materials. If the drying process is not carried out long enough there may still be too much residual solvent in the material. But in some cases a certain amount of residual solvent is desirable, especially when the API is in a solvated form, and if too much solvent is removed then the API may no longer be physically stable and may convert to another physical form, lower order solvate or desolvated form. In some cases the removal of the solvent molecules from a solvate can lead to collapse of the crystal structure and result in an amorphous material.

1.4.4 Compression

Compression is used in two different unit operations, dry granulation and tableting, during the manufacture of pharmaceutical solids. Dry granulation is an alternative to wet granulation but rather than using a liquid to facilitate aggregation, the powder is compressed and then lightly broken apart. In

tableting a tablet press uses enormous compression forces to compact the formulation into a hard tablet. Some API physical forms are sensitive to pressure and can undergo conversions during compression.[29-31]

1.5 Summary and Overview of Subsequent Chapters

In the previous sections the concepts of physical forms as they relate to pharmaceutical solids have been introduced. It was shown that the drug formulation does not simply involve the selection of a physical form that is to be used in a formulation. Rather it is necessary to monitor the entire manufacturing process and the final product for changes in the physical form of the API. The remainder of this dissertation will describe the methods that are used to identify and quantify the physical forms of API's. These methods will then be used to analyze multiple pharmaceutical systems. The following sections provide brief descriptions of each of the subsequent chapters of this dissertation.

Chapter 2: Understanding the Dehydration of Levofloxacin Hemihydrate

Levofloxacin is a fluoroquinolone antibiotic and is known to have several physical forms. Previous reports have claimed that dehydration of levofloxacin hemihydrate leads to collapse of the crystal lattice and produces a mixture of physical forms.[32] However, additional studies will be presented which show that dehydration of the hemihydrate leads to a pure anhydrous form. Additionally, a previously unknown form of anhydrous levofloxacin was discovered and interesting observations concerning the mobility of functional groups within these physical forms will be discussed.

Chapter 3: Detection of Physical Forms in Formulations

It has been shown previously that the physical form of an API can be changed during the manufacture of a formulation. Formulations are mixtures of several materials and it can be difficult to accurately determine the physical form of the API in the end product. In addition, advanced drug delivery technologies (i.e., nanotechnology) can complicate the analysis. Three cases involving nanoparticles of API will be presented: one where the desired API physical form was achieved, one where an undesired API physical form was produced, and another case where a previously unknown form or forms were produced. Additionally, the superior ability of SSNMR spectroscopy, as compared to differential scanning calorimetry, in detecting the physical form of all three APIs within the formulations is demonstrated.

Chapter 4: Quantitation of Physical Forms in Formulations by SSNMR Spectroscopy

Previous studies have demonstrated the ability of SSNMR spectroscopy to quantitate the relative amounts of physical forms. These methods will be extended to the analysis of API within formulations. In this chapter the analysis of API that has been diluted in an excipient in order to mimic a formulation is shown. In addition, improvements in the efficiency of quantitative SSNMR spectroscopy experiments are presented. The precision of these quantitative methods is also discussed.

Chapter 5: Comparison of Physical Form Quantitation by Solid-State Characterization Techniques

The quantitative SSNMR method developed in Chapter 4 is utilized to analyze physical form mixtures of both pure API and API in a mock formulation. The same mixtures are also analyzed by other solid-state characterization techniques that are commonly used for physical form characterization and quantitation. The results from each of the techniques are compared and the relative abilities of each of the techniques to detect and quantitate the physical forms are discussed. Additionally, issues related to the homogeneity of samples prepared by mixing powders are discussed.

Chapter 6: Conclusions and Future Work

A brief discussion of the general results and implications of this thesis will be provided. In addition, suggestions for future work will be presented.

1.6 References

1. Bugay D 1993. Solid-state nuclear magnetic resonance spectroscopy: Theory and pharmaceutical applications. Pharm Res 10(3):317–327.

2. Vasanthavada M, Wang Y, Haefele T, Lakshman JP, Mone M, Tong W, Joshi YM, M Serajuddin AT 2011. Application of melt granulation technology using twin-screw extruder in development of high-dose modified-release tablet formulation. J Pharm Sci 100(5):1923-1934.

3. Byrn S, Pfeiffer R, Stowell J *Solid-state chemistry of drugs*, 1999, pp 576.

4. Storey R, Docherty R, Higginson P, Dallman C, Gilmore C, Barr G, Dong W 2004. Automation of solid form screening procedures in the pharmaceutical industry - How to avoid the bottlenecks. Crystallography Reviews 10(1):45-56.

5. Burger A, Ramberger R 1979. On the polymorphism of pharmaceuticals and other molecular crystals. II. Applicability of thermodynamic rules. Mikrochimica Acta 72:273–316.

6. Burger A, Ramberger R 1979. On the polymorphism of pharmaceuticals and other molecular crystals. I. Theory of thermodynamics rules. Mikrochimica Acta 72:259–271.

7. Reutzel-Edens SM, Kleemann RL, Lewellen PL, Borghese AL, Antoine LJ 2003. Crystal forms of LY334370 HCl: isolation, solid-state characterization, and physicochemical properties. J Pharm Sci 92(6):1196-1205.

8. Murphy BJ, Huang J, Casteel MJ, Cobani A, Krzyzaniak JF 2010. Varenicline L-tartrate crystal forms: Characterization through crystallography, spectroscopy, and thermodynamics. J Pharm Sci 99(6):2766-2776.

9. Katrincic LM, Sun YT, Carlton RA, Diederich AM, Mueller RL, Vogt FG 2009. Characterization, selection, and development of an orally dosed drug polymorph from an enantiotropically related system. Int J Pharm 366(1-2):1-13.

10. Barbas R 2006. Polymorphism of norfloxacin: Evidence of the enantiotropic relationship between polymorphs A and B. Crystal Growth & Design 6(6):1463-1467.

11. Barbas R, Prohens R, Puigjaner C 2007. A new polymorph of norfloxacin: Complete characterization and relative stability of its trimorphic system. Journal of Thermal Analysis and Calorimetry 89(3):687-692.

12. Manduva R, Kett VL, Banks SR, Wood J, Reading M, Craig DQM 2008. Calorimetric and spatial characterization of polymorphic transitions in caffeine using quasi-isothermal MTDSC and localized thermomechanical analysis. J Pharm Sci 97(3):1285-1300.

13. Bauer J, Spanton S, Henry R, Quick J, Dziki W, Porter W, Morris J 2001. Ritonavir: an extraordinary example of conformational polymorphism. Pharmaceutical research 18(6):859-866.

14. Chemburkar S, Bauer J, Deming K, Spiwek H, Patel K, Morris J, Henry R, Spanton S, Dziki W, Porter W, Quick J, Bauer P, Donaubauer J, Narayanan B, Soldani M, Riley D, McFarland K 2000. Dealing with the impact of

ritonavir polymorphs on the late stages of bulk drug process development. Organic Process Research & Development 4(5):413–417.

15. Hancock BC, Parks M 2000. What is the true solubility advantage for amorphous pharmaceuticals? Pharm Res 17(4):397-404.

16. Murdande SB, Pikal MJ, Shanker RM, Bogner RH 2010. Solubility Advantage of Amorphous Pharmaceuticals: II. Application of Quantitative Thermodynamic Relationships for Prediction of Solubility Enhancement in Structurally Diverse Insoluble Pharmaceuticals. Pharmaceutical research 27(12):2704-2714.

17. Hancock BC, Shamblin SL, Zografi G 1995. Molecular mobility of amorphous pharmaceutical solids below their glass transition temperatures. Pharm Res 12(6):799-806.

18. Qian F, Huang J, Zhu Q, Haddadin R, Gawel J, Garmise R, Hussain M 2010. Is a distinctive single Tg a reliable indicator for the homogeneity of amorphous solid dispersion? Int J Pharm 395(1-2):232-235.

19. Shamblin SL, Taylor LS, Zografi G 1998. Mixing behavior of colyophilized binary systems. J Pharm Sci 87(6):694-701.

20. Datta S, Grant DJW 2004. Crystal structures of drugs: Advances in determination, prediction and engineering. Nat Rev Drug Discov 3(1):42-57.

21. Newman AW, Reutzel-Edens SM, Zografi G 2008. Characterization of the "hygroscopic" properties of active pharmaceutical ingredients. J Pharm Sci 97(3):1047-1059.

22. Nguyen TNP, Kim K-J 2008. Kinetic study on hemipenta hydrate risedronate monosodium in batch crystallization by cooling mode. Int J Pharm 364(1):1-8.

23. Brittain HG 2010. Polymorphism and solvatomorphism 2008. J Pharm Sci 99(9):3648-3664.

24. Croker D, Hodnett B 2010. Mechanistic features of polymorphic transformations: The role of surfaces. Cryst Growth Des 10:2806-2816.

25. Meenan PA, Anderson SR, Klug DL In *Handbook of Industrial Crystallization*; Second ed.; Myerson AS, Ed.; Butterworth-Heinemann: Woburn, MA, 2002; pp 67-100.

26. Elder DP, Delaney E, Teasdale A, Eyley S, Reif VD, Jacq K, Facchine KL, Oestrich RS, Sandra P, David F 2010. The utility of sulfonate salts in drug development. J Pharm Sci 99(7):2948-2961.

27. Guerrieri P, Taylor LS 2009. Role of salt and excipient properties on disproportionation in the solid-state. Pharm Res 26(8):2015-2026.

28. Stephenson GA, Aburub A, Woods TA 2011. Physical stability of salts of weak bases in the solid-state. J Pharm Sci 100(5):1607-1617.

29. Feng T, Pinal R, Carvajal MT 2008. Process induced disorder in crystalline materials: differentiating defective crystals from the amorphous form of griseofulvin. J Pharm Sci 97(8):3207-3221.

30. Imamura K, Nomura M, Tanaka K, Kataoka N, Oshitani J, Imanaka H, Nakanishi K 2010. Impacts of compression on crystallization behavior of freeze-dried amorphous sucrose. J Pharm Sci 99(3):1452-1463.

31. Okumura T, Ishida M, Takayama K, Otsuka M 2006. Polymorphic transformation of indomethacin under high pressures. J Pharm Sci 95(3):689-700.

32. Kitaoka H, Wada C, Moroi R, Hakusui H 1995. Effect of dehydration on the formation of levofloxacin pseudopolymorphs. Chem Pharm Bull 43(4):649-653.

Chapter 2

Understanding the Dehydration of Levofloxacin Hemihydrate

2.1 Introduction

The specific aim of this chapter is to understand the dehydration behavior of levofloxacin hemihydrate. Previous studies concluded that dehydration of the hemihydrate form of levofloxacin lead to collapse of the crystal lattice and produces a mixture of physical forms, including amorphous levofloxacin.[1] Thus in a manufacturing process, drying of levofloxacin hemihydrate could generate amorphous material which is chemically or physically unstable. Therefore, further investigations into the dehydration behavior of levofloxacin hemihydrate were undertaken to better understand the materials that are generated.

Significant efforts are typically invested in attempts to identify all of the possible physical forms in which a drug can exist.[2-4] In the case of levofloxacin, a broad spectrum fluoroquinolone antibiotic which is the S-enantiomer of ofloxacin and is twice as potent as the racemate,[5] initial studies showed that it could exist in three anhydrous forms (α, β, and γ), a hemihydrate form, and a monohydrate form.[1] An additional six forms (A, B, C, F, G, and H) were discovered later and are primarily solvates.[6]

The crystal structures and dehydration behavior of the hemihydrate and monohydrate forms of levofloxacin were reported by Kitaoka et al.[1] They produced the γ and α anhydrate forms, respectively, upon dehydration. When the hemihydrate was heated in a differential scanning calorimeter (DSC), the melting of all three anhydrous forms was observed. The authors concluded that the dehydration of the hemihydrate resulted in a collapse of the crystal lattice and, in some cases, produced a mixture of the anhydrous forms. This conclusion

was based primarily on DSC experiments in which either the nitrogen gas flow rate or sample heating rate was changed, but little supporting data was provided from orthogonal techniques to reinforce those claims. They also claimed that several of the experiments produced some amount of amorphous material, but they never directly observed any amorphous material.

The primary methods of characterization of levofloxacin so far have been DSC and powder X-ray diffraction (PXRD). PXRD is effective at studying differences in crystal structure, which has made it the most common technique for the determination of polymorphic forms. However, preferred orientation can cause dissimilarities in the PXRD patterns of samples that have the same crystal structure due to differences in the shape of the particles in the samples.[7] DSC also has limitations because the material can convert between forms during the experiment. Thus, the characterization of pharmaceutical solids often utilizes a variety of techniques in addition to DSC and PXRD.[8-12]

Levofloxacin was initially investigated as a possible model compound for physical form detection and quantitation studies. However, the initial characterizations and attempts to produce the anhydrous forms led to observations that suggested the possible existence of a previously unknown physical form, the δ anhydrate, which was observed when the γ anhydrate was cooled below 54 °C. Additionally, data suggests that the crystal structure of the hemihydrate is closely related to the crystal structures of the δ and γ anhydrous forms. These three forms appear to interconvert reversibly based upon their storage conditions (temperature and relative humidity). The initial observations and the subsequent characterization of the materials are reported below.

2.2 Experimental

2.2.1 Materials

Levofloxacin was purchased from Sigma-Aldrich (Fluka 28266 Lot 1238030, St. Louis, MO) and used without further processing, except where noted. Single crystals of levofloxacin hemihydrate were grown from mixtures of acetonitrile and water with water activities of 0.1 to 0.5 (0.0035 to 0.0280 mL H_2O/mL acetonitrile). Excess levofloxacin was added to each solution at room temperature. The solutions were then heated to approximately 80 °C to dissolve all of the material and then allowed to slowly cool back to room temperature overnight.

XRF Thin Mylar® support film was purchased from SPI Supplies (West Chester, PA). The film was microfine polyester (Mylar®) with a thickness of 0.00010" or 2.5 μm.

2.2.2 Thermogravimetric Analysis (TGA)

Levofloxacin was analyzed by TGA (Q50 TGA from TA Instruments, New Castle, DE) to ascertain residual solvent content and determine the degradation temperature. Approximately 2.75 mg of material was placed in a platinum pan and heated from room temperature to 500 °C at a rate of 10 °C/min under a dry nitrogen atmosphere (total N_2 flow rate = 100 mL/min). The temperature was calibrated by the Currie point method with alumel (T_C = 154.16 °C) and nickel (T_C = 358.28 °C).

2.2.3 Differential Scanning Calorimetry (DSC)

A Q100 DSC from TA Instruments (New Castle, DE), with a refrigerated cooling system, was utilized to characterize levofloxacin samples. Approximately 2.6 mg of levofloxacin was placed in an aluminum pan without a lid and was heated from 0 to 250 °C at a rate of 10 °C/min. A hermetically sealed aluminum pan containing 1.14 mg of levofloxacin hemihydrate was heated from 0 to 150 °C at a rate of 20 °C/min, then cooled to 0 °C, and finally heated to 250 °C at 20 °C/min.

The thermal behavior of each of the anhydrous forms of levofloxacin was investigated using DSC by analyzing 2.7 to 3.7 mg of levofloxacin hemihydrate placed in aluminum pans without lids. The γ anhydrous form of levofloxacin was studied by heating from -50 to 90 °C at a rate of 10 °C/min, held isothermally for 30 min, then cooled to -50 °C at 10 °C/min, reheated to 90 °C at a rate of 10 °C/min, cooled back to -50 °C at 10 °C/min, and finally heated to 250 °C at 30 °C/min. The β and α anhydrous forms of levofloxacin were studied by heating from 40 to 226 or 231 °C (for the β and α forms respectively) at a rate of 30 °C/min, held at the appropriate temperature for 2 min, cooled to 0 °C, and then heated to 250 °C at 30 °C/min.

All samples were analyzed in a dry nitrogen atmosphere (N_2 flow rate = 50 mL/min). The temperature was calibrated by observation of the melting point of decane (T_M = -26.7 °C), indium (T_M = 156.60 °C), and tin (T_M = 231.9 °C). The melting of indium (ΔH_F = 28.11 J/g) was also used to measure the cell constant.

2.2.4 Raman Spectroscopy

Raman spectra of levofloxacin were collected on a HoloLab series 5000 Raman Microscope from Kaiser Optical Systems, Inc. (Ann Arbor, MI). Single crystals of levofloxacin hemihydrate were placed on gold-coated microscope slides for analysis with the 20x objective. Data was collected with the HoloGRAMS software (version 4.1) using a 10 sec exposure time repeated 6 times with cosmic ray filtering. The spectra were collected from 75 to 1876.8 cm^{-1} with a data spacing of 0.3 cm^{-1}. Data was transferred to GRAMS/32 software (version 6.00) and then saved. Variable temperature studies were performed with a Mettler Toledo FP82HT HotStage and a FP90 Central Processor (Columbus, OH). Levofloxacin hemihydrate crystals were heated on the hot stage to remove the water of hydration. While at elevated temperature, the crystals were covered with a microscope cover slip and high vacuum grease was placed around the edges to prevent adsorption of water when the crystals were cooled. The temperature of the hot stage was checked by observing the melting point of 3-methylglutaric acid (mp ~86 °C).

2.2.5 Powder X-Ray Diffraction (PXRD)

PXRD patterns were collected on a Bruker AXS GADDS/D8 Discover diffractometer system (Madison, WI) with a CuKα radiation source. The sample was oscillated during the 60 sec period of data collection, which covered a 2θ range from 6 to 38.2° with a resolution of 0.05°. The sample was held on a variable temperature XYZ stage and the sample temperature was controlled with the GADDS software. Hemihydrate material was heated to 90 °C to remove the

water of hydration and prior to cooling to ambient temperature the material was covered with two layers of Mylar® film, attached with high vacuum grease, to prevent rehydration of the material. The dehydrated levofloxacin was heated from 25 to 95 °C and subsequently cooled to 30 °C with diffraction patterns collected approximately every 5 °C, during both the heating and cooling steps, following a 10 min equilibration period at each temperature.

2.2.6 Solid-State NMR (SSNMR) Spectroscopy

Levofloxacin ^{13}C data was collected with a Chemagnetics CMX-300 spectrometer (Fort Collins, CO) operating at a ^{1}H resonance frequency of 300 MHz. Samples were packed into 7.5 mm ZrO_2 rotors and held in the rotor with Kel-F® end caps, with the top cap containing a small hole to allow water vapor to escape. The packed rotor was spun at the magic angle (MAS)[13] at a rate of 4 kHz with dry compressed air (dew point -40 °C). Free induction decays (FIDs) were collected on a Chemagnetics HX probe using a ramped amplitude cross-polarization (CP)[14] sequence with total suppression of spinning sidebands (TOSS)[15,16] and approximately 66 kHz of proton decoupling using the SPINAL-64[17] method. Between 800 and 3,600 transients were collected for each FID with a pulse delay of either 1, 3, or 5 sec and a contact time of either 2.5 or 1 msec for hemihydrate and the dehydrate respectively. The FIDs contain 2,048 points with a dwell time of 33.3 μsec. Spectra were externally referenced to tetramethylsilane (TMS) using the methyl peak of 3-methylglutaric acid (MGA) at 18.84 ppm.[18] The temperature of the exhaust gas was used to determine the sample temperature based upon calibration with lead nitrate.[19] Peaks in the spectra were assigned based upon ^{13}C chemical shift predictions from the ChemBioDraw Ultra software

package (version 11.0 from CabridgeSoft) and dipolar dephasing experiments using a 60 μsec delay between CP and decoupling.[20]

The ^{13}C MAS direct polarization spectra were collected on the same CMX-300 spectrometer. In these experiments the ^{13}C nuclei were polarized with a 5.1 μsec pulse followed by continuous wave (CW) proton decoupling. Each FID was the sum of between 32 and 168 transients that were collected with a pulse delay of 120 sec and consisted of 1024 points with a dwell time of 33.3 μsec. The spectra were the result of applying 20 Hz of exponential apodization prior to Fourier transformation and they were externally referenced in the same manner as the ^{13}C CPMAS spectra.

Additional SSNMR spectra of levofloxacin were collected on a Bruker Avance DSX 500 MHz (^{1}H frequency) NMR spectrometer (Billerica, MA). Samples were packed into 4 mm ZrO_2 rotors and held in the rotor with either a Kel-F® or o-ring sealed Torlon® drive cap, for levofloxacin hemihydrate and dehydrated levofloxacin hemihydrate respectively. The dehydrated material was prepared by storage of a rotor, packed with levofloxacin hemihydrate, over P_2O_5 at 70 °C for 16 hrs prior to insertion of the o-ring sealed drive cap. The packed rotors were oriented at the magic angle[13] and spun at a rate of 15 kHz with compressed nitrogen gas. FIDs were collected on a Bruker-Biospin BL HFX probe using either a direct polarization sequence, for ^{1}H and ^{19}F, or a ramped amplitude CP[14] sequence, for ^{13}C. The ^{19}F and ^{13}C data was also collected using approximately 85 kHz of proton decoupling via the two-pulse phase modulated (TPPM)[21] method. The ^{1}H spectra are the result of 1 to 2 transients collected with an effective pulse delay of 40 sec and the FIDs consist of 3,598 points with a

dwell of 11.1 μsec. ^{19}F spectra are the result of 64 transients collected with a pulse delay of 13 and 60 sec for hemihydrate and dehydrated materials respectively, and the FIDs contain 1,024 data points with a dwell of 10.9 μsec. The ^{13}C spectra are the result of between 2,048 and 4,096 transients collected with a pulse delay of either 1.5 or 2 sec and a contact time of 2 msec, while the FIDs contain 1,024 data points with a dwell of 33.3 μsec. Spectra were externally referenced to TMS using either H_2O at 4.7 ppm for ^{1}H, trifluoroacetic acid in water at -76.54 ppm for ^{19}F, or the upfield peak of adamantane at 29.5 ppm for ^{13}C. The temperature of the exhaust gas was used to reflect the sample temperature but was not calibrated due to safety concerns related to the use of lead compounds within the facility.

2.2.7 Single Crystal X-Ray Diffraction

The levofloxacin hemihydrate crystal structure was determined at 296 K (23 °C) on a Bruker APEX diffractometer using CuKα radiation (1.54178 Å). The crystal structure was solved by direct methods with SHELX Version 5.1 (Bruker AXS) and subsequently refined by the full-matrix least squares method. The locations of the hydrogen atoms of the carboxylic acid groups were found with the Fourier difference map and were refined with restrained distances. A final difference Fourier revealed no missing or misplaced electron density. Data was visualized using the Mercury 2.2 software package from the Cambridge Crystallographic Data Centre (CCDC).

2.3 Results & Discussion

2.3.1 Thermal Analysis (DSC/TGA)

The material that was obtained from Sigma-Aldrich was characterized by TGA and showed a mass loss of 2.59% when heated to 70 °C (Figure 2.1). This mass loss agrees well with the theoretical water content of levofloxacin hemihydrate (2.43%) and previous observations.[1] The observed mass loss is slightly higher than the theoretical value and may reflect the presence of some additional water adsorbed to the surface of the particles. Thus the levofloxacin material will from this point forward be referred to as levofloxacin hemihydrate. No further significant mass loss was observed until the material reached 240 °C, at which point the material appears to undergo degradation. DSC of the levofloxacin hemihydrate (Figure 2.1) shows an endothermic transition over a broad temperature range (20 to 70 °C) that corresponds to the 2.59% mass loss that was observed by TGA. Three endotherms are also observed, which correspond to melting of the three anhydrous forms of levofloxacin,[1] γ (225.4 °C), β (229.6 °C), and α (232.7 °C). Additionally, an exothermic event was observed between the melting of the γ and β forms, likely due to crystallization of α or β forms from the melted γ form. It is not clear from the data shown in Figure 2.1 if dehydration resulted in a mixture of physical forms, as Kitaoka et al.[1] hypothesized, or a pure γ form that produced the other forms after it melted.

If dehydration of levofloxacin hemihydrate results in collapse of the crystal lattice, it would be expected that the material would not readily take up water to reform the hemihydrate. In order to test this hypothesis, the

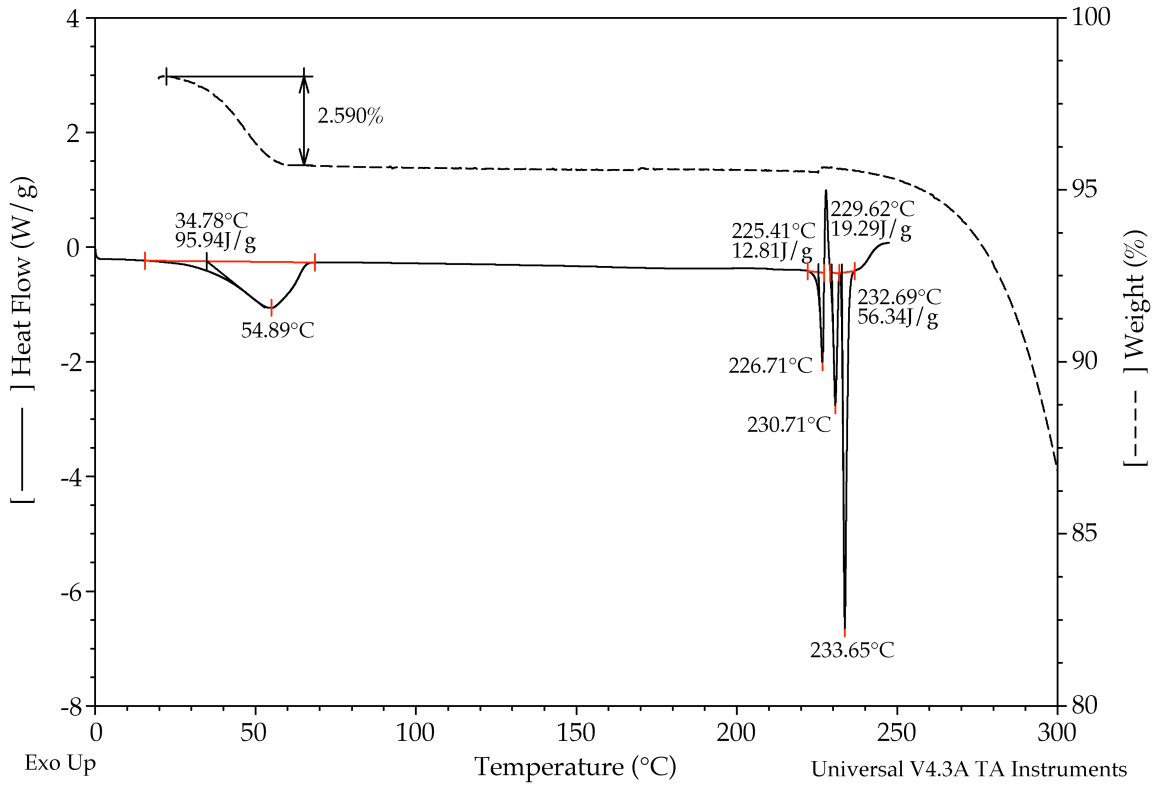

Figure 2.1 DSC (——) and TGA (- - -) thermographs for levofloxacin hemihydrate. Loss of the water of hydration occurs over a temperature range from 30 to 70 °C. The mass loss (2.59%) is consistent with the theoretical water content of 2.43% for levofloxacin hemihydrate. Melting of all three anhydrous forms of levofloxacin is also observed in the DSC thermograph, γ (225.4 °C), β (229.6 °C), and α (232.7 °C).

levofloxacin material was heated in a hermetically sealed pan and subsequently cooled to observe the behavior of the dehydrated material. The resulting DSC thermograph is shown in Figure 2.2. The increased pressures in the sealed pan resulted in dehydration at a higher temperature (approximately 110 °C). A broad exotherm was observed at 100 °C when the material was cooled. This appears to indicate that the water vapor adsorbed to the material at approximately the same temperature as the dehydration event. The similarity of the dehydration endotherm and adsorption exotherm appears to indicate that the crystal lattice did not collapse. When the material was reheated the same endotherm was observed at 110 °C, indicating that the hemihydrate was produced during the cooling step. Further heating of the material resulting in a relatively sharp endotherm that was consistent with melting of the γ form.

If amorphous levofloxacin was produced by the dehydration of the hemihydrate it might readily crystallize as the hemihydrate in the presence of the water vapor, which could explain the exotherm that was observed in Figure 2.2. Therefore, a similar experiment (Figure 2.3) was performed except the water vapor was allowed to escape to reduce the likelihood of crystallization due to the presence of the water, which was seen in the sealed pan. Levofloxacin hemihydrate was heated to 90 °C in an open pan and held isothermally for 30 min. The subsequent heating and cooling steps did not show any events that would be consistent with the presence of any amorphous material. However, the dehydrated material does show various endo- and exothermic events when heated and cooled, respectively.

A previously unreported exothermic event was observed at 54 °C when the dehydrated levofloxacin hemihydrate was cooled (Figure 2.3). The event

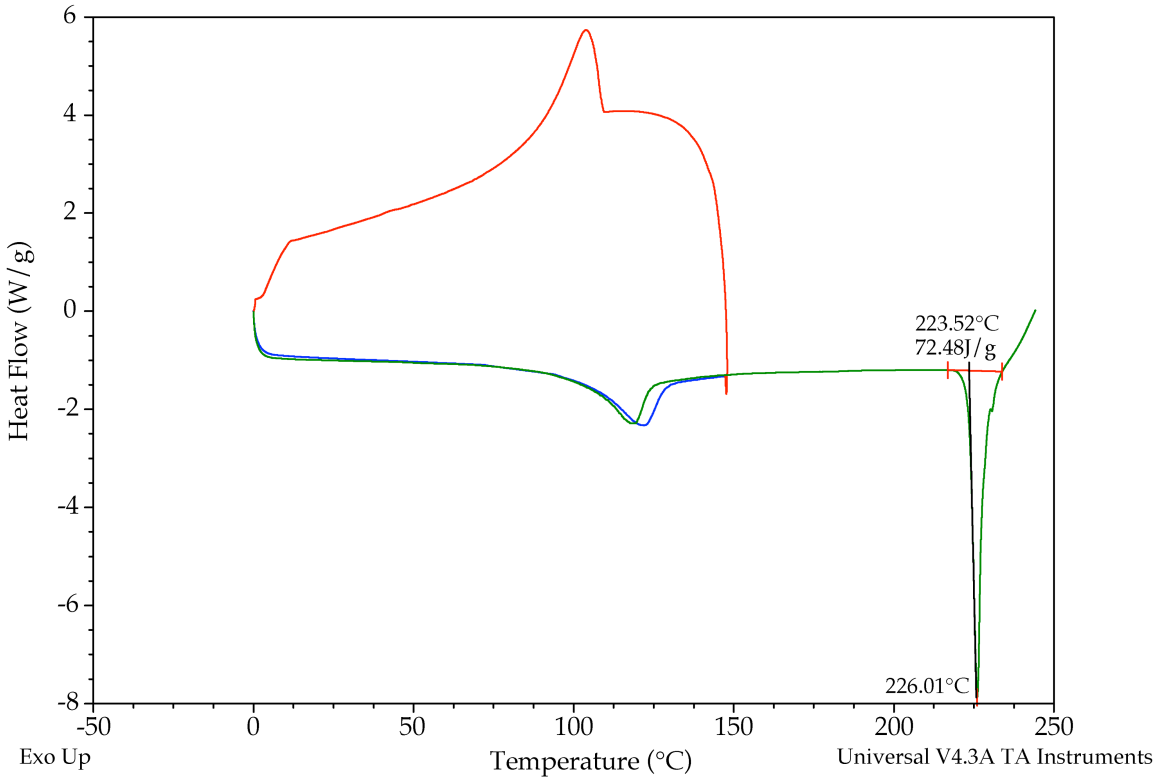

Figure 2.2 DSC thermograph of levofloxacin hemihydrate sealed in a hermetic aluminum pan. The initial heating (**blue**) shows an endotherm centered at 110 °C, which likely corresponds to dehydration. When the sample is cooled (**red**) an exotherm occurs at a similar temperature. The second heating (**green**) of the sample shows an endotherm at a slightly higher temperature than the first heating period and the sample eventually melts as the γ anhydrate of levofloxacin.

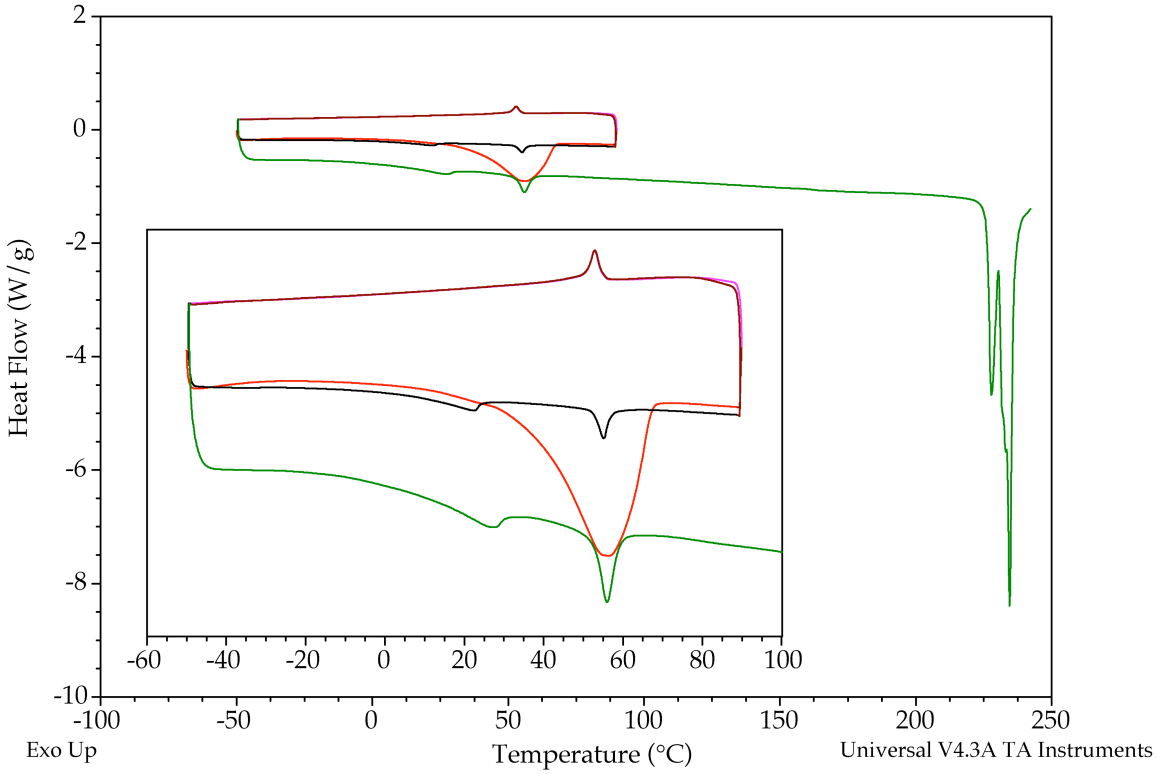

Figure 2.3 DSC thermograph of levofloxacin hemihydrate analyzed in an aluminum pan without a lid. The insert expands the data from the temperature cycles between -50 and 90 °C. The initial heating (**red**) shows dehydration at approximately 55 °C. When the sample was cooled (**fuchsia**) an exotherm is observed at 55 °C. The second heating (**black**) of the sample presents two endotherms at 20 and 55 °C, respectively. A second cooling period (**magenta**) shows an exotherm, comparable to the first cooling period. The final heating (**green**) shows two endotherms that appear similar to the endotherms that were observed during the second heating period. Melting of the three, anhydrate forms of levofloxacin (γ, β, and α) is also observed in the final heating period.

occurred at the same temperature as the dehydration but has a significantly smaller heat of transition. Heating of the material resulted in two endothermic events at 20 and 54 °C. The endotherm at 54 °C was similar to the heat of transition and the temperature of the exotherm that was observed during cooling. This suggests that the process may be reversible but it does not seem to be consistent with the previously observed dehydration/hydration behavior. The second cooling of the dehydrated material displayed behavior that was virtually identical to the first cooling. Subsequent heating of the material at an elevated heating rate showed the same two endotherms, suggesting that both of the events are reversible. The event at 54 °C did not change in temperature when the heating rate was changed, suggesting that the event is thermodynamic, rather than kinetic. Conversely the 20 °C event appears to be kinetic because it shifted to approximately 26 °C when the heating rate was increased. However, while the event does seem to be reversible, a corresponding exotherm is not observed when the sample is cooled.

It is not clear what physical changes in the dehydrated levofloxacin produce the transitions that are observed in Figure 2.3. When the dehydrated levofloxacin was finally heated to 250 °C, melting of all three anhydrous forms was observed (Figure 2.3). In an effort to understand if the low temperature transitions were related to the γ anhydrate, another anhydrous form, or a combination of the forms, the data in Figures 2.4 and 2.5 were collected. During these experiments the levofloxacin hemihydrate was heated to either 226 or 231 °C to ensure melting of only γ or both γ and β forms, respectively. The resulting materials were cooled and reheated to see if the same low temperature

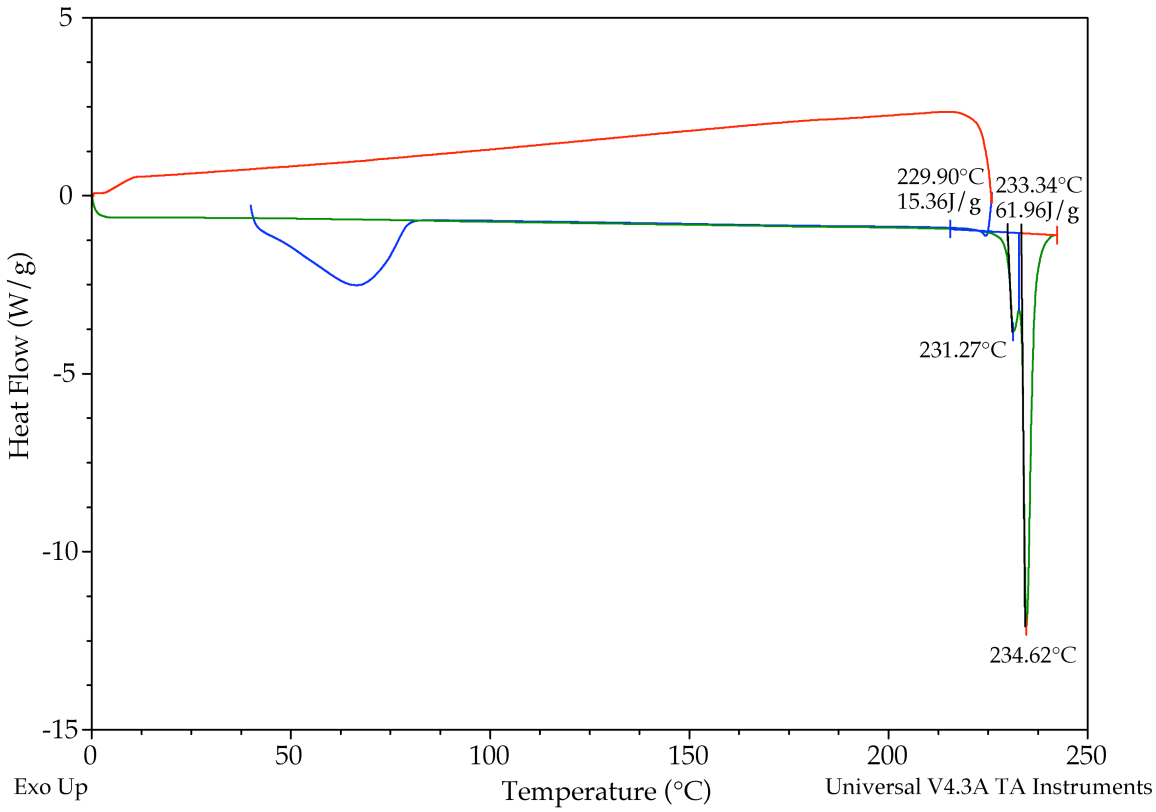

Figure 2.4 DSC thermograph of levofloxacin hemihydrate analyzed in an aluminum pan without a lid. The initial heating (**blue**) to 226 °C shows an endotherm centered at 75 °C, which is consistent with dehydration. When the sample is cooled (**red**) no exotherm or other event is observed. The second heating (**green**) of the sample shows only two endotherms corresponding to melting of the β and α anhydrous forms of levofloxacin.

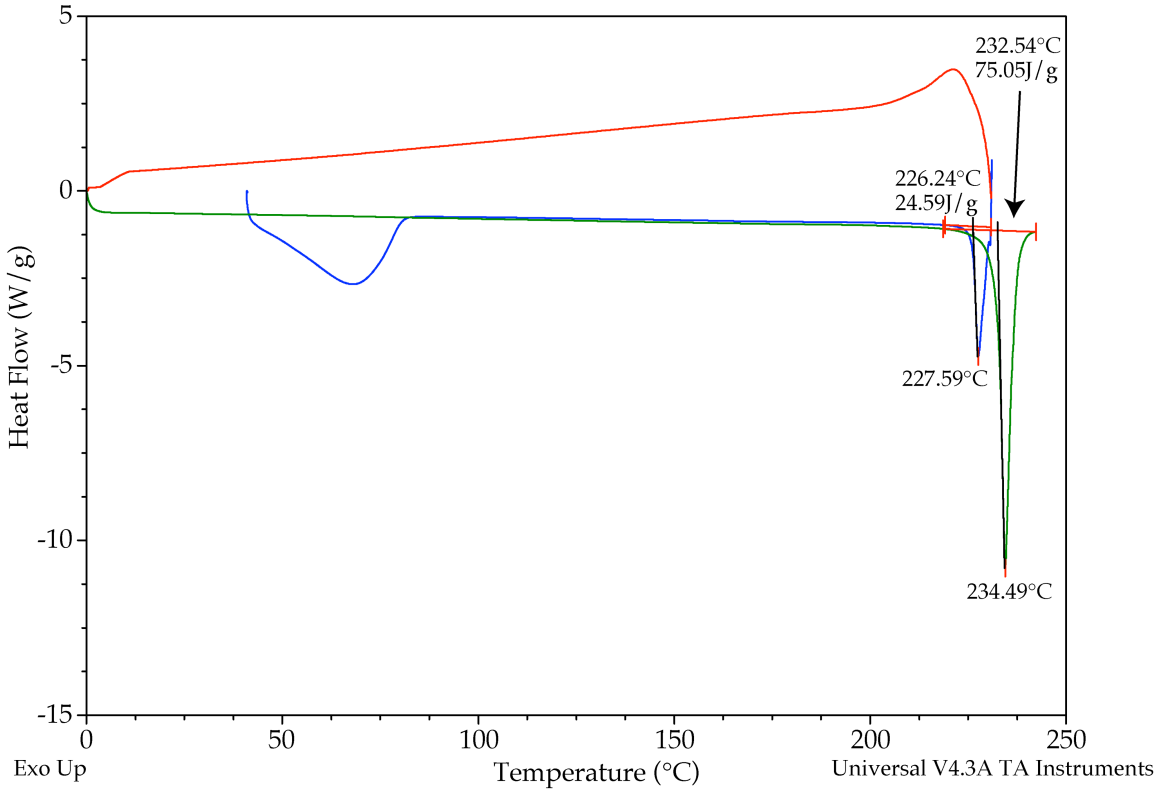

Figure 2.5 DSC thermograph of levofloxacin hemihydrate analyzed in an aluminum pan without a lid. The initial heating (**blue**) to 231 °C shows an endotherm centered at 75 °C, which is consistent with dehydration, and melting of the γ anhydrous form of levofloxacin. When the sample is cooled (**red**) a broad exotherm is observed at approximately 225 °C. The second heating (**green**) of the sample shows only one endotherm corresponding to melting of the α anhydrous form of levofloxacin.

transitions would be observed. Figure 2.4 contains the data from the experiment where the material was initially heated to 226 °C to melt only the γ form. When the sample was cooled and reheated the only observed events were melting of the β and α forms. Similar results were observed when the material was initially heated to 231 °C (Figure 2.5), except only melting of the α form was observed during the second heating step. An exothermic event may also have occurred at the beginning of the cooling step (Figure 2.5), and likely represents crystallization of the α form from melted levofloxacin. This data indicates that the low temperature transitions are either isolated to the γ form or at least require the presence of the γ form.

2.3.2 Raman Spectroscopy

The Raman spectrum of levofloxacin hemihydrate is shown in Figure 2.6. Unfortunately there is no previously reported Raman data that can be used to confirm that the material is consistent with the previously reported hemihydrate materials. The spectrum was collected on a microscope in order to use a hot stage to examine the effects of dehydration and temperature upon levofloxacin hemihydrate. When the levofloxacin hemihydrate was dehydrated there were significant changes in the Raman spectrum (Figure 2.6). Unfortunately, there is also no reference Raman data for the anhydrous forms of levofloxacin. Therefore, it is not possible to identify the physical form or forms that were present in the dehydrated material.

The dehydrated levofloxacin hemihydrate was sealed under a glass cover slip with grease, which prevented levofloxacin hemihydrate from forming when

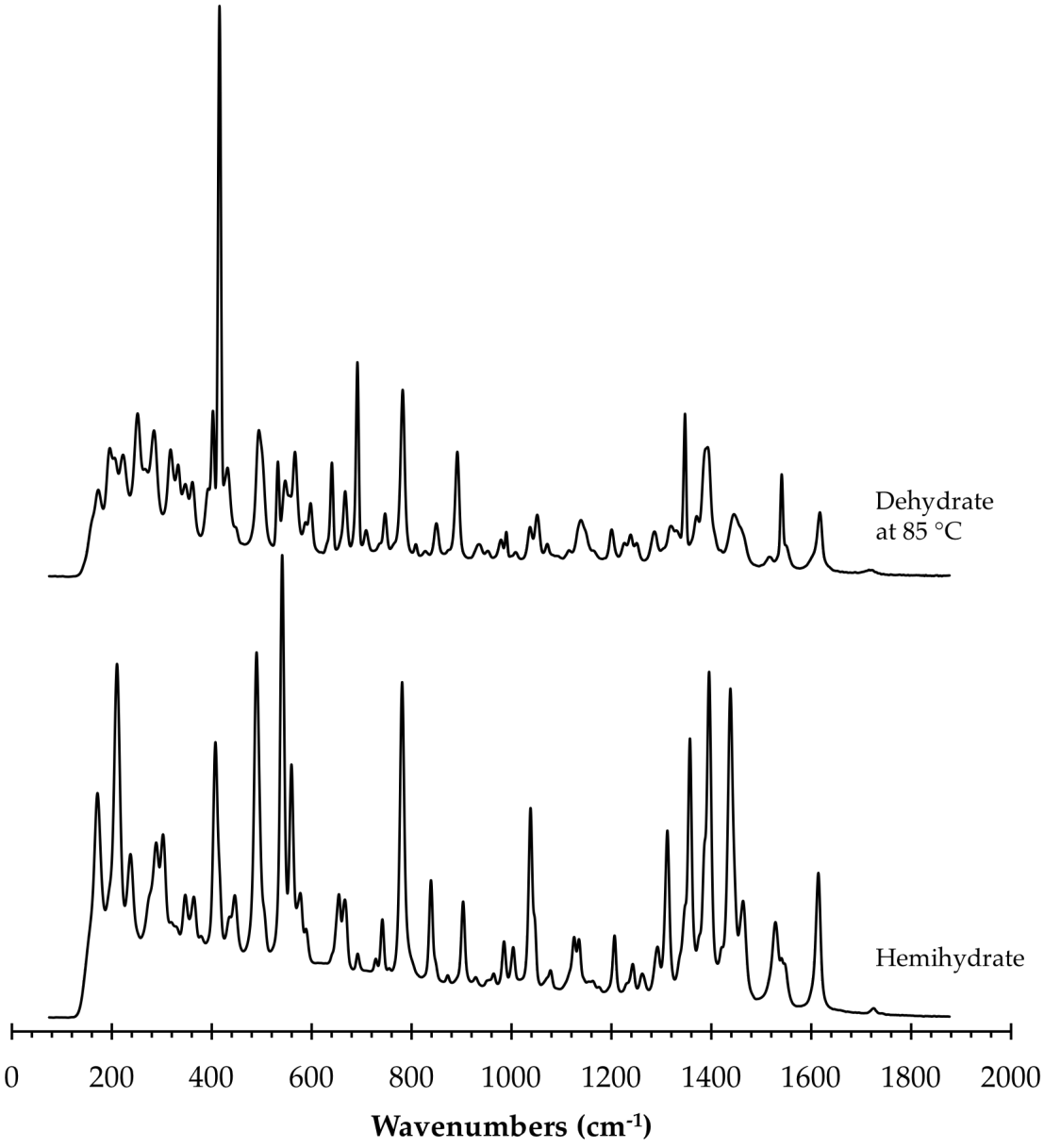

Figure 2.6 Raman spectrum of a single crystal of levofloxacin hemihydrate that was grown from an acetonitrile solution with a water activity of 0.2. The crystal was heated to 85 °C to remove the water of hydration. The spectrum of the resulting anhydrous material is shown for comparison.

the material was cooled to 30 °C. The dehydrated material was then heated and Raman spectra were collected at various temperatures (Figure 2.7). There were no obvious changes in the Raman spectra that were collected from 30 to 100 °C; however, some very subtle changes were observed below 700 cm^{-1}. The changes are indicated by arrows in Figure 2.7 and were most apparent at approximately 206, 268, 318 to 364, 494, 557, 588, 598, and 631 cm^{-1}. In addition, these changes occurred around 48 °C and were reversible when the material was cooled (data not shown). At the conclusion of the experiment the cover slip was removed and the Raman spectrum of the resulting material matched the spectrum of the initial levofloxacin hemihydrate.

These variable temperature Raman investigations were consistent with the previous DSC observations. Following dehydration of levofloxacin hemihydrate the resulting material has the ability to readily reform levofloxacin hemihydrate when cooled in the presence of water vapor. In addition, when the dehydrated levofloxacin hemihydrate is protected from water vapor it undergoes a reversible transformation at approximately 50 to 55 °C. Unfortunately, the hot stage did not have the ability to cool the sample so it was not possible to use Raman to investigate the endothermic event that was observed at around 20 °C by DSC for the dehydrated material.

2.3.3 PXRD

A reference PXRD pattern of levofloxacin hemihydrate was published by Kitaoka et al.[1] and could be compared with the pattern in Figure 2.8. Unfortunately the relatively low quality of the reference data prevents an unambiguous match of the patterns. However, the two patterns are similar and

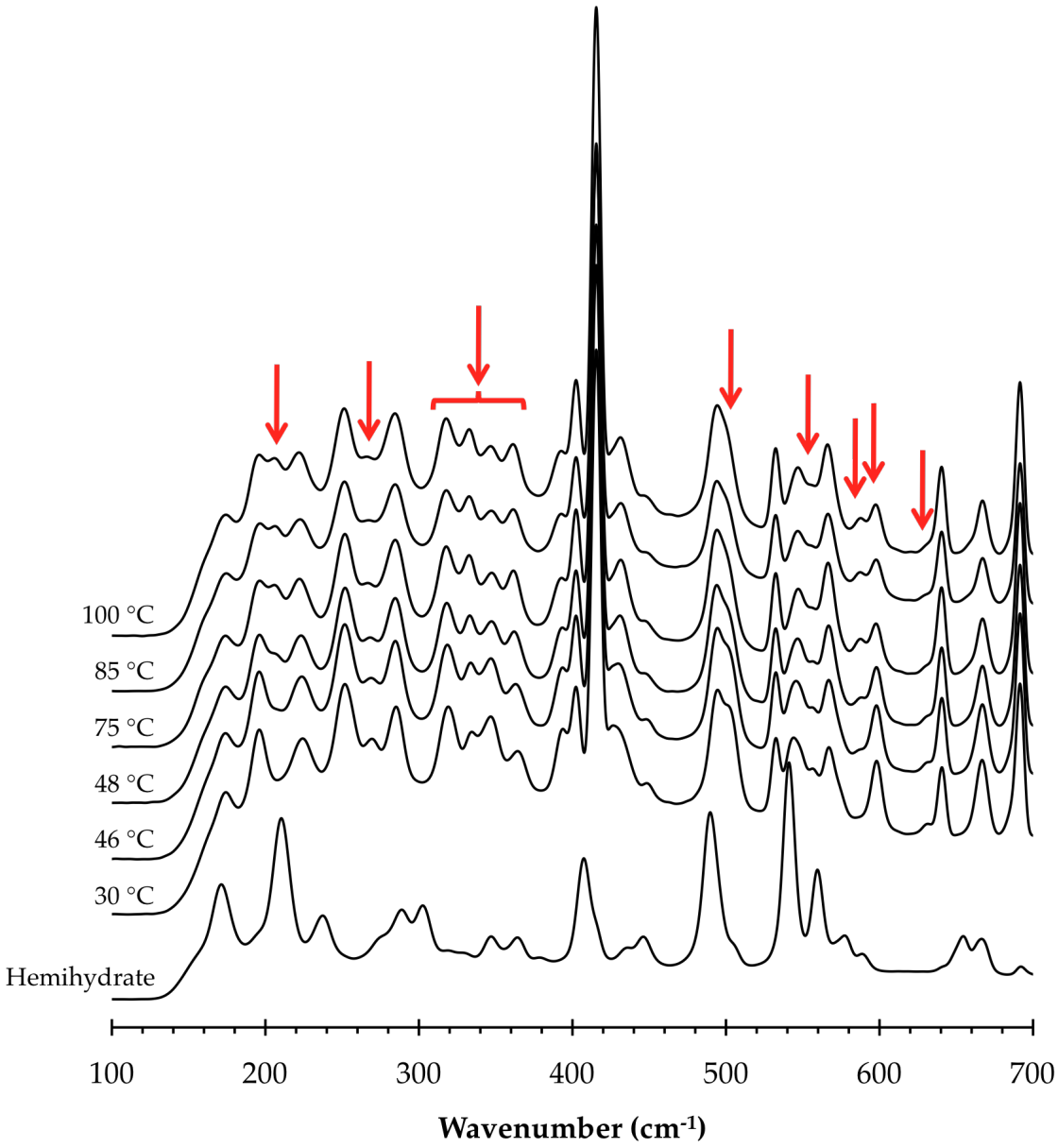

Figure 2.7 Raman spectra of the dehydrated levofloxacin hemihydrate single crystal (Figure 2.6) collected at the indicated temperatures. The crystal was dehydrated at 85 °C and then was protected from water vapor with a cover slip and high vacuum grease. The anhydrous material was then cooled to 30 °C and then progressively heated to 100 °C with spectra collected at various points during the heating. The red arrows designate locations of spectra changes that occur during heating. The spectrum of the original hemihydrate material is shown for comparison; note that this spectrum was collected without the cover slip in place. Other portions of the spectra were omitted because they did not change during the experiment.

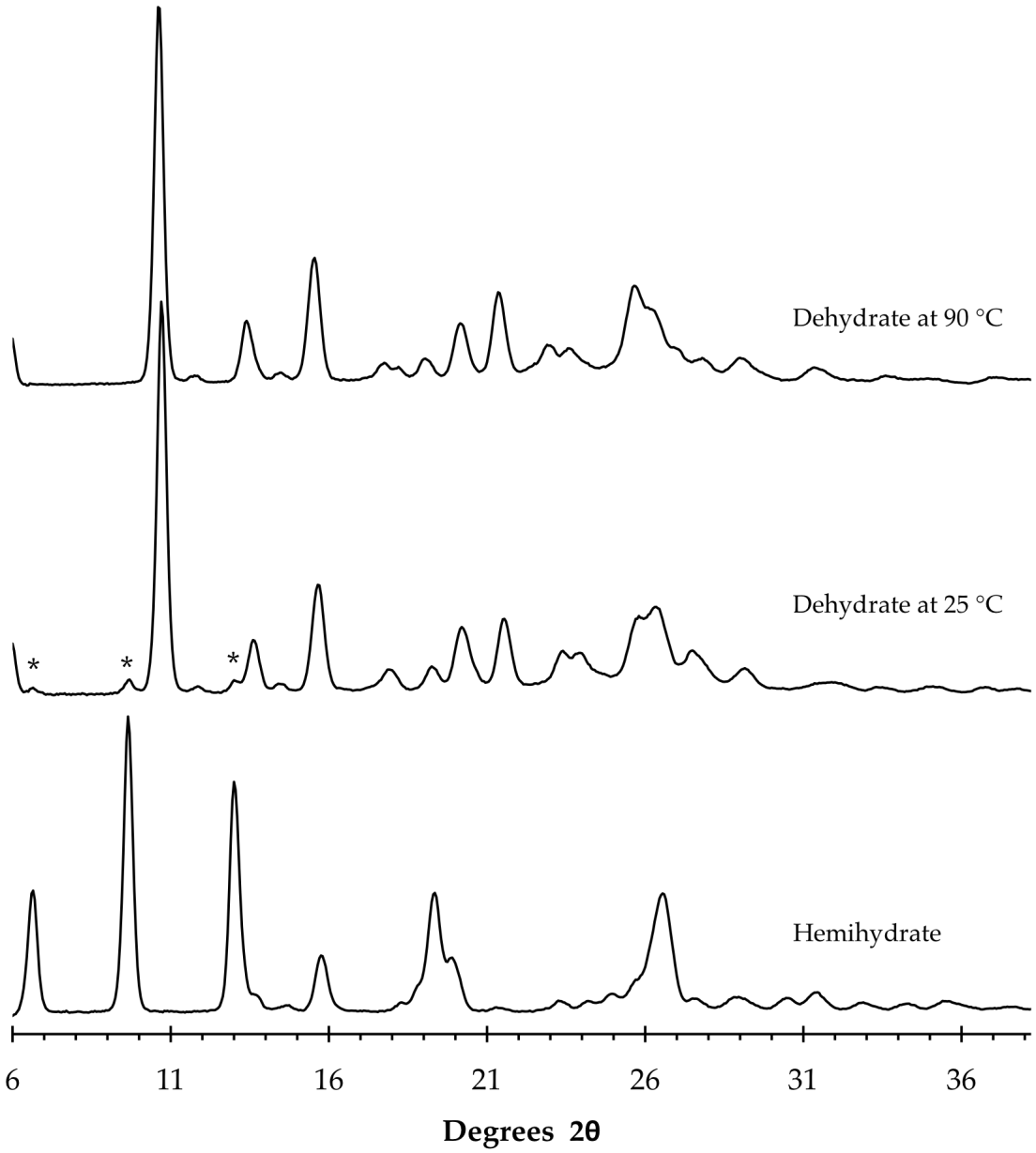

Figure 2.8 PXRD pattern of levofloxacin hemihydrate. The material was heated to 90 °C to remove the water of hydration, and the PXRD pattern of the resulting anhydrous material is shown at 90 °C. The material was protected from water vapor with a double layer of Mylar® film prior to cooling to 25 °C. The PXRD pattern of the cooled, dehydrated material is also shown. * = Peaks that are characteristic of levofloxacin hemihydrate.

the pattern in Figure 2.8 is not consistent with the diffraction patterns of any of the other levofloxacin materials that the authors reported.[1]

Dehydration of levofloxacin hemihydrate at 90 °C produced significant changes in the PXRD pattern (Figure 2.8), reflecting significant changes in the crystal structure upon dehydration. The diffraction pattern of the dehydrated material at 90 °C is similar to the data that was reported by Kitaoka et al.[1] when levofloxacin hemihydrate was heated to 108 °C. However, as with the Raman spectra it is not possible to identify the physical form or forms that may be present due to a lack of reference data for the anhydrous forms. The dehydrated levofloxacin hemihydrate was protected from atmospheric water vapor with Mylar® film and the material was cooled to 25 °C. The resulting diffraction pattern is shown in Figure 2.8 and displays subtle differences from the dehydrated material at 90 °C. In addition, three small diffraction peaks were observed in the cooled material, which indicate that a small amount of hemihydrate was present in the material.

PXRD patterns were collected at a variety of temperatures in order to identify the temperature at which these subtle changes in the diffraction pattern occur (Figure 2.9). The diffraction pattern changed when the dehydrated material was heated from 47 to 52 °C. Specifically, changes were observed at 13.5, 18, 21.4, 22.9 to 24, 25.8 to 28, and 31.4 °2θ. These changes were reversible when the material was cooled, and the temperature of the conversion was the same as when the material was heated. The observations are consistent with the DSC and Raman studies where an unidentified transition occurs in the dehydrated levofloxacin at 50 to 55 °C and appears to be reversible. Additionally, the PXRD results indicate that the transition is related to a change

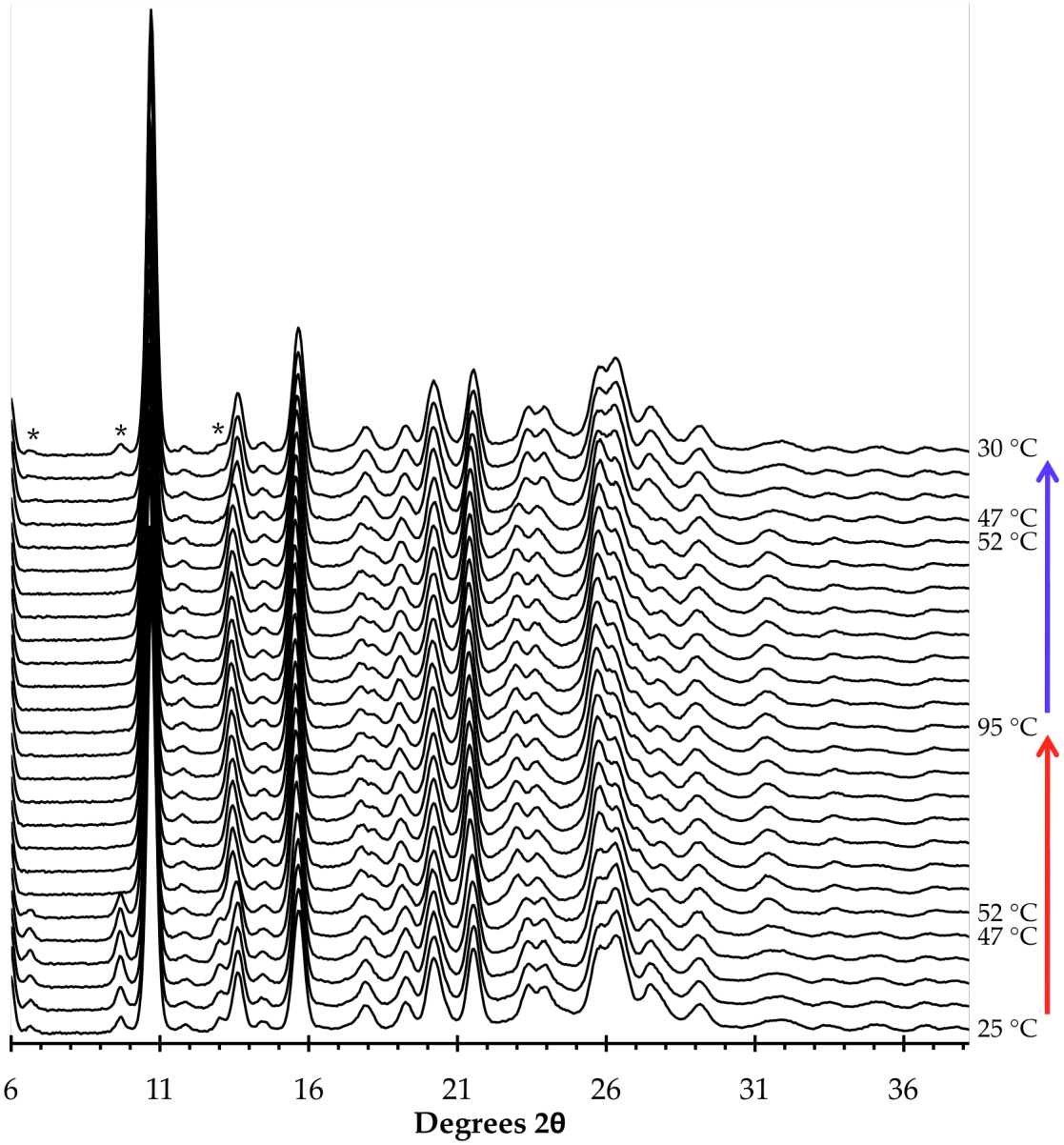

Figure 2.9 PXRD patterns of hemihydrate hemihydrate following dehydration at 90 °C and protection from water vapor with a double layer of Mylar® film. Diffraction patterns were collected approximately every 5 °C as the material was heated from 25 to 95 °C and subsequently cooled to 30 °C. * = Peaks that are characteristic of levofloxacin hemihydrate.

in the crystal structure, albeit a subtle change. Unfortunately, the equipment did not have the ability to cool the sample and thus PXRD could not be used to investigate the lower temperature transition that was observed in the DSC experiments.

The peaks associated with levofloxacin hemihydrate increased in intensity (Figure 2.9) until the sample was heated over 52 °C, at which point the peaks disappeared. When the dehydrated material was cooled back to 35 °C the peaks were observed and increased in intensity when the sample was cooled further. The Mylar® film is not impervious to water and thus water vapor is able to slowly diffuse though the film and generate levofloxacin hemihydrate when the temperature is sufficiently low. However, this process is very slow which minimized the levels of hemihydrate that formed during the variable temperature experiments. After the dehydrated material was cooled back to 30 °C the Mylar® film was removed and the PXRD pattern (not shown) revealed that the material rapidly converted back to levofloxacin hemihydrate after exposure to atmospheric water vapor. This observation is also consistent with the earlier studies, which showed that the dehydrated levofloxacin hemihydrate readily takes up water vapor to produce the hemihydrate when it is below the dehydration temperature.

2.3.4 SSNMR (^{1}H 300 MHz)

The ^{13}C cross-polarization magic angle spinning (CPMAS) spectrum of levofloxacin hemihydrate is shown in Figure 2.10. The assignments of the peaks in the spectrum reveal that, for the most part, each carbon atom gives rise to one peak in the spectrum. The piperazine ring contains four carbons but only

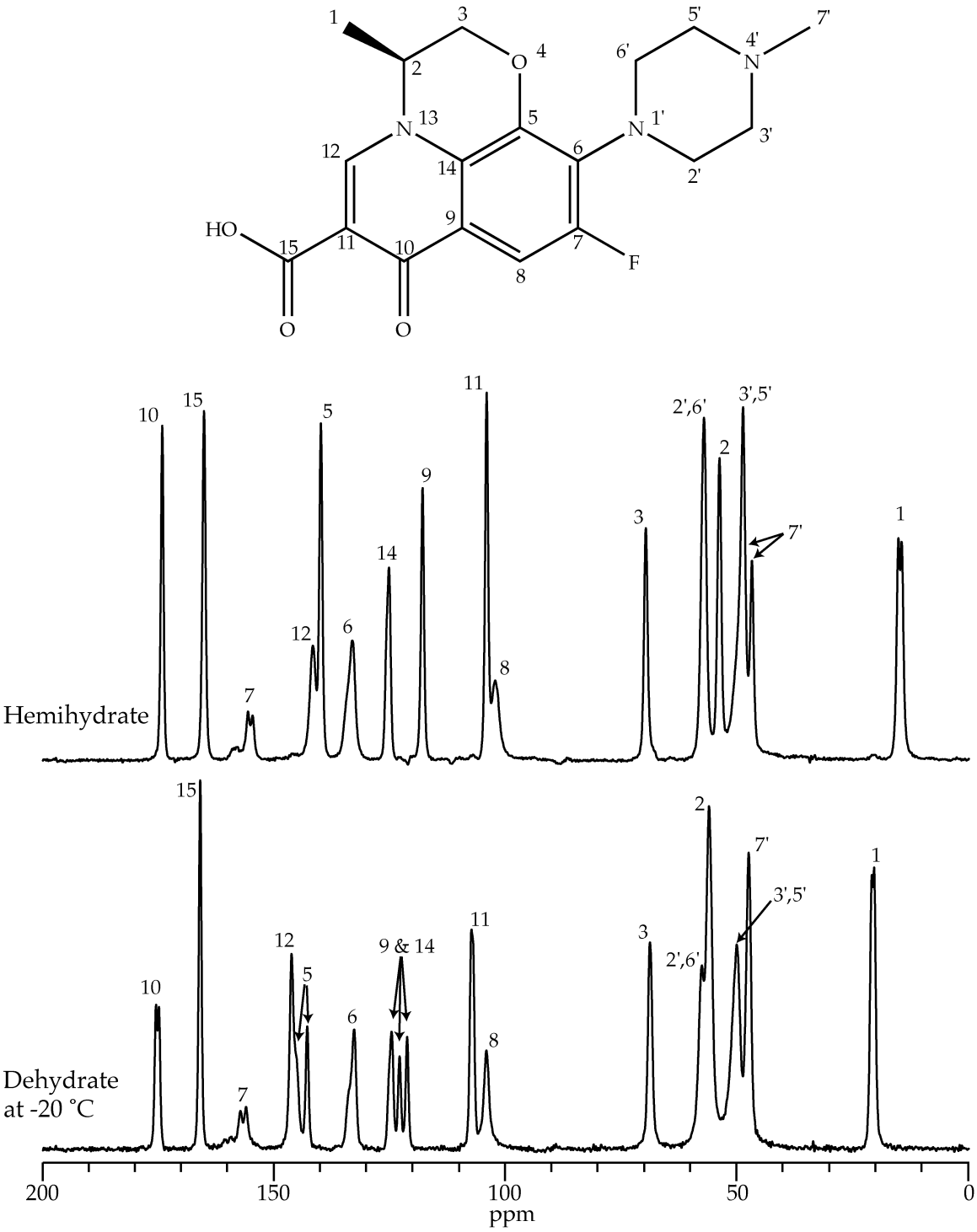

Figure 2.10 ^{13}C CPMAS spectra (^{1}H 300 MHz) of levofloxacin hemihydrate and dehydrated levofloxacin hemihydrate. The peak assignments are from dipolar dephasing experiments and ChemBioDraw software predictions of ^{13}C chemical shifts in solution.

displays two peaks because in the levofloxacin hemihydrate the chemically equivalent pairs (C-3′,5′ and C-2′,6′) likely do not have sufficiently different environments to yield distinct peaks. Three carbons (C-1, C-7, and C-7′) are split into two peaks each, which can be explained by the previously reported crystal structure of levofloxacin hemihydrate.[1] The crystal structure consists of two molecules in the asymmetric unit cell (Z′ = 2) indicating that there are two different molecular conformations that exist within the crystal structure. Therefore, some carbons give rise to two peaks, one for each of the conformations that exist in the crystal structure.

When levofloxacin hemihydrate was dehydrated there were significant changes in the ^{13}C spectrum; however, due to a number of complicating factors the assignment of the peaks was performed at -20 °C. Figure 2.10 shows the peak assignments for the dehydrated material. Many of the carbon atoms produce a single peak after dehydration, and the piperazine ring carbons still yield only two peaks. However, C-5 (assignments from dipolar dephasing experiment) and C-10 show peak splitting that is consistent with a Z′ = 2, and C-7′ is no longer split into two peaks. In addition, splitting is observed in the peaks around 123 ppm (three peaks representing two carbon atoms) but it is not clear which carbon atom is associated with the splitting. The shape of the downfield peak (124.7 ppm) suggests that it is coupled to nitrogen and thus would be C-14, and the other two peaks (121.3 and 123.0 ppm) appear more symmetrical in shape and seem to be consistent with C-9. These observations suggest that only one crystalline form of levofloxacin was present following dehydration. If multiple crystalline forms were present it would be expected that more peaks would be observed. In addition, there is no evidence of any amorphous levofloxacin being

present after dehydration of the hemihydrate.

As the dehydrated levofloxacin hemihydrate was heated to 20 °C (Figure 2.11) the peaks of the piperazine ring carbons gradually decreased in intensity and broadened. One potential explanation is a reduction in CP efficiency resulting in reduced magnetization transfer to the piperazine carbons. If changes in CP efficiency are the cause of the peak disappearance then direct polarization experiments should not show the same behavior because CP is not used to polarize the ^{13}C nuclei. In fact, direct polarization experiments (Figure 2.12) do show the same disappearance of the piperazine peaks, which suggests that the actual cause is a loss of ^{1}H decoupling. This effect is isolated to the piperazine ring and suggests that the ring is undergoing motions and that those motions are beginning to occur on the timescale of the decoupling (66 kHz) or MAS rate (4 kHz) at around 0 to 20 °C.

When the dehydrated material was heated further (Figure 2.11) all of the peaks that were split appear to merge into a single peak. Thus above 50 °C each carbon atom yields only one peak, except for the piperazine ring carbons which are still too broad to be observed. The splitting in the ^{13}C CPMAS spectra of the dehydrated levofloxacin hemihydrate at temperatures below 50 °C suggested that the crystal structure contained two molecules in the asymmetric unit cell ($Z' = 2$). The loss of that splitting above 50 °C indicates that the crystal structure has changed and now only contains one molecule per asymmetric unit cell ($Z' = 1$). The levofloxacin hemihydrate (Figure 2.13) did not display any changes over the entire temperature range (-20 to 60 °C), with the exception of the highest temperature where peaks associated with the dehydrated material were observed.

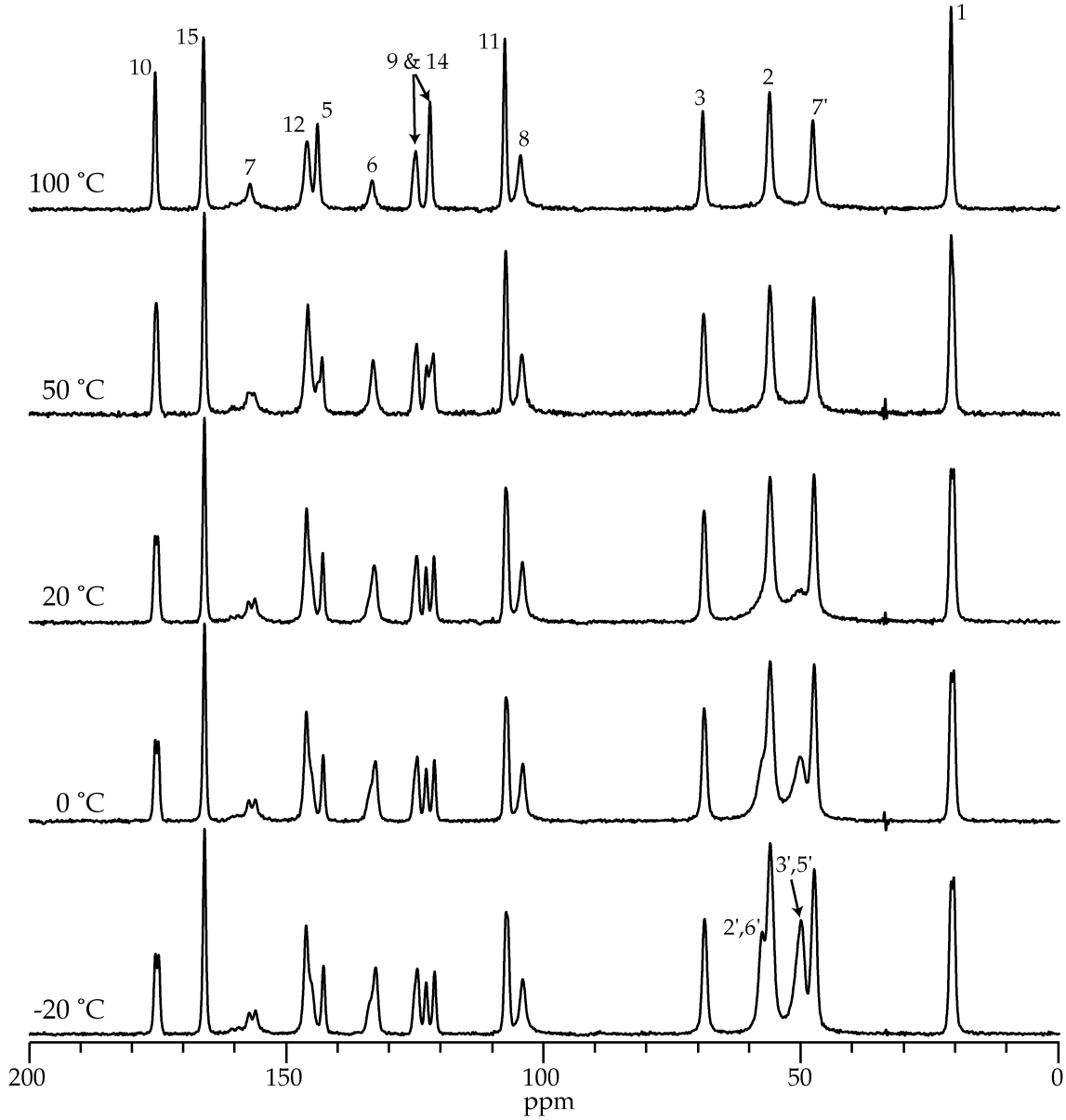

Figure 2.11 ^{13}C CPMAS spectra (^{1}H 300 MHz) of dehydrated levofloxacin hemihydrate at various temperatures. Between -20 and 20 °C significant changes are observed in the peaks for the piperazine ring carbons. At 50 °C there is a change in the splitting behavior of the peaks of carbons 1, 5, 10, and either 9 or 14.

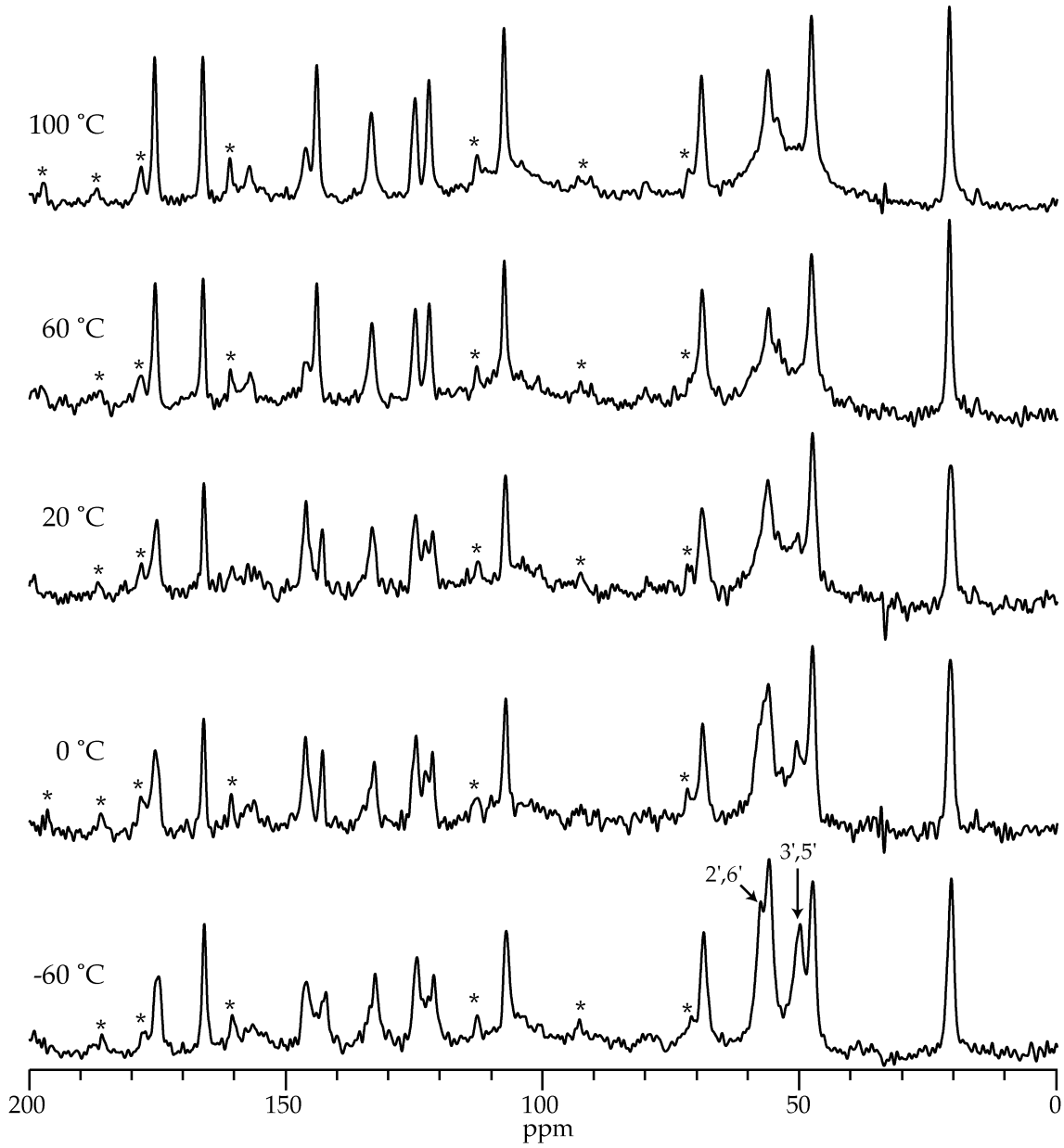

Figure 2.12 ^{13}C MAS spectra (^{1}H 300 MHz) of dehydrated levofloxacin hemihydrate at various temperatures. The spectra display the same trends as the CPMAS spectra in Figure 2.13, indicating that none of the changes are due to a change in the ability to perform cross polarization between ^{1}H and ^{13}C. * = spinning sidebands

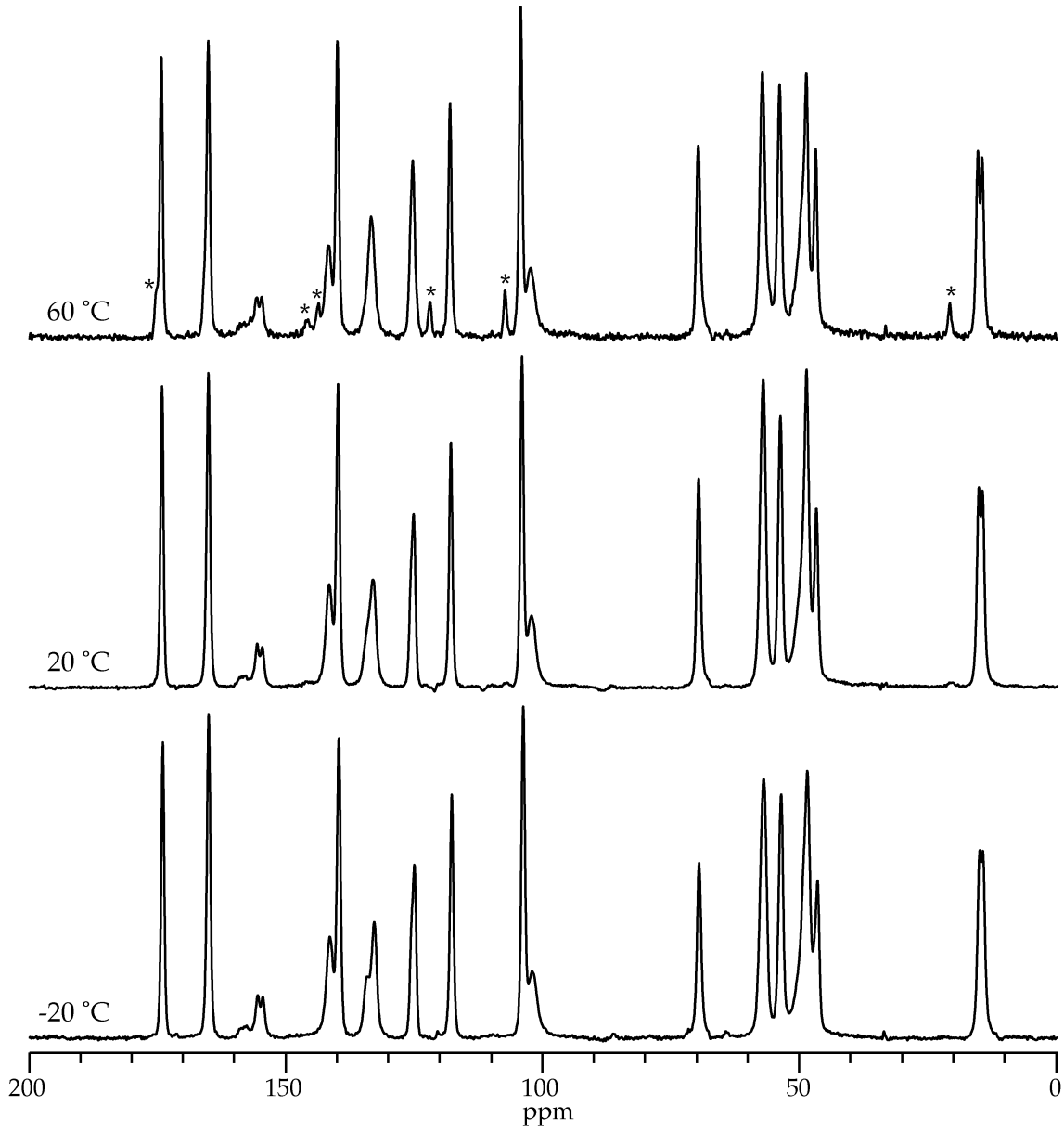

Figure 2.13 ^{13}C CPMAS spectra (^{1}H 300 MHz) of levofloxacin hemihydrate at various temperatures. There are no significant differences in the spectra apart from the appearance of small peaks in the spectrum at 60 °C due to some dehydration of the material. * = Peaks that are associated with dehydrated levofloxacin hemihydrate.

2.3.5 SSNMR (^{1}H 500 MHz)

In order to confirm the SSNMR observations and see how they would change with field strength, both the hemihydrate and the anhydrous materials were also studied with a spectrometer operating at a ^{1}H frequency of 500 MHz. The ^{1}H spectrum of levofloxacin hemihydrate (Figure 2.14) does not display any clearly resolved peaks, which is typical for pharmaceutical solids. But when the material was dehydrated the resolution of the peaks improved, suggesting that there is increased mobility of the material. Based on the previous data (^{1}H 300 MHz) the increased mobility is likely associated with the piperazine ring. This is supported by the ^{13}C spectra (Figure 2.15), which are consistent with the previous experiments (Figure 2.11).

Safety concerns prevented calibration of the sample temperature. Thus the reported temperatures reflect the temperature of the gas that was escaping the spin module, which contained the sample. Based upon previous work it is known that spinning of a sample, in the probe that was used, results in sample heating of approximately 35 °C when no temperature control is used. Therefore, the reported temperatures in Figures 2.14, 2.15, and 2.16 could be as much as 35 °C below the actual sample temperature, although the use of temperature control likely reduces the differences between the measured temperature and actual sample temperature.

The ^{13}C spectra (Figure 2.15) are consistent with the previously observed changes in dehydrated levofloxacin hemihydrate when the temperature is changed. The disappearance of the piperazine ring peaks appears to occur at about the same temperature but is actually occurring at a higher sample temperature (see discussion above about sample heating). This transition was

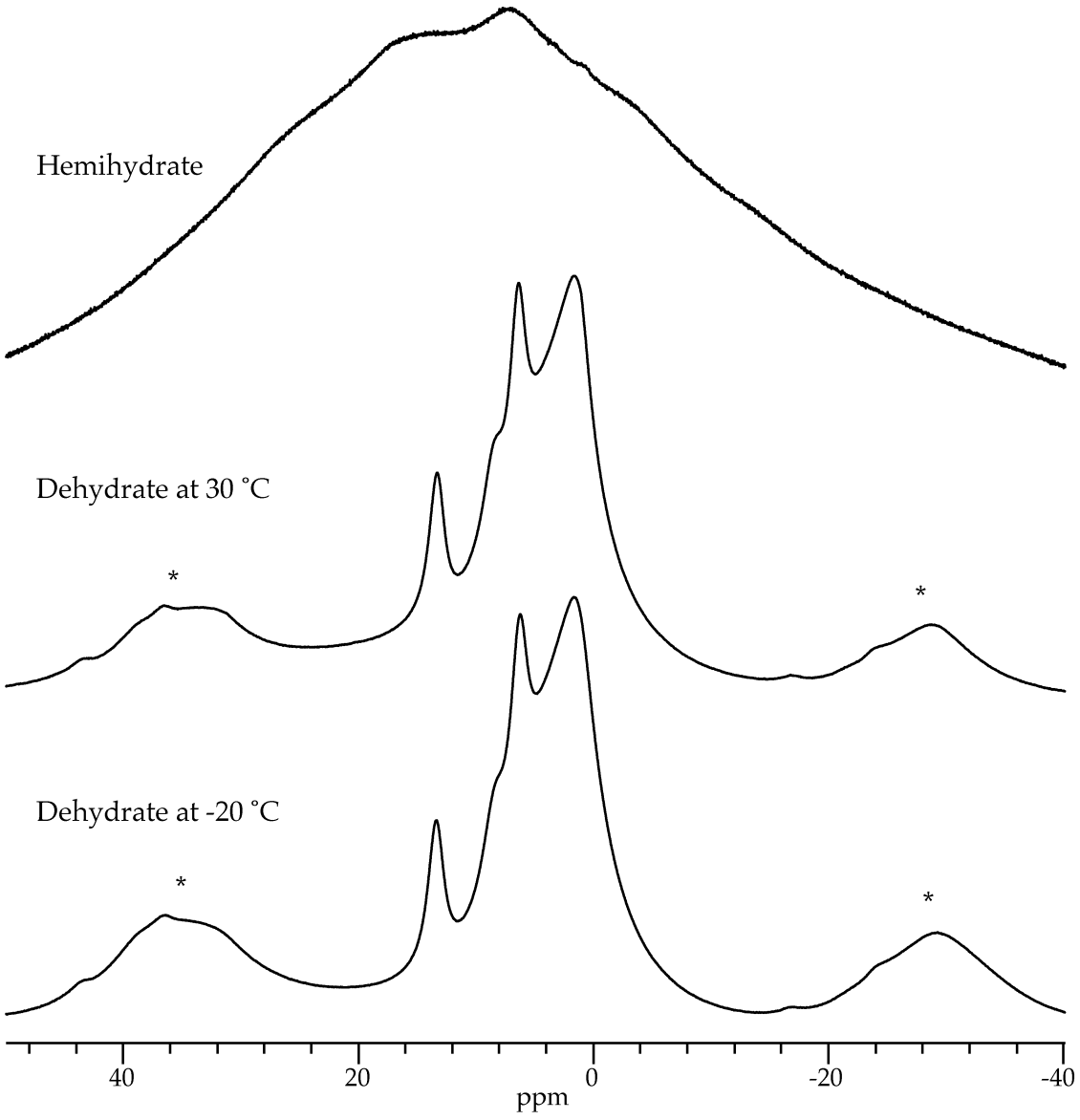

Figure 2.14 ^{1}H MAS spectra (^{1}H 500 MHz) of levofloxacin hemihydrate and dehydrated material at various temperatures. Temperatures are only approximate as spinning at 15 kHz results in sample heating of approximately 35 °C when the temperature of the sample is not controlled. * = spinning sidebands

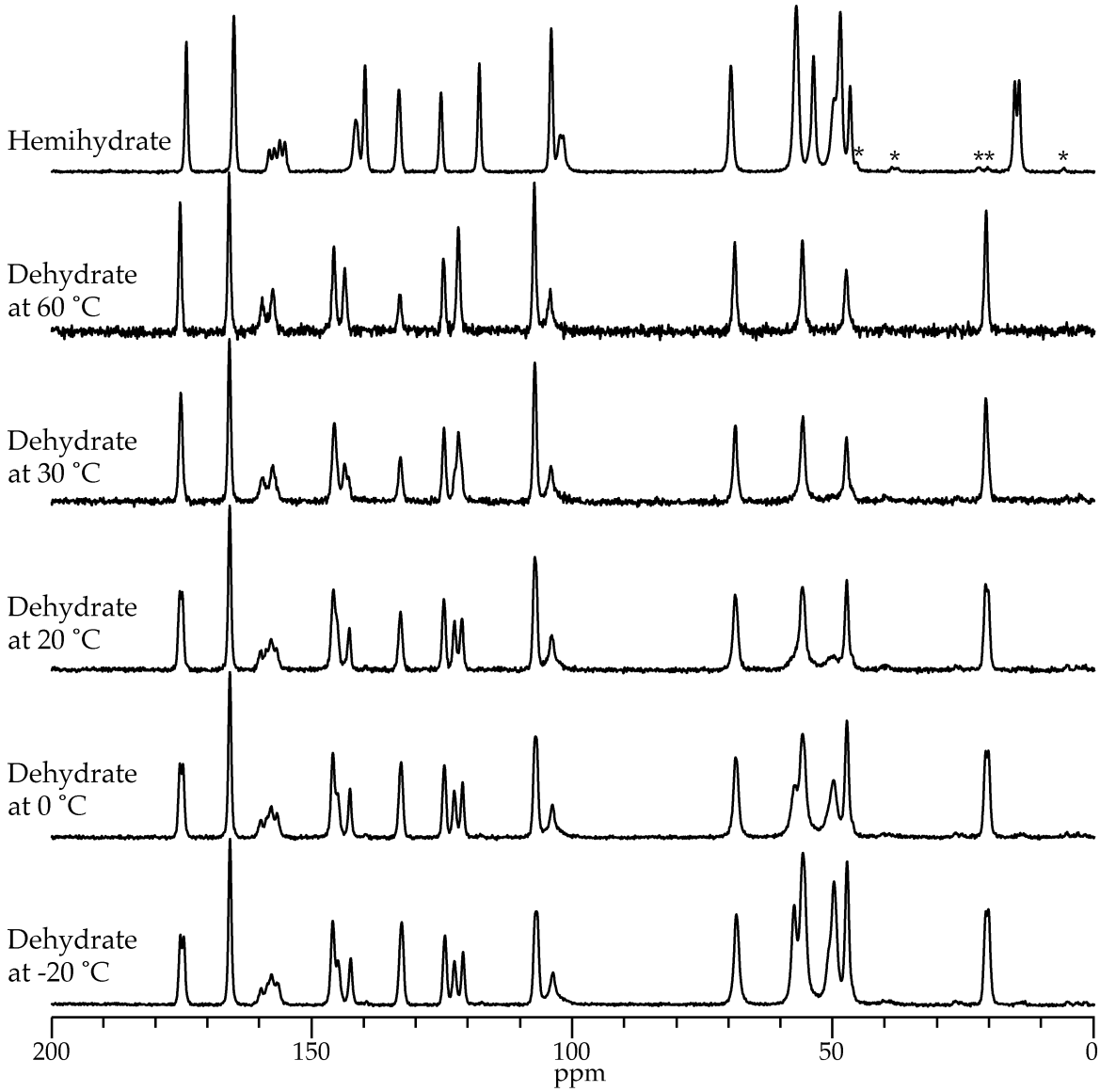

Figure 2.15 ^{13}C CPMAS spectra (^{1}H 500 MHz) of levofloxacin hemihydrate and dehydrated material at various temperatures. The spectra are consistent with the spectra collected at lower field strength (^{1}H 300 MHz), particularly the disappearance of the piperazine ring carbon peaks and loss of peak splitting in the dehydrated material. Temperatures are only approximate as spinning at 15 kHz results in sample heating of approximately 35 °C when the temperature of the sample is not controlled. * = spinning sidebands

previously explained as a change in mobility of the ring resulting in a loss of decoupling efficiency. The data in Figure 2.15 was collected with a higher decoupling field than the previous data (85 vs. 66 kHz) and thus it is not surprising that the peak disappearance would occur at a higher temperature. The motions would have to occur faster (shorter timescale) to match the higher decoupling frequency and as the temperature of the material increases so will the rate of the motions.

The loss of the peak splitting in the ^{13}C spectrum appeared to occur at a lower temperature (30 °C in Figure 2.15) than the previous experiments (50 °C). The unaccounted sample heating likely results in an actual sample temperature that is approximately 15 to 25 °C higher than the observed temperature, thus the loss of splitting probably occurs closer to a sample temperature of 45 to 55 °C, which is consistent with the previous study. This is also true of the ^{19}F spectra that are shown in Figure 2.16.

Levofloxacin contains only one fluorine atom; however the ^{19}F spectrum of the hemihydrate (Figure 2.16) displays two peaks due to the $Z' = 2$. When the hemihydrate is dehydrated and cooled to -20 °C it also displays two peaks, indicating that the crystal structure still has a $Z' = 2$. But the changes in the peak positions and the separation of the two peaks suggest that the crystal structures are different. Interestingly, when the dehydrated material is heated the two peaks decrease in intensity and a new peak appears between them. The presence of three distinct peaks indicates that these are separate molecular conformations or states. If the transition was associated with exchange between two conformations or states then the peaks should coalesce into a single peak.

All of the previous DSC, Raman, and PXRD suggested that when

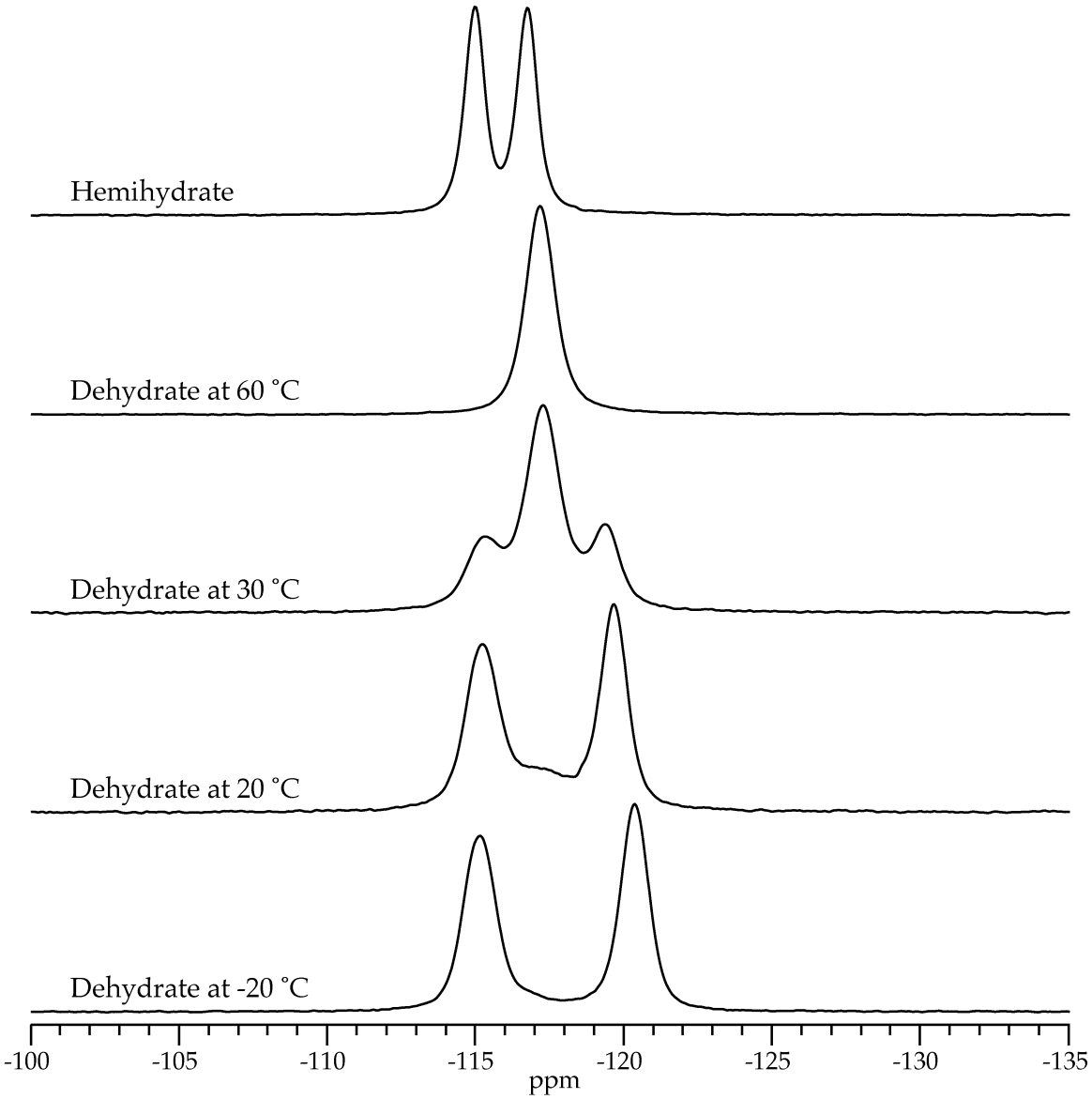

Figure 2.16 ^{19}F MAS spectra (^{1}H 500 MHz) of levofloxacin hemihydrate and dehydrated material at various temperatures. The ^{19}F spectra display the same change in peak splitting for the dehydrated material as the ^{13}C spectra (Figure 2.15). Temperatures are only approximate as spinning at 15 kHz results in sample heating of approximately 35 °C when the temperature of the sample is not controlled.

levofloxacin hemihydrate is dehydrated there is a change in the physical form of the material. In addition, if the material was protected from water vapor to prevent rehydration there appears to be a change in the crystal structure at around 50 to 55 °C. SSNMR at two field strengths supports this hypothesis and suggests that the dehydration of the hemihydrate leads to a relatively pure crystalline form which has a Z′ of 1 at temperatures above 50 to 55 °C and a Z′ of 2 below that temperature range. This indicates that the dehydrated material undergoes a polymorphic transition between two anhydrous forms at approximately 54 °C, according to DSC.

The physical form above 54 °C must be the γ form based on the melting point of the material; however, it is not clear if the form below 54 °C is one on the other known anhydrous forms. According to the heat of transition rule, physical form changes observed as an endothermic transition (such as the one observed at 54 °C by DSC) indicate that the polymorphs are enantiotropically related.[22,23] The heat of fusion rule states that in an enantiotropic system the melting point of the form that is more stable at lower temperatures will be lower than the form that is more stable at high temperatures. [22,23] This dictates that both the α and β forms cannot be the polymorph below 54 °C because they have melting points that are higher than the γ form. Hence the low temperature form must be a new anhydrous form, the δ form.

Additionally, DSC of the levofloxacin displayed a reversible event that appeared to be kinetic in nature at approximately 20 °C (Figure 2.3). The previous techniques could not study the phenomenon due to an inability to cool the samples during the analysis. However, SSNMR was able to investigate lower

temperatures and did observe changes in mobility of the piperazine ring of levofloxacin over similar temperature ranges. This suggests that the DSC may have been detecting changes in the mobility of the ring in the dehydrated material.

2.3.6 Hemihydrate Crystal Structure

The crystal structure of levofloxacin hemihydrate was previously determined by Kitaoka et al.[1]; however, it is not available from the Cambridge Structure Database. Therefore single crystals of levofloxacin hemihydrate were grown and then subjected to single crystal X-ray diffraction. The resulting crystallographic data is provided in Table 2.1 and is in good agreement with the previously reported values.[1]

The molecular packing of the levofloxacin hemihydrate unit cell is show in Figure 2.17. Interestingly, the water molecules appear to be hydrogen bonded to the methylated nitrogens of the piperazine rings. In addition, the asymmetric unit cell contains two molecules ($Z' = 2$), indicating that levofloxacin exists in two different conformations within the crystal structure. When the levofloxacin molecules are colored according to their conformations (Figure 2.17, lower image) it is obvious that both molecules of levofloxacin that are hydrogen bound to a particular water molecule are in the same conformation. Furthermore, these two conformations pack such that they produce planes that run parallel to the b-axis and only one conformation is found within a plane.

The existence of these planes in the crystal structure suggests that the water molecules may align in a channel through the crystal. The alignment of solvent molecules as a channel in the crystal structure is an important property

Table 2.1 Crystal structure data and refinement parameters.

	Hemihydrate
Emerical Fomula	$C_{18}H_{20}FN_3O_4 \bullet 0.5\ H_2O$
Formula Weight (g/mol)	379.39
Crystal System	Monoclinic
Space Group	C2
Unit Cell Dimensions	
A (Å)	28.758
b (Å)	6.799
c (Å)	18.765
β (°)	113.85
Volume ($Å^3$)	3355.7
Z	8
Density (g/cm^3)	1.431
Absorption Coefficient (mm^{-1})	0.921
F(000)	1520
Reflections Collected	9932
Independent Reflections	4745
Parameters	500
Goodness-of-fit on F^2	1.099
Final R indices [I>2σ (I)]	$R_1 = 0.0474$ $\omega R_2 = 0.1121$
Largest Diffraction Peak and Hole ($e/Å^3$)	0.590 and -0.757

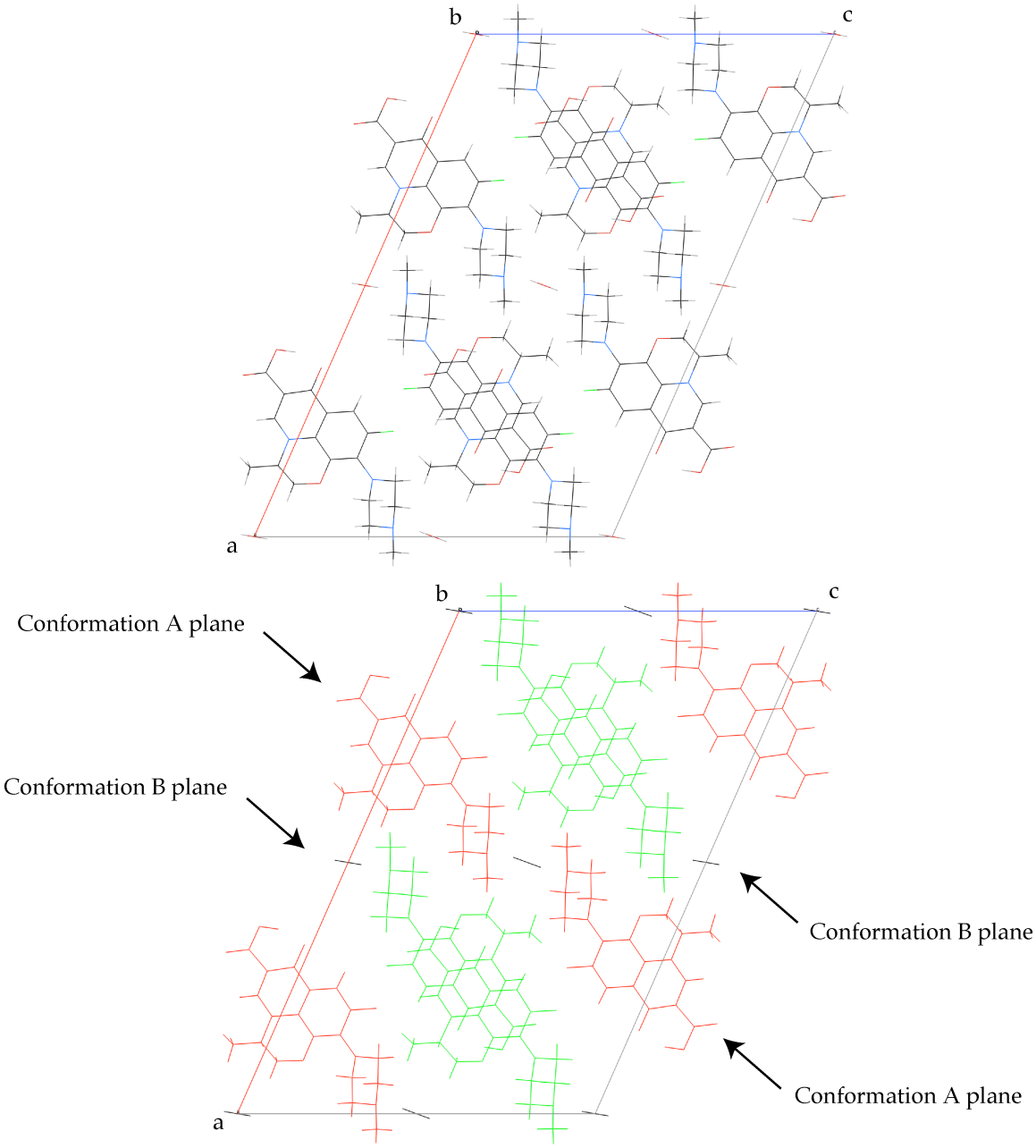

Figure 2.17 Crystal structure of levofloxacin hemihydrate viewed along the b-axis. The image in the top portion of the figure shows the packing of the molecules in the unit cell with the molecules colored according to the element of each atom. The bottom image is identical to the top image except that the levofloxacin molecules have been colored according to their conformation, Conformation A (**red**) and Conformation B (**green**), and water molecules are shown in **black**.

because it can allow the crystal structure to take up or release solvent molecules without destroying the crystal lattice.[24] The previous experiments (DSC, Raman, PXRD, and SSNMR) all demonstrated that levofloxacin hemihydrate could be dehydrated and would readily rehydrate in the presence of water vapor if the temperature was below approximately 55 °C. This lends support to the idea that levofloxacin hemihydrate could be a channel hydrate.

The crystal structure of the hemihydrate is shown in Figure 2.18 with the atoms of the molecules represented in a space-filling model to represent the actual space that is taken up by each molecule. When the water molecules are removed from the crystal structure (Figure 2.18, lower image) it is possible to see a void or "channel" though the crystal structure where the water molecules had been. However, the Mercury CSD software package was used to perform a void space calculation on the crystal structure after the water molecules were removed. This showed that while the water molecules are aligned in the crystal structure their locations are not connected by open spaces that are large enough to allow the passage of water molecules. Therefore, levofloxacin hemihydrate does not meet the traditional definition of a channel hydrate.

While the hemihydrate does not fit the traditional definition of a channel hydrate it does seem to behave like one. It was observed previously that the water molecules are associated with the piperazine rings by hydrogen bonding. Therefore, the rings line the water "channels". In addition, it was observed by SSNMR that the rings undergo dynamic motions once the water molecules are removed. Thus it may be possible for a water molecule at the surface of the crystal to be removed and subsequently allow its neighboring piperazine ring to move. The movement of the ring may open a space large enough for the

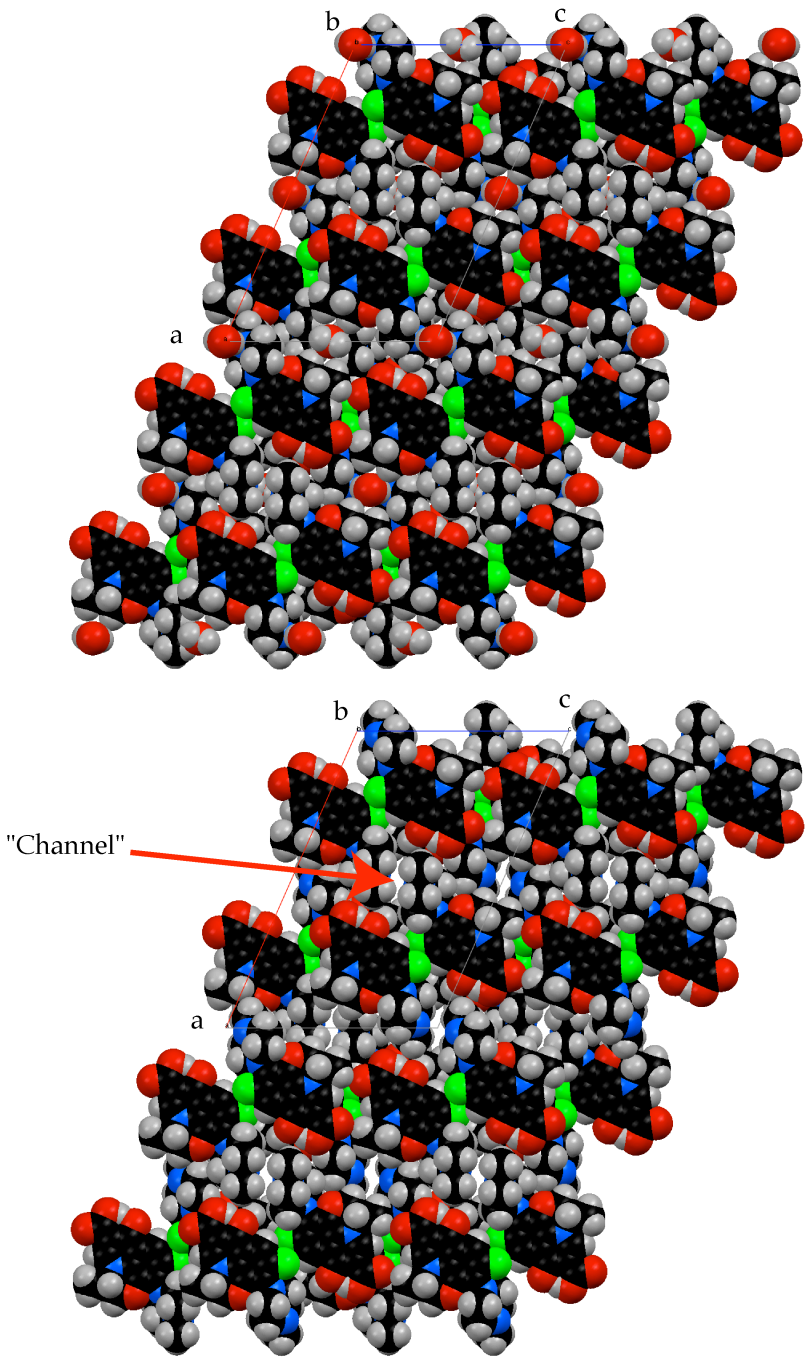

Figure 2.18 Crystal structure of levofloxacin viewed along the b-axis with a space-filling model. The packing has been replicated in each of the crystallographic dimensions to aid visualization. The image in the top portion of the figure shows the levofloxacin hemihydrate crystal structure. The bottom image is identical to the top image except that the water molecules were removed from the crystal structure.

neighboring water molecule to escape. This behavior may then propagate down the "channel" and allow all of the water to be removed without causing the crystal lattice to collapse. Conversely, under the appropriate conditions water molecules may be able to populate the channel and progressively fill the channel to reform the hydrate. The formation of empty channels that are lined by the piperazine rings would also explain the ability of the rings to undergo dynamic motions in the dehydrated material. In the hemihydrate the rings are held in place due to the presence of the water molecules, but once the water is gone the rings would have more space in which to undergo small motions.

The differences in the γ and δ forms of levofloxacin appeared to be associated with a change from a crystal structure with a Z′ of 2 at low temperatures to a crystal structure with a Z′ of 1 at higher temperature. The two conformations of levofloxacin from the crystal structure of the hemihydrate are overlaid in Figure 2.19. Apart from the piperazine ring, levofloxacin is a fairly rigid molecule and thus carbons in the more rigid portion of the molecule were chosen for alignment to identify the differences in the conformations. There are subtle differences in the methyl group (C-1), but it is not clear if those are due to uncertainties in the crystal structure. More dramatic differences are observed in the piperazine ring, which is rotated approximately 90° about the C-6 N-1′ bond. Assuming that the crystal lattice of the hemihydrate is maintained upon dehydration it would appear that the most likely conformational change that would result in the Z′ change would be rotation about the C-6 N-1′ bond so that the two molecules are virtually identical. This is also supported by the previous discussion regarding the presence of channels in the crystal structure. The piperazine rings appear to have space to move and it may be sufficient for

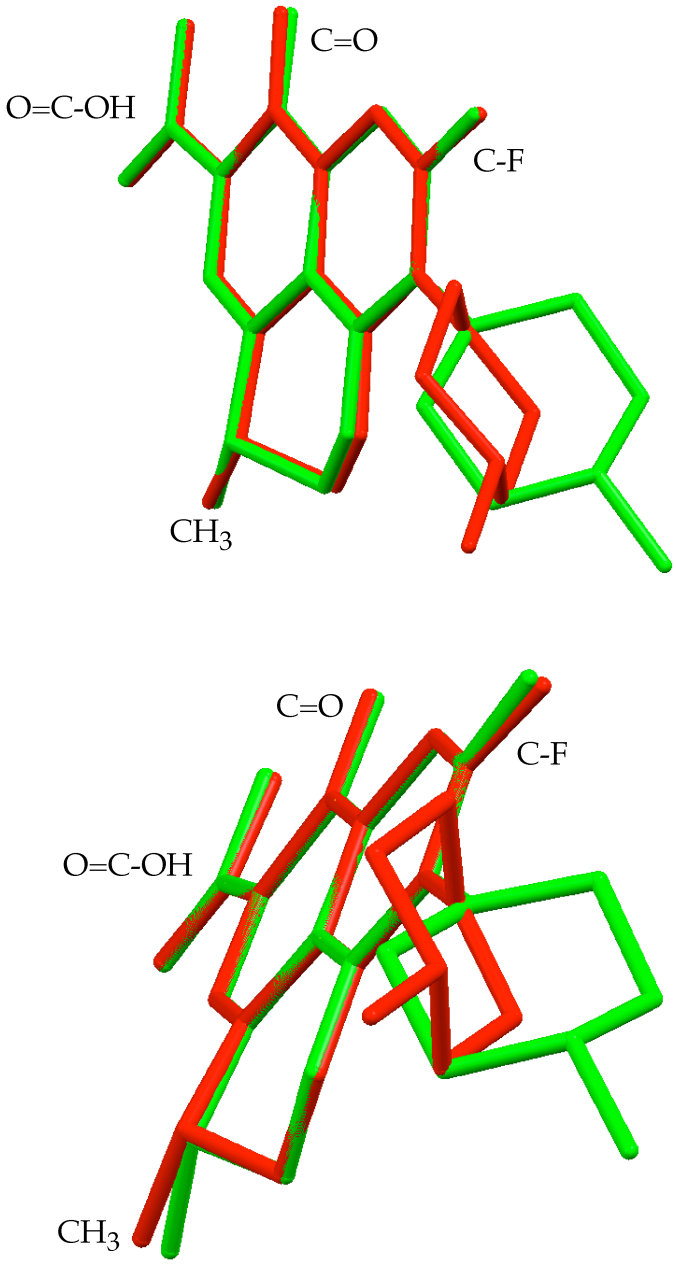

Figure 2.19 Overlay of the two conformations of levofloxacin in the levofloxacin hemihydrate crystal structure: Conformation A (**red**) and Conformation B (**green**). The top and bottom images are different rotations of the overlay. Hydrogen atoms have been removed and functional groups have been labeled to aid visualization.

rotation about that bond. Therefore, it is thought that the crystal structure of the δ and γ forms are very similar and primarily differ in the orientations of the piperazine rings to the remainder of the levofloxacin molecule.

2.4 Summary

Kitaoka et al.[1] previously studied the hemihydrate form of levofloxacin and hypothesized that dehydration of the material lead to collapse of the crystal lattice and resulted in formation of a mixture of anhydrous forms and in some cases produced amorphous levofloxacin. They believed that the dehydration conditions determined which forms were generated and their relative proportions. However, they offered limited data to support their claims.

SSNMR suggests that when levofloxacin hemihydrate is dehydrated a relatively pure crystalline form, specifically the γ form, is produced. Additionally, when the dehydrated material is cooled below 54 °C, the levofloxacin converts to the δ form, which has not been reported previously. The results also suggest that the crystal structures of the hemihydrate, γ, and δ forms are all closely related, primarily with changes in the conformation and orientation of the piperazine ring relative to the rest of the molecule.

The crystal structure of levofloxacin hemihydrate does not fit the traditional definition of a channel hydrate. However, the γ and δ anhydrous forms readily hydrate to produce the hemihydrate in the presence of water vapor. Additionally, the water molecules of the hemihydrate are aligned through the crystal structure. Therefore, it proposed that levofloxacin

hemihydrate is a pseudo channel hydrate that behaves like a channel hydrate, but does not fit the traditional definition.

2.5 References

1. Kitaoka H, Wada C, Moroi R, Hakusui H 1995. Effect of dehydration on the formation of levofloxacin pseudopolymorphs. Chem Pharm Bull 43(4):649-653.

2. Brittain HG 2010. Polymorphism and solvatomorphism 2008. J Pharm Sci 99(9):3648-3664.

3. Datta S, Grant DJW 2004. Crystal structures of drugs: Advances in determination, prediction and engineering. Nat Rev Drug Discov 3(1):42-57.

4. Storey R, Docherty R, Higginson P, Dallman C, Gilmore C, Barr G, Dong W 2004. Automation of solid form screening procedures in the pharmaceutical industry - How to avoid the bottlenecks. Crystallography Reviews 10(1):45-56.

5. Davis R, Bryson HM 1994. Levofloxacin: A review of its antibacterial activity, pharmacokinetics and therapeutic efficacy. Drugs 47(4):677-700.

6. Niddam-Hildesheim V, Gershon N, Amir E, Wizel S, *Preparation of levofloxacin and forms thereof*. In patent number WO 03/028664 A2, issued 10 Apr 2003, pp 1-38.

7. Byrn S, Pfeiffer R, Stowell J *Solid-state chemistry of drugs*, 1999, pp 576.

8. Hasegawa G, Komasaka T, Bando R, Yoshihashi Y, Yonemochi E, Fujii K, Uekusa H, Terada K 2009. Reevaluation of solubility of tolbutamide and polymorphic transformation from Form I to unknown crystal form. Int J Pharm 369(1-2):12-18.

9. Katrincic LM, Sun YT, Carlton RA, Diederich AM, Mueller RL, Vogt FG 2009. Characterization, selection, and development of an orally dosed drug polymorph from an enantiotropically related system. Int J Pharm 366(1-2):1-13.

10. Murphy BJ, Huang J, Casteel MJ, Cobani A, Krzyzaniak JF 2010. Varenicline L-tartrate crystal forms: Characterization through crystallography, spectroscopy, and thermodynamics. J Pharm Sci 99(6):2766-2776.

11. Strydom S, Liebenberg W, Yu L, De Villiers M 2009. The effect of temperature and moisture on the amorphous-to-crystalline transformation of stavudine. Int J Pharm 379(1):72-81.

12. Thirunahari S, Aitipamula S, Chow PS, Tan RBH 2010. Conformational polymorphism of tolbutamide: A structural, spectroscopic, and thermodynamic characterization of Burger's forms I-IV. J Pharm Sci 99(7):2975-2990.

13. Stejskal E, Schaefer J, Waugh J 1977. Magic-angle spinning and polarization transfer in proton-enhanced NMR. J Mag Res 28(1):105–112.

14. Metz G, Wu X, Smith S 1994. Ramped-amplitude cross polarization in magic-angle-spinning NMR. Journal of Magnetic Resonance, Series A 110(2):219–227.

15. Antzutkin ON, Song Z, Feng X, Malcolm H 1994. Suppression of sidebands in magic-angle-spinning nuclear magnetic resonance: General principles and analytical solutions. J Chem Phys 100(1):130–140.

16. Song Z, Antzutkin ON, Feng X, Levitt MH 1993. Sideband suppression in magic-angle-spinning NMR by a sequence of 5 pi pulses. Solid state nuclear magnetic resonance 2(3):143-146.

17. Fung BM, Khitrin AK, Ermolaev K 2000. An improved broadband decoupling sequence for liquid crystals and solids. J Mag Res 142(1):97–101.

18. Barich DH, Gorman EM, Zell MT, Munson EJ 2006. 3-Methylglutaric acid as a 13C solid-state NMR standard. Solid state nuclear magnetic resonance 30(3-4):125-129.

19. Ferguson DB, Haw JF 1995. Transient methods for in situ NMR of reactions on solid catalysts using temperature jumps. Anal Chem 67(18):3336-3341.

20. Opella S, Frey M 1979. Selection of nonprotonated carbon resonances in solid-state nuclear magnetic resonance. Journal of the American Chemical Society 101(19):5854-5856.

21. Bennett AE, Rienstra CM, Auger M, Lakshmi KV, Griffin RG 1995. Heteronuclear decoupling in rotating solids. J Chem Phys 103(16):6951-6958.

22. Burger A, Ramberger R 1979. On the polymorphism of pharmaceuticals and other molecular crystals. I. Theory of thermodynamics rules. Mikrochimica Acta 72:259–271.

23. Burger A, Ramberger R 1979. On the polymorphism of pharmaceuticals and other molecular crystals. II. Applicability of thermodynamic rules. Mikrochimica Acta 72:273–316.

24. Vogt FG, Dell'Orco PC, Diederich AM, Su Q, Wood JL, Zuber GE, Katrincic LM, Mueller RL, Busby DJ, Debrosse CW 2006. A study of variable hydration states in topotecan hydrochloride. J Pharm Biomed Anal 40(5):1080-1088.

Chapter 3

Detection of Physical Forms in Formulations

3.1 Introduction

The specific aim of this chapter is to characterize the physical form of the API within formulations. Specifically, three formulations will examined to determine if the processing of the materials resulted in changes in the physical forms of the APIs. The formulations will be evaluated by both DSC and SSNMR to evaluate the ability of each technique to determine the physical form of the API in the final formulation.

Particle engineering, particularly the preparation of nanoparticles, is one of the most popular technologies that is currently being developed and used to improve the delivery of poorly water soluble drugs. When the particle size of a material is reduced, the relative surface area of that material is increased. This increase in surface area leads to increases in dissolution rate, apparent solubility, and ultimately can dramatically impact the bioavailability of the drug.[1,2] In addition, the drug can be dispersed in a slowly dissolving matrix to allow prolonged release of the drug.[3-7]

These formulations are carefully designed and developed to provide specific drug release profiles in order to achieve the desired outcomes. However, the physical form of the API will also impact the release profile of the formulation.[8] Therefore it is critical not only to measure physical properties such as particle size, but also to know the physical form of the API and if that form is physically stable. A nanoparticle formulation may give improved dissolution properties immediately after production; however, those gains could be due to the formation of a metastable form of the API. Over time the API may convert to a more stable form, resulting in changes in the dissolution or release profile and

ultimately diminishing the initial improvements that were observed with the formulation. Despite these potential ramifications, some studies make no attempt to characterize the API physical form that is present within the formulation.[9,10]

Most characterization studies of the API physical form in nano- and microparticle formulations are limited to DSC,[11] PXRD,[12,13] or a combination of both techniques.[8,14-16] In the introduction of the previous chapter some of the limitations of both DSC and PXRD in the detection of physical forms of pharmaceuticals are discussed; however, the presence of excipients can complicate the analysis of these materials. One of the biggest issues in analyzing formulations by both DSC and PXRD is the potential for overlap of API and excipient signals. Additionally, the drug loading may not be sufficient for detection by the instrumentation that is being utilized. Furthermore, melting of a crystalline API may not be observed by DSC if the API forms a eutectic with a formulation component.[17] It has also been observed that when the particle size of a material is reduced there will be a decrease in the observed melting point of the material.[18] Therefore, interpretation of DSC thermographs of these types of formulations are fraught with complications and typically require several assumptions about the behavior of the materials that are being analyzed.

SSNMR has been used to identify physical forms of APIs within formulations,[19,20] but not for the analysis of pharmaceutical nanoparticle formulations. This chapter will present three examples of nanoparticle formulations that were analyzed by both DSC and SSNMR to compare the ability of both techniques to identify the API physical form within the formulations. The formulations were developed in the laboratory of Dr. Cory Berkland while

the subsequent characterization of the materials was performed in collaboration with the Munson laboratory.[21-23]

The remainder of this chapter has a non-traditional organization and is divided into subchapters that cover each of the APIs that were analyzed (budesonide, nifedipine, and ciprofloxacin). Each of these subchapters contains a brief introduction to the work, experimental methods, results with discussion, and a brief summary. Additionally, an overall summary of the general conclusions will be presented at the end of this chapter.

3.2 Budesonide

3.2.1 Background

Budesonide (Figure 3.1) is a corticosteroid that is used for the prophylactic treatment of asthma. Dry powder and metered dose inhalation formulations have previously been developed for pulmonary delivery. However, it was hypothesized that nanosuspension technology could be utilized to develop a formulation that, once inhaled, would provide rapid dissolution of budesonide despite its poor water solubility (approximately 21.5 μg/mL). Nanoparticles of budesonide were generated and subsequently aggregated to produce particles with good aerodynamic characteristics and improved dissolution. Unfortunately DSC analysis of the materials offered no clear insight into the physical state of the budesonide in the formulation. SSNMR was able to clearly show that most of the budesonide was in an amorphous state and even suggests that a small amount of crystalline budesonide may be present within the formulation.[22]

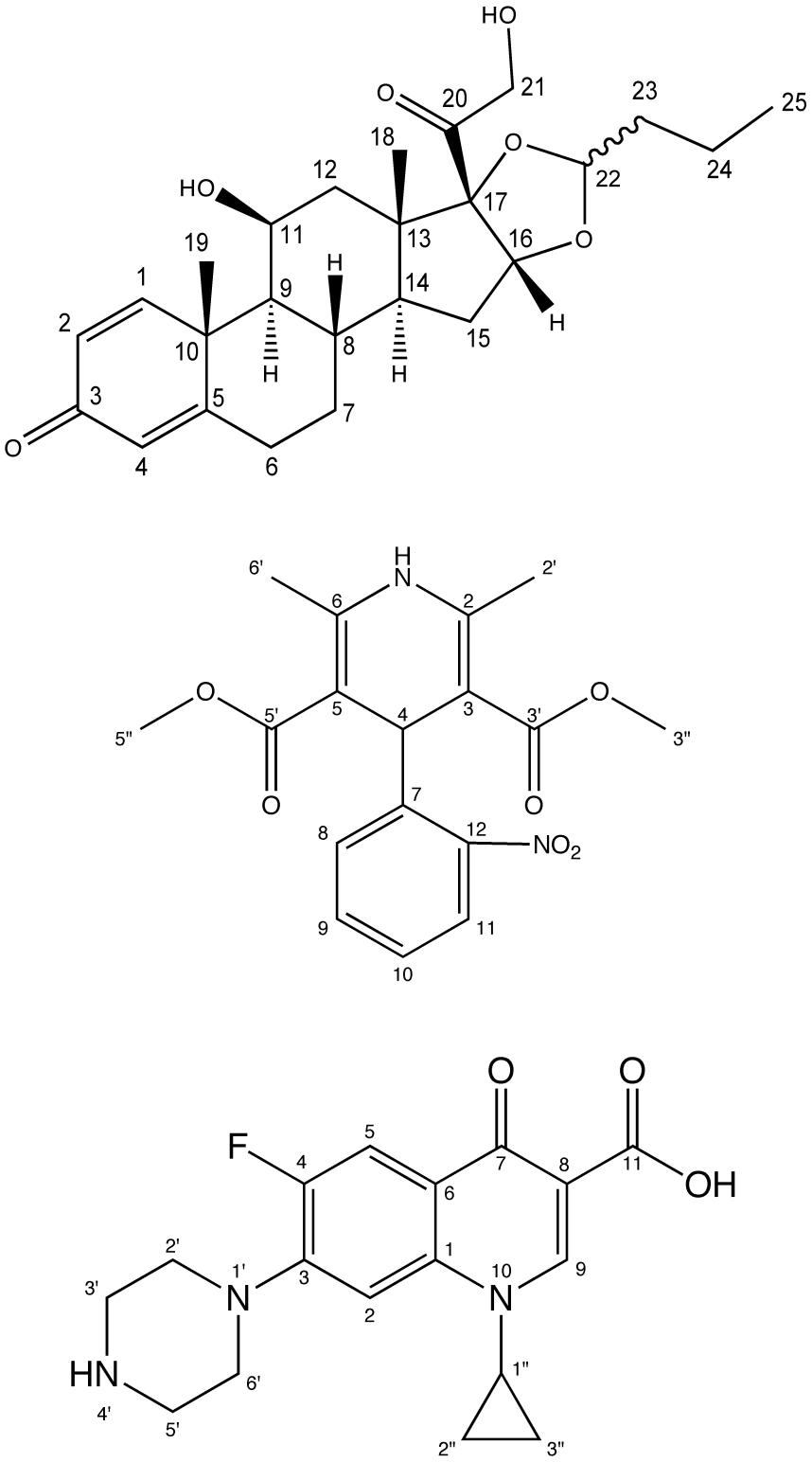

Figure 3.1. Chemical structures of budesonide (top), nifedipine (middle), and ciprofloxacin (bottom), shown with assigned atom numbering.

3.2.2 Experimental

3.2.2.1 Materials

Budesonide, sodium chloride, L-α-phosphatidylcholine (lecithin), cetyl alcohol, L-leucine, polyvinylpyrrolidone, and sorbitan trioleate (Span 85) were obtained from Sigma Chemicals Co. (St. Louis, MO). Pluronic F-127 (MW = 12,220) was purchased from BASF, The Chemical Company (Shakopee, MN). Polyvinyl alcohol (MW = 22,000, 88% hydrolyzed) was purchased from Acros Organics (Fair Lawn, NJ). Ethanol, acetone, acetonitrile, potassium dihydrogen phosphate, and disodium hydrogen phosphate were purchased from Fisher Scientific (Fair Lawn, NJ). Deionized water was obtained from a Millipore EASYpure® RODI (Barnstead International, Model # D13321, Dubuque, IA). All materials were used without further purification, and solvents were of HPLC grade.

3.2.2.2 Nanoparticle and Agglomerate Preparation

Solutions of budesonide in acetone at concentrations of 0.1% (w/v) budesonide and 0.02% (w/v) lecithin were produced. In order to form nanoparticles, water was utilized as an anti-solvent and was added to the budesonide/lecithin solution at a rate of 1 mL/min with simultaneous sonication (Fisher Scientific, Sonic Dismembrator, amplitude 46%) in an ice bath.

To agglomerate the nanoparticles, a 1% (w/v) L-leucine solution in water was slowly added to the nanoparticle suspension until a 1:1 budesonide:leucine ratio was achieved. The addition of the L-leucine was performed with homoginization at 25,000 rpm for 30 sec. Evaporation of the acetone was done

overnight at room temperature, at which point the nanoparticle agglomerate suspension was frozen at -80 °C and subsequently lyophilized for ~36 hr (Labconco, FreeZone 1, Kansas City, MO).

In order to produce amorphous budesonide, approximately 1 g of budesonide was placed in an oven that was preheated to 250 °C. After the material melted it was immersed in liquid nitrogen. This "melt-quenched" material was subsequently used as an amorphous budesonide reference material for subsequent analyses.

3.2.2.3 DSC

A Q100 DSC from TA Instruments (see Section 2.2.3 of Chapter 2, New Castle, DE) was utilized to assess the physical form present in each of the materials: budesonide, lecithin, nanoparticles, and agglomerates. Approximately 5 mg of each nanoparticle/agglomerate sample was placed in a crimped aluminum pan for analysis; 1, 10, and 20 mg of material were used for stock budesonide, melt-quenched budesonide, and lecithin, respectively. Lecithin was analyzed by heating from -70 to 260 °C at a rate of 5 °C/min. Stock budesonide was heated from -40 to 260 °C at 10 °C/min, held isothermally for 5 min, then cooled back to -40 °C and reheated to 260 °C at 10 °C/min to check the feasibility of producing amorphous material from a melt-quench method. The nanoparticles and agglomerates were heated from 40 to 260 °C at a rate of 5 °C/min, except for the modulated DSC (MDSC) experiment which was performed on the nanoparticle sample by heating from -20 to 230 °C at 5 °C/min with a modulation of ± 0.8 °C every 60 sec. (heat only conditions).

3.2.2.4 TGA

Stock budesonide and leucine were analyzed by TGA (see Section 2.2.2 of Chapter 2, New Castle, DE) to ascertain residual solvent content and determine the degradation temperatures. Approximately 2 mg of budesonide and 10 mg of leucine were each placed in platinum pans and heated from room temperature to over 300 °C at a rate of 10 °C/min.

3.2.2.5 SSNMR Spectroscopy

SSNMR data was collected on a Chemagnetics CMX-300 spectrometer (see Section 2.2.6 of Chapter 2, Fort Collins, CO). Samples were packed into 7 mm zirconia rotors and held in place with Teflon® end caps (Revolution NMR, Fort Collins, CO). Packed rotors were spun with MAS[24] at a rate of 4 kHz in a 7 mm spin module (Revolution NMR, Fort Collins, CO).

All ^{13}C FIDs were collected with a ramped amplitude CP[25] sequence with ~81 kHz of proton decoupling using the SPINAL-64[26] method. Between 2,000 and 48,000 transients were collected for each FID with a pulse delay of 1 – 1.5 sec, a contact time of 0.5 – 2 msec, and a ^{1}H 90° pulse width of 3 – 4.5 μsec. The FIDs contain 512 – 2,048 points with a dwell time of 33.3 μsec. Spectra were externally referenced to TMS using the methyl peak of MGA at 18.84 ppm.[27]

3.2.3 Results & Discussion

3.2.3.1 Particle Characterization

The budesonide nanoparticles had an average particle size of 161 ± 16 nm, while the nanoparticle agglomerates had geometric and aerodynamic diameters of approximately 3 and 1.4 μm, respectively. The agglomerates gave favorable aerosolization characteristics with high emitted and respirable fractions of 75 and 96%, respectively. The fraction of budesonide that was dissolved after 8 hrs was highest for the nanoparticles (62%) and lowest for the stock budesonide, with the agglomerates showing intermediate dissolution (42%). The differences in dissolution behavior were initially attributed to the differences in particle size, but further investigation was necessary to eliminate physical form differences as a contributing factor.

3.2.3.2 Thermal Analysis (DSC/TGA)

The DSC thermograph of stock budesonide (Figure 3.2) contains an endotherm at 254 °C, which is assumed to be the melting point of the material. This is supported by TGA of budesonide which showed no significant mass loss below 300 °C (Figure 3.3). The molten budesonide was rapidly cooled to -40 °C in the DSC and then reheated. A glass transition was then observed at 96 °C (Figure 3.2), indicating that amorphous budesonide could be formed by rapid cooling of melted budesonide.

L-leucine shows complete mass loss above approximately 190 °C (Figure 3.3), which agrees with its previously reported sublimation temperature.[28] TGA

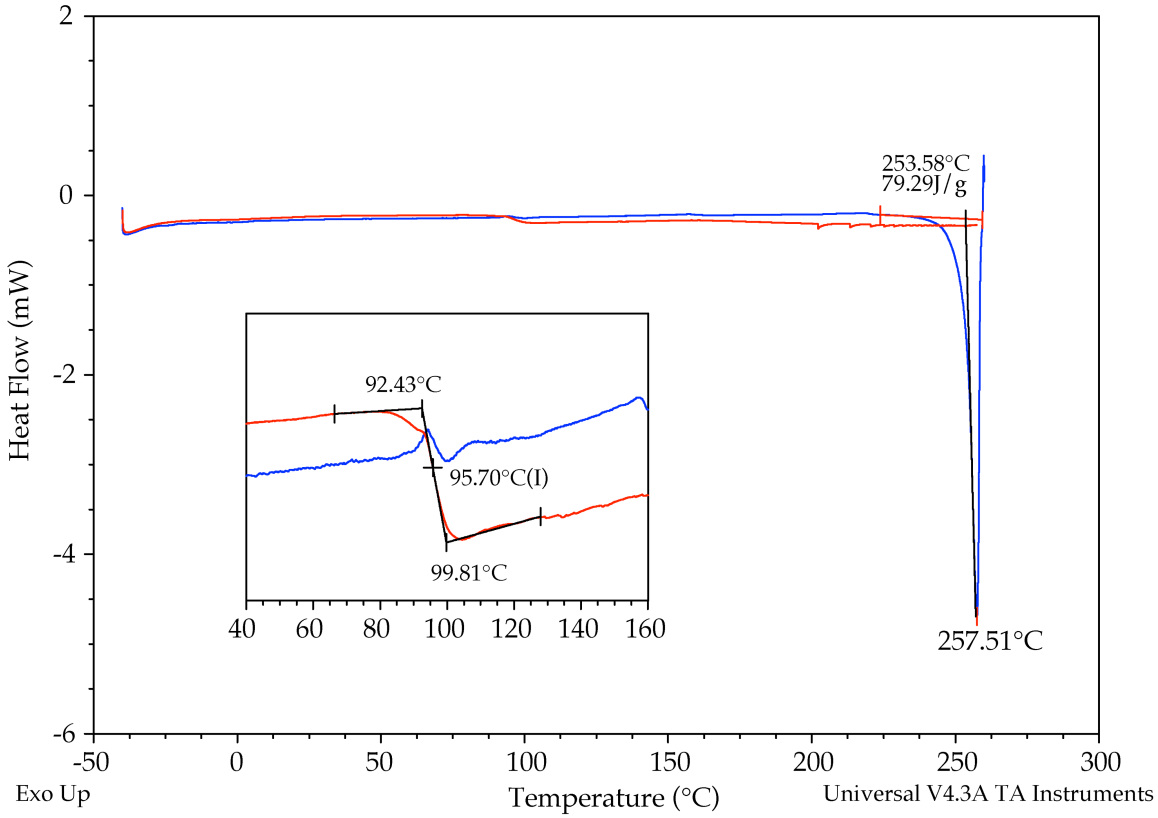

Figure 3.2. DSC of stock budesonide heated to 260 °C (**blue**), cooled to -40 °C, and then reheated to 260 °C (**red**). The insert shows the glass transition that was observed during the second heating. The T_g measurement is shown with the onset, offset, and inflection point (I) temperatures.

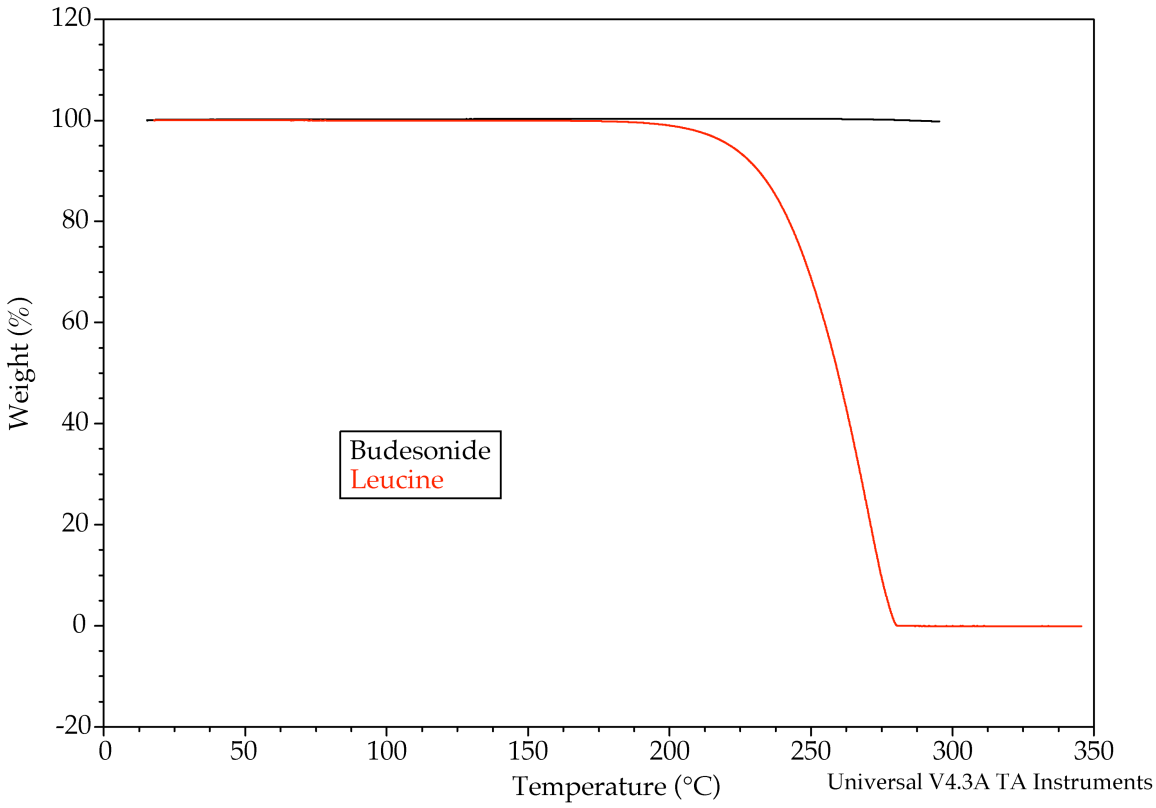

Figure 3.3. TGA of stock budesonide and leucine heated to > 300 °C. The mass loss for leucine agrees with the temperature of sublimation (approximately 175 to 190 °C) for L-leucine, based on vapor pressure measurements reported by Svec and Clyde.[28] The observed sublimation of L-leucine is likely observed at higher temperatures in the TGA because the system is being heated and not at equilibrium.

was not performed on lecithin; however, the series of sharp endotherms in its DSC thermograph suggest that it undergoes degradation above 160 °C (Figure 3.4). The broad endotherm in the lecithin DSC thermograph at 25 °C is likely due to melting of the material because the material has a soft, waxy appearance when it is handled at ambient conditions.

Amorphous budesonide was prepared by melting stock budesonide at 250 °C in an oven, and then the molten material was immediately immersed in liquid nitrogen. The DSC of the resulting melt quenched material did not show any endotherm at 254 °C that would correspond to the melting that was observed for stock budesonide (Figure 3.4). Instead, the material shows a broad endotherm at 80 °C and then a small, sharp endotherm at 220 °C followed by what appears to be degradation. Amorphous materials typically contain adsorbed water and so the 80 °C endotherm likely represents dehydration of adsorbed water. Unfortunately, water acts as a plasticizer and will decrease the T_g of amorphous materials. This endotherm occurs at temperatures just below the T_g that was observed when the stock material was temperature cycled in the DSC (Figure 3.2), thus any glass transition that may be occurring in the melt quenched sample is probably masked by the dehydration endotherm. There have been no reports of additional crystalline forms of budesonide (polymorphs or solvates) and the relatively small size of the endotherm at 220 °C suggests that the sample did not melt or contained only very small amounts of crystalline material. So there is no clear evidence that the melt quenched sample displayed a glass transition; however, it did seem to contain adsorbed water and did not melt which suggests that it is actually amorphous.

Analysis of the nanoparticles by DSC showed two broad endotherms at 60

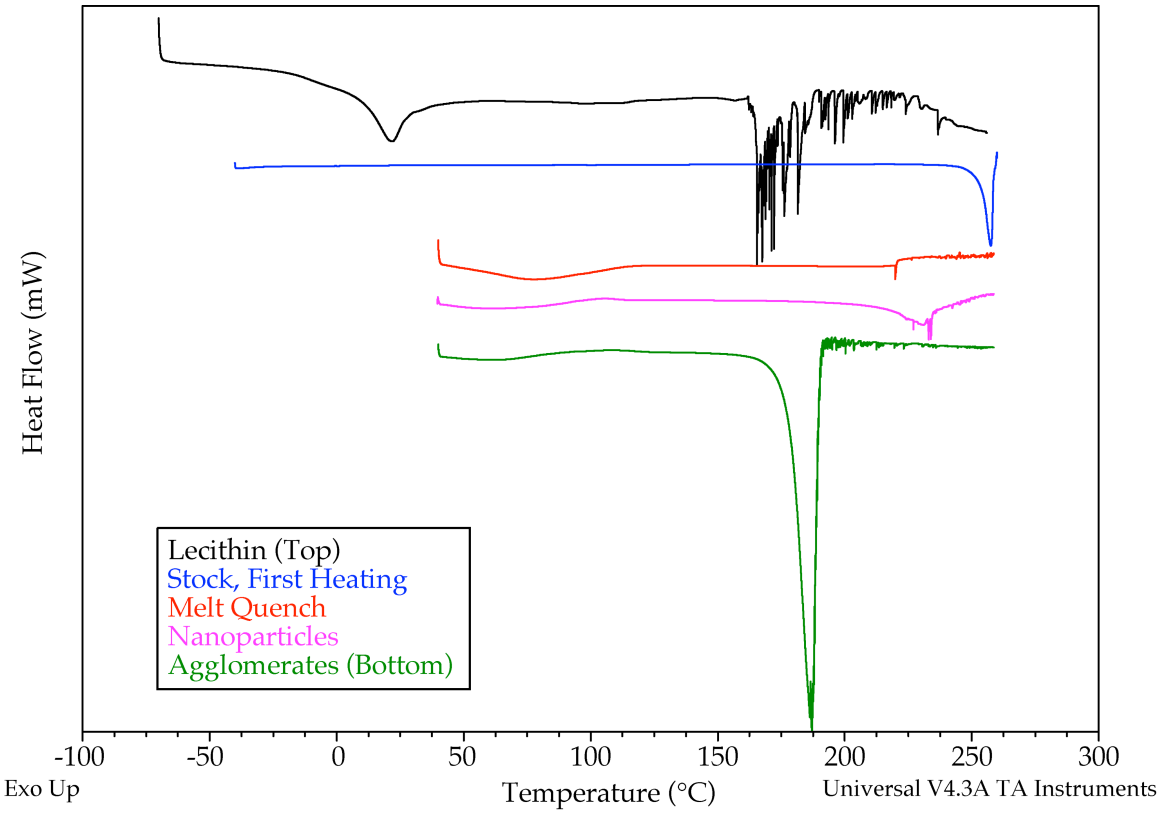

Figure 3.4. DSC overlay of stock budesonide, melt quenched budesonide, budesonide nanoparticles, agglomerates of budesonide nanoparticles, and lecithin. For the stock budesonide the first heating (Figure 3.2) is shown to display the observed melting of budesonide. The large endotherm at approximately 187 °C in the thermography of the agglomerates is consistent with sublimation of L-leucine (Figure 3.3).

and 230 °C (Figure 3.4). The first endotherm is likely due to loss of adsorbed water; however the origin of the higher temperature transition is not as clear. The event is much broader and lower in temperature than the observed melting point of the stock budesonide. The size of the nanoparticles cannot explain the dramatic difference in the temperatures of the melting point and the new endotherm (> 20 °C difference) because particles that are ~160 nm should only display a melting point depression of approximately 8 °C.[18] Additionally, neither of the endotherms correspond to transitions that were observed for lecithin. Thus, the origins of the endotherm at 230 °C is unclear but likely due to either the presence of a previously unknown crystalline form of budesonide or formation of a eutectic with lecithin and budesonide.

Furthermore Figure 3.4 shows the DSC of the agglomerates, which also displays two broad endotherms. One of the endotherms is at approximately 60 °C and is similar to the endotherm that was observed with melt quenched budesonide and nanoparticles, and was attributed to dehydration. However the second endotherm is very large and has an onset of 177 °C, which is consistent with sublimation of L-leucine (Figure 3.3).[28] Therefore, the agglomerate thermograph does not seem to display any transitions that can be clearly attributed to budesonide in order to determine its physical state within the sample.

The melt quenched budesonide, nanoparticles, and agglomerates did not show any clear melting endotherms for crystalline budesonide and they lacked any obvious glass transition events. Therefore, the thermographs in Figure 3.4 were expanded to show the region in which the T_g of the temperature cycled stock budesonide was observed. This expansion of the data is shown in Figure

3.5 with the exception that the second heating of the stock budesonide is shown to visualize the observed glass transition.

Figure 3.5 clearly shows the T_g, at 96 °C, of the stock budesonide when it was reheated. The lecithin shows several small endotherms in this same temperature range, which are of unknown origin. The melt quenched budesonide, nanoparticles, and agglomerates all show the broad endotherm at 60 – 80 °C that was previously described and attributed to dehydration. It was previously pointed out that the melt quenched material is most likely amorphous but no glass transition is observed due to overlap with the dehydration endotherm.

Similar behavior is observed with both the nanoparticles and agglomerates (Figure 3.5). However, there do appear to be transitions that follow the endotherms from both of these samples. These signals might be due to glass transitions but their close proximity to the endotherms makes interpretation of the results difficult. Additionally, if these events are glass transitions they are higher in temperature than the previously observed T_g of pure budesonide.

Modulated DSC (MDSC) of the nanoparticles is shown in Figure 3.6 and was used to help identify this transition. A glass transition should appear in the reversing signal of an MDSC experiment, but the results do not show any transitions in the reversing heat flow that are consistent with a glass transition. Therefore, the data is not consistent with the presence of any amorphous budesonide. However, closer inspection of Figure 3.5 appears to show that the transition following the endotherm may actually be an exotherm that is poorly resolved from the endotherm. An exotherm could result from a polymorphic

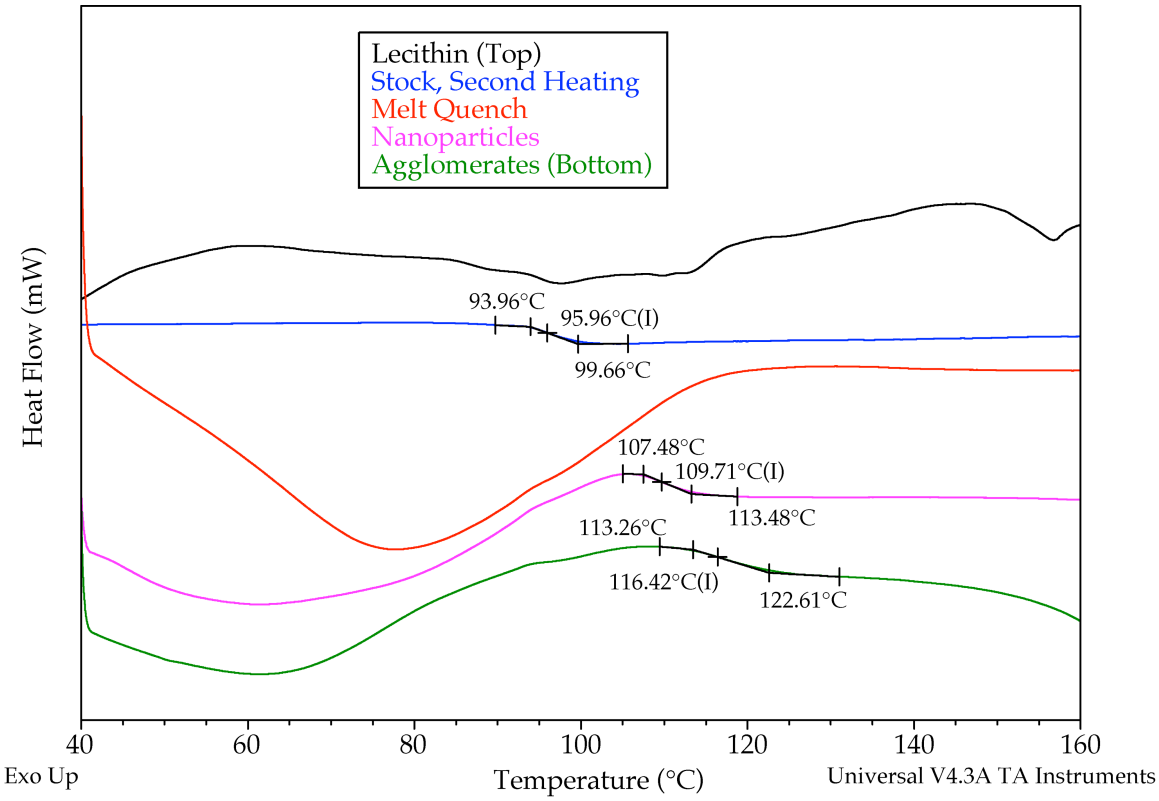

Figure 3.5. Expansion of DSC thermographs shown in Figure 3.4, but for the stock budesonide the second heating (Figure 3.2) is shown to display the observed T_g for budesonide. The T_g measurements are shown with onset, offset, and inflection point (I) temperatures.

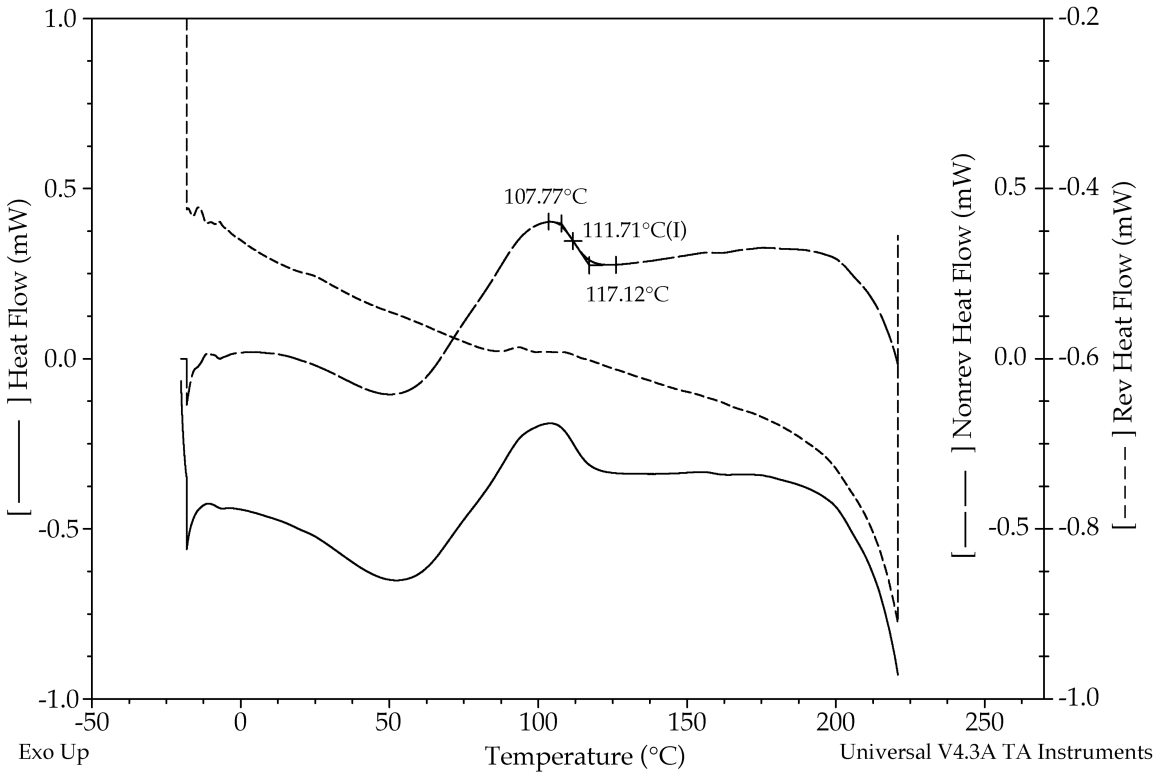

Figure 3.6. MDSC of budesonide nanoparticles. The T_g measurement is shown with the onset, offset, and inflection point (I) temperatures. The "Nonrev" and "Rev" heat flow signals are the non-reversing and reversing heat flow signals, respectively, that are obtained from the modulation of the heating rate while the heat flow signal is analogous to the heat flow from the previous conventional DSC experiments (Figures 3.2, 3.4, and 3.5).

form conversion or crystallization of amorphous material. Unfortunately the DSC offers no clear evidence as to the physical state of the budesonide within the melt quenched budesonide, nanoparticles, or agglomerates.

3.2.3.3 SSNMR Spectroscopy

The ^{13}C CPMAS spectrum of stock budesonide (Figure 3.7) contains relatively narrow peaks indicating that the material is in a crystalline form, while the spectrum of melt-quenched material has relatively broad peaks and is consistent with amorphous material. Examination of the spectra for both the nanoparticles and agglomerates clearly shows that the budesonide is amorphous in both samples. However, a small but relatively narrow peak is seen at 185 ppm in the spectra of both the nanoparticles and the agglomerates, and there is another small peak at 23 ppm in the spectrum of the agglomerates. These peaks are consistent with peaks from the stock budesonide and suggest that the samples contain small amounts of crystalline budesonide.

The other narrow peaks in the spectrum of the agglomerates are due to the presence of L-leucine (Figure 3.8). Again, the narrow width of the L-leucine peaks in the spectrum signifies that it is in a crystalline form while the budesonide is amorphous. This indicates that both compounds exist in distinct phases within the sample. Additionally, no peaks associated with lecithin are observed in the spectra of the nanoparticles or the agglomerates. This is likely due to the relatively low concentrations of lecithin that were used, since the lecithin concentrations were approximately an order of magnitude lower than the budesonide concentrations, on a molar basis.

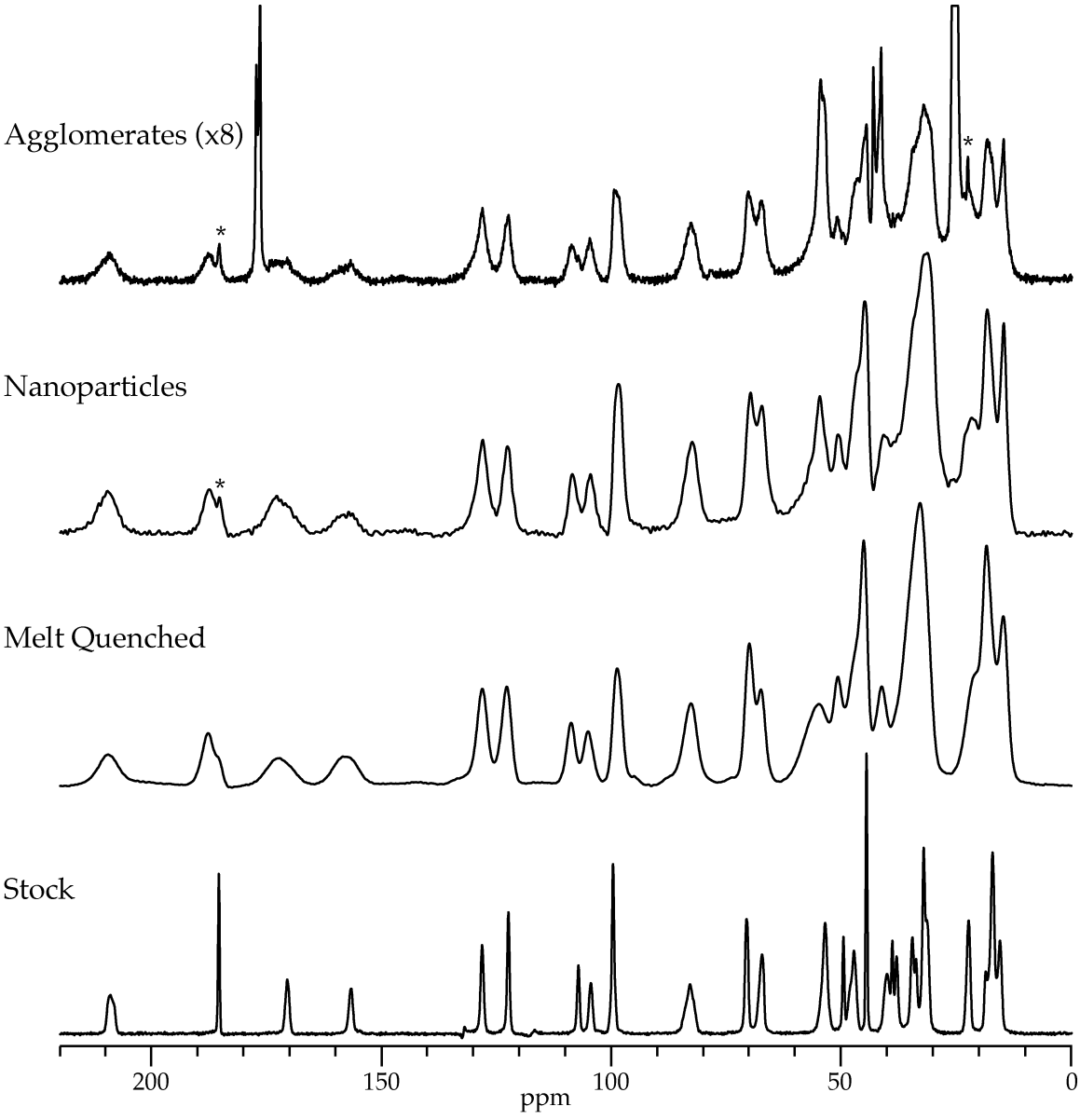

Figure 3.7. ^{13}C CPMAS spectra of budesonide samples. The bottom two spectra are of the stock budesonide and budesonide melted at 250 °C and then immersed in liquid nitrogen. Note that an 8-fold vertical expansion has been performed on the top spectrum to aid visualization of the budesonide peaks. * = Peaks in the nanoparticle and agglomerate spectra that align with peaks that were observed for stock budesonide.

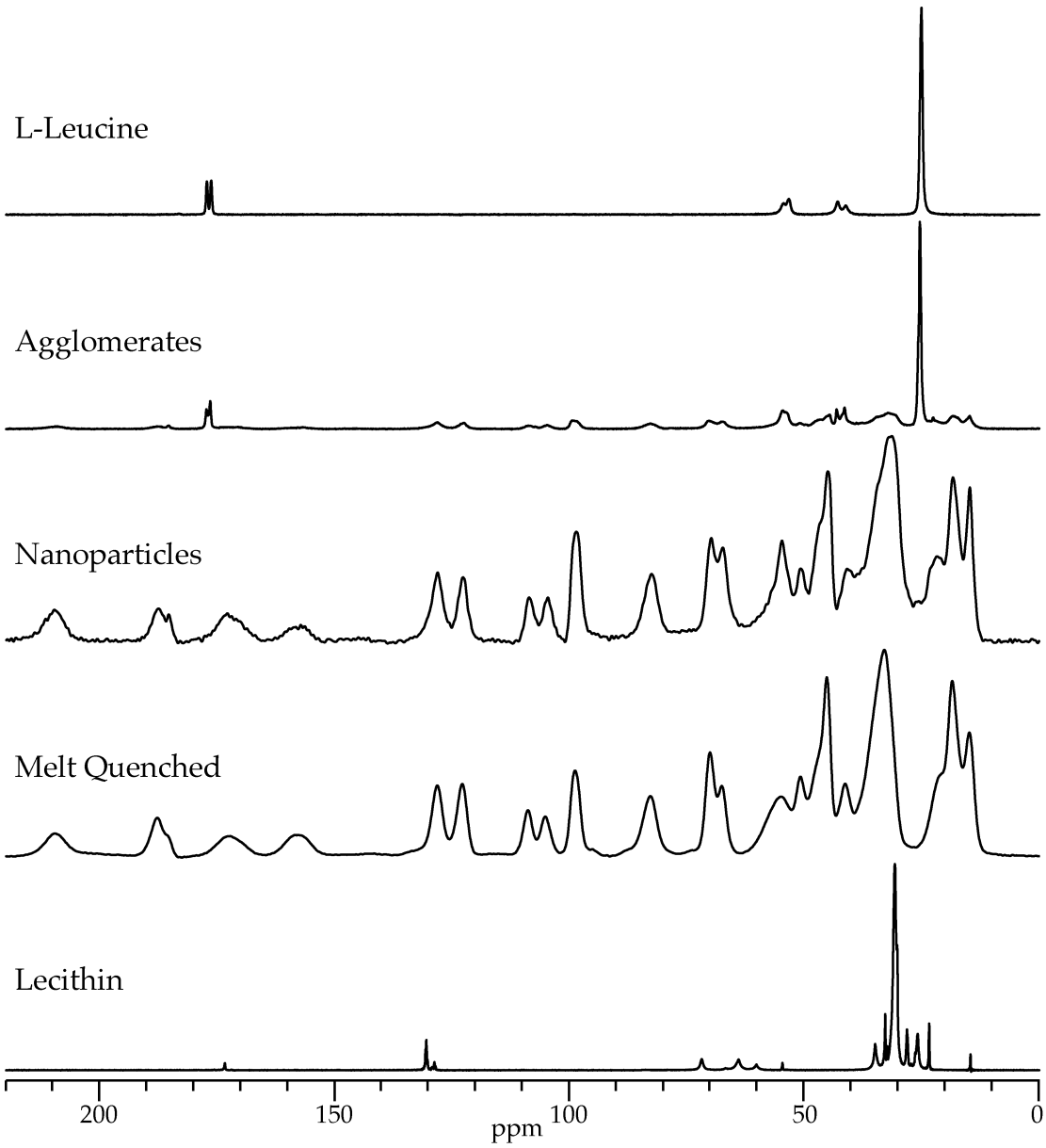

Figure 3.8. ^{13}C CPMAS spectra of L-leucine, lecithin, and budesonide samples (melt quenched, nanoparticles, and agglomerates). The melt quenched spectrum is the result of budesonide that was melted at 250 °C and then immersed in liquid nitrogen.

3.2.4 Summary

While DSC was unable to clearly identify the physical form of budesonide that was present in either the nanoparticles or agglomerates, SSNMR was able to unambiguously show that the budesonide was mostly amorphous in both materials. Finally, it is clear that there was a change in the physical form of the budesonide when it was processed to form the nanoparticles and agglomerates, but it is not obvious what impact the changes had on the observed dissolution of the materials.

3.3 Nifedipine

3.3.1 Background

Nifedipine (Figure 3.1) is a calcium channel blocker with a variety of therapeutic indications including hypertension and chronic angina. Its use is typically limited due to side effects that are associated with the high oral dosages that are usually needed for treatment. The primary site of action is in the heart and lungs, thus it is hypothesized that pulmonary delivery may permit the use of smaller targeted doses that would limit the side effects that are often experienced with oral delivery (i.e., diarrhea, hepatotoxicity, mental confusion, and gastritis). Additionally, nanoparticles of nifedipine may improve dissolution and release since its water solubility is relatively low (approximately 10 μg/mL). Therefore, a formulation strategy similar to the one used for budesonide was utilized to produce agglomerates of nifedipine nanoparticles. The materials showed trends in the dissolution behavior that were similar to the budesonide, and once again DSC did not offer conclusive evidence as to the physical form of the nifedipine

within the materials. However, SSNMR was able to show that all of the materials contained the same crystalline form of nifedipine.[23]

3.3.2 Experimental

3.3.2.1 Materials

Nifedipine, stearic acid, and sodium chloride were obtained from Sigma Chemicals Co. USA (St. Louis, MO). Ethanol (95% denatured), acetone, and phosphate buffered salts, and Spectra/Por cellulose dialysis membranes (MW cut-off = 6 – 8 kDa) were purchased from Fisher Scientific (Fair Lawn, NJ). Deionized water was obtained from a Millipore EasyPure unit or EASYpure1 RODI (Barnstead International, Model # D13321, Dubuque, IA). All materials were used without further purification, and solvents were of HPLC grade.

3.3.2.2 Nanoparticle and Agglomerate Preparation

Whenever possible, steps were taken to protect nifedipine solutions and samples from excessive exposure to light, since it is known to undergo photodegradation (~10% in 24 hr).[29] Approximately 10 mg of nifedipine and 1 mg of stearic acid was dissolved in 1 mL of ethanol and stirred overnight to ensure complete dissolution. Under probe sonication (Fisher Sonic Dismembrator, model 500, amplitude 60%), ~29 mL of cold deionized water was rapidly added to the ethanol solution and sonication was continued for 20 sec to produce nifedipine nanoparticles. The suspension was frozen at -20 °C and subsequently either lyophilized (FreeZone 1, Labconco, Kansas City, MO) or stored at 4 °C.

Nifedipine nanoparticle agglomerates were prepared by adding sodium chloride, sufficient to achieve a concentration of 0.1 M, to the refrigerated nanoparticle suspension followed by homogenization at 20,000 rpm. The material was allowed to sit at room temperature for either ~4 hr or 24 hr (followed by decantation of the liquid to remove most of the salt) before being frozen at -20 °C and subsequently lyophilized (FreeZone 1, Labconco, Kansas City, MO).

3.3.2.3 DSC

The DSC described in Section 3.2.2.3 of this chapter, was utilized to assess the physical form present in each of the materials: stearic acid, stock nifedipine, nanoparticles, and agglomerates. Approximately 1 to 4 mg of either nanoparticles or agglomerates were heated from 50 to 200 °C at a heating rate of 10 °C/min. While ~9 mg of stock nifedipine was heated form 120 to 200 °C and ~11 mg of stearic acid was heated from 40 to 190 °C, both at a heating rate of 10 °C/min.

3.3.2.4 TGA

Stock nifedipine and stearic acid were analyzed by TGA (see Section 3.2.2.4 of this chapter) to ascertain residual solvent content and determine the degradation temperatures. Approximately 7 mg of each sample was placed in a platinum pan and heated from room temperature to over 400 °C at a rate of 20 °C/min.

3.3.2.5 SSNMR Spectroscopy

SSNMR data was collected on the CMX-300 spectrometer with the same rotors and MAS spinning conditions reported in Section 3.2.2.5. FIDs were collected with a ramped amplitude CP[25] TOSS[30,31] sequence with ~81 kHz of proton decoupling using the SPINAL-64[26] method. Between 1,600 and 3,600 transients were collected for each FID with a pulse delay of 20 – 45 sec, a contact time of 2 – 7 msec, and a ^{1}H 90° pulse width of 3.1 μsec. The FIDs contain 2,048 – 3,072 points with a dwell time of 33.3 μsec. Spectra were externally referenced to TMS using the methyl peak of MGA at 18.84 ppm.[27]

3.3.3 Results & Discussion

3.3.3.1 Particle Characterization

The nanoparticles had an average particle size of 470 ± 40 nm, while the agglomerates had geometric and aerodynamic particle diameters of approximately 10 and 2 μm, respectively. The agglomerates displayed high emitted and respirable fractions of 91 and 94%, respectively. Also the materials followed the same dissolution trends as the budesonide[22] materials for both extent and rate of dissolution (nanoparticles > agglomerates > stock). It was even possible to correlate the particle size to the dissolution rate of the materials, which suggested that the particle size and thus surface area was the controlling factor in the rate of dissolution for the materials. However, the physical state of the nifedipine in the materials still needed to be eliminated as a contributing factor.

3.3.3.2 Thermal Analysis (DSC/TGA)

Nifedipine is known to have three anhydrous polymorphs (Form I, II, and III) and has the ability to form amorphous materials.[32] Form I has a reported melting point of 173 °C and amorphous nifedipine has a T_g of 45 °C.[32] The DSC of the stock nifedipine (Figure 3.9) is consistent with Form I, and the endothermic event that is observed for stearic acid is consistent with its reported melting point (69 – 70 °C).[33] Neither nifedipine nor stearic acid showed any significant loss of mass below approximately 190 °C (Figure 3.10).

When nanoparticles were prepared in the absence of stearic acid the only observed transitions were a broad endotherm at 150 °C followed by a broad exotherm at 160 °C (Figure 3.9). This cannot be due to formation of a eutectic as the sample only contains nifedipine. Also, the event is significantly lower (> 20 °C difference) in temperature than melting of Form I, and melting point depression due to reduced particles size should only result in a change of ~0.5 °C (500 nm particles). Thus it would appear that the nifedipine might be in a different physical form, possibly a crystalline state, in the nanoparticles. However the endotherm is not consistent with melting of either Form II (163 °C) or Form III (135 °C).[34] The nanoparticles that were prepared with stearic acid show a very similar thermograph, but also show melting of stearic acid at 65 °C.

The agglomerates thermograph (Figure 3.9) also shows the melting endotherm for stearic acid. However, only a broad endothermic transition is observed at higher temperatures (170 °C) but it is still not consistent with melting point depression or one of the known crystalline forms.[18,34] It should also be noted that none of the materials were analyzed at low enough temperatures to

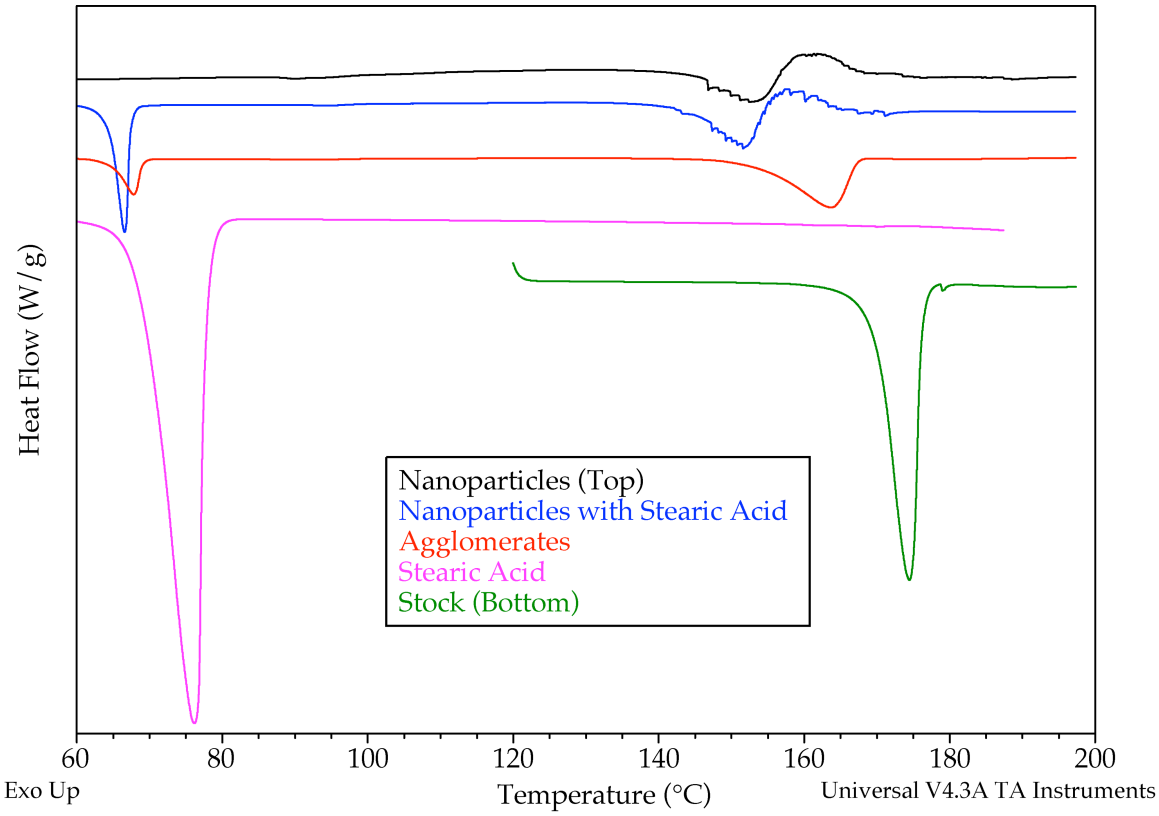

Figure 3.9. DSC thermographs of nifedipine materials and stearic acid. Two preparations of nanoparticles were analyzed, one processed with and the other without stearic acid. The agglomerates were prepared with stearic acid, following aggregate formation the supernatant was not removed before lyophilization.

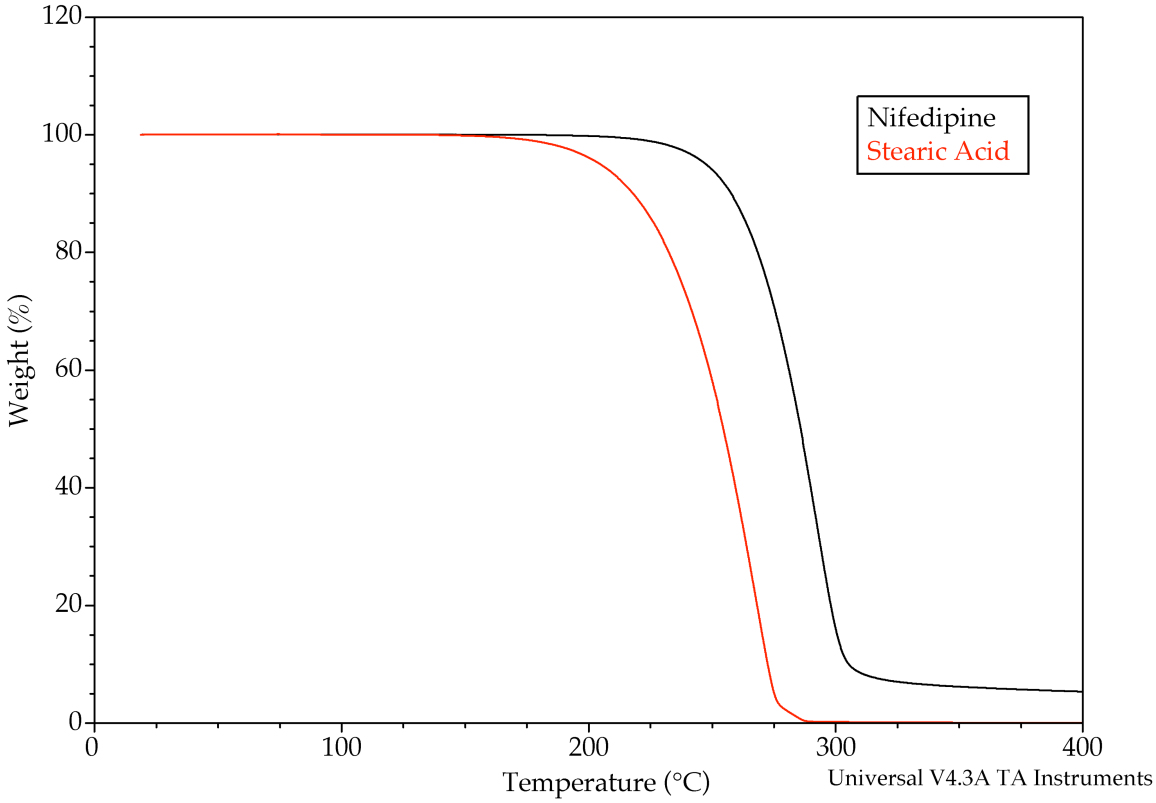

Figure 3.10. TGA thermographs of stock nifedipine and stearic acid.

permit observation of a glass-transition event (T_g ~45 °C)[32] so it is not possible to eliminate the presence of amorphous nifedipine in any of the materials. Thus, DSC was not able to unambiguously identify the physical form of nifedipine that is present in the nanoparticles and agglomerates.

3.3.3.3 SSNMR Spectroscopy

The stock nifedipine ^{13}C CPMAS spectrum in Figure 3.11 agrees well with the previously reported SSNMR characterization of Form I.[32] The spectra of the nanoparticles and agglomerates match the spectrum of stock material, indicating that the physical form was not changed during the processing steps. Additionally, the nifedipine peaks in the nanoparticle sample were slightly broader (~2 Hz) and the material had a shorter ^1H T_1 relaxation time when compared to the stock material (15 vs. 37 sec). This is consistent with previous reports regarding the relationship of particle size to SSNMR line width and relaxation properties.[35,36]

The nanoparticle sample was prepared with stearic acid and peaks are can be clearly observed in the ^{13}C CPMAS spectrum, indicating the presence of stearic acid in the sample (Figure 3.11). However, the spectrum of the agglomerates only shows peaks from nifedipine, but the DSC clearly showed melting of stearic acid (Figure 3.9). These differences were caused by the methods in which the two samples were isolated. The DSC sample was lyophilized without any further processing after the agglomeration was performed. Conversely the SSNMR sample was allowed to settle for 24 hrs, the supernatant was then poured off and the remaining material was lyophilized. This isolation method was used to remove most of the salt from the sample to

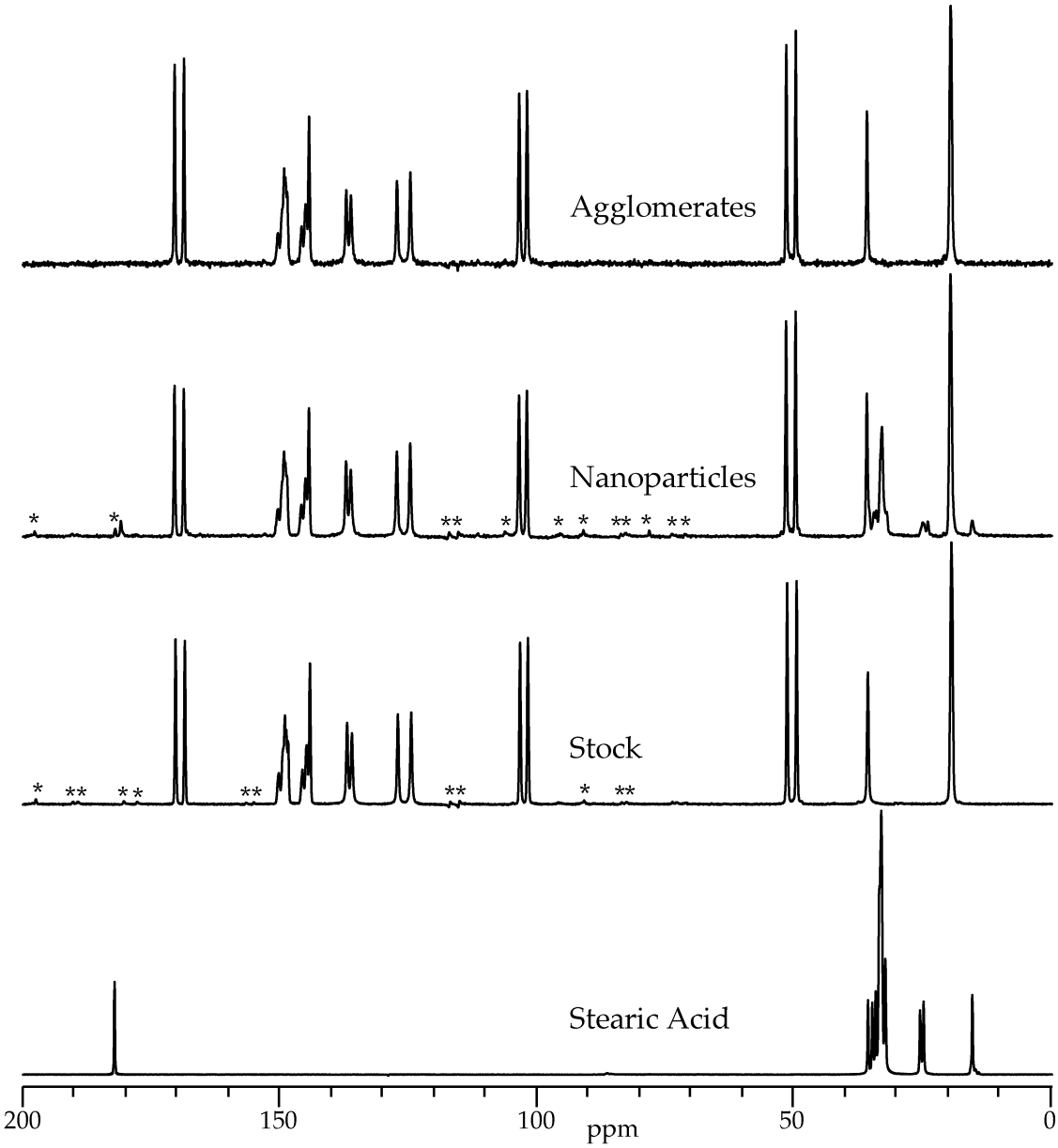

Figure 3.11. ^{13}C CPMAS spectra of nifedipine materials and stearic acid. The nanoparticles and agglomerates were prepared with stearic acid, but following aggregate formation the supernatant was removed before lyophilization. * = spinning sidebands

avoid any potential complications due to the large amounts of salt that would have been present in the SSNMR sample under the other isolation method. Thus, the SSNMR and DSC data demonstrate the dramatic differences that can occur in the sample composition when small, seemingly insignificant modifications are made to processing steps. These differences also suggest that the stearic acid, or at least most of it, is not interacting directly with the nifedipine. This conclusion is supported when the ^{1}H T_1 values of the nifedipine and stearic acid in the nanoparticle sample. The two materials have different T_1 values (nifedipine 15 sec and stearic acid 8 sec) indicating that they are each in independent phases.

3.3.4 Summary

As with budesonide, DSC was unable to clearly identify the physical form of nifedipine that was present in either the nanoparticles or agglomerates, However, SSNMR was able to unambiguously show that the nifedipine existed as Form I in all of the materials. Thus, the processing steps did not result in any physical changes in the nifedipine, except for the altered particle sizes. Thus it can be concluded that the changes in the observed dissolution of the materials was not due to any changes in the physical form of the API.

3.4 Ciprofloxacin

3.4.1 Background

Ciprofloxacin (Figure 3.1) is a fluoroquinolone antibiotic that is particularly effective against several types of lung infection. It is typically

administered orally, but a pulmonary formulation that provides prolonged release might help ensure complete elimination of lung infections while limiting systemic drug concentrations. In order to achieve the desired prolonged release, nanoparticles of ciprofloxacin were encased in microspheres of poly(D,L-lactic-co-glycolic acid) (PLGA). Following inhalation, the PLGA should slowly erode and release the ciprofloxacin while the relatively large size of the microspheres would prevent the alveolar macrophages from clearing the formulation from the lungs. DSC of the ciprofloxacin nanoparticles displayed an endothermic transition that occurred at a temperature significantly below the melting point of ciprofloxacin, but there was no corresponding mass loss observed by TGA, suggesting that the nanoparticles and stock material may contain different physical forms. This was confirmed with both ^{13}C and ^{19}F SSNMR; however, due to poor encapsulation efficiencies the microparticles could not be analyzed to see which form of ciprofloxacin they contained.[21]

3.4.2 Experimental

3.4.2.1 Materials

Poly(D,L-lactide-co-glycolide) (50:50 lactic acid:glycolic acid; i.v. = 0.31 dL/g; MW ~ 31,000) was obtained from Absorbable Polymers, Inc (Pelham, AL). Polyvinyl alcohol (MW = 22,000, 88% hydrolyzed) was purchased from Polysciences, Inc. (Warrington, PA). Ciprofloxacin was obtained from Sigma Chemicals Co. USA (St. Louis, MO). Commercial grade canola oil and silicone oil (viscocity = 57 cP and 100 cP, respectively) were used as porogens. Dichloromethane, dimethylsulfoxide, and heptane were purchased from Fisher

Scientific (Fair Lawn, NJ). All materials were used without further purification, and solvents were of HPLC grade.

3.4.2.2 Nanoparticle Preparation

A solution of 0.5 – 5% (w/v) poly(D,L-lactide-co-glycolide) (PLGA) in dichloromethane was prepared. A nanosuspension was prepared by adding ciprofloxacin to the PLGA/dichloromethane solution and sonicating (Fisher Scientific Sonic Dismembrator, Model 500) the mixture for 90 sec. If pore formation was desired, either canola or silicone oil were added to the nanosuspension (0.87 – 3.58 w/w oil:PLGA) and the mixture was sonicated for an additional 90 sec. Microparticles were then produced from the nanosuspension by Precision Particle Fabrication technology,[4-6,37-40] stirred in a solution of 1% PVA for ~3 hr, filtered, washed with heptane to remove the canola or silicone oil, and finally washed with deionized water. The resulting microspheres were lyophilized for at least 48 hr and stored at -20 °C under desiccating conditions.

3.4.2.3 DSC

A Q100 DSC (see Section 3.2.2.3 of this chapter) was used to evaluate the physical form of the ciprofloxacin nanoparticles. Samples were placed in crimped aluminum pans and consisted of 1.5 – 4 mg of material. Unless indicated otherwise, samples were heated from -80 to 400 °C at a heating rate of 20 °C/min. In order to differentiate thermal and kinetic events, some materials were heated at three different rates (3, 10, and 20 °C/min).

3.4.2.4 TGA

The TGA reported in Section 3.2.2.4 of this chapter, was used to determine if any residual solvent was present in the nanoparticles and to determine the degradation temperature of the ciprofloxacin. Approximately 3 mg of material was placed in a platinum pan and was heated from room temperature to 400 °C at a rate of 20 °C/min.

3.4.2.5 SSNMR Spectroscopy

All ^{13}C SSNMR data was collected on the CMX-300 spectrometer (see section 3.2.2.5 of this chapter) but the packed samples were spun at 7.5 kHz. FIDs were collected using a variable amplitude CP[41] sequence with ~68 kHz of proton decoupling using the two pulse phase modulation (TPPM) method.[42] Between 2,048 and 23,000 transients were collected for each FID with a pulse delay of 2 – 8 sec, a contact time of 1.5 – 2 msec, and a ^{1}H 90° pulse width of 3.7 μsec. The FIDs contain 1,024 points with a dwell time of 33.3 μsec. Spectra were externally referenced to TMS using the methyl peak of MGA at 18.84 ppm.[27]

All ^{19}F SSNMR data was collected on a Tecmag Apollo spectrometer (Houston, TX) operating at a ^{1}H resonance frequency of 300 MHz. Samples were packed into 3.2 mm zirconia rotors and held in place with Torlon® end caps (Varian, Palo Alto, CA). The packed rotors were spun with MAS[24] at a rate of 21 kHz in a 3.2 mm spin module (Varian, Palo Alto, CA). The FIDs were collected using a ramped amplitude CP[25] sequence with ~83 kHz of proton decoupling using the TPPM method.[42] Between 256 and 1,024 transients were collected for each FID with a pulse delay of 2 – 15 sec, a contact time of 3 msec, and a ^{1}H 90° pulse width of 3 μsec. The FIDs contain 1,024 points with a dwell time of 10 μsec.

Spectra were externally referenced to Teflon® at -121.0 ppm.

3.4.3 Results & Discussion

3.4.3.1 Particle Characterization

The particle size of the nanoparticles was not directly measured but was estimated to be approximately 400 nm from scanning electron microscopy (SEM) images of the microspheres. The PLGA microspheres had geometric and aerodynamic diameters ranging from approximately 4 to 30 μm. The ciprofloxacin nanoparticles dissolved completely within about 5 days, but when they were encapsulated their release rate decreased as the size of the microspheres increased, with some of the materials releasing ciprofloxacin over the course of 25 days. The target drug loading for the microspheres was 4 – 5% (w/w) but the encapsulation efficiency was very poor and only resulting in loadings of < 0.2% (w/w) with the exception of one sample that had a loading of 0.4% (w/w). Therefore, only the nanoparticles were examined for physical form changes, because it was not clear if the microspheres contained sufficient amounts of ciprofloxacin to be detected by any of the characterization techniques.

3.4.3.2 Thermal Analysis (DSC/TGA)

The DSC of stock ciprofloxacin (Figure 3.12) displayed an endothermic transition with an onset of 271 °C that could be consistent with melting or degradation of ciprofloxacin. Therefore, DSC thermographs were collected at

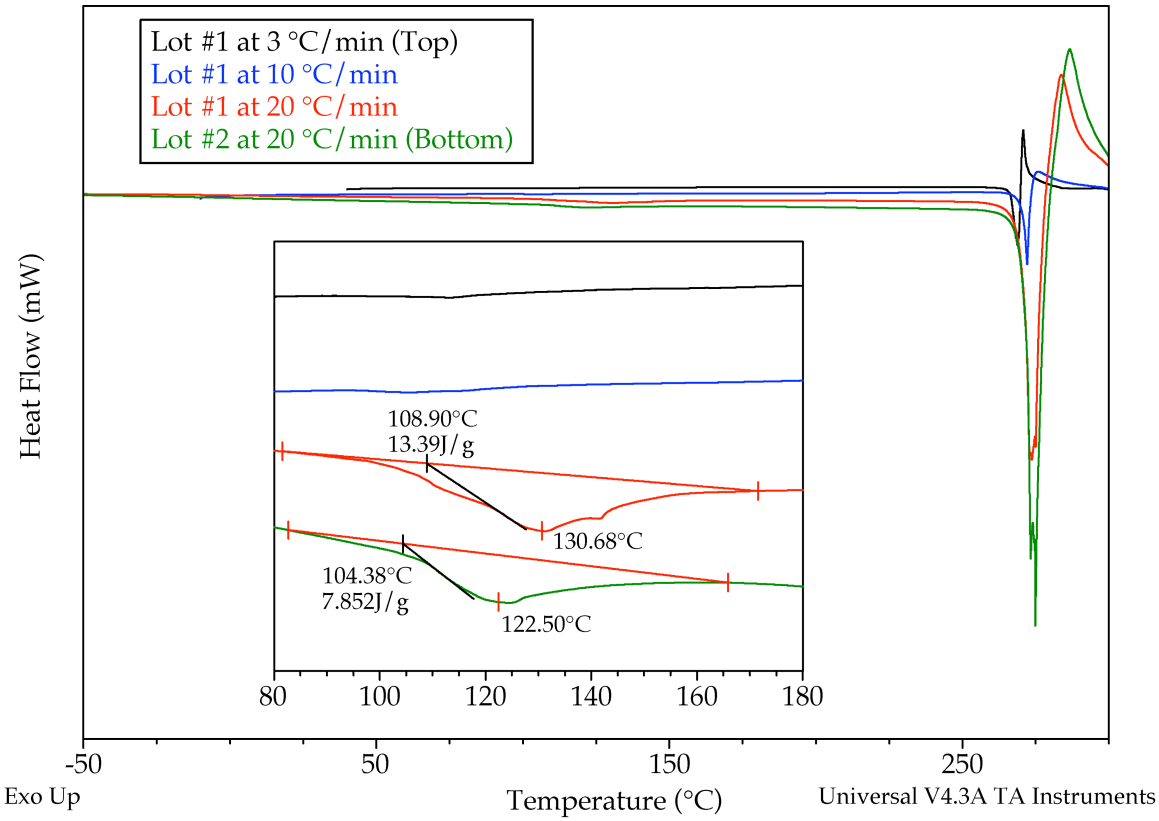

Figure 3.12. DSC of two lots of stock ciprofloxacin that were received from Sigma. Lot #1 was analyzed at three different heating rates and Lot #2 was analyzed at the fastest of those three heating rates. All of the thermographs showed melting of ciprofloxacin at 271 °C with the exception of Lot #1 heated at 3 °C/min which melted at 267 °C. The insert is an expansion of the data to show the lower temperature endotherm that was observed.

several heating rates and the results showed that the onset temperature of the endotherm did not change significantly, indicating that the endotherm was due to melting of ciprofloxacin. The peak of the transition was relatively noisy and was followed by additional events, which suggest that ciprofloxacin degrades at approximately the same temperature. When the heating rate was dropped to 3 °C/min there was a slight drop in the temperature of the transition (267 °C), this change was probably due to the kinetics of the ciprofloxacin degradation.

The stock ciprofloxacin also showed an endotherm at 130 °C when it was heated at the fastest heating rate (Figure 3.12). The origin of this endotherm was unknown as there are no reported polymorphs of ciprofloxacin and it was smaller in size and at a higher temperature than would typically be expected for desolvation. Another lot of ciprofloxacin was purchased from Sigma and it showed the same behavior when analyzed by DSC.

A batch of nanoparticles was also analyzed by DSC and showed the same melting behavior at 271 °C when the heating rate was changed (Figure 3.13). However, at all three heating rates there was a very large endotherm that was similar to the observed event in the two lots of stock material except that it was significantly larger in the nanoparticle sample. In order to confirm the observations and identify how reproducible they were, another batch of nanoparticles were prepared and analyzed by DSC (Figure 3.14). Again they showed the same transitions but the size of the 130 °C transition was much smaller and matched more closely with the stock ciprofloxacin. In addition, the transition did not correlate to any observed mass loss by TGA (Figure 3.15). The nanoparticles did show a mass loss of 2.1% below 70 °C and then no further

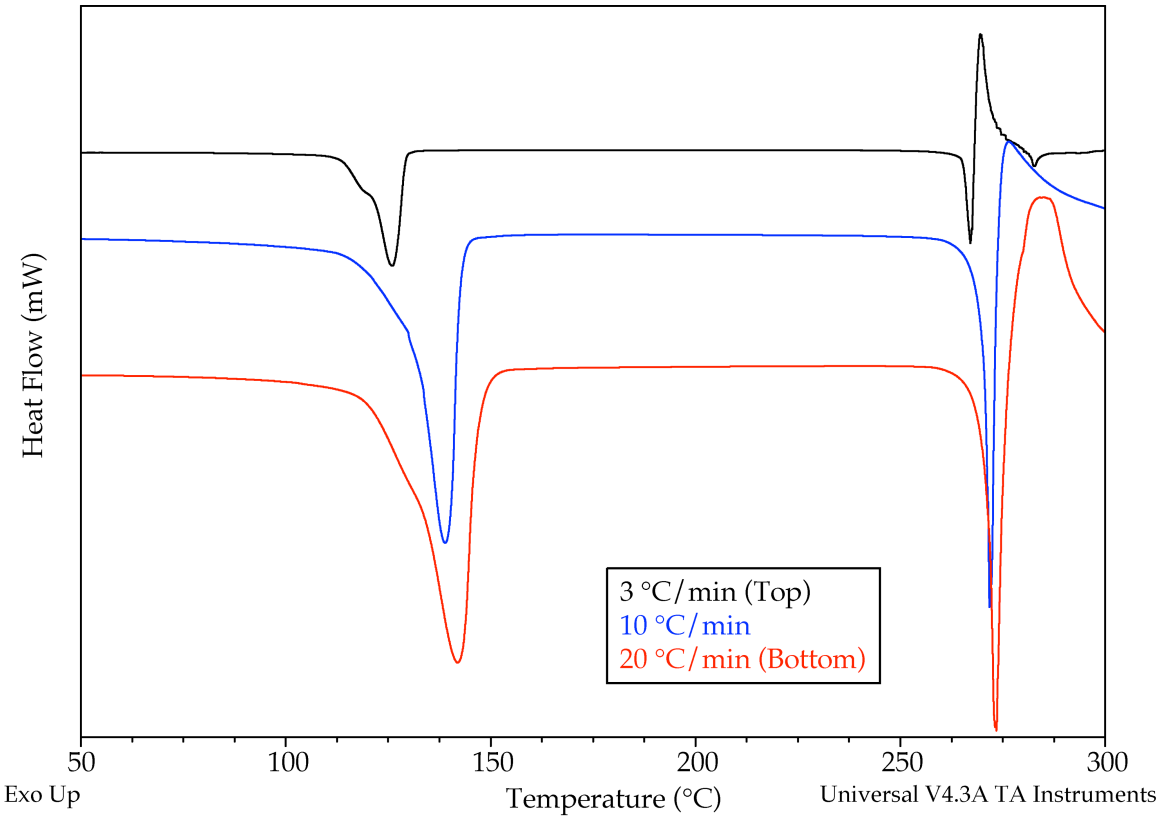

Figure 3.13. DSC of ciprofloxacin nanoparticles from Batch #1, analyzed at three heating rates. The material melted at 271 °C for the two fastest heating rates, but melting was observed at 265 °C when the heating rate was reduced to 3 °C/min. The peak temperature of the other endotherm in each thermograph shifted from 126 to 142 °C when the heating rate was increased from 3 to 20 °C/min.

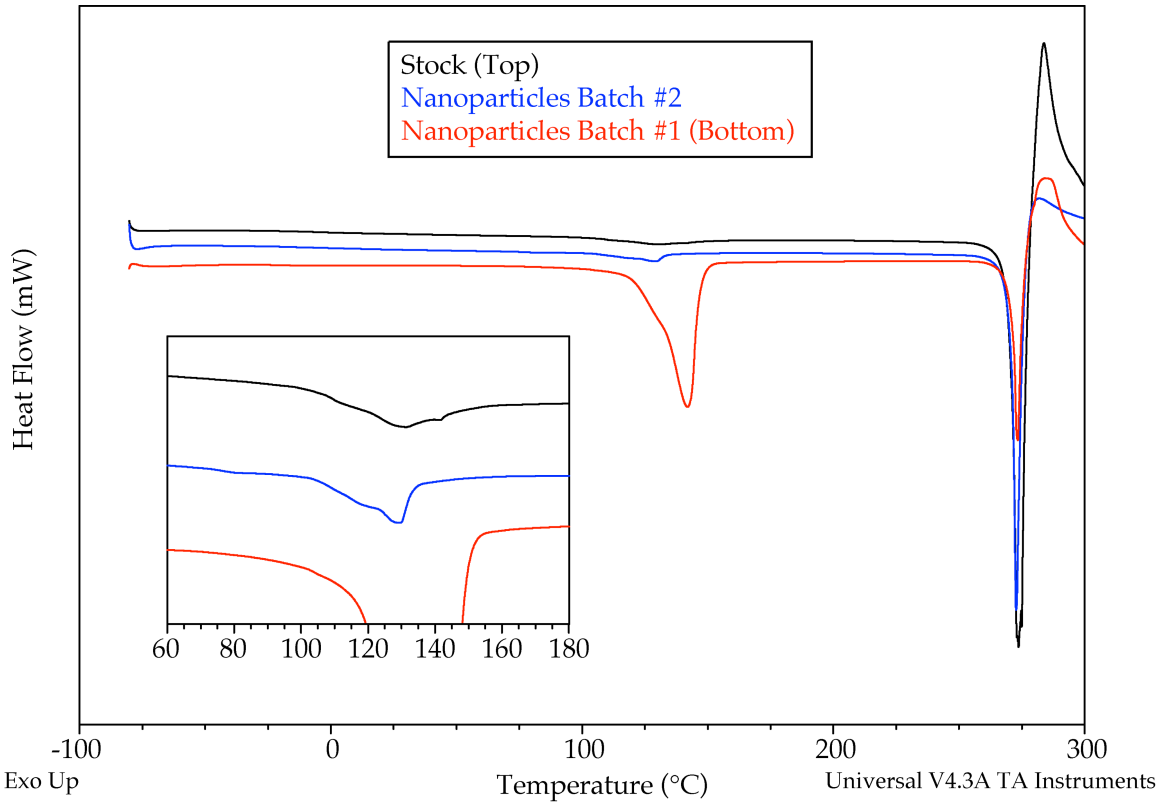

Figure 3.14. DSC of stock ciprofloxacin Lot #1 and two batches of nanoparticles. The inset is an expansion of the thermographs to show the lower temperature endotherms for the samples, particularly the stock ciprofloxacin and Batch #2 of the nanoparticles.

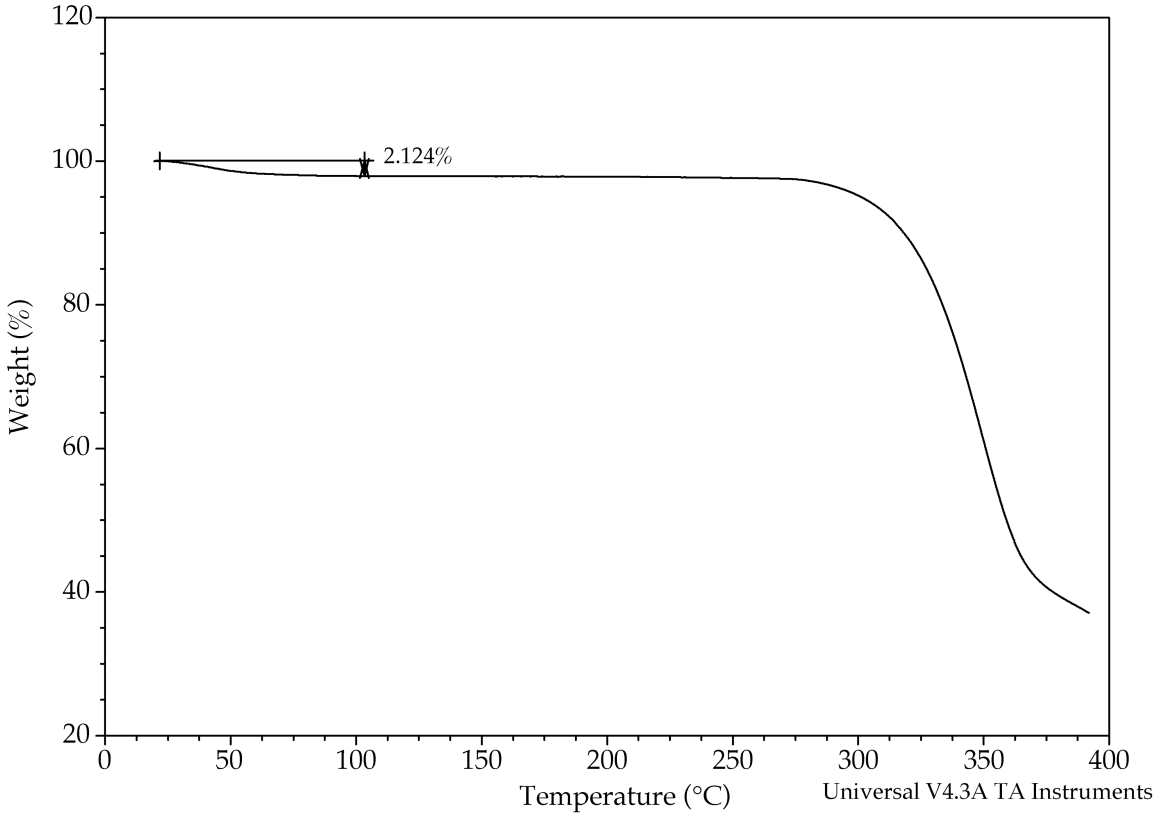

Figure 3.15. TGA of ciprofloxacin nanoparticles Batch #2.

changes were observed until approximately 275 °C (Figure 3.15). It is thought that the 2.1% mass loss is either due to residual dichloromethane or water that is adsorbed to the surface of the particles, while the mass loss at 275 °C agrees with the previous observations regarding the similarity of the melting and degradation temperatures of the stock ciprofloxacin (Figure 3.12).

Consequently, the DSC appears to suggest that the samples contained different forms of ciprofloxacin. It also implies that production of the nanoparticles can alter the relative amounts of the forms. However, the extent of the form changes does not appear to be completely reproducible. Additionally, closer inspection of the endotherms in Figure 3.13 suggests that there may actually be at least two overlapping endotherms at approximately 130 °C, which may indicate that several forms are present or several form conversions may occur around that temperature. SSNMR was used to obtain a more complete picture of the differences between these materials.

3.4.3.3 SSNMR Spectroscopy

The ^{13}C CPMAS spectrum of stock ciprofloxacin (Figure 3.16) displays relatively narrow peaks, particularly the peaks in the aromatic and carbonyl regions. This indicates that it is crystalline and it seems to be of a relatively pure form and not a mixture of forms. Comparison of the spectra of the stock material and the first batch of nanoparticles reveals numerous, differences between them. However, the peaks in the spectrum of the nanoparticle sample are also narrow, indicating that it is crystalline, and the large number of peaks suggests that it is either a mixture of crystalline forms or that the crystal structure has a $Z' > 1$.

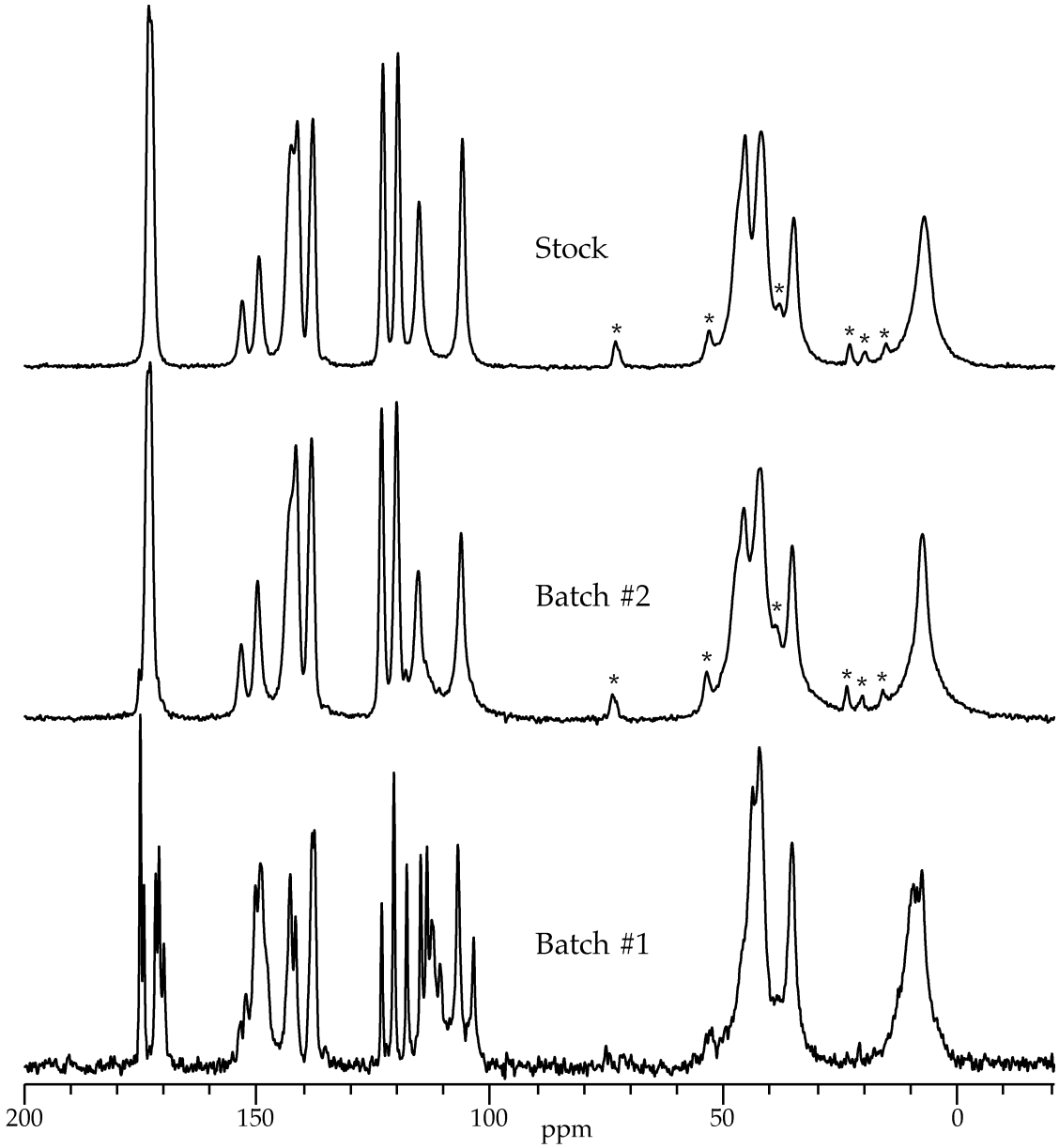

Figure 3.16. ^{13}C CPMAS spectra of stock ciprofloxacin Lot #1 and both batches of ciprofloxacin nanoparticles. * = spinning sidebands

The spectrum of the second batch of nanoparticles (Figure 3.16) appears to match very closely with the stock material, but it does appear to contain some small peaks that may be consistent with the other batch of nanoparticles. In order to make the differences more apparent, the carbonyl region of the spectra in Figure 3.16 have been expanded and are shown in Figure 3.17. The spectrum of the stock material has two peaks in this portion of the spectrum, one each for C-7 and C-11 (Figure 3.1). However, the first batch of nanoparticles has five peaks in this region of the spectrum and none of the peaks correspond with the peaks in the stock material. None of the peaks appear to be similar in intensity which suggests that the sample is simply a mixture of forms and does not seem to display any signs of peak splitting due to a $Z' > 1$. That would imply that the first nanoparticle batch is a mixture of at least three crystalline forms that are all different from the form in the stock ciprofloxacin.

The carbonyl region of the second batch of nanoparticles (Figure 3.17) shows two prominent peaks that correlate with the peaks of the form in the stock material. Yet, there is also a small peak at ~175 ppm that corresponds with a peak in the first batch. Additionally, there appear to be several other small signals and shoulders that correlate with the peaks from the first batch of nanoparticles, but the signal-to-noise ratio (S/N) of the spectrum is not sufficient to state with certainty that they are peaks. Thus, the ^{13}C spectra of the materials are consistent with the DSC observations that the first batch of nanoparticles appears to be primarily a mixture of several crystalline forms and the second batch may contain small amounts of the forms but primarily consists of the form that was present in the stock material.

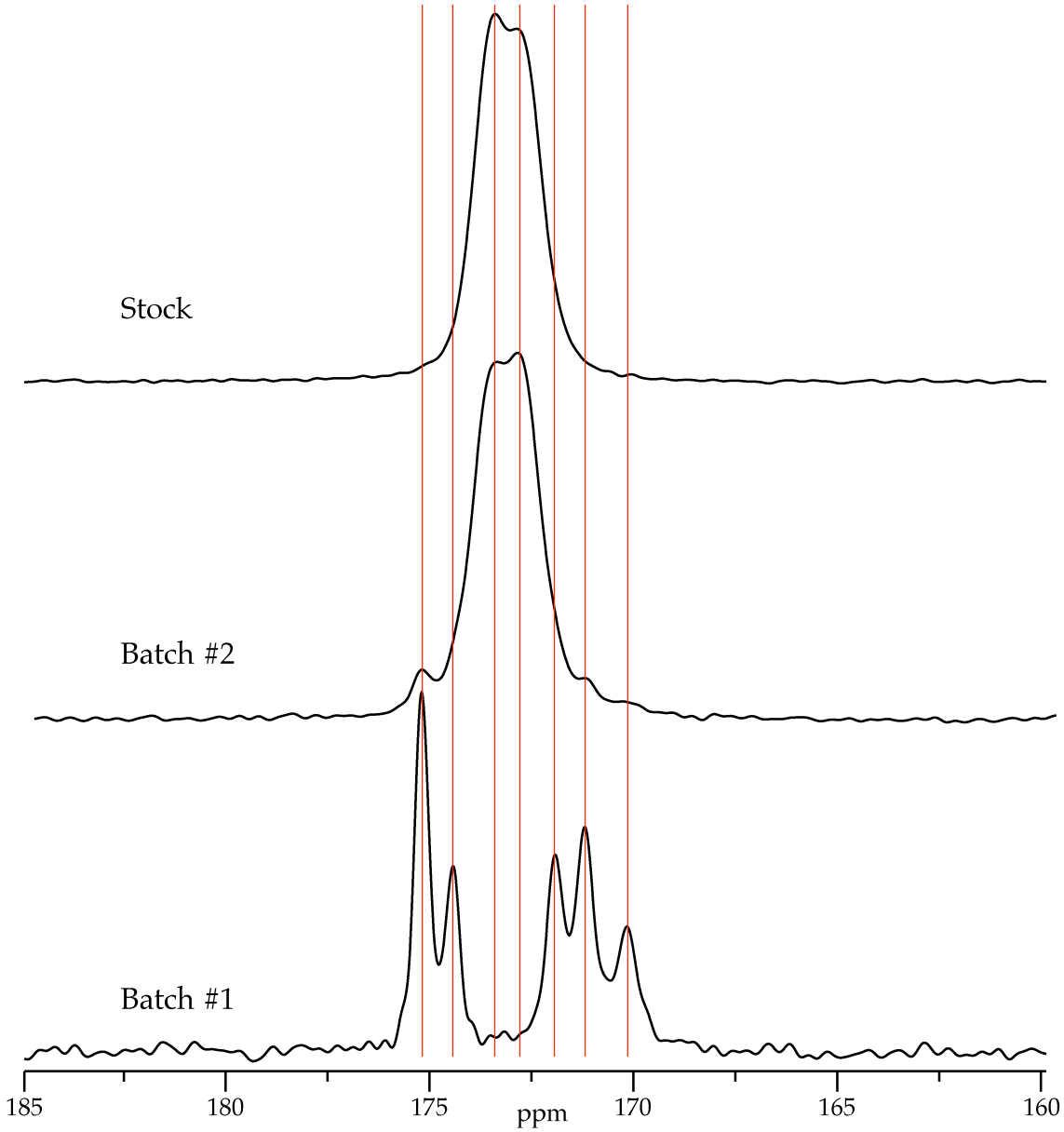

Figure 3.17. ^{13}C CPMAS spectra from Figure 3.16, expanded to show only the carbonyl peaks for each of the materials. The red lines are intended to aid visualization of the relative positions of the peaks in the spectra.

The ciprofloxacin molecule also contains a fluorine atom, which can also be observed with SSNMR and is considerably more sensitive than ^{13}C. The ^{19}F CPMAS spectra (Figure 3.18) show the same results as the previous ^{13}C experiments. The stock material displays a single peak while the first batch of nanoparticles shows at least four peaks. Additionally, the other batch of nanoparticles is almost an exact match of the stock material but may display some very small peaks due to the presence of a small amount of other forms.

Unfortunately, due to poor encapsulation efficiency during the production of the microspheres it was not possible to examine how the additional processing steps may have further altered which ciprofloxacin physical forms that were present. Also, it was not possible to determine what, if any, affect the ciprofloxacin forms had on the release profiles of the microspheres. However, when all of the stock ciprofloxacin and nanoparticles were stored at ambient conditions for approximately one month and then reanalyzed, they all matched the DSC and SSNMR results for the stock material, and the endotherm at 130 °C was no longer observed. This indicates that the physical forms in the first nanoparticle batch are metastable at ambient conditions. Therefore, if the forms were present in the microspheres they would likely have converted to the stable form over the course of the dissolution studies (up to 25 days) and probably would have impacted the dissolution rates.

3.4.4 Summary

DSC was able to detect the change in the physical form of the ciprofloxacin when the nanoparticles were generated. But SSNMR was able to show that the processing actually generated a mixture of crystalline forms.

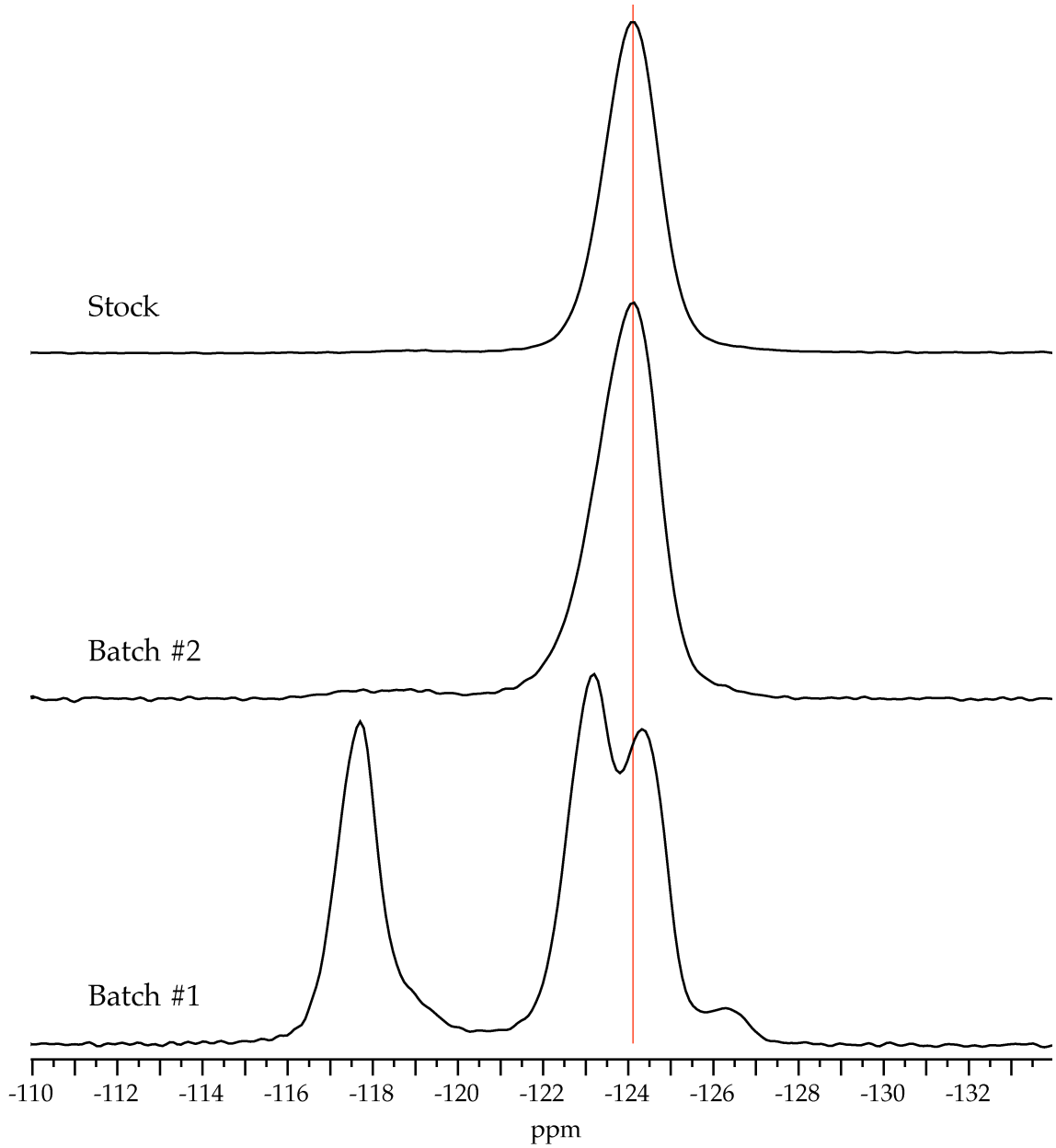

Figure 3.18. ^{19}F CPMAS spectra of ciprofloxacin stock material and both nanoparticle batches.

Unfortunately, the ciprofloxacin in the PLGA microspheres had a low encapsulation efficiency and so the physical form of the ciprofloxacin in those materials were not determined. The generation of the metastable ciprofloxacin forms appears to be inconsistent and they could have converted to the stable form over the course of the dissolution studies if they were present in the microspheres.

3.5 Overall Summary

It has been shown previously that the physical form of the API in a formulation, even a formulation utilizing nanoparticles, will influence the dissolution behavior of the formulation.[8] Thus it is critical to characterize formulations to identify the physical form of the API in the final formulation. The above sections have presented three cases demonstrating some of the pitfalls that can be encountered when developing a new formulation.

The budesonide and nifedipine examples showed that one processing method can sometimes result in API physical form changes and at other times have no impact. In the case of budesonide the stock material was crystalline but in the final formulation it was amorphous. Nifedipine showed no change in its physical form even though the processing steps were almost identical, although the actual compounds used in the formulations were different. Additionally, the nifedipine example demonstrated how significantly the composition of the final formulation can be altered by small changes in the processing of the materials.

The third example, ciprofloxacin, is a case in which new physical forms are discovered unexpectedly. The generation of the physical forms was not well

controlled or understood and likely influenced the dissolution profile of the formulations. Furthermore, the new forms were metastable and so not only was the level of each of the forms likely different in each of the formulations, but they were probably changing over the course of the dissolution studies.

These examples also help to illustrate the limitations of techniques such as DSC. In both the budesonide and nifedipine cases DSC was not able to offer any significant insight into the physical form of the API in any of the samples, apart from the stock materials. DSC did offer some limited information in the ciprofloxacin example; however, it was not information that could not also be obtained from the SSNMR spectra. Instead, a technique such as SSNMR is clearly more applicable to these types of studies. It limits the likelihood of form changes during the experiment and offers a wealth of information about the sample (relaxation properties, etc.), which is not available from other techniques.

3.6 References

1. Kesisoglou F, Panmai S, Wu Y 2007. Nanosizing--oral formulation development and biopharmaceutical evaluation. Adv Drug Deliv Rev 59(7):631-644.

2. Rabinow BE 2004. Nanosuspensions in drug delivery. Nat Rev Drug Discov 3(9):785-796.

3. Batycky RP, Hanes J, Langer R, Edwards DA 1997. A theoretical model of erosion and macromolecular drug release from biodegrading microspheres. J Pharm Sci 86(12):1464-1477.

4. Berkland C, Kim K, Pack DW 2003. PLG microsphere size controls drug release rate through several competing factors. Pharm Res 20(7):1055-1062.

5. Berkland C, King M, Cox A, Kim K, Pack DW 2002. Precise control of PLG microsphere size provides enhanced control of drug release rate. J Control Release 82(1):137-147.

6. Berkland C, Kipper MJ, Narasimhan B, Kim KK, Pack DW 2004. Microsphere size, precipitation kinetics and drug distribution control drug release from biodegradable polyanhydride microspheres. J Control Release 94(1):129-141.

7. Raman C, Berkland C, Kim K, Pack DW 2005. Modeling small-molecule release from PLG microspheres: effects of polymer degradation and nonuniform drug distribution. J Control Release 103(1):149-158.

8. Lai F, Sinico C, Ennas G, Marongiu F, Marongiu G, Fadda AM 2009. Diclofenac nanosuspensions: influence of preparation procedure and crystal form on drug dissolution behaviour. Int J Pharm 373(1-2):124-132.

9. Rizi K, Green RJ, Donaldson M, Williams AC 2011. Production of pH-responsive microparticles by spray drying: investigation of experimental parameter effects on morphological and release properties. J Pharm Sci 100(2):566-579.

10. de Oliveira HP, Tavares GF, Nogueiras C, Rieumont J 2009. Physico-chemical analysis of metronidazole encapsulation processes in Eudragit copolymers and their blending with amphiphilic block copolymers. Int J Pharm 380(1-2):55-61.

11. Dong Y, Ng WK, Shen S, Kim S, Tan RBH 2009. Preparation and characterization of spironolactone nanoparticles by antisolvent precipitation. Int J Pharm 375(1-2):84-88.

12. Onoue S, Aoki Y, Kawabata Y, Matsui T, Yamamoto K, Sato H, Yamauchi Y, Yamada S 2011. Development of inhalable nanocrystalline solid dispersion of tranilast for airway inflammatory diseases. J Pharm Sci 100(2):622-633.

13. Zhang Z-B, Shen Z-G, Wang J-X, Zhang H-X, Zhao H, Chen J-F, Yun J 2009. Micronization of silybin by the emulsion solvent diffusion method. Int J Pharm 376(1-2):116-122.

14. Adi H, Young PM, Chan H-K, Stewart PJ, Agus H, Traini D 2008. Cospray dried antibiotics for dry powder lung delivery. J Pharm Sci 97(8):3356-3366.

15. Fakes MG, Vakkalagadda BJ, Qian F, Desikan S, Gandhi RB, Lai C, Hsieh A, Franchini MK, Toale H, Brown J 2009. Enhancement of oral bioavailability of an HIV-attachment inhibitor by nanosizing and amorphous formulation approaches. Int J Pharm 370(1-2):167-174.

16. Natarajan V, Krithica N, Madhan B, Sehgal PK 2011. Formulation and evaluation of quercetin polycaprolactone microspheres for the treatment of rheumatoid arthritis. J Pharm Sci 100(1):195-205.

17. Fini A, Cavallari C, Ospitali F, Gonzalez-Rodriguez ML 2011. Theophylline-loaded compritol microspheres prepared by ultrasound-assisted atomization. J Pharm Sci 100(2):743-757.

18. Planinsek O, Zadnik J, Kunaver M, Srcic S, Godec A 2010. Structural evolution of indomethacin particles upon milling: Time-resolved quantification and localization of disordered structure studied by IGC and DSC. J Pharm Sci 99(4):1968-1981.

19. Byrn S, Pfeiffer R, Stowell J *Solid-state chemistry of drugs*, 1999, pp 576.

20. Katrincic LM, Sun YT, Carlton RA, Diederich AM, Mueller RL, Vogt FG 2009. Characterization, selection, and development of an orally dosed drug polymorph from an enantiotropically related system. Int J Pharm 366(1-2):1-13.

21. Arnold MM, Gorman EM, Schieber LJ, Munson EJ, Berkland C 2007. NanoCipro encapsulation in monodisperse large porous PLGA microparticles. J Control Release 121(1-2):100-109.

22. El-Gendy N, Gorman EM, Munson EJ, Berkland C 2009. Budesonide nanoparticle agglomerates as dry powder aerosols with rapid dissolution. J Pharm Sci 98(8):2731-2746.

23. Plumley C, Gorman EM, El-Gendy N, Bybee CR, Munson EJ, Berkland C 2009. Nifedipine nanoparticle agglomeration as a dry powder aerosol formulation strategy. Int J Pharm 369(1-2):136-143.

24. Stejskal E, Schaefer J, Waugh J 1977. Magic-angle spinning and polarization transfer in proton-enhanced NMR. J Mag Res 28(1):105–112.

25. Metz G, Wu X, Smith S 1994. Ramped-amplitude cross polarization in magic-angle-spinning NMR. J Mag Res, Series A 110(2):219–227.

26. Fung BM, Khitrin AK, Ermolaev K 2000. An improved broadband decoupling sequence for liquid crystals and solids. J Mag Res 142(1):97–101.

27. Barich DH, Gorman EM, Zell MT, Munson EJ 2006. 3-Methylglutaric acid as a 13C solid-state NMR standard. Solid state nuclear magnetic resonance 30(3-4):125-129.

28. Svec H, Clyde D 1965. Vapor pressures of some α-amino acids. Journal of Chemical and Engineering Data 10(2):151–152.

29. Grundy JS, Kherani R, Foster RT 1994. Photostability determination of commercially available nifedipine oral dosage formulations. J Pharm Biomed Anal 12(12):1529-1535.

30. Antzutkin ON, Song Z, Feng X, Malcolm H 1994. Suppression of sidebands in magic-angle-spinning nuclear magnetic resonance: General principles and analytical solutions. J Chem Phys 100(1):130–140.

31. Song Z, Antzutkin ON, Feng X, Levitt MH 1993. Sideband suppression in magic-angle-spinning NMR by a sequence of 5 pi pulses. Solid state nuclear magnetic resonance 2(3):143-146.

32. Apperley DC, Forster AH, Fournier R, Harris RK, Hodgkinson P, Lancaster RW, Rades T 2005. Characterisation of indomethacin and

nifedipine using variable-temperature solid-state NMR. Magnetic Resonance in Chemistry 43(11):881-892.

33. *The Merck Index*; 10th ed.; Merck & Co., Inc.: Rahway, NJ, 1983, pp 1463.

34. Eckert T, Müller J 1977. Über polymorphe Modifikationen des Nifedipine aus unterkühlten Schmelzen. Arch Pharm Pharm Med Chem 310(2):116-118.

35. Barich DH, Davis JM, Schieber LJ, Zell MT, Munson EJ 2006. Investigation of solid-state NMR line widths of ibuprofen in drug formulations. J Pharm Sci 95(7):1586-1594.

36. Lubach JW, Xu D, Segmuller BE, Munson EJ 2007. Investigation of the effects of pharmaceutical processing upon solid-state NMR relaxation times and implications to solid-state formulation stability. J Pharm Sci 96(4):777-787.

37. Berkland C, Kim K, Pack DW 2001. Fabrication of PLG microspheres with precisely controlled and monodisperse size distributions. J Control Release 73(1):59-74.

38. Berkland C, Pollauf E, Pack DW, Kim K 2004. Uniform double-walled polymer microspheres of controllable shell thickness. J Control Release 96(1):101-111.

39. Berkland C, Pollauf E, Raman C, Silverman R, Kim KK, Pack DW 2007. Macromolecule release from monodisperse PLG microspheres: control of release rates and investigation of release mechanism. J Pharm Sci 96(5):1176-1191.

40. Berkland C, Pollauf E, Varde N, Pack DW, Kim KK 2007. Monodisperse liquid-filled biodegradable microcapsules. Pharm Res 24(5):1007-1013.

41. Peersen O, Wu X, Kustanovich I, Smith S 1993. Variable-amplitude cross-polarization MAS NMR. J Mag Res, Series A 104(3):334–339.

42. Bennett AE, Rienstra CM, Auger M, Lakshmi KV, Griffin RG 1995. Heteronuclear decoupling in rotating solids. J Chem Phys 103(16):6951-6958.

Chapter 4

Quantitation of Physical Forms in Formulations by SSNMR Spectroscopy

4.1 Introduction

The specific aim of this chapter is to understand how SSNMR can be used to measure the relative amounts of API physical forms within a formulation. Ideally this understanding will show why SSNMR does not require the use of pure reference materials or the preparation of a calibration curve. In addition, the efficiency of these measurements will be addressed and improved relative to traditional SSNMR quantitation approaches.

NMR spectroscopy has found widespread use within the pharmaceutical industry for both qualitative[1-3] and quantitative[4-6] applications, typically in the solution state. However, SSNMR spectroscopy has gradually expanded in prominence for the analysis of pharmaceuticals[7] but has primarily been used for the qualitative characterization of these materials.[8-16] This is especially true for the analysis of pharmaceutical formulations.[17-19]

NMR spectroscopy is inherently quantitative because the equilibrium magnetization (M_0), and hence the observed signal (S), of a sample is given by Equation 4.1 and is directly proportional to the number of nuclei (N) that

$$S \propto M_0 = \frac{N(\gamma\hbar)^2 B_0}{4kT} \qquad \text{Equation 4.1}$$

contribute to the signal. In this equation the signal is related to the gyromagnetic ratio (γ) of the nucleus, Planck's constant ($\hbar$), the static magnetic field (B_0), Boltzmann's constant (k), and the temperature (T). For the same nucleus, such as ^{13}C, it is possible to determine the relative amounts of two components within a sample by taking the ratios of the signals because all of the terms in Equation 4.1,

with the exception of N, are identical (Equation 4.2). Therefore, relative

$$\frac{S_X}{S_Y} \propto \frac{\left[\frac{N_X(\gamma\hbar)^2 B_0}{4kT}\right]}{\left[\frac{N_Y(\gamma\hbar)^2 B_0}{4kT}\right]} = \frac{N_X}{N_Y} \qquad \text{Equation 4.2}$$

quantitation can be achieved by NMR spectroscopy without the use of calibration standards and the development of calibration curves. This is not the case with other spectroscopic techniques such as UV-Vis, infrared, and Raman spectroscopy, where the extinction coefficient (i.e., response factor) may vary for each peak.

Although NMR is inherently a quantitative technique, there are several caveats that must be considered before a quantitative spectrum can be aquired. For example, an important stipulation regarding quantitation with all NMR methods is related to the rate at which a sample approaches its equilibrium state, M_0. In most modern NMR spectrometers the sample is allowed to come to equilibrium with the magnetic field. A series of radio frequency (RF) pulses is then applied to the sample and a free induction decay (FID) is collected. However, since NMR is a relatively insensitive technique, the experiment is repeated several times and each time the data is added to the FID in a process called signal averaging. These repetitions are generally identified as transients, and an FID can be the result of averaging thousands of transients. After the sample is perturbed, it will begin to relax back to its equilibrium state, and different components within the sample may relax at different rates. Therefore,

when performing quantitative measurements, it is generally accepted that the sample must be allowed to completely relax back to its equilibrium state between transients or the signals will not be directly proportional to the composition of the sample.

Quantitation studies in the solution state typically utilize ^{1}H spectra because of its relatively high sensitivity and fast relaxation rates, which leads to reasonably short experiment durations. However, in ^{1}H SSNMR spectroscopy it is typically not possible to resolve the signals due to the strong homonuclear dipolar coupling that exists between the ^{1}H nuclei (see the ^{1}H MAS spectra of levofloxacin in Chapter 2, Figure 2.14). In addition, other NMR active nuclei that have high natural abundance (such as ^{19}F) are not commonly present in pharmaceutical compounds. Therefore, the ^{13}C is typically employed for the quantitative analysis of pharmaceutical systems with SSNMR spectroscopy. Additionally, this analysis has generally been focused on relatively simple mixtures of API physical forms, as opposed to formulated materials, due to the relative insensitivity of the ^{13}C nucleus.[20-23]

In SSNMR spectroscopy, ^{13}C data is either collected with a direct polarization (DP) or cross polarization (CP) experiment, and each method offers benefits and disadvantages. In a DP experiment the observed signals are directly proportional to the sample composition, provided that the sample is allowed to fully relax to its equilibrium magnetization between transients.[24] However, the relaxation rate of the ^{13}C nuclei can be slow and often requires delays of minutes to hours between the collection of transients. This leads to very long analysis times, since one spectrum is typically the result of hundreds or thousands of transients. On the other hand, CP experiments allows dilute spins, such as ^{13}C, to

be investigated while utilizing the relatively fast relaxation rates of abundant spins, such as ^{1}H. Additionally, ^{13}C spectra that are collected with CP from ^{1}H nuclei result in spectra that have a four-fold enhancement in their sensitivity or signal-to-noise ratio (S/N), which reduces the number of transients that are required. One major complication of CP experiments is that the signals are not directly proportional to the sample composition because the transfer of the magnetization from the abundant spin to the dilute spin does not occur at a uniform rate. Some studies involving the relative quantitation of API physical forms within formulations have relied upon calibration curves[25] or reference spectra of pure forms for spectral addition[26] in order to correct for the CP dynamics. But, by understanding the CP dynamics of each of the materials it is possible to obtain quantitative results without pure standards or calibration curves.[21,27]

Another method for increasing the sensitivity of ^{13}C is by utilizing isotopic labels. The ^{13}C isotope makes up only 1.1% of all carbon atoms in nature, and NMR does not detect the other naturally occurring isotopes of carbon (^{12}C and ^{14}C). Therefore, if the relative abundance of ^{13}C is increased via isotopic labeling the sensitivity of the NMR experiment can be increased. This can be particularly beneficial for the analysis of formulated APIs.[17] However, if two adjacent carbon atoms in a molecule are both ^{13}C then they will undergo dipolar coupling and result in broadening of the peaks in the ^{13}C spectrum, in addition to experiencing J-coupling interactions.[28] This ^{13}C coupling is not observed in natural abundance materials because the probability of having two adjacent ^{13}C nuclei is exceptionally low. Additionally, the generation of even small amounts of isotopically labeled material is relatively expensive and large amounts of labeled

material may be needed to study the effect of various processing steps of the physical form of an API in a formulation. Therefore, most processing steps would need to be scaled down in order to utilize labeled API, but changing the scale of processing could alter the product that is obtained. Hence, isotopic labeling is not perceived as a feasible method for increasing the sensitivity of quantitative SSNMR spectroscopic studies, especially when trying to characterize the formulated API.

In a previous SSNMR study, Apperley et al.[29] reported that they were able to detect fomoterol fumerate dihydrate when it was diluted to a level of 0.45% (w/w) in α-lactose monohydrate. Additionally, they were able to quantify the relative amounts of fomoterol fumerate dihydrate and anhydrate (45% anhydrate) when the mixture was diluted to 2% (w/w) in α-lactose monohydrate. They were able to achieve these results while using a method that did not wait the traditionally accepted period for complete relaxation to equilibrium. In addition, the method benefited from several fortuitous properties of the materials, which simplified the quantitative analysis.

The goal of the work reported in this chapter is to develop a systematic approach to quantitation by SSNMR spectroscopy that is based on the method of Apperley et al.[29] Specifically, the reproducibility of peak intensity and area measurements will be addressed. The phenomenon of spinning sidebands and their potential impact on quantitation will be addressed. In addition, the measurement of relaxation rates as they pertain to quantitation will be considered. Efforts will also be made to improve the sensitivity of quantitative SSNMR measurements without increasing the total experiment time. Finally,

two model formulations will be investigated to assess the accuracy of this approach to API physical form quantitation by SSNMR spectroscopy.

4.2 Experimental

4.2.1 Materials

3-methylglutaric acid (MGA), hexamethylbenzene (HMB, purified by sublimation), and cortisone 21-acetate (CortA) were purchased from Sigma-Aldrich (St. Louis, MO) and were used without further purification or processing, unless indicated. α-Lactose monohydrate was obtained as Foremost #310 Regular Lactose NF from Foremost Farms USA (Baraboo, WI) and was used without further purification or processing. Starch 1500, a partially pregelatinized maize starch, from Colorcon (Harleysville, PA) was kindly provided by Dr. John Haslam.

A mixture of MGA and HMB was prepared by mixing 350.7 mg of MGA and 87.2 mg of HMB and is referred to in the text as "4:1 MGA:HMB." Stock CortA was heated to 200 °C for one hour to generate Form I.[30,31] CortA Form II was produced by dissolving ~3 g of the material in 200 mL of chloroform, which was allowed to evaporate at ambient conditions for 24 hr. A 1:1 Form I:II mixture of CortA was produced by mixing 220.73 mg of Form I and 223.95 mg of stock material. Additionally, two CortA formulations in Starch 1500 were prepared by mixing either 13.30 mg of Form I and 14.59 mg of stock CortA with 371.81 mg Starch 1500 to produce a 7% (w/w) formulation, or 17.51 mg of stock CortA was mixed directly with 874.41 mg Starch 1500 to produce a 2% (w/w) formulation.

4.2.2 SSNMR Instrumentation

Unless otherwise indicated all ^{13}C data was collected using the Chemagnetics CMX-300 spectrometer that was reported in Chapter 2 (Section 2.2.6). Some data sets were collected on a similar Chemagnetics CMX-400 spectrometer, operating at a ^{1}H resonance frequency of 400 MHz. ^{19}F SSNMR spectra were collected with the Bruker Avance DSX 500 MHz spectrometer (Chapter 2, Section 2.2.6). The data collection parameters for ^{19}F were also the same as the previous reported values with the exception of the MAS rate and the number of transients that were collected (see caption of Figure 4.10).

4.2.3 Signal Reproducibility

All of the data that was collected for this portion of the study using the 4:1 MGA:HMB mixture utilized the following instrument parameters: 3.2 μsec ^{1}H 90° pulse width, 15 msec contact time, 5 sec pulse delay, 4 kHz MAS, and ~81 kHz of proton decoupling. In addition, two dummy pulses were always applied to the sample prior to beginning each experiment and all FIDs contain 2,048 points with a dwell of 33.3 μsec.

Three separate data sets (4x96 [4], 12x32 [12], and 384x1 [384]) were collected for the 4:1 MGA:HMB mixture and are named according to the number of transients that were used to collect the FIDs and how many times the experiment was repeated ("transients"x"repetitions" [original transients]). Thus, in the 4x96 [4] data set 4 transients were collected for each FID and 96 separate FIDs were collected with the same conditions. A systematic approach of FID addition was developed in order to simulate an experiment in which more

transients were collected for each FID. To simulate an experiment in which 8 transients were collected, the 1st and 49th FID of the 4x96 [4] data set were summed to produce a new FID. This process was repeated until all of the original FIDs had been utilized (2nd and 50th, 3rd and 51st, …, 48th and 96th FIDs). The resulting FIDs simulated a data set in which 8 transients were collected 48 times. The 1st, 33rd, and 65th FIDs of the 4x96 [4] data set were summed to produce a new FID to simulate an experiment of 12 transients per FID, and this process was again repeated to yield a data set which simulates 12 transients per FID repeated 32 times. This process was continued and ultimately resulted in 11 simulated data sets: 8x48 [4], 12x32 [4], 16x24 [4], 24x16 [4], 32x12 [4], 48x8 [4], 64x6 [4], 96x4 [4], 128x3 [4], 192x2 [4], and 384x1 [4].

The 4x96 [4] data set and its associated 11 simulated data sets were processed and various S/N, intensity, integration, and deconvolution measurements were performed. The relationship between the absolute values and errors of these measurements to the number of transients was then examined. The 12x32 [12] data set was collected to determine if the simulation approach introduced bias. Additional simulated data sets were generated from the 12x32 [12] data set using the same systematic approach. This resulted in 5 simulated data sets: 24x16 [12], 48x8 [12], 96x4 [12], 192x2 [12], and 384x1 [12]. As an additional check for bias a 384x1 [384] data set was also collected to for comparison to the simulations.

The S/N measurements were performed by searching for the smallest root-mean-square (RMS) noise in a 30 ppm window over the entire spectral width. A noise window of 30 ppm corresponds to approximately 7.7% of the entire spectral width. The MGA and HMB methyl peaks were integrated over

ranges of 21 – 18.3 and 18.3 – 15 ppm, respectively. The deconvolution model was optimized on the MGA and HMB methyl peaks in the 384x1 data set. The optimal MGA peak model was determined to be a peak centered at 18.8 ppm with a width of 17.6 Hz and an 18% Gaussian shape. The HMB peak model was restricted to a single peak centered at 17.4 ppm with a width of 58.5 Hz and an 86% Gaussian shape. All of the data sets were fit with these models and only the intensity was allowed to vary during the fitting routine.

4.2.4 T_1 Measurements

The MGA ^{13}C T_1 measurements were performed on the CMX-400 spectrometer, along with the ^{1}H T_1 comparisons of the saturation recovery, inversion recovery, and Torchia[32] methods of T_1 measurement. The data was collected at an MAS rate of 7 kHz, contact time of 1.5 msec, and a pulse delay of 7 sec except for the saturation recovery measurements, which used a pulse delay of 2 sec. The FIDs contained 4,096 points and were the result of either 16 or 64 transients for ^{13}C and ^{1}H T_1 measurements, respectively.

The MGA and α-lactose monohydrate ^{1}H T_1 repeatability experiments were collected on the CMX-300 spectrometer, with an MAS rate of 4 kHz. The MGA measurements used a contact time of 1.5 msec, a pulse delay of 3 sec, and the FIDs consisted of 3,072 points that were the result of either 64 or 256 transients. The experiments were repeated three times and were labeled A, B, and C. The α-lactose monohydrate measurements used a contact time of 1.5 msec, a pulse delay of 1 sec, and the FIDs consisted of 2,048 points that were the result of 4 transients. The experiments were repeated three times and were

labeled A, B, and C. In order to simulate a ^1H T_1 data set of 12 transients per FID the corresponding FIDs from each of the A, B, and C data sets were summed to yield the simulated ABC data set.

Relaxation profiles from each of the T_1 measurement experiments were fit to the appropriate mathematical models with KaleidaGraph version 4.0 from Synergy Software in a nonlinear regression method utilizing the Levenberg–Marquardt algorithm to minimize the χ^2 of the model. The reported error values are the standard errors for each respective parameter that were obtained from the nonlinear regression.

4.2.5 CP Dynamics (T_{CH} and $T_{1\rho}$)

The CP dynamics of MGA were determined by collecting spectra with ramped-amplitude CP, where the duration of the CP pulse was varied from 0.01 to 18 msec. This data was collected on the Chemagnetics CMX-400 spectrometer with a pulse delay of 7 sec and MAS rate of 7 kHz. The FIDs were the result of 128 transients and consisted of 4,096 points. The data was fit to the appropriate model by nonlinear regression with the KalediaGraph software (Section 4.2.4).

4.2.6 Quantitation Measurements

All of the CortA data was collected with a variable amplitude CP experiment utilizing two-pulse phase modulated (TPPM) proton decoupling. The FIDs consisted of 4,096 points and were the result of between 1,024 and 58,176 transients. Unless otherwise indicated the contact time was between 1.5 and 5 msec, the pulse delay was 8 sec, and MAS was performed at a rate of 4kHz.

4.3 Results & Discussion

4.3.1 Signal Reproducibility

When performing quantitative measurements it is necessary to consider both the accuracy and the precision of the method that is being used. Ultimately, both are dependent upon several factors including errors in preparing the samples and the reproducibility of the instrument's response. Thus, an experiment was devised in which a single sample was repeatedly investigated to assess the reproducibility of the SSNMR spectrometer's response.

A mixture of MGA and HMB was selected for this study because they are routinely used as standards in SSNMR, have very favorable relaxation properties that allow for rapid data collection. They were mixed in a ratio of 4:1 MGA:HMB so that all of the peaks of MGA would have a greater intensity, but the HMB peaks would have a greater integrated area due to the differences in the width of the peaks from each material (Figure 4.1). While the HMB peaks are smaller in intensity, they are approximately 3 times broader, thus the peak areas of the HMB are larger than those of MGA.

In order to test the stability of the spectrometer response, 96 FIDs consisting of 4 transients each were collected of the 4:1 MGA:HMB mixture, and the data are referred to as the 4x96 [4] data set. The FIDs were then subjected to Fourier transformation (FT) to produce 96 corresponding spectra. The peak intensity of the MGA and HMB peaks in each spectrum were determined and then the average and standard deviations (SD) of the peak intensities were calculated. The results were 1,810 ± 10 and 920 ± 10 for MGA and HMB, respectively. It is generally accepted that the intensity of the NMR signal

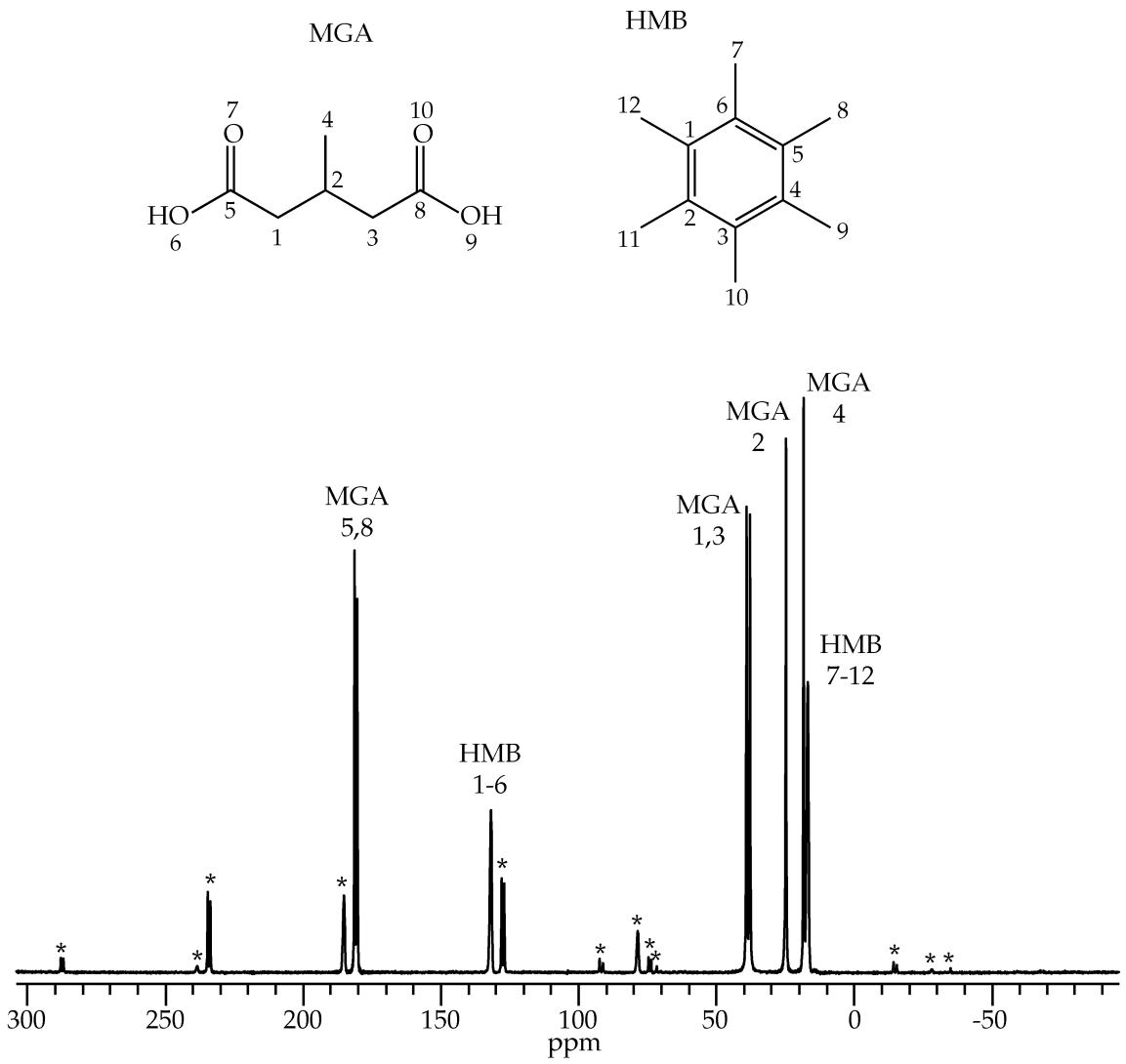

Figure 4.1. ^{13}C CPMAS spectrum (from 384x1 [384] data set) of 4:1 MGA:HMB mixture. Chemical structures of both MGA and HMB are provided with carbon numbering. * = spinning sidebands

increases linearly with the number of transients and that the noise increases with the square root of the number of transients. Therefore, if more transients are collected per FID, the relative SD (RSD) of the peak intensity should decrease. In order to test this hypothesis, 11 data sets were simulated from the 4x96 [4] data set (see Section 4.2.3) and the resulting average MGA and HMB peak intensity from each data set is plotted against the number of transients of that data set in Figure 4.2 (MGA 4x96 and HMB 4x96).

It can be seen from the linear fits of both MGA and HMB that the signal does increase linearly with the number of transients (R^2 = 1.0000) as would be expected. In order to determine if this relationship was due to the simulation of the data sets, another data set consisting of 32 FIDs, each consisting of 12 transients, was collected, and the same simulation method was applied to generate an additional 5 data sets (see Section 4.2.3). The average peak intensities from these data sets are also shown in Figure 4.2 (MGA 12x32 and HMB 12x32) and agree very well with the previous results. As a final check, the intensities of the methyl peaks from the spectrum in Figure 4.1 were measured and are also shown in Figure 4.2 (MGA 384x1 and HMB 384x1) and also agree very well. Therefore, two FIDs of a sample can be summed and the signals will scale linearly with the number of transients that were used to collect the data. One caveat is that the FIDs must be collected with the same instrument parameters.

As an additional check of these data sets, the S/N of both peaks were measured for all of the spectra, and the average values for each data set are shown in Figure 4.3. This figure is analogous to Figure 4.2 but the relationship is no longer linear. Since the signal increases linearly and the noise increases with

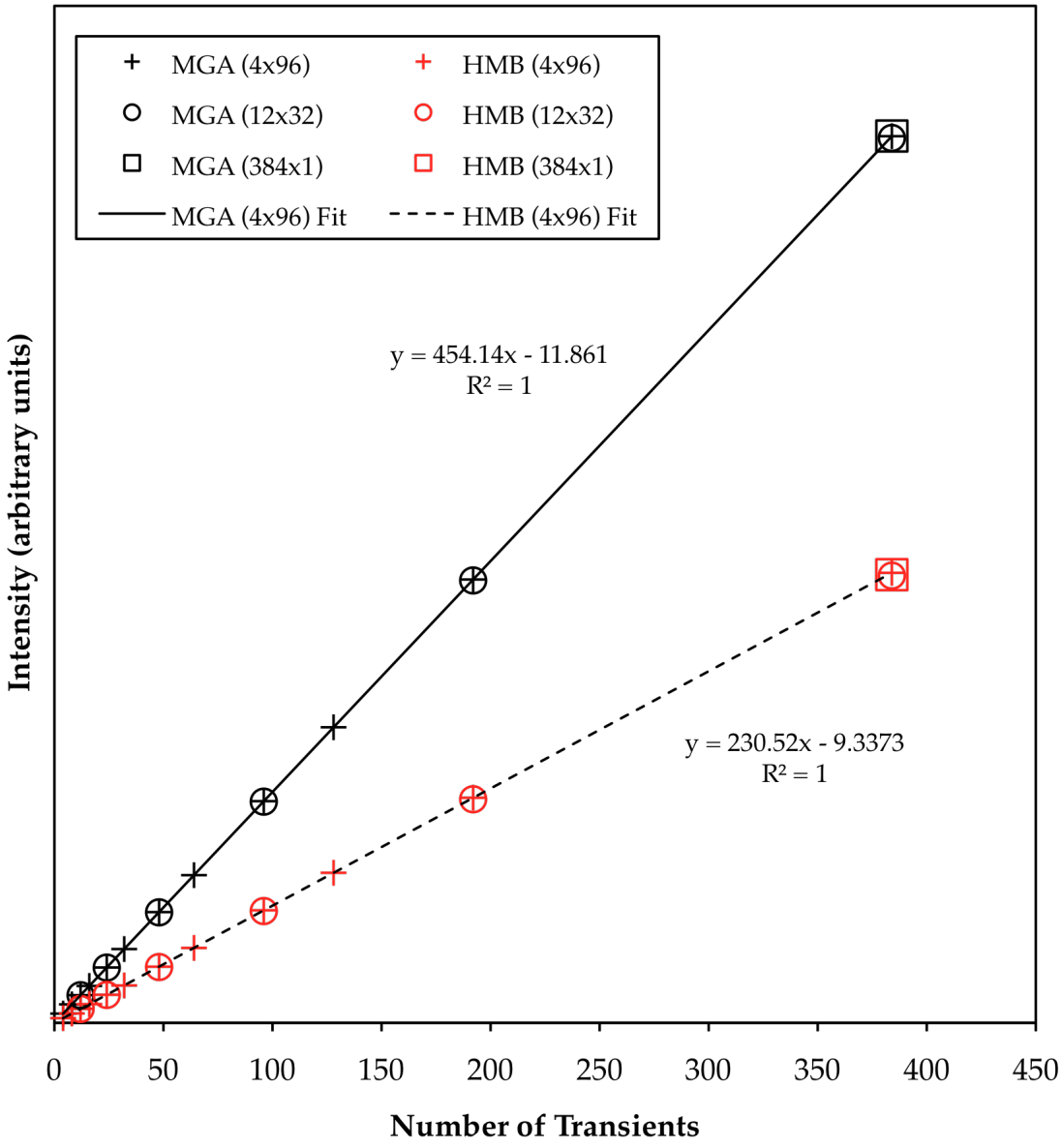

Figure 4.2. Average methyl peak intensities of MGA and HMB plotted against the number of transients used to collect the data for the 4:1 MGA:HMB mixture. The plot shows the results from the 4x96 [4], 12x32 [12], and 384x1 [384] data sets and their associated simulations (see section 4.2.3 for details). The linear fit was only applied to the results from the 4x96 [4] data set. The relative intensities of MGA and HMB are not directly proportional to the sample composition due to differences in the widths of the two peaks (see Figure 4.4). SDs are not shown because they are significantly smaller than the size of the symbols that are shown, and the RSDs were not more than 0.6% and 1% for MGA and HMB, respectively.

the square root of the number of transients, the S/N increases with the square root of the number of transients (Equation 4.3). This relationship is well

$$\frac{S}{N} \propto \frac{\text{Transients}}{\sqrt{\text{Transients}}} = \sqrt{\text{Transients}} \qquad \text{Equation 4.3}$$

established and accepted within the NMR community.[33,34] Thus, the approach of FID summation to achieve higher S/N and simulate the acquisition of additional transients is a valid approach because the results in Figure 4.3 abide by the square root relationship between S/N and thee number of transients.

While the measurement of signal intensity is relatively easy and straightforward, it cannot be used for relative quantitation in NMR if calibration curves are not used. In NMR, the signal is distributed over some chemical shift range, which results in the observed peak, and different materials will display different distributions of their signals. The most obvious example of this in SSNMR is the peaks of crystalline and amorphous materials, where the amorphous peaks are approximately an order of magnitude broader than their crystalline counterparts. Thus, for the same mass of material, amorphous form peaks will be about an order of magnitude less intense than the crystalline form peaks. For this reason it is generally necessary to measure the actual area of the peaks rather than the intensity of the peaks.

There are two main approaches to measuring peak areas in NMR spectroscopy: integration and deconvolution. Integration is generally preferred due to its relative simplicity, but it has certain disadvantages. One major issue with integration is that the peak often extends well beyond the observed width of

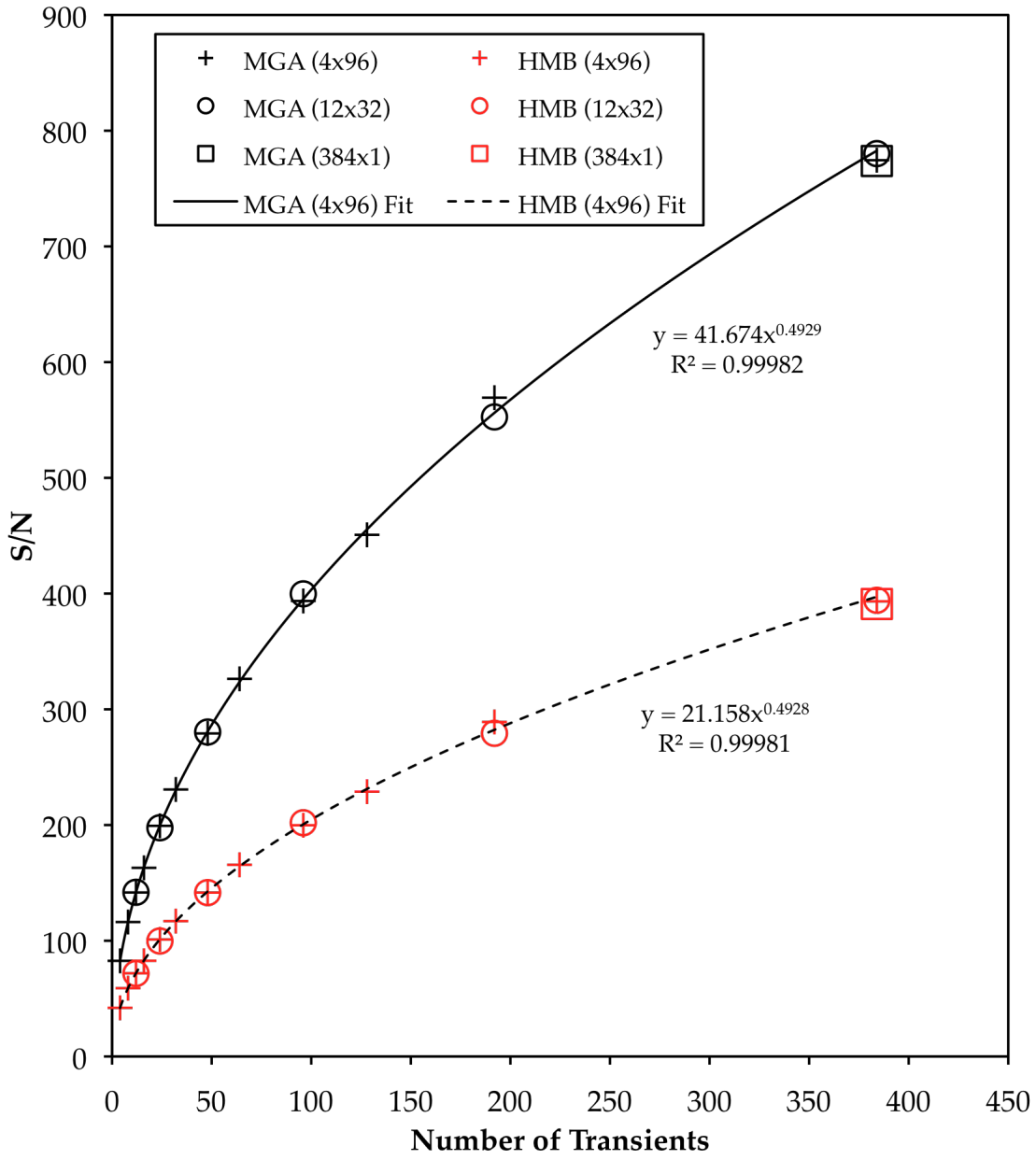

Figure 4.3. Average methyl peak S/N of MGA and HMB plotted against the number of transients used to collect the data for the 4:1 MGA:HMB mixture. The plot shows the results from the 4x96 [4], 12x32 [12], and 384x1 [384] data sets and their associated simulations (see section 4.2.3 for details). The power fit was only applied to the results from the 4x96 [4] data set. The relative S/N of MGA and HMB peaks are not directly proportional to the sample composition due to differences in the widths of the two peaks (see Figure 4.4). SDs are not shown because they are smaller than, or on the order of, the size of the symbols that are shown. The RSDs were not more than 3% for both MGA and HMB.

the base of the peak. Therefore, in order to integrate the entire peak the integration range must be relatively broad. However, the edges of the peak only contain a very small fraction of the entire signal and increasing the integration range incorporates more noise in the measurement. Thus a tradeoff exists between accuracy (wider integration range to measure the total peak area) and precision (narrow integration range to limit the contribution of noise). Additionally, if peaks of two components are not fully resolved it can be difficult to accurately integrate the peaks.

Deconvolution can be used to minimize the issues that are encountered with integration. Because deconvolution uses a mathematical model to represent the peaks, it is able to, in theory, exclude the noise that is present in the data. Since it is modeling the peak it should be able to more accurately estimate the entire peak area without being influenced by the noise as heavily as a wide integration range would be. Additionally, it can be used to model two overlapping peaks, although ideally the shape and width of the peaks are known to help develop an accurate model. Unfortunately, peaks are not always symmetrical and do not fit a model perfectly, therefore deconvolution is not perfect and it is more difficult to perform routinely and accurately on large sets of data.

In order to determine the reproducibility of peak intensity, integration, and deconvolution measurements, each was used to analyze the methyl peaks of the entire 4x96 [4] data set of the 4:1 MGA:HMB mixture. The intensity and integration methods are depicted in Figure 4.4. The peaks appear to be sufficiently resolved so that the intensity at the peak maxima should not be significantly influenced by the tail of the adjacent peak. The integration ranges

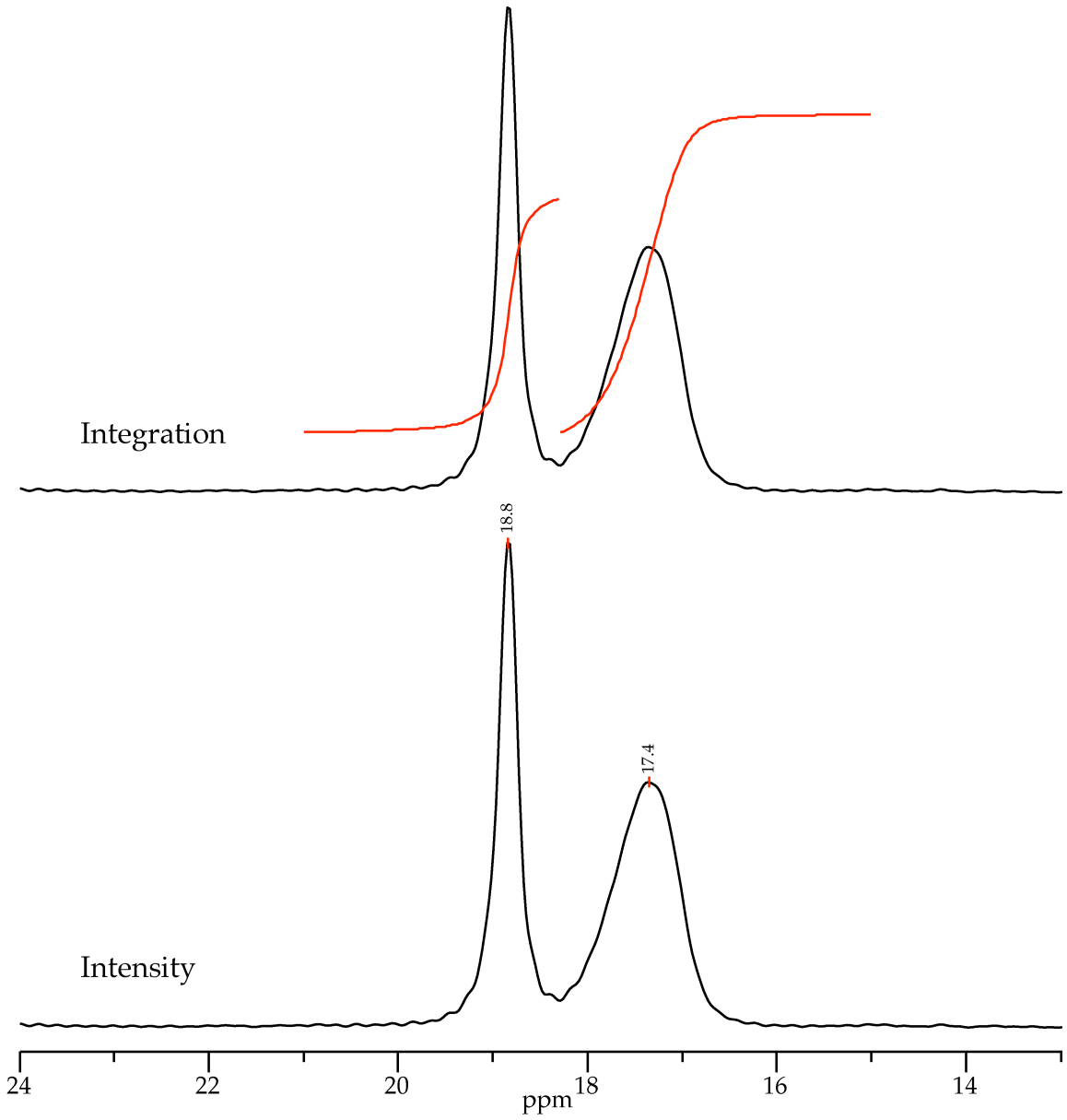

Figure 4.4. ^{13}C CPMAS spectrum of 4:1 MGA:HMB mixture from Figure 4.1, expanded to show methyl peaks. The top spectrum demonstrates the integration method with the MGA peak integrated from 21 to 18.3 ppm and the HMB from 18.3 to 15 ppm. The bottom spectrum demonstrates the intensity method, where the maximum intensity is measured for each peak is determined at the positions indicated by red lines.

are shown by the red traces in Figure 4.4 and demonstrate the difficulties of integrating overlapped peaks because one tail of the HMB peak is included in the MGA integral and one tail of the MGA peak is included in the integration of the HMB peak. The deconvolution models were developed with the 384x1 [384] data set because it had the best S/N and thus offered the best opportunity to accurately model the peaks (Figure 4.5). When the data was modeled with two peaks the raw data was represented fairly well; however, the difference between the model and raw data in the region of the HMB signal did show noticeable systematic "noise". A third peak was added to help model the HMB signal and the χ^2 of the fit improved from 0.03 to 0.01. But the fit of the MGA signal was not noticeably improved by the addition of a fourth peak (data not shown), and it was not clear why the HMB signal might be represented by two poorly resolved peaks. Therefore, the two peak model was fit to one of the spectra from the 4x96 [4] data set with all parameters held constant, except for the peak intensity. The result was an acceptable fit, and the difference of the raw data and the model showed no large residual signals. The same issues with the fit of the HMB signal were observed; the errors in the fit however, appeared to average out over the width of the signal. Therefore, the two peak model was used for all of the subsequent deconvolutions of the 4:1 MGA:HMB mixture.

The 4x96 [4] data set and ten of its simulated data sets were analyzed by measuring the size of the MGA and HMB signals by intensity, integration, and deconvolutions. The 384x1 [4] was not used for this portion of the study because it contained only one spectrum and thus provided no statistical information. The integrated and deconvoluted peak areas were seen to exhibit the same linear relationship to the number of transients (data not shown) as was observed for the

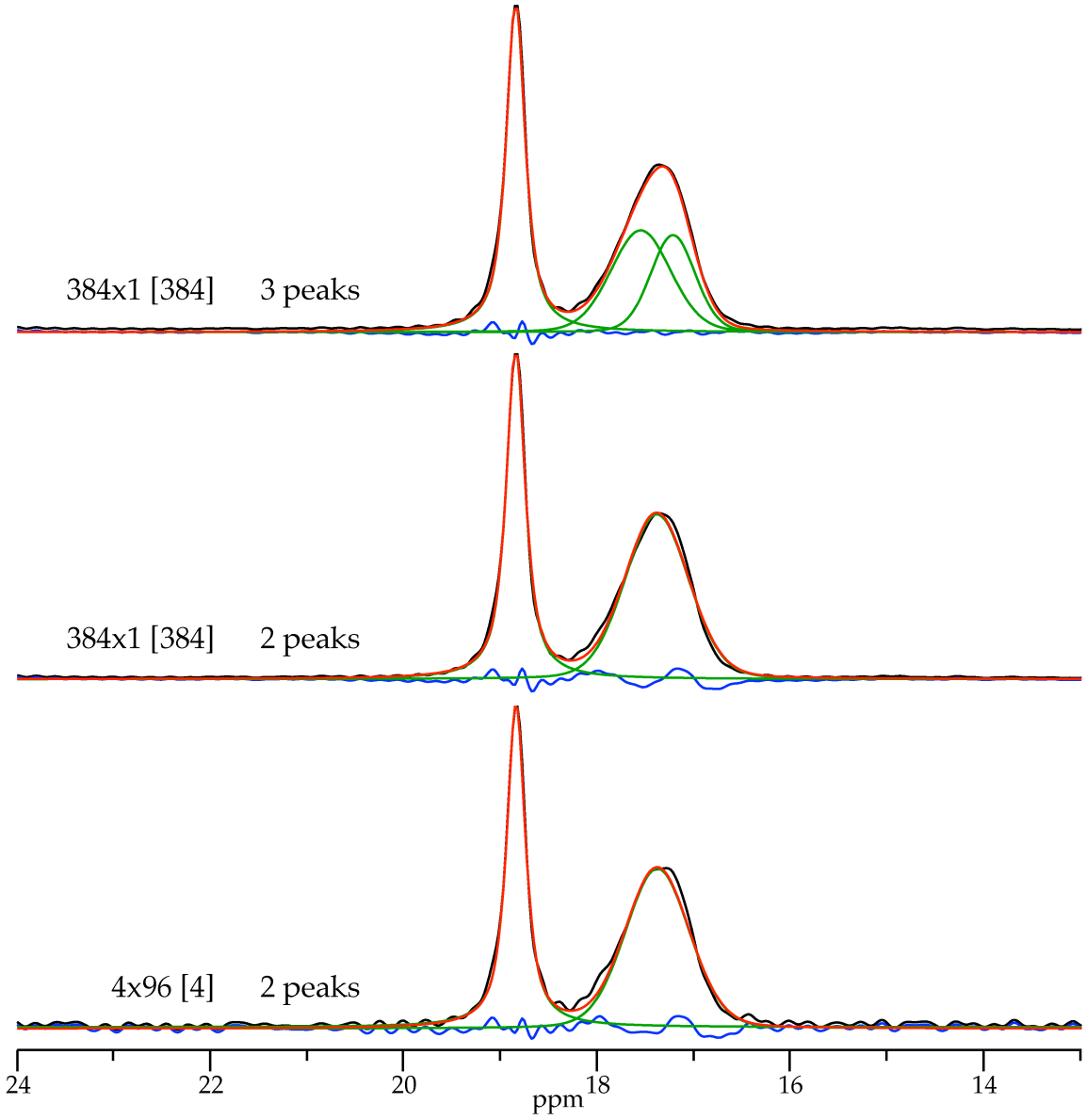

Figure 4.5. ^{13}C CPMAS spectrum of 4:1 MGA:HMB mixture from Figure 4.1 (top and middle) and the first increment of the 4x96 [4] data set (bottom), expanded to show methyl peaks. In all cases the raw data is shown in **black**, the individual peaks of the model are shown in **green**, the sum of the model peaks is shown in **red**, and the difference between the raw data and the model is shown in **blue**. The top spectrum was deconvoluted with a model containing three peaks. The middle spectrum shows the deconvolution of the same spectrum but with a model consisting of only two peaks. The bottom spectrum shows the two peak model from the middle spectrum but will all variables (peak width, position, and shape) held constant and only the intensity was allowed to change.

intensities (Figure 4.2). The RSD of the MGA intensity, integration, and deconvolution measurements are plotted against the corresponding average S/N of each data set (Figure 4.6). It can be seen from the data that as the S/N of the spectra increases, the RSD of all three measurement techniques decreases, indicating that the reproducibility of the measurements is related to relative size of the noise. Additionally, the deconvolution tended to give the lowest RSDs while integration tended to result in the highest RSDs.

The RSD values for the HMB peak measurements are provided in Figure 4.7, and show the same general relationship of RSD and S/N. As with MGA, the deconvolutions typically give smaller RSDs than the intensities and integrations. However, for HMB the intensity measurements tended to have higher RSDs than the integrations. This change in the relative behavior of the two measurement methods between MGA and HMB is probably due to the difference in the width of the peaks. The MGA peak is relatively narrow so that most of the signal is concentrated near the peak maximum, but the HMB signal is more dispersed. Therefore, in a given spectrum the absolute intensity of the HMB peak is small relative to the MGA peak but the size of the noise is constant and thus the noise has greater influence on the HMB intensity measurement.

The data in Figures 4.6 and 4.7 indicate that there is a trade off when choosing between collecting multiple FIDs or increasing the number of transients for each FID. When the S/N of the data is relatively low, the data suggests that the experiment should be biased towards fewer FIDs and more transients. Most NMR measurements are typically collected only once with the highest number of transients, and thus S/N, that can be obtained in a reasonable amount of time. It is then assumed that the error involved in preparing the sample (masses and

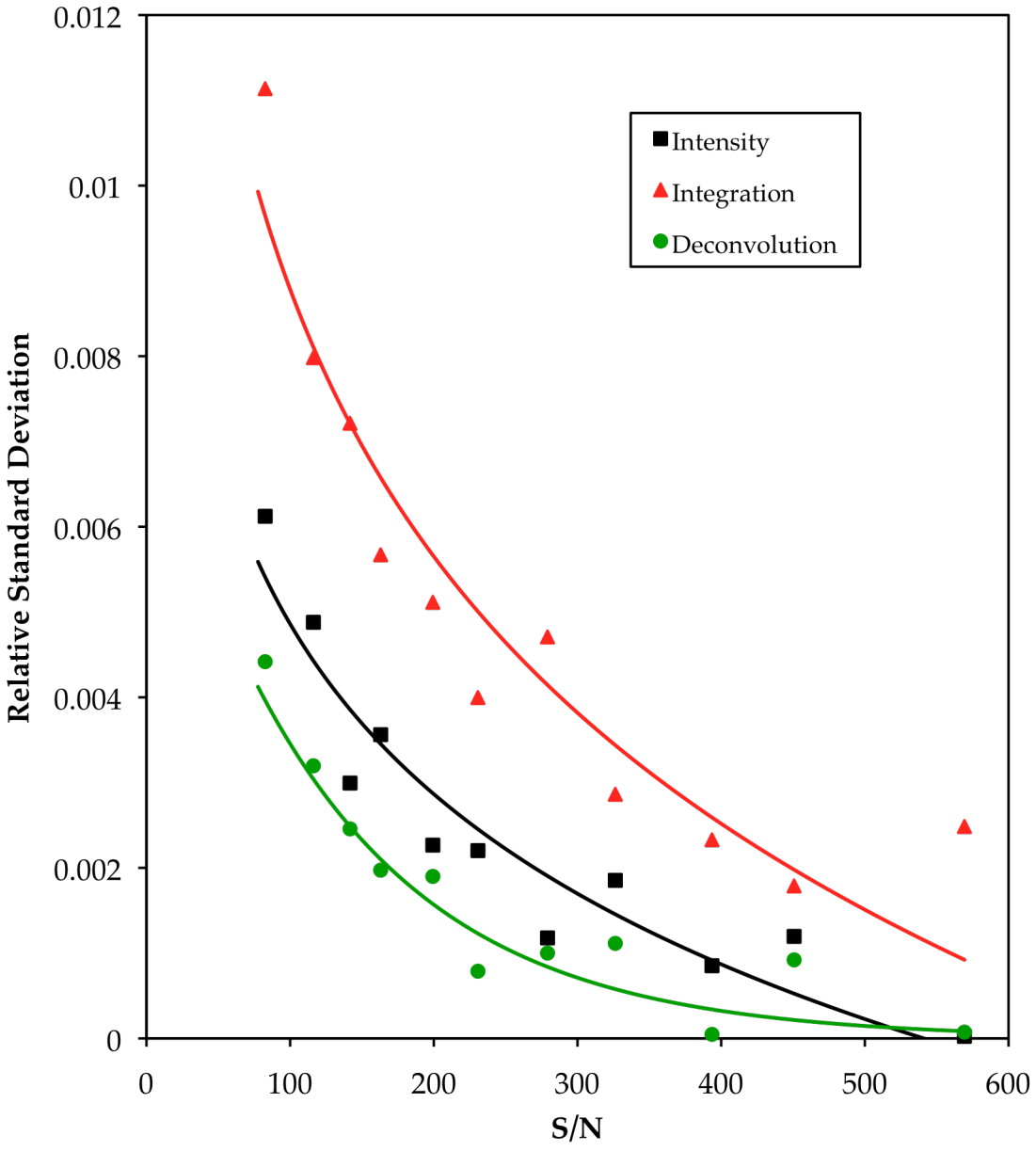

Figure 4.6. RSDs of the analysis of the MGA methyl peak from the entire 4x96 data set for the 4:1 MGA:HMB data set. The RSD values are plotted against the average S/N value for the MGA methyl peaks for each of the subsets of 4x96 data set (S/N values shown in Figure 4.5). The colored lines are intended only to help show the relative trends for each of the measurement methods (intensity, integration, and deconvolution). Note that the number of measurements that were used to determine the RSDs is not constant, as the S/N ratio increases n drops changes in the following order 96, 48, 32, 24, 16, 12, 8, 6, 4, 3, and 2.

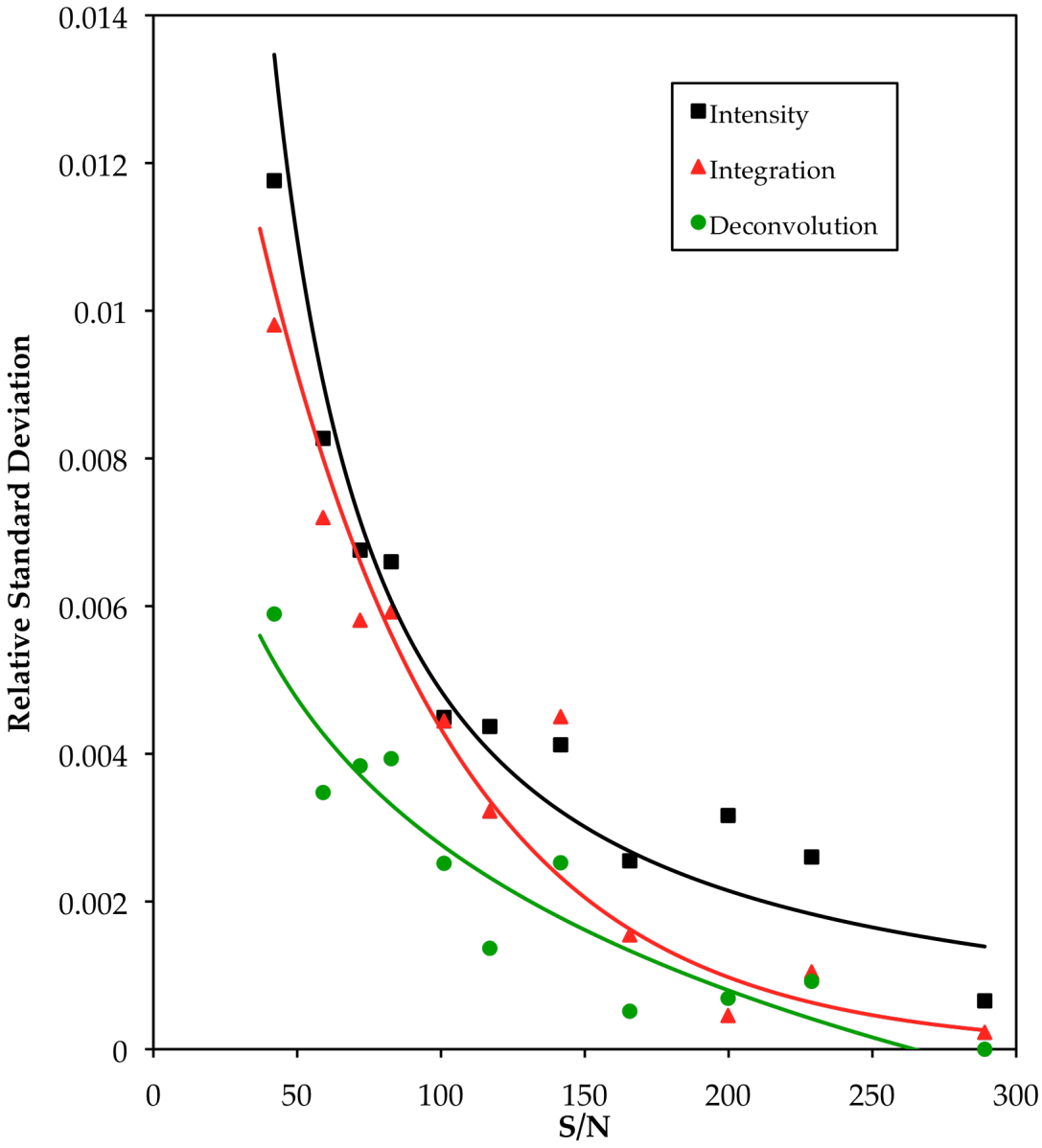

Figure 4.7. RSDs of the analysis of the HMB methyl peak from the entire 4x96 data set for the 4:1 MGA:HMB data set. The RSD values are plotted against the average S/N value for the HMB methyl peaks for each of the subsets of 4x96 data set (S/N values shown in Figure 4.5). The colored lines are intended only to help show the relative trends for each of the measurement methods (intensity, integration, and deconvolution). Note that the number of measurements that were used to determine the RSDs is not constant, as the S/N ratio increases n drops changes in the following order 96, 48, 32, 24, 16, 12, 8, 6, 4, 3, and 2.

volumes) will contribute more to the uncertainty in the NMR results than the response of the NMR spectrometer. Thus, error of NMR measurements are typically assessed by comparing independently prepared samples rather than replicate measurements of a single sample.

In Figures 4.6 and 4.7 the number of measurements that contribute to the RSD values shown decreases as the S/N increases, for example the RSD at the lowest S/N was calculated from 96 measurements while the RSD at the highest S/N was calculated from only two measurements. The confidence interval (CI) (Equation 4.4) was calculated for each of the data sets to correct for these

$$CI_{95\%} = \frac{t_{95\%} s}{\sqrt{n}} \qquad \text{Equation 4.4}$$

differences, where $t_{95\%}$ is the Student's t value for the 95% confidence level, s is the SD, and n is number of observations. The 95% CIs for the intensities, integrations, and deconvolutions increase as the S/N of the data sets increases. The absolute value for the measurements also increase so the relative CIs (RCIs) were calculated by dividing the CI by the average of the corresponding measurement and were found to be approximately constant for each measurement method. The RCIs for the intensities, integrations, and deconvolutions were approximately 0.001, 0.002, and 0.0007 for MGA and 0.002, 0.002, and 0.001 for HMB. Thus, it appears that even when a single spectrum is collected the 95% CI can be estimated by multiplying the measured value by the appropriate RCI. For example, the intensities of the MGA peak in the 384x1 [4], 384x1 [12], and 384x1 [384] data sets were 174,373, 174,018, and 174,408,

respectively. If the RCI is used to predict the CIs the following results are obtained for the three data sets: 174,400 ± 200, 174,000 ± 200, and 174,400 ± 200. This suggests that the RCIs can be used to estimate the confidence intervals of peak measurements that are performed on a single spectrum.

For SSNMR quantitative studies, particularly for formulated materials, the S/N of the spectra will be significantly lower than the values that were observed with the 4:1 MGA:HMB data sets. Therefore, another series of experiments were devised to test these observations with spectra that had lower S/N values. Lactose, specifically α-lactose monohydrate, was selected because its spectrum (Figure 4.8) contains several well resolved peaks at 107.3, 92.9, and 87.4 ppm. Additionally, the peaks had S/N values of ~30 to 40. Three FIDs (A, B, and C) of the lactose were collected and each consisted of 4 transients, and the three FIDs were summed to yield one FID (ABC) consisting of 12 transients. Each of the FIDs were Fourier transformed to produce spectra, and the three resolved peaks were analyzed by measuring the S/N, intensity, integral, and deconvoluted area of each peak (Table 4.1).

The raw measurements of the A, B, and C data sets for the lactose data are shown in Table 4.1, along with the averages and the 95% CI for the measurements. The measurements of the ABC data, which was simulated by summing the other three FIDs, are also shown; however, these measurements cannot be directly compared to the averages of the other measurements because the signals increase with increasing transients. The relationship of all four measurements with the number of scans were shown previously and were used to scale the results from ABC to be of the same relative scale as the other measurements. The scaled S/N measurements from all three peaks in the ABC

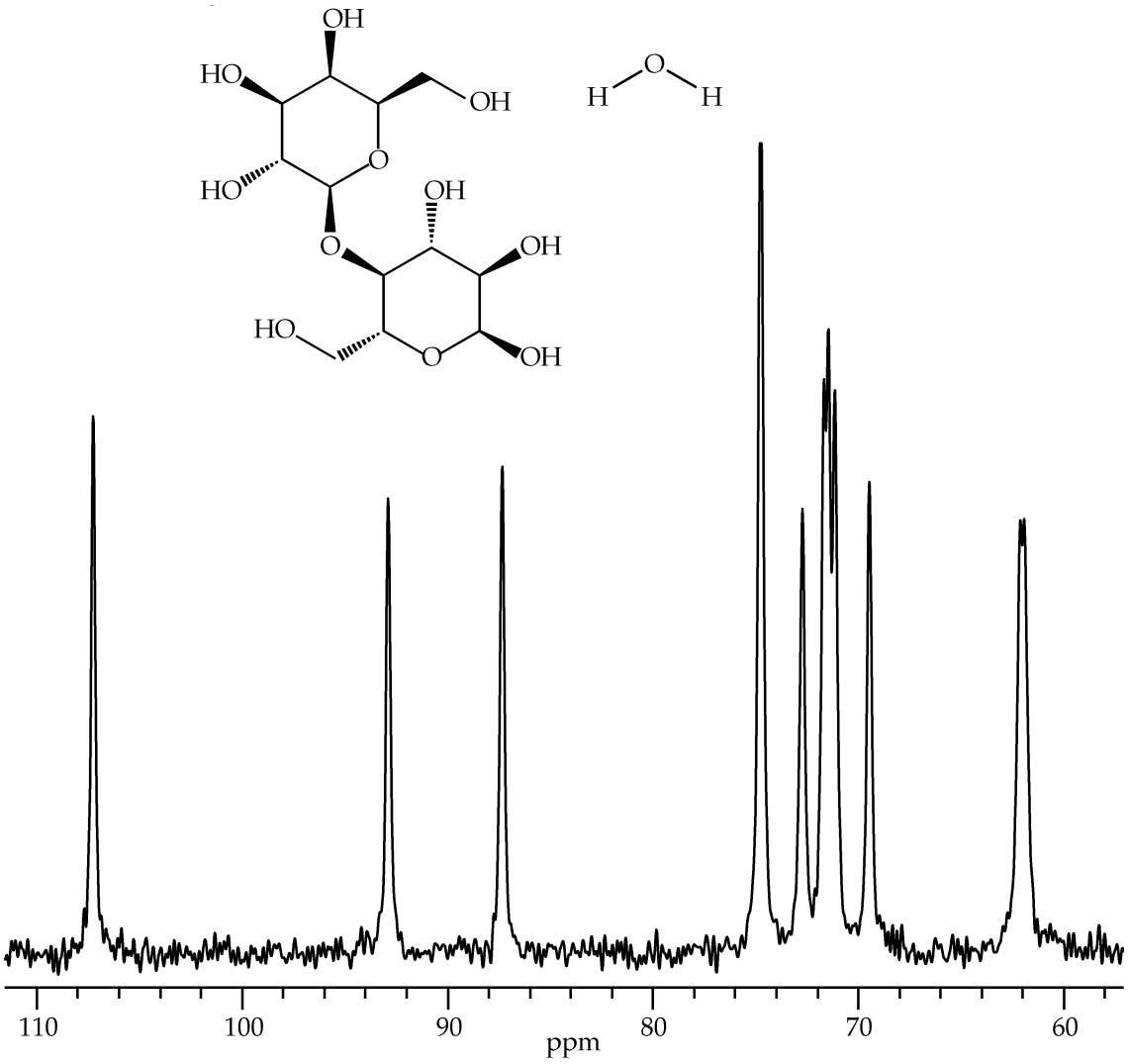

Figure 4.8. Chemical structure and ^{13}C CPMAS spectrum of α-lactose monohydrate. The spectrum was extracted from longest relaxation period of a ^{1}H T_1 experiment. No peaks were observed outside the spectral region that is shown.

Table 4.1. S/N, intensity, integration, and deconvolution measurements of three peaks in the ^{13}C CP/MAS spectrum of α-lactose monohydrate. The spectra were taken from the longest tau increment of the ^{1}H T_1 data sets: A, B, C, and the "simulated" ABC data set.[†]

Peak	Analysis Method	A	B	C	Average ± $CI_{95\%}$	ABC[†]	Scaled ABC[‡]
107.3 ppm	S/N	38.4	35.7	34.8	36 ± 5	61.9	35.7
	Intensity	785	792	801	800 ± 20	2,291	764
	Integral[a]	0.6794	0.6792	0.6804	0.680 ± 0.002	2.0832	0.6944
	Deconvolution[b]	0.7086	0.7112	0.7106	0.710 ± 0.003	2.1061	0.7020
92.9 ppm	S/N	33.8	30.3	29.7	31 ± 6	53.3	30.8
	Intensity	692	671	685	680 ± 20	1,971	657
	Integral[a]	0.6303	0.6058	0.6219	0.62 ± 0.03	1.9181	0.6394
	Deconvolution[b]	0.6317	0.6137	0.6279	0.62 ± 0.01	1.8582	0.6194
87.4 ppm	S/N	35.9	34.0	33.1	34 ± 4	58.1	33.5
	Intensity	735	753	762	750 ± 30	2,147	716
	Integral[a]	0.6156	0.6663	0.6608	0.65 ± 0.07	1.9833	0.6611
	Deconvolution[b]	0.6729	0.6779	0.6898	0.68 ± 0.02	2.0155	0.6718

[†] = The ABC data set was generated by summing the corresponding FIDs from the A, B, and C data sets. See experimental section 4.2.4 for details.

[‡] = To compare the Averages from the measurements of the A, B, and C data sets to the measurements of the ABC data set the results must be scaled. S/N was scaled by dividing the observed value by $3^{0.5}$ according to the square root relationship seen in Figure 4.3. The intensity, integral, and deconvolution results were scaled by dividing the results by 3, according to the linear relationship seen in Figure 4.2.

[a] = Integration regions for the peaks were 109 –105.5 ppm, 94.5 – 91.5 ppm, and 89 – 86 ppm.

[b] = All of the deconvolutions were performed by fitting the peaks to models that were restricted to a line width of 21 Hz and a 50% Gaussian line shape.

data match very well with the averages from the other measurements. However, none of the scaled intensities from the ABC data set were within the 95% CIs of the average value of the other experiments. This is likely because of the significantly higher noise levels that are present in this data relative to the previous 4:1 MGA:HMB study. In contrast, the scaled integration and deconvolution areas for the peaks at 92.9 and 87.4 ppm in the ABC data are in very good agreement with the averages of A, B, and C. This is likely due to the relative insensitivity of deconvolution to the noise that is present in the data.

The integration and deconvolution areas for the peak at 107.3 ppm are also in good agreement with, but fall outside of, the 95% CI for the A, B, and data. It can be seen that the $CI_{95\%}$ values for the integration and deconvolution measurements are approximately an order of magnitude lower for the peak at 107.3 ppm than for the other two peaks. This is probably not an accurate representation of the true confidence intervals for these two measurements of the peak at 107.3 ppm because these $CI_{95\%}$ values are considerably different than the values from the analysis of the other peaks. The results in Table 4.1 for the lactose data supports the earlier observations from the 4:1 MGA:HMB mixture.

Thus, several general conclusions can be drawn from these experiments. When performing relative quantitation studies with NMR the signal sizes should be determined by measuring the peak areas, rather than the intensities because differences in the width of the peaks will result in dissimilar distributions of the total signal intensity. In addition, when feasible, the areas should be determined by deconvolution rather than integration to help reduce the influence of the noise that is present in the data. When the S/N of the data is limited by long experiment times it is also possible to reduce the uncertainty in the measured

peak areas by maximizing the number of transients per FID, rather than trying to limit the uncertainties by collecting multiple FIDs.

4.3.2 Spinning Sidebands

In NMR spectroscopy the observed chemical shifts are the result of differences in the chemical environment of the nuclei. However, the rigid nature of solid materials results in a phenomenon called chemical shift anisotropy, which results in broad SSNMR signals when analyzing powders due to the various orientations of the molecules to the external magnetic field. When magic-angle spinning (MAS) is used the broad signal is split into a series of peaks that are separated by the rate at which the sample is rotated.

This phenomenon is demonstrated in Figure 4.9 with levofloxacin hemihydrate ^{19}F spectra collected at three MAS rates. The spectra show that as the MAS rate is increased there is a proportional increase in the separation between the isotropic peaks and the spinning sidebands. If the MAS rate was increased sufficiently all of the spinning sidebands would disappear; however, in the demonstrated case of levofloxacin hemihydrate an MAS rate of > 45 kHz would be required to eliminate all of the spinning sidebands in the ^{19}F spectrum. Most commonly used MAS rotors are limited to rates < 35 kHz so eliminating spinning sidebands through MAS spinning is typically not feasible.

The spectra in Figure 4.9 also show that as the MAS rate is increased the fraction of the total signal (isotropic peaks and spinning sidebands) that appears in the isotropic peaks also increases. Therefore, using a relatively fast MAS rate will simplify the spectrum (fewer spinning sidebands) and will increase the sensitivity of the isotropic signals. However, there is a tradeoff because sample

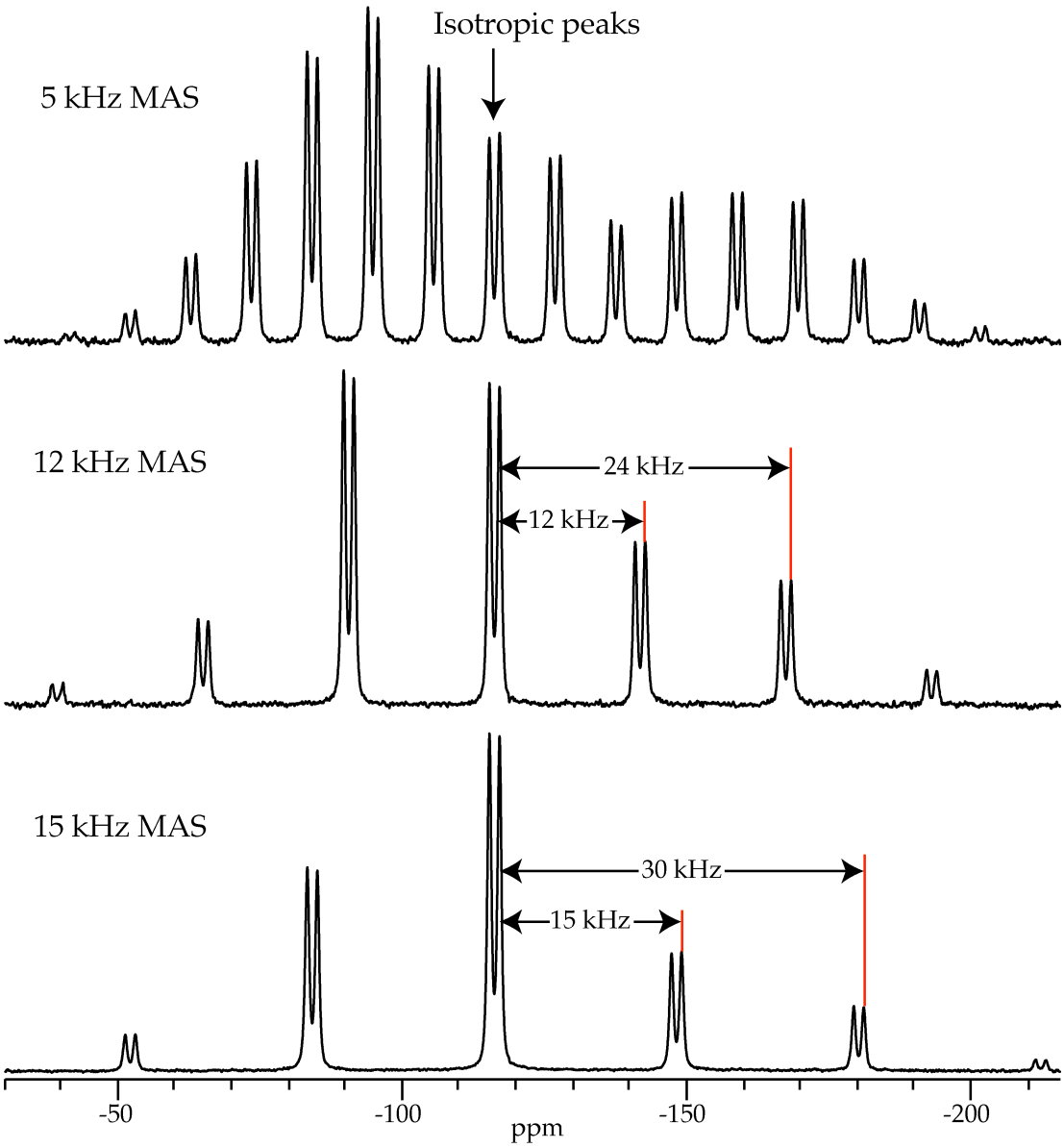

Figure 4.9. Chemical structure and ^{19}F MAS spectra of levofloxacin hemihydrate. See Chapter 2, Section 2.2.6, for instrument details and parameters. The 5 and 15 kHz MAS data was collected 64 transients, while the 12 kHz data was collected with 16 transients. The separation distances of one isotropic peak and some of the corresponding spinning sidebands are shown for the bottom two spectra. The separation distance in Hz can be divided by the operating frequency of the spectrometer (469 MHz for ^{19}F) to determine the separation in ppm, for example 15,000 Hz / 470 MHz = 32 ppm.

heating is observed at MAS rates above approximately 7 kHz,[35] which could result in physical form changes. Therefore, pulse sequences are often used to suppress the appearance of the spinning sidebands in the data and are generally referred to as total suppression of spinning sideband (TOSS) methods.

The fraction of the SSNMR signal that is contained in the isotropic peaks and spinning sidebands is influenced by the packing of the molecules within the material. Thus, different physical forms can result in different distributions of the signal. Therefore, it is necessary to integrate the isotropic peak and its associated spinning sidebands for each physical form that is being analyzed in order to obtain quantitative information. An alternative is to select an appropriate MAS rate for the experiments and then characterize the fraction of the total signal (f_{MAS}) that is contained within the isotropic signal (A_0). Then, when a quantitative analysis of that form is done, the isotropic signal can be measured and then divided by the fraction of the total signal that it represents at that MAS rate to estimate the total signal area (S), Equation 4.5.

$$S = \frac{A_0}{f_{MAS}} \qquad \text{Equation 4.5}$$

As mentioned previously, a faster MAS rate will result in larger isotropic signals and minimize the size of the spinning sidebands. However, in addition to sample heating, it is important to consider the potential overlap of signals. Therefore, the MAS rate should be carefully selected so that the isotropic peaks of interest do not overlap with the spinning sidebands of other signals within the spectrum. This can be especially difficult when performing quantitation with ^{13}C

spectra for formulated APIs because not only must the spinning sidebands of the API peaks be considered, but the excipients may also interfere with the signals of interest. The use of TOSS methods does not negate these considerations because the suppression is not always complete, so sideband artifacts could impact the analysis even when TOSS methods are used. The issues of MAS rate selection and the analysis of signal distribution in spinning sidebands will be addressed again in Section 4.3.6 as they apply to a specific example of relative quantitation of CortA physical forms diluted in an excipient.

4.3.3 Longitudinal Relaxation Time (T_1)

The introduction to this chapter pointed out that the rate at which the magnetization of the sample approaches equilibrium is an important variable in quantitative NMR measurements. This is an exponential process (Equation 4.6)

$$S \propto M_{z,\tau} = M_{z,\infty}\left(1 - e^{-\tau/T_1}\right) \qquad \text{Equation 4.6}$$

and is referred to as spin-lattice or longitudinal relaxation and is often reported as a time constant (T_1). In Equation 4.6 the observed signal (S) is directly proportional to the magnetization along the z-axis ($M_{z,tau}$) when the sample is allowed to relax for a given time (τ), and is a function of equilibrium magnetization ($M_{z,\infty}$). According to Equation 4.6, a quantitative NMR experiment should use a τ that is approximately 5-times the T_1 so that the exponential term is negligible (e^{-5} = 0.00674) and the sample is able to relax completely to its equilibrium state before the collection of each transient. This is especially

important when the sample components relax at different rates and thus have different T_1s; in these cases the delay between transients is 5-times the longest T_1 value of the components that are being analyzed.

This is demonstrated in Figure 4.10, which shows the profiles of the MGA peaks from a ^{13}C T_1 experiment. While the magnetization of the sample grows along the z-axis (parallel with the B_0) with increased relaxation time, the Torchia method[32] results in a peak profile that displays an exponential decay. The profile can then be fit to obtain the T_1 of the relaxation (Table 4.2). The results demonstrate the primary issue with collecting quantitative spectra via DP of ^{13}C nuclei. The methyl carbon (C-4) relaxes very quickly (T_1 = 0.4 sec), but the acid carbons (C-5,8) relax much more slowly (T_1 > 100 sec). Therefore, in order to obtain a quantitative ^{13}C spectrum by DP, a delay of >500 sec must be used between transients to avoid incomplete relaxation, also referred to as saturation, of C-5,8.

As a comparison, the CP spectra that were collected for the signal reproducibility study (Section 4.3.1) with 4 transients had a S/N of ~80 for the MGA C-4 peak and each FID was collected in 20 sec. If a DP spectrum of similar S/N were to be collected it would require the collection of approximately 16 transients (CP results in approximately a 4-fold sensitivity enhancement for ^{13}C) and with a 500 sec delay between transients would take over 2 hours to collect. Additionally, in order to obtain a DP spectrum similar to the one in Figure 4.1, the experiment would take approximately 9 days, as compared to the 32-min acquisition that was required to collect the CP spectrum.

In CP experiments, magnetization is transferred from an abundant spin, such as ^{1}H, to a dilute spin, such as ^{13}C. As mentioned previously, in the case of

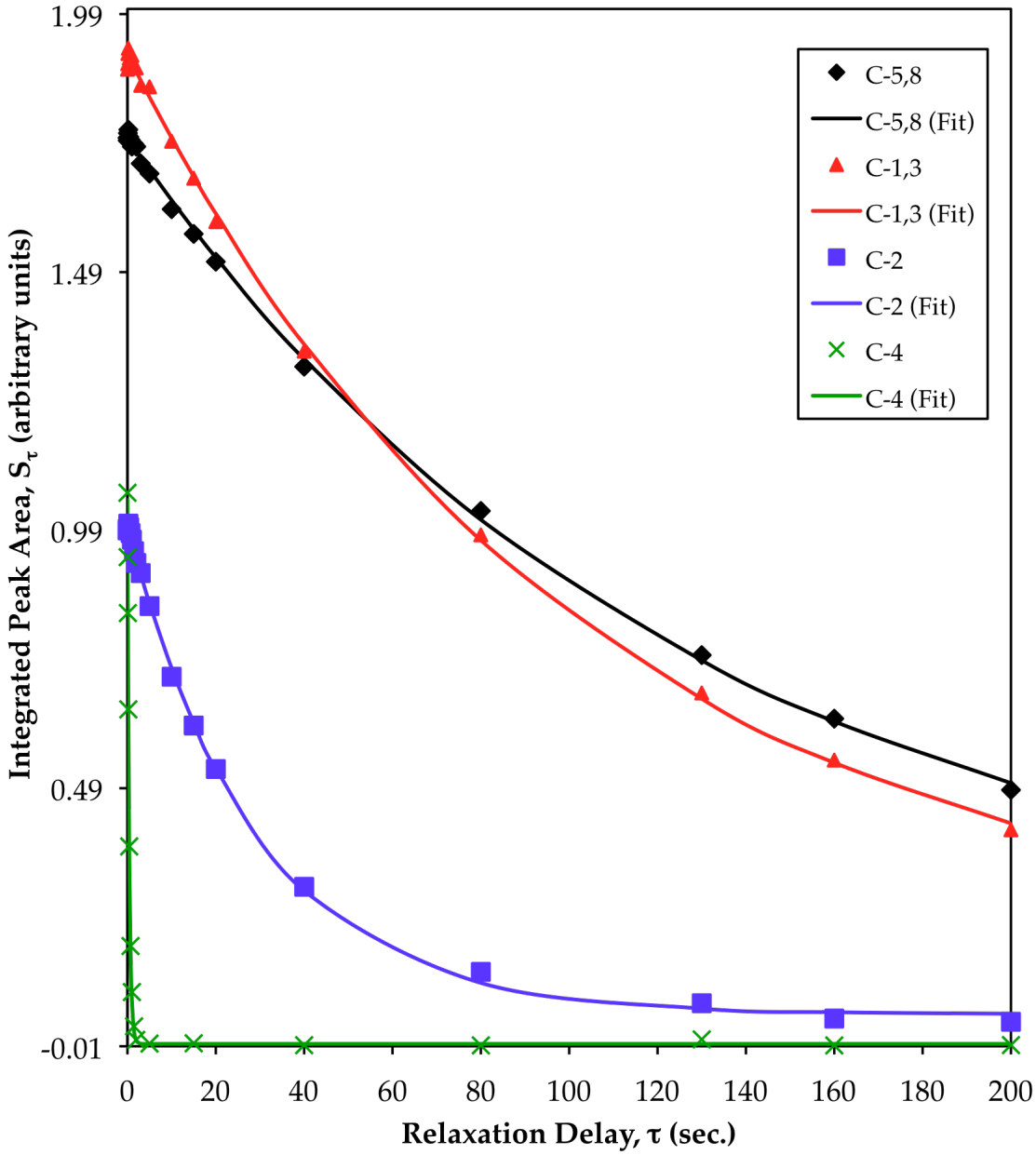

Figure 4.10. Relaxation profiles of MGA peaks in ^{13}C T_1 measurement experiment performed via the Torchia method.[32] In the Torchia method the integrated peak area decays as the relaxation delay (τ) is increased. The symbols represent the integrated peak areas while the lines show the results from the nonlinear regression of the data (results shown in Table 4.2). See Figure 4.1 for the carbon numbering scheme of MGA.

Table 4.2 Results of nonlinear regression analysis† of the MGA ^{13}C relaxation data that is shown in Figure 4.10. See Figure 4.1 for the carbon numbering scheme for MGA.

Parameter‡	C-5,8	C-1,3	C-2	C-4
$S_0 \pm$ Error	1.57 ± 0.03	1.74 ± 0.03	0.945 ± 0.007	1.081 ± 0.006
$T_1 \pm$ Error (sec)	125 ± 5	102 ± 4	29.1 ± 0.7	0.395 ± 0.006
Offset	0.2	0.2	0.05	-0.006
χ^2	0.00219	0.00324	0.00190	0.00101
R^2	0.99933	0.99932	0.99925	0.99958

† = The profiles in Figure 4.10 were fit to the equation below with the KaleidaGraph software package. S_0 represents the signal area at $\tau = 0$.

$$S_\tau = \left(S_0 e^{-\tau / T_1} \right) + \text{Offset}$$

‡ = The Error of the S_0 and T_1 parameters reflect the standard error of the corresponding parameter from the nonlinear regression. The χ^2 and R^2 represent the quality of the regressions.

^{1}H and ^{13}C, this results in approximately a 4-fold increase in the ^{13}C signal that is observed. In addition, the ^{13}C nuclei do not have to relax significantly between transients. Instead, the delay between transients in CP experiments is dictated by the T_1 of the abundant spins, and ^{1}H T_1s are typically on the order of a few seconds (Table 4.3).

In SSNMR, ^{1}H T_1 values are typically measured by one of three methods: saturation recovery, inversion recovery, or the Torchia[32] method. All three methods were used with CP to indirectly detect the ^{1}H T_1 of MGA, and the results are shown in Table 4.3. The results from the inversion recovery and Torchia methods agree with one another very well both within and between the methods. This data also demonstrates that ^{1}H T_1s are typically uniform for a material (all of the ^{13}C peaks give the same value) because of the dipolar coupling that exists between the ^{1}Hs in the material. The saturation recovery method gave similar results but tended to give values that were slightly higher than those obtained with the other two methods. Additionally, the standard errors from the nonlinear regressions also agreed well with the $CI_{95\%}$ values that were calculated.

It was unclear if the differences that were observed in the ^{1}H T_1 values in Table 4.3 were due to the methods used to measure the values or uncertainties in the measurements. Therefore, the ^{1}H T_1 of MGA was measured with the saturation recovery method three times to assess the reproducibility of the measurement. Additionally, two separate data sets were collected with either 64 or 256 transients per FID in order to determine the influence of S/N of the data. The results are shown in Table 4.4, and it should be noted that the T_1 value was significantly different from the value that was observed in Table 4.3 because the measurements were done at different field strengths (Table 4.3 and Table 4.4 at

Table 4.3 ^{1}H T_1 values for MGA from three different experimental methods: Saturation Recovery, Inversion Recovery, and the Torchia[32] Method. See Figure 4.1 for the carbon numbering scheme for MGA.

	Saturation Recovery‡	Inversion Recovery‡	Torchia‡
C-5,8	1.40 ± 0.01	1.34 ± 0.01	1.326 ± 0.007
C-1,3	1.39 ± 0.01	1.330 ± 0.005	1.33 ± 0.01
C-2	1.376 ± 0.009	1.323 ± 0.006	1.33 ± 0.01
C-4	1.343 ± 0.008	1.333 ± 0.005	1.334 ± 0.009
Average ± $CI_{95\%}$	1.38 ± 0.04	1.32 ± 0.01	1.33 ± 0.01

‡ = The errors of the T_1 values for C-5,8, C-1,3, C-2, and C4 are the standard errors from the nonlinear regressions. The averages and $CI_{95\%}$ values are calculated from the T_1 values for each experimental methods, respectively.

Table 4.4 ^{1}H T_1 values for MGA from the saturation recovery method repeated three times (#1, #2, and #3) with either 64 or 256 transients collected for each FID. See Figure 4.1 for the carbon numbering scheme for MGA.

64 transients

	#1 ± Error‡	#2 ± Error ‡	#3 ± Error‡	Average ± $CI_{95\%}$ ‡
C-5,8	1.086 ± 0.009	1.080 ± 0.005	1.08 ± 0.01	1.083 ± 0.008
C-1,3	1.089 ± 0.009	1.090 ± 0.008	1.08 ± 0.01	1.09 ± 0.01
C-2	1.079 ± 0.009	1.088 ± 0.008	1.07 ± 0.01	1.08 ± 0.02
C-4	1.075 ± 0.007	1.079 ± 0.007	1.068 ± 0.008	1.07 ± 0.01
Average ± $CI_{95\%}$ ‡	1.08 ± 0.01	1.084 ± 0.009	1.08 ± 0.1	

256 transients

	#1 ± Error‡	#2 ± Error ‡	#3 ± Error‡	Average ± $CI_{95\%}$ ‡
C-5,8	1.085 ± 0.006	1.094 ± 0.008	1.090 ± 0.006	1.09 ± 0.01
C-1,3	1.092 ± 0.007	1.102 ± 0.008	1.106 ± 0.008	1.10 ± 0.02
C-2	1.087 ± 0.008	1.096 ± 0.008	1.097 ± 0.007	1.09 ± 0.01
C-4	1.073 ± 0.005	1.076 ± 0.004	1.075 ± 0.005	1.075 ± 0.005
Average ± $CI_{95\%}$ ‡	1.08 ± 0.01	1.09 ± 0.02	1.09 ± 0.02	

‡ = The errors of the T_1 values for C-5,8, C-1,3, C-2, and C4 are the standard errors from the nonlinear regressions. The averages and $CI_{95\%}$ values are calculated for each peak (C-5,8, C-1,3, C-2, and C4) and data set (#1, #2, and #3).

400 MHz and 300 MHz ^{1}H frequencies, respectively) and the T_1 is dependant upon the magnetic strength of the spectrometer. It is clear from the data in Table 4.4 that the standard error of the nonlinear regression is a relatively accurate predictor of the $CI_{95\%}$ for replicate measurements and performing a ^{1}H T_1 measurement multiple times does not give significantly different values. Additionally, doubling the S/N of the spectra by quadrupling the number of transients that are collected does not significantly impact the values.

The ^{1}H T_1 of α-lactose monohydrate was previously shown to be approximately 250 sec,[36] and so it was investigated to determine if the general conclusions from the data in Table 4.4 could be extended to materials with long T_1s and data sets that contain spectra with low S/N values. The T_1 was measured by the saturation recovery method using 4 transients per FID and the experiment was repeated three times (A, B, and C). The corresponding FIDs from the A, B, and C data sets were summed to simulate an experiment in which 12 transients were collected for each FID and this simulated data set was designated ABC. The results of the analysis are shown in Table 4.5.

The relative error of the T_1 values in Table 4.5 are significantly larger than the previous observations with MGA. This is most likely due to the significantly lower S/Ns of the spectra within the data sets for α-lactose monohydrate. In fact, when the peaks between 78 and 68 ppm were integrated the error of the T_1 value was significantly lower than that of the other integration regions that only contained one peak. It is also observed that when the $CI_{95\%}$ is calculated for each data set, it is in good agreement with the largest error within the data set. When the T_1 values from the ABC data set are compared to the other data sets, they do

Table 4.5 ^{1}H T_1 values for α-lactose monohydrate from the saturation recovery method repeated three times (A, B, and C) with 4 transients collected for each FID and the simulated ABC data set.

Integration Range (ppm)	A ± Error‡	B ± Error ‡	C ± Error‡	ABC ± Error‡
110 – 104	300 ± 20	290 ± 20	290 ± 10	291 ± 8
96 – 90	270 ± 20	260 ± 10	320 ± 20	281 ± 9
90 – 84	270 ± 20	240 ± 20	280 ± 20	261 ± 9
78 – 68	267 ± 5	268 ± 4	274 ± 4	270 ± 3
65 – 59	269 ± 9	270 ± 10	273 ± 9	271 ± 5
Average ± $CI_{95\%}$ ‡	270 ± 20	260 ± 20	290 ± 20	270 ± 10

‡ = The errors of the T_1 values for each integration range are the standard errors from the nonlinear regressions. The averages and $CI_{95\%}$ values are calculated from all of the integration ranges within each data set (A, B, C, and ABC).

not vary as significantly across the spectrum as with the A, B, and C data sets. This is also likely due to the relatively higher S/N of the spectra in the ABC data set. Thus, all of the data in Tables 4.4 and 4.5 suggests that when performing ^{1}H T_1 measurements each of the peaks in the spectrum can be integrated independently and then compared to determine the $CI_{95\%}$ of the measurement. Additionally, if only one peak is available for analysis then the standard error of the T_1 from the nonlinear regression can be used as an estimate of the $CI_{95\%}$. Finally, when choosing between performing multiple ^{1}H T_1 measurements and increasing the number of transients collected for low S/N data sets, increasing the number of transients and performing the measurement once should yield values with more confidence than performing replicate measurements.

The accurate measurement of ^{1}H T_1 values is important for quantitation measurements because different physical forms will have different T_1 values. Therefore, if the delay between transients is not at least 5 times the ^{1}H T_1 of the slowest relaxing species that is being analyzed, then its peaks will be artificially small compared to the other component and will yield inaccurate quantitative measurements.

4.3.4 Optimization of Pulse Delay

The delay between transients is referred to as the pulse delay because during this time no RF pulses are applied to the sample. With fast relaxing materials, such as MGA, this delay is relatively short. MGA has a ^{1}H T_1 of 1.1 sec (in a spectrometer operating at ^{1}H resonance frequency of 300 MHz) and thus the pulse delay should be at least 5.5 sec to allow the magnetization to relax fully when collecting quantitative spectra of MGA. A delay of approximately 6

seconds is not prohibitive, especially considering the relatively high S/N of MGA spectra when only a few transients are collected. However, α-lactose monohydrate has a ^1H T_1 of approximately 270 sec, so a quantitative spectrum of a mixture of MGA and α-lactose monohydrate would need to be collected with a pulse delay of more than 23 min. That permits only one transient every half hour, or just 48 transients in a day.

With most organic molecules, when spectra are collected with these long pulse delays, only a tiny fraction of the time is actually spent manipulating the magnetization and acquiring the FID. The majority of the time the spectrometer is idle. For the case of MGA only about 2% of the time is spent applying the RF pulses and acquiring the data. The other 98% of the time is spent waiting for the magnetization to return to equilibrium. In the case of α-lactose monohydrate >99.99% of the time is spent waiting for the material to relax. Therefore, these experiments are exceptionally inefficient.

Recall that Equation 4.6 shows the exponential relationship between the fraction of the magnetization that is present when the sample is allowed to relax for some time (τ). When τ is at least 5 times the T_1 value of the material, the magnetization will be at >99% of its equilibrium value. But if τ is twice the T_1 then the magnetization will only be at approximately 86% of its equilibrium value. If two sets of data are collected with the same number of transients but with pulse delays of 5 and 2 times the T_1 of the sample, then the relative intensity of the second spectrum will only be about 86% that of the first spectrum. However, if the duration of the experiment is held constant it is possible to collect more transients with the shorter pulse delay and the spectrum of the data

collected with the shorter pulse delay will be approximately 38% more intense than the spectrum from the data where full relaxation was achieved. In fact, it can be shown that for the time that is invested in collecting data, a pulse delay that is 1.26 times the T_1 will yield the highest S/N.[37]

When attempting to detect the physical form or forms of an API within a formulation, the S/N of the spectra is typically the primary issue. By using a pulse delay that is approximately 1.25 to 2 times the average T_1s of the known forms the resulting S/N of the data will be as high as is feasibly possible for the amount of time that is spent collecting the data, which can be anywhere from hours to days. However, since the components were not allowed to relax fully the relative sizes of the signals are not directly proportional to the sample composition. If the T_1s of the forms are known, then Equation 4.6 may be rearranged to predict the size of the signals, had they been allowed to fully relax (Equation 4.7). In Equation 4.7, S_{tau} is the observed signal size, τ is the pulse

$$S_\infty = \frac{S_\tau}{\left(1 - e^{-\tau/T_1}\right)} \qquad \text{Equation 4.7}$$

delay, T_1 is the longitudinal relaxation time constant of the material, and S_∞ is the signal size when complete relaxation to the equilibrium state is allowed. It is important to note that when collecting quantitative data with a pulse delay that is significantly shorter than 5 times the T_1, several "dummy" transients should be performed at the beginning of the experiment. These dummy transients should be identical to the conditions under which the actual transients are collected and

are used to ensure that "steady state" conditions are established before data acquisition begins. This approach to performing efficient quantitation studies in SSNMR will be tested with the CortA examples in Section 4.3.5.

4.3.5 CP Dynamics (T_{CH} and $T_{1\rho}$)

The major advantages of using CP to collect ^{13}C spectra of solid materials have been discussed previously. The two main advantages are a 4-fold sensitivity enhancement relative to DP ^{13}C spectra and a reduction in experiment times due to the faster relaxation of ^{1}H nuclei. Unfortunately, the magnetization transfer between the nuclei does not happen instantaneously and simultaneously the material is undergoing additional relaxation processes.

Generally, the CP process can be represented by Equation 4.8, where S is

$$S \propto \frac{M_0\left(\frac{\gamma_H}{\gamma_C}\right)\left[e^{-t/T_{1\rho,H}} - e^{-t/T_{CH}}\right]}{1 - \frac{T_{CH}}{T_{1\rho,H}}} \qquad \text{Equation 4.8}$$

the observed ^{13}C signal, M_0 is the equilibrium magnetization of the ^{13}C nuclei, γ_H and γ_C are the gyromagnetic ratios of the ^{1}H and ^{13}C nuclei, respectively, t is the duration of the CP pulse, T_{CH} is the time constant of magnetization transfer from the ^{1}H nuclei to the ^{13}C nuclei, and $T_{1\rho,H}$ is the time constant for spin-lattice, or longitudinal, relaxation in the rotating frame of the ^{1}H nuclei.[20,38] Equation 4.8 shows that as the duration of the CP pulse is increased the observed signal will also increase according to T_{CH}. However, at long CP pulse duration the signal

will be diminished according to $T_{1\rho,H}$. This behavior is demonstrated in Figure 4.11 with MGA.

The CP dynamics depend upon several variables and thus peaks in a ^{13}C CP spectrum will exhibit different CP dynamics and their relative sizes will depend upon the duration of the CP pulse. Therefore, in order to obtain quantitative information it is necessary to correct for these differences in the CP dynamics of the peaks that are used in the analysis. The duration of the CP pulse is typically selected to correspond to the maximum signal for the CP dynamics profiles in order to maximize the S/N of the spectra. However, it is necessary to apply a correction factor to obtain quantitative information since the dynamics are dissimilar for different peaks, compounds, and physical forms. Determining the appropriate correction factor from Equation 4.8 is rather cumbersome; however, the relationship can be simplified to make the analysis simpler. At short CP pulse durations the observed signal intensity is determined by both the T_{CH} and $T_{1\rho,H}$; but, when t is more than 5 times the T_{CH} Equation 4.8 can be simplified (Equation 4.9) and yields a simple monoexponential decay where the

$$S \propto \frac{M_0\left(\frac{\gamma_H}{\gamma_C}\right)}{1-\frac{T_{CH}}{T_{1\rho,H}}}\left[e^{-t/T_{1\rho,H}}\right] \approx C\left(e^{-t/T_{1\rho,H}}\right) \qquad \text{Equation 4.9}$$

M_0, γ, and denominator of Equation 4.9 are collapsed into a single constant (C). Therefore, when the spectra are collected in this manner the observed signals can

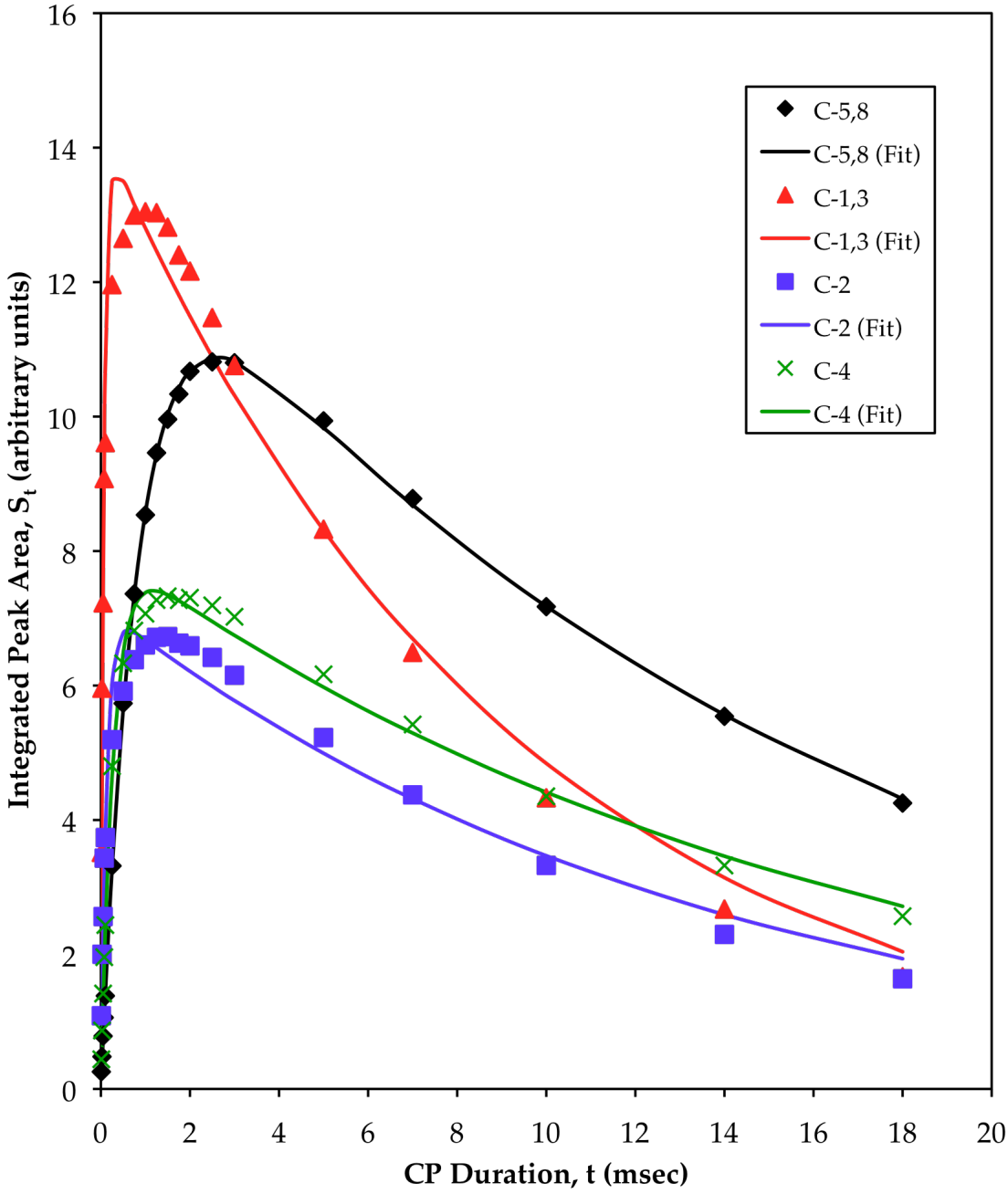

Figure 4.11. CP dynamics profiles of MGA peaks from spectra collected by varying the duration of the CP pulse (t). The symbols represent the integrated peak areas while the lines show the results from the nonlinear regression of the data using Equation 3.8 with M_0 and the gyromagnetic ratios treated as a single parameter. See Figure 4.1 for the carbon numbering scheme of MGA.

be scaled with the CP time (t) and the appropriate $T_{1\rho,H}$.

The CP dynamics profiles can be fit to Equation 4.8 in order to determine the T_{CH} and $T_{1\rho,H}$ values and ultimately determine the appropriate CP pulse duration for quantitation experiments and for use in scaling the observed signals for the differences in the CP dynamics. Figure 4.11 shows the results from the nonlinear regression of the MGA CP dynamics profile. Protonated carbons typically display relatively short T_{CH} values relative to non-protonated carbons, and this is demonstrated in the MGA data because the C-5,8 signal requires a longer CP pulse to achieve its maximum value as compared to the other signals. The C-5,8 profile also is modeled very well by Equation 4.8. Unfortunately, some of the assumptions that lead to Equation 4.8 do not hold up in the case of the other MGA signals, evidenced by the relatively poor fits to the observed profiles. If accurate T_{CH} values were required, a more sophisticated model could be used to model the data; however, the T_{CH} of these signals is clearly much shorter than the C-5,8 signal and thus will have no significant impact on determining the t that would be used to quantitative studies. Therefore, in order to more accurately determine all of the $T_{1\rho,H}$ values all of the data points with $t < 1$ msec were excluded and the profiles were modeled again (Figure 4.12). The T_{CH} and $T_{1\rho,H}$ of the C-5,8 signal and the standard error of each did not change significantly between the regressions shown in Figures 4.11 and 4.12; however, the standard errors of the $T_{1\rho,H}$ values for the other signals dropped significantly when the short t points were excluded. The results of the regressions in Figure 4.12 are shown in Table 4.6.

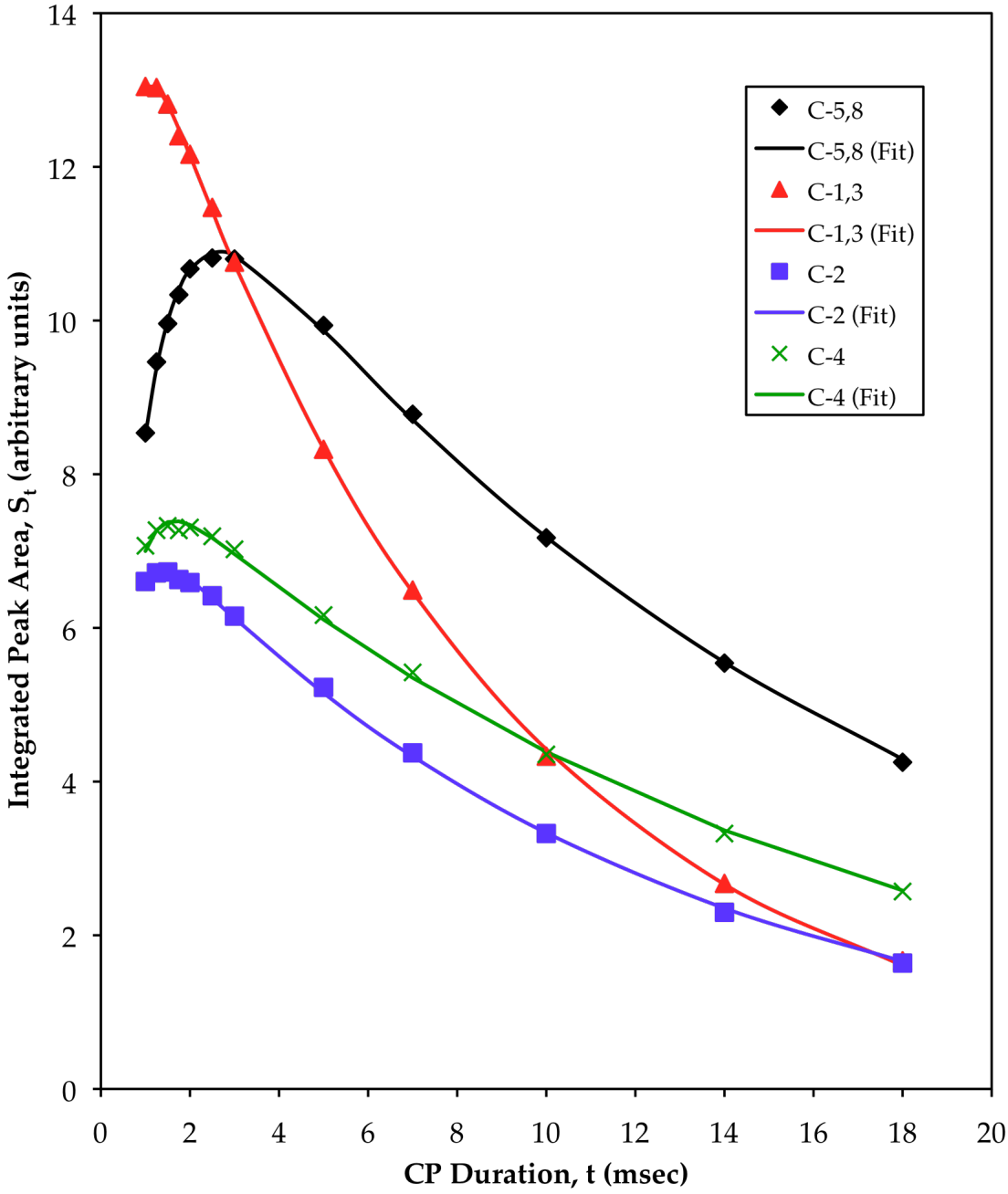

Figure 4.12. CP dynamics profiles of MGA peaks from Figure 4.11, with t values shorter than 1 msec excluded. The symbols represent the integrated peak areas while the lines show the results from the nonlinear regression of the data using Equation 3.8 with M_0 and the gyromagnetic ratios treated as a single parameter. See Figure 4.1 for the carbon numbering scheme of MGA.

Table 4.6 CP dynamics for MGA from the data shown in Figure 4.12.

Parameter‡	C-5,8	C-1,3	C-2	C-4
$S_0 \pm$ Error	12.91 ± 0.06	15.04 ± 0.04	7.67 ± 0.04	8.25 ± 0.04
$T_{CH} \pm$ Error (msec)	0.87 ± 0.01	0.33 ± 0.01	0.42 ± 0.02	0.46 ± 0.02
$T_{1\rho,H} \pm$ Error (msec)	15.5 ± 0.2	7.89 ± 0.05	11.5 ± 0.2	15.1 ± 0.3
χ^2	0.0298	0.0241	0.0244	0.0383
R^2	0.99942	0.99988	0.99936	0.99881

† = The profiles in Figure 4.12 were fit to the equation below with the KaleidaGraph software package, which was adapted from Equation 4.8.

$$S_t = \frac{S_0\left[e^{-t/T_{1\rho,H}} - e^{-t/T_{CH}}\right]}{1-\left(\frac{T_{CH}}{T_{1\rho,H}}\right)}$$

‡ = The Error of the S_0, T_{CH}, and $T_{1\rho,H}$ parameters reflect the standard error of the corresponding parameter from the nonlinear regression. The χ^2 and R^2 represent the quality of the regressions.

According to the results in Table 4.6, quantitative MGA spectra should be collected with a CP pulse duration of at least 4.4 msec (5 times the longest T_{CH}) and then each of the peaks should be scaled with the exponential relationship in Equation 4.9 to correct for the $T_{1\rho,H}$ relaxation that occurred as part of the CP process. Thus, CP can be used to obtain ^{13}C with a higher S/N and in less time than an analogous DP spectrum of the same sample. In addition, by accounting for differential distributions of signal in spinning sidebands and relaxation rates of materials, it should be possible to achieve quantitative measurements from ^{13}C spectra without producing a calibration curve and without waiting for the sample to completely relax to its equilibrium state between transients. The last section of the chapter will combine all of these concepts and apply them to CortA to test the validity of this approach.

4.3.6 Quantitation of Cortisone 21-Acetate (CortA) Polymorphs Diluted in Starch

CortA was chosen as a model compound to test this approach to quantitation via SSNMR because this commonly used anti-inflammatory agent has several relatively stable crystalline forms. In addition, it falls within the "typical" range of most drug molecules with a molecular weight of 402.5, various types of functional groups, and displays moderate NMR relaxation rates. In addition, Harris et al.[31] have previously reported reference ^{13}C CPMAS spectra and chemical shifts for the known crystalline forms.

The ^{13}C CPMAS spectra of CortA Forms I and II are shown in Figure 4.13 along with the spectrum of Starch 1500. The CortA spectra display relatively narrow peaks, consistent with crystalline materials, and the observed chemical

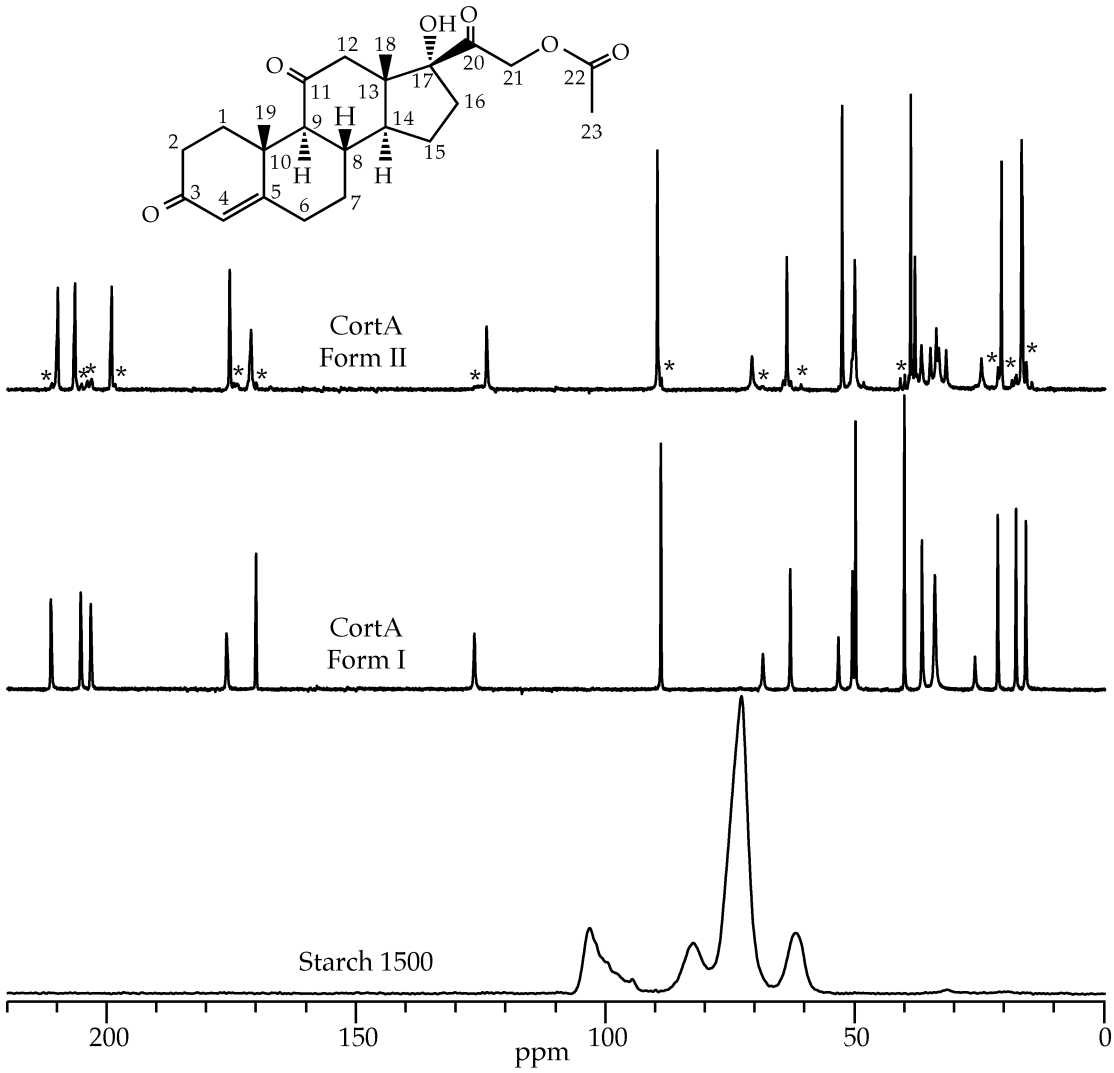

Figure 4.13. ^{13}C CPMAS/TOSS spectra of Starch 1500 and CortA Forms I and II. Form I was prepared by heating the CortA to 200 °C for an hour while Form II was produced by recrystallization from chloroform. The chemical structure of CortA is provided with carbon numbering. * = Form I and III impurities

shifts in each spectrum agree with the previously reported values for each of the forms.[31] Additionally, the spectrum of Form II displays numerous small peaks that are consistent with both Forms I and III, indicating that when the CortA was crystallized from chloroform a mixture of physical forms was produced. The spectrum of Starch 1500 displays very broad peaks, consistent with an amorphous material, that do not overlap significantly with most of the CortA peaks. Therefore, Starch 1500 should not hinder the quantitative analysis of the CortA peaks.

Equations for quantitation by SSNMR can be derived based upon the previous discussions regarding the relationship of spinning sidebands, relaxation rates, and experimental parameters upon quantitative analysis by SSNMR spectroscopy. For the relative quantitation of two physical forms (X and Y) by SSNMR, the fraction of the material in the X form (F_X) is given by Equation 4.10

$$F_X = \frac{1}{1 + \left(\frac{A_Y}{A_X} \times \frac{f_X}{f_Y} \times \frac{e^{-t/T_{1\rho,H,X}}}{e^{-t/T_{1\rho,H,Y}}} \times \frac{\left[1 - e^{-d/T_{1,X}}\right]}{\left[1 - e^{-d/T_{1,Y}}\right]} \right)} \qquad \text{Equation 4.10}$$

In this equation f is the fraction of the relevant signal that is observed in the isotopic peak, t is the duration of the CP pulse, and d is the delay between transients. All of these variables can either be measured for the relevant physical forms (f, $T_{1\rho,H}$, and T_1) or are parameters that are chosen by the spectrometer operator (t and d). Additionally, Equation 4.10 assumes that CP is utilized to

collect the spectra, in which case the ^{1}H T_1 is used. If however, DP is to be used, the appropriate ^{13}C T_1 values must be used and the $e^{-t/T1\rho}$ terms are removed from the equation.

In the case of CortA, the chemical shifts for C-3, C-11, and C-20 were selected for quantitative analysis because they were all relatively well resolved. The observed chemical shifts of the three carbons are 202.6, 210. 6, and 204.6 ppm and 198.7, 209.5, and 206.0 for C-3, C11, and C-20 in Forms I and II, respectively.[31] Figure 4.14 shows the isotropic peaks (0) and spinning sidebands (+1, -1, and -2) for these three peaks in both Form I and II, and Table 4.7 shows that for all three carbons the isotropic peaks contain approximately half of the total signal intensity for both Forms I and II.

The relaxation properties of Form I and II were also measured and are shown in Table 4.8. Based on the ^{1}H T_1 values, a delay of approximately 30 sec between transients should allow the sample to relax fully to its equilibrium magnetization, but a delay of about 8 sec would yield spectra with the best S/N for the total amount of time that is spent collecting the data. Additionally, a CP duration of at least 4.5 msec must be used in order to utilize Equation 4.10 for quantitative measurements. Thus, all of the material properties that are needed to perform relative quantitation studies of CortA Forms I and II with Equation 4.10 are provided in Tables 4.7 and 4.8. However, in order to test this approach samples of known composition must be prepared and only pure Form I is available.

Several attempts to produce pure Form II were made but always generated a mixture of forms similar to what is observed in Figure 4.13.

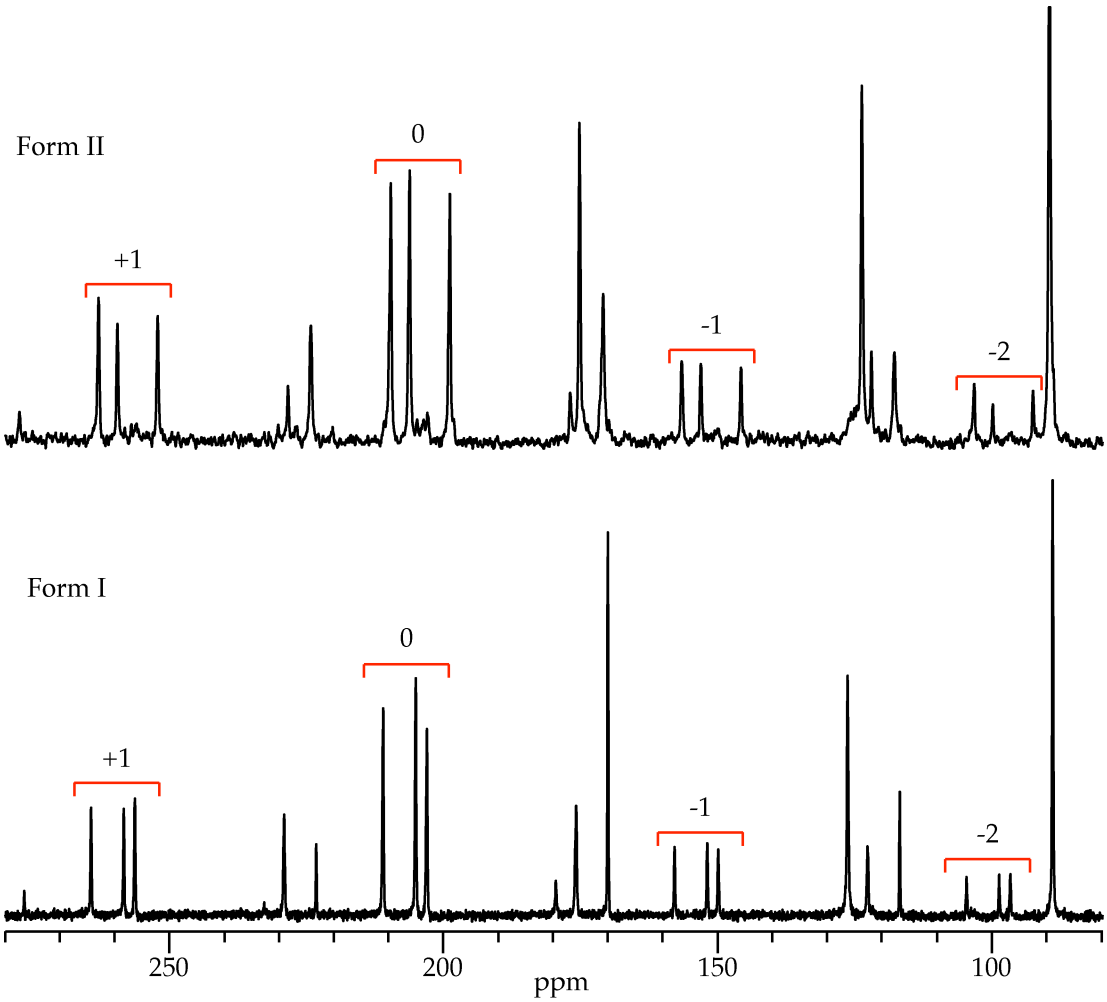

Figure 4.14. ^{13}C CPMAS spectra of CortA Forms I and II, expanded to show the carbonyl peaks (198 to 211 ppm) and their spinning sidebands. The numbers indicate the isotropic peaks (0) and the first (+1 and -1) and second (-2) order spinning sidebands of C-3, C-11, and C-20 (Figure 4.13).[31]

Table 4.7 Determination of f_I and f_{II} for C-3, C-11, and C-20 of CortA, from the spectra shown in Figure 4.14.

Physical Form		C-3	C-11	C-20
Form I	+1	8.0190	7.9641	7.6646
	0	13.8942	15.4586	17.4136
	-1	4.7003	4.7060	4.8422
	-2	2.6348	1.9443	2.0871
	$f_I \pm CI_{95\%}$ †	0.475 ± 0.004	0. 514± 0.004	0.544 ± 0.004
Form II	+1	1.6788	2.0854	1.5073
	0	3.3834	3.8199	3.6650
	-1	0.9019	1.0718	0.9462
	-2	0.6127	0.782	0.2962
	$f_I \pm CI_{95\%}$ †	0.514 ± 0.009	0.492 ± 0.008	0.57 ± 0.01

† = The f of each carbon is calculated based on the equation below where A is the integrated peak area. The $CI_{95\%}$ is estimated by the propagation of CI of each integration, assuming a $RCI_{95\%}$ of 0.002 from the 4:1 MGA:HMB mixture (Section 4.3.1).

$$f = \frac{A_0}{A_{+1} + A_0 + A_{-1} + A_{-2}}$$

Table 4.8 ^{1}H T_1 and CP dynamics for CortA Forms I and II.

		Form I	Form II
^{1}H $T_1 \pm CI_{95\%}$ (sec)[†]		4.3 ± 0.1	5.4 ± 0.7
$T_{CH} \pm$ Error (msec)[‡]	C-3	0.70 ± 0.04	0.42 ± 0.01
	C-11	0.58 ± 0.02	0.34 ± 0.01
	C-20	0.80 ± 0.04	0.50 ± 0.02
^{1}H $T_{1\rho} \pm$ Error (msec)[‡]	C-3	20 ± 1	120 ± 10
	C-11	24 ± 1	130 ± 20
	C-20	25 ± 2	130 ± 20

[†] = Measured by saturation recovery method and reported as the Average ± $CI_{95\%}$ based on integrations of five separate regions of the spectra.

[‡] = The Error of the T_{CH} and $T_{1\rho}$ parameters reflect the standard error of the corresponding parameter from the nonlinear regression.

Additionally, even the stock CortA from Sigma was found to contain primarily Form II, with some unknown amounts of Forms I and III (Figure 4.15). Without pure standards it was not possible to determine the relative amounts of the three forms in the stock material by other solid-state characterization techniques such as DSC, PXRD, or Raman spectroscopy. Therefore, an SSNMR quantitation method that was previously reported by Offerdahl et al.[21] was used to determine the relative amounts of Forms I and II in the stock CortA. The relative amount of Form III was not determined because it was only observed at very low levels and thus it was difficult to estimate its relaxation properties and f_{III}. Also, it is assumed that the amount of Form III will be below the limit of detection of the later quantitation studies.

According to the method of Offerdahl et al.,[21] five FID's were collected with a 30 sec delay between transients to allow full relaxation of the nuclei. Each FID was collected with a different CP pulse duration, but in all cases it was longer than 5 times the T_{CH} to yield a monoexponential decay in the observed signals, dictated by $T_{1\rho}$. The C-3, C-11, and C-20 peak areas of Form I and Form II in the stock material were then measured and plotted on a semi-log plot against the CP pulse duration. The profiles were extrapolated to find the y-intercepts, which represent the peak areas without the influence of the $T_{1\rho}$ relaxation, and are proportional to the relative amounts of Form I and II in the stock material. Since this was done with three separate carbons it was possible to directly obtain the $CI_{95\%}$ based on the difference in the values that were obtained from each of the carbons. This experiment indicated that the fractions of stock CortA that are present as Forms I and II are 0.15 ± 0.02 and 0.85 ± 0.02,

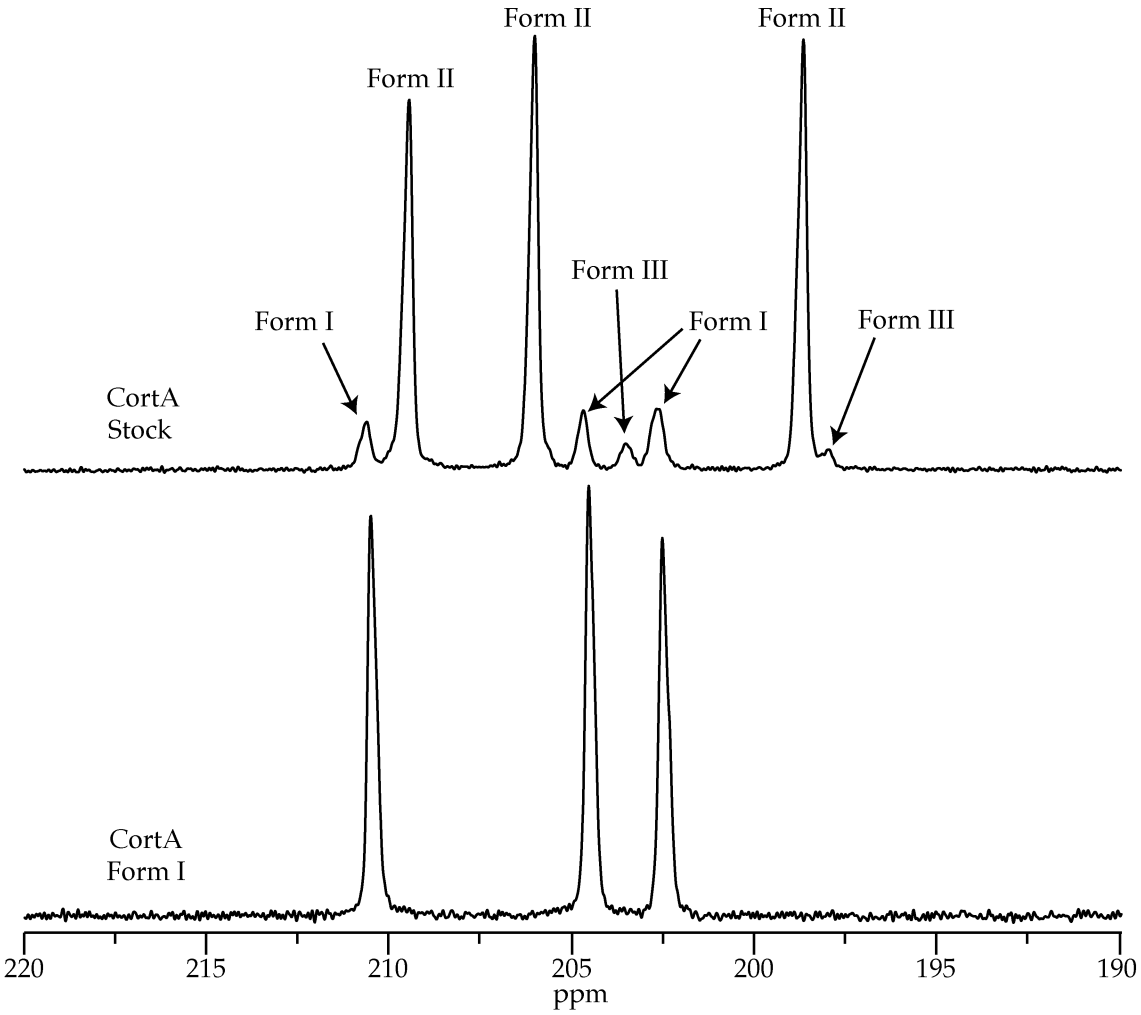

Figure 4.15. ^{13}C CPMAS spectra of CortA Form I and stock material, expanded to show the peaks of C-3, C-11, and C-20 (Figure 4.13).[31] The spectrum of stock material displays peaks that are consistent with Form I and some of the reported chemical shifts of Form III.[31]

respectively. However, recall that this experiment neglected to include the Form III, but if it is assumed that the NMR properties (relaxation rate, etc.) of all three forms are similar it is possible to estimate that Form III constitutes approximately 5% of the stock CortA.

The goal of this work is to apply this method to quantitation of physical forms when they are present in formulations. Therefore, the API will only constitute a fraction of the entire sample and the S/N of the data will be one of the primary limiting factors in the analysis. Thus, it is desirable to collect data in the most efficient manner possible so that the data will have the highest S/N that can be achieved in the time that is spent collecting the data, which could be a period of hours or even days. For this reason CP is used to yield the 4-fold sensitivity enhancement and shorter relaxation delay between transients; however, according to Equation 4.10 it should be possible to correct the observed peak areas for saturation due to incomplete T_1 relaxation when the relaxation delay is shorter than 5 times the longest T_1.

A 1:1 Form I:II CortA mixture was prepared in order to test the validity of the T_1 saturation correction of Equation 4.10. The mixture was then analyzed by collecting ^{13}C CPMAS spectra where the delay between transients was varied from $<^1H$ T_1 to 5-times the longest ^1H T_1. Each experiment was preceded by 16 "dummy" transients to ensure that a steady state was achieved prior to acquisition of the corresponding FID. The C-3, C-11, and C-20 of Form I and II were then analyzed for each of the resulting spectra and processed with Equation 4.10. The results of these measurements are shown in Table 4.9. The F_I measurement that was obtained from each of the carbons did not differ significantly when the delay was changed. Therefore, it appears that the delay

Table 4.9 Comparison of F_I measured from data collected with delays between transients of $<^1$H T_1 to 5-times the longest T_1 of the sample, on the 1:1 Form I:II CortA mixture.

Delay	Delay / ^{1}H $T_{1,II}$ [†]	C-3[‡]	C-11[‡]	C-20[‡]
3 sec	0.56	0.64 ± 0.02	0.55 ± 0.03	0.62 ± 0.02
5 sec	0.93	0.63 ± 0.02	0.54 ± 0.02	0.62 ± 0.02
7 sec	1.3	0.63 ± 0.02	0.54 ± 0.02	0.62 ± 0.02
10 sec	1.9	0.62 ± 0.01	0.54 ± 0.01	0.61 ± 0.01
15 sec	2.8	0.629 ± 0.007	0.543 ± 0.008	0.608 ± 0.008
30 sec	5.6	0.618 ± 0.005	0.549 ± 0.005	0.603 ± 0.005

[†] = The ratio of the relaxation delay between transients and the T_1 of CortA Form II. The 30 sec. delay provides full relaxation of the nuclei and the 7 sec. delay provides data with the highest S/N for the time that is spent on the experiment.

[‡] = The $F_I \pm CI_{95\%}$ are obtained from Equation 4.10, the $CI_{95\%}$ is an estimate of the uncertainty based on the propagation of the uncertainties from the parameters (f, $T_{1\rho}$, T_1).

between transients can be relatively short in order to maximize S/N and not significantly impact the results obtained from Equation 4.10, provided that sufficient "dummy" transients are performed before the data is acquired. The F_I that was obtained from each of the carbons differed, particularly C-11, this was most likely due to the relatively short CP pulse duration (2.5 msec) so that magnetization transfer may not have been complete (5-times T_{CH}).

The C-3, C-11, and C-20 peaks from the spectrum of a model CortA formulation are shown in Figure 4.16, with the deconvolution model that was used to fit the peaks. The sample was prepared by mixing stock CortA and Form I with Starch 1500 so that CortA composed 7% (w/w) of the mixture. The fraction of the CortA in the formulation that was present as Form I (F_I) was 0.56 ± 0.03. The areas of the Form I and II peaks were treated with Equation 4.10 and gave F_I values of 0.66 ± 0.02, 0.61 ± 0.02, and 0.62 ± 0.02 for C-3, C-11, and C-20, respectively. Thus, the results agree very well with the known composition from the mass. However, all of the NMR results where slightly higher than the F_I from the prepared mass, and this may be due to the impact of the Form III that was ignored in the purity calculations or reflect an error in the preparation of the sample, but most likely it is the result of both factors.

In order to limit the errors from mixing the physical forms, another sample was prepared in which the stock CortA was simply diluted in the Starch 1500. The sample was prepared with a CortA content of 2% (w/w) to test the method in situations of very low drug loading. The stock CortA was previously determined to have a F_I of 0.15 ± 0.02 based on a different SSNMR method. When the peaks of the 2% CortA formulation spectrum were analyzed (Figure 4.17) the C-3, C-11, and C-20 peaks gave F_I values of 0.143 ± 0.007, 0.130 ± 0.007,

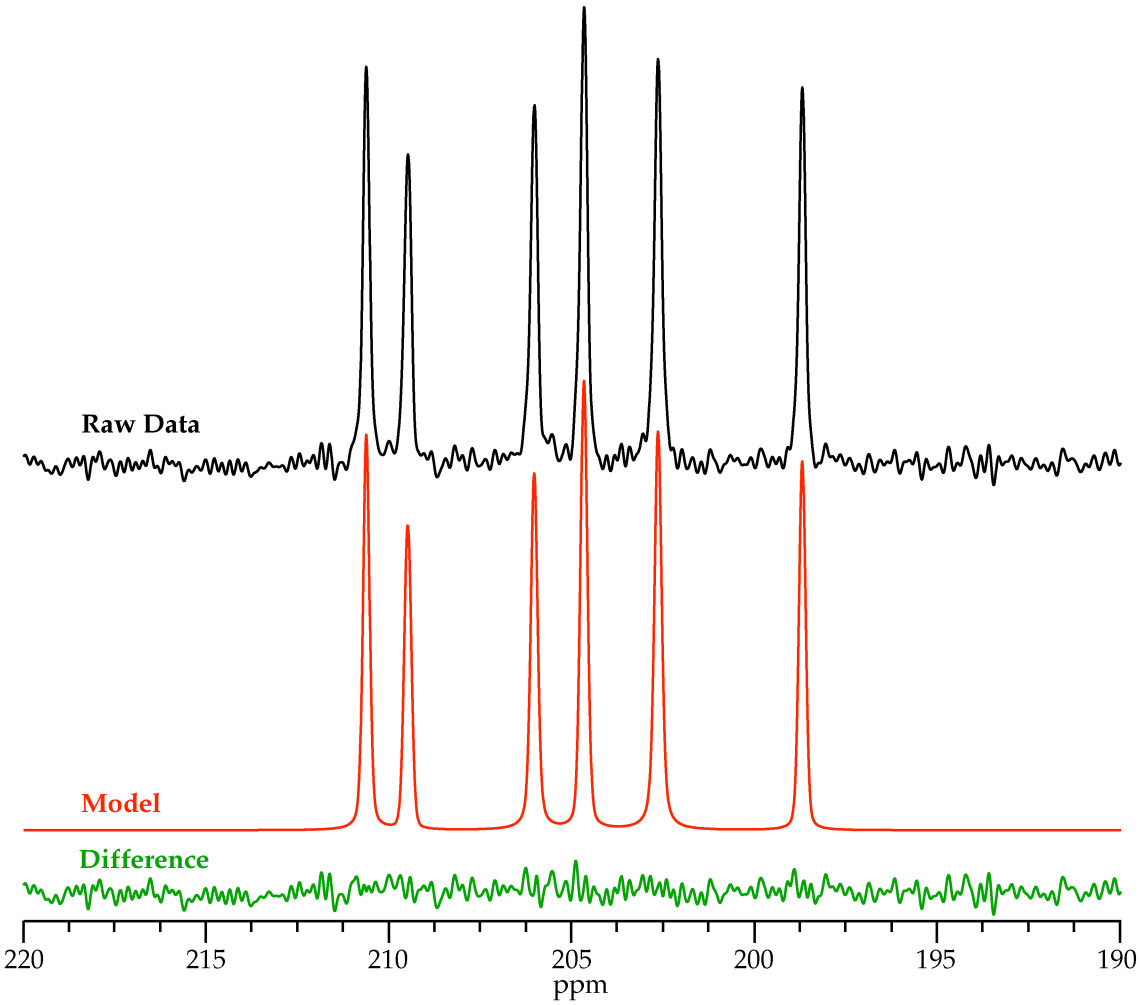

Figure 4.16. ^{13}C CPMAS spectra of the 7% CortA formulation, expanded to show the peaks of C-3, C-11, and C-20 (Figure 4.13).[31] The spectrum is shown in **black,** the deconvolution model is shown in **red**, and the difference between the spectrum and model is shown in **green**. No peaks of Form III were observed in the spectrum.[31] The S/N of all of the peaks are between 25 and 38.

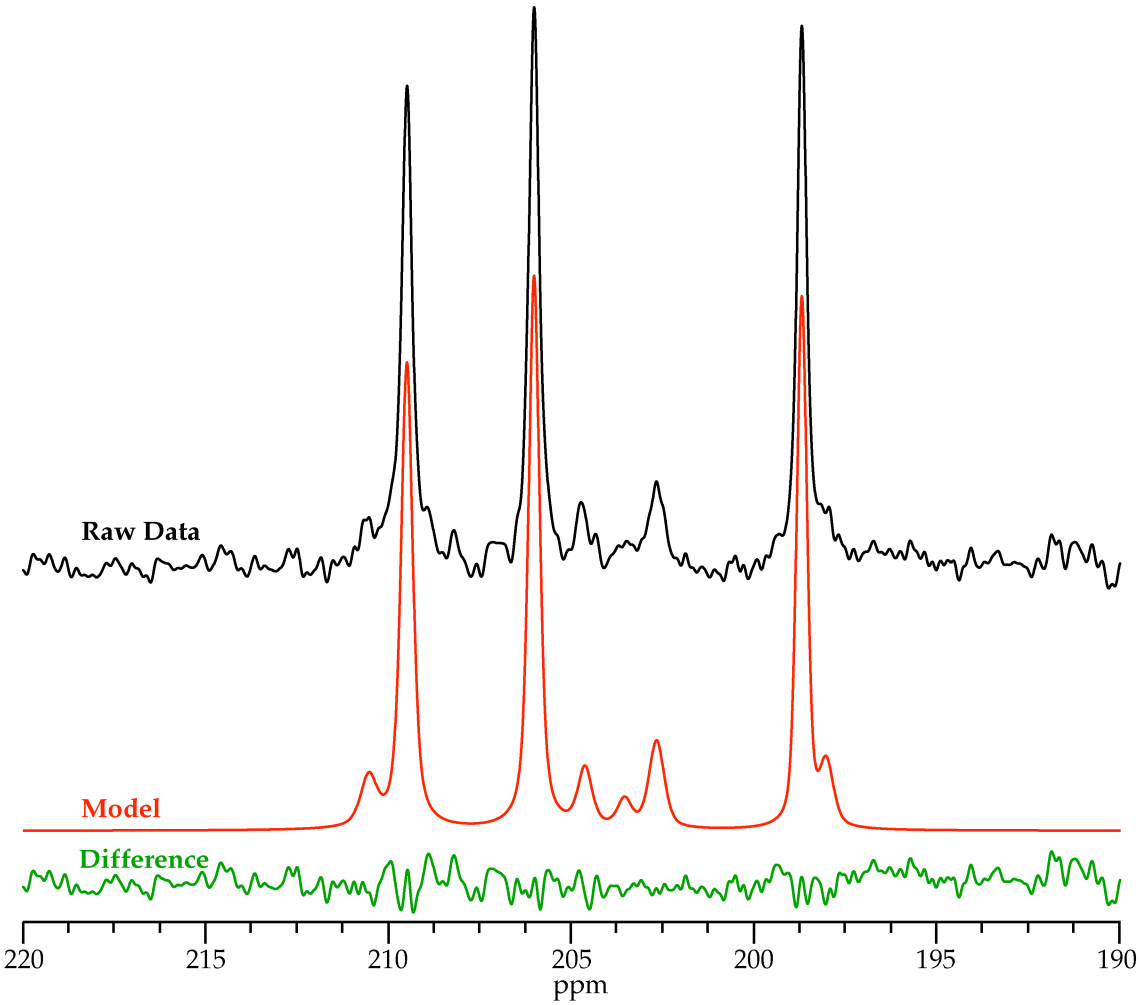

Figure 4.17. ^{13}C CPMAS spectra of the 2% CortA formulation, expanded to show the peaks of C-3, C-11, and C-20 (Figure 4.13).[31] The spectrum is shown in **black,** the deconvolution model is shown in **red**, and the difference between the spectrum and model is shown in **green**. The deconvolution model was improved by the inclusion of peaks at 203.6 and 198.0 ppm, which correspond to the peaks of Form III in Figure 4.15. The FID was treated with 10 Hz of exponential apodization prior to Fourier transformation. The S/N of the peaks at 198.7 and 202.7 ppm are 32.5 and 5.5, respectively.

and 0.134 ± 0.007 for C-3, C-11, and C-20, respectively. Additionally, the spectrum of the 2% formulation in Figure 4.17 does not show any clearly resolved peaks for Form III; however, when the deconvolution model was fit to the data it was clearly improved by the addition of the peaks at 203.5 and 198.0 ppm, which are consistent with peaks that have been observed for Form III (Figure 4.15).[31]

Thus, this approach of performing relative quantitation of physical forms of APIs within formulations appears to quite accurate. In addition, traditional quantitative SSNMR methods required the measurement of ^{1}H T_1 values to ensure that the materials are allowed to relax fully between transients; however, this work shows that the data can actually be collected in situations where full relaxation does not occur and the T_1 can simply be included as part of the correction for the CP dynamics and TOSS.

4.4 Summary

This chapter has addressed the reproducibility and uncertainty of variousNMR measurements and properties including the reproducibility of signal intensities and relaxation measurements. This work demonstrates that, in SSNMR, signal averaging supplements replicates as a method for reducing the uncertainty in measurements. The collection of many transients to obtain the FID acts to increase the absolute signal and results in a relative reduction in the size of the noise.

It was shown that performing a measurement (spectrum, relaxation rate, etc.) very well once is comparable or better than repeating the measurement

multiple times with data that is of lower quality. This may prevent the direct observation of the uncertainty of the measurement. But, in these cases, indirect measures such as the error of a nonlinear regression to determine a relaxation rate, may offer a good relative measure of the uncertainty.

Additionally, the quantitation method of Apperley et al.[29] was extended to a more general case (Equation 4.10), which may be simplified when the properties of physical forms are very similar. This method also allows the duration between transient to be shortened relative to "traditional" quantitative methods and can lead to a sensitivity enhancement of ~44% without increasing the total experiment duration. It was possible to apply this method to a formulation of CortA and obtain quantitative information on a component that made up <0.3% of the entire sample, and it suggested the presence of Form III would be present at levels of ~0.1%. These results are much better than can be achieved with traditional SSNMR quantitative methods and other solid-state characterization techniques, particularly for formulated APIs.

4.5 References

1. Joshi BK, Ramsey B, Johnson B, Patterson DE, Powers J, Facchine KL, Osterhout M, Leblanc MP, Bryant-Mills R, Copley RCB, Sides SL 2010. Elucidating the pathways of degradation of denagliptin. J Pharm Sci 99(7):3030-3040.

2. Olson DL, Norcross JA, O'Neil-Johnson M, Molitor PF, Detlefsen DJ, Wilson AG, Peck TL 2004. Microflow NMR: concepts and capabilities. Anal Chem 76(10):2966-2974.

3. Pan C, Liu F, Motto M 2011. Identification of pharmaceutical impurities in formulated dosage forms. J Pharm Sci 100(4):1228-1259.

4. Malz F, Jancke H 2005. Validation of quantitative NMR. J Pharm Biomed Anal 38(5):813-823.

5. Rizzo V, Pinciroli V 2005. Quantitative NMR in synthetic and combinatorial chemistry. J Pharm Biomed Anal 38(5):851-857.

6. Bekiroglu S, Myrberg O, Ostman K, Ek M, Arvidsson T, Rundlöf T, Hakkarainen B 2008. Validation of a quantitative NMR method for suspected counterfeit products exemplified on determination of benzethonium chloride in grapefruit seed extracts. J Pharm Biomed Anal 47(4-5):958-961.

7. Vogt F 2010. Evolution of solid-state NMR in pharmaceutical analysis. Future Medicinal Chemistry 2(6):915-921.

8. Apperley DC, Forster AH, Fournier R, Harris RK, Hodgkinson P, Lancaster RW, Rades T 2005. Characterisation of indomethacin and

nifedipine using variable-temperature solid-state NMR. Magnetic Resonance in Chemistry 43(11):881-892.

9. Aso Y, Yoshioka S 2006. Molecular mobility of nifedipine-PVP and phenobarbital-PVP solid dispersions as measured by 13C-NMR spin-lattice relaxation time. J Pharm Sci 95(2):318-325.

10. Aso Y, Yoshioka S, Kojima S 2001. Explanation of the crystallization rate of amorphous nifedipine and phenobarbital from their molecular mobility as measured by 13C nuclear magnetic resonance relaxation time and the relaxation time obtained from the heating rate dependence of the glass transition temperature. J Pharm Sci 90(6):798-806.

11. Barich DH, Davis JM, Schieber LJ, Zell MT, Munson EJ 2006. Investigation of solid-state NMR line widths of ibuprofen in drug formulations. J Pharm Sci 95(7):1586-1594.

12. Guilbaud J-B, Baker H, Clark BC, Meehan E, Khimyak YZ 2009. Effect of encapsulating arginine containing molecules on PLGA: A solid-state NMR study. J Pharm Sci 99(6):2697-2710.

13. Murphy BJ, Huang J, Casteel MJ, Cobani A, Krzyzaniak JF 2010. Varenicline L-tartrate crystal forms: Characterization through crystallography, spectroscopy, and thermodynamics. J Pharm Sci 99(6):2766-2776.

14. Nishiwaki A, Watanabe A, Higashi K, Tozuka Y, Moribe K, Yamamoto K 2009. Molecular states of prednisolone dispersed in folded sheet mesoporous silica (FSM-16). Int J Pharm 378(1-2):17-22.

15. Vogt FG, Clawson JS, Strohmeier M, Edwards AJ, Pham TN, Watson SA 2009. Solid-State NMR Analysis of Organic Cocrystals and Complexes. Crystal Growth & Design 9(2):921-937.

16. Vogt FG, Dell'Orco PC, Diederich AM, Su Q, Wood JL, Zuber GE, Katrincic LM, Mueller RL, Busby DJ, Debrosse CW 2006. A study of variable hydration states in topotecan hydrochloride. J Pharm Biomed Anal 40(5):1080-1088.

17. Booy K-J, Wiegerinck P, Vader J, Kaspersen F, Lambregts D, Vromans H, Kellenbach E 2005. The use of 13C labeling to enhance the sensitivity of 13C solid-state CPMAS NMR to study polymorphism in low dose solid formulations. J Pharm Sci 94(2):458-463.

18. Lee G, Craig D, Kannangara GS, Dawson M, Conn C, Robertson J, Wilson M 1999. Analysis of 3,4-methylenedioxy-N-methylamphetamine (MDMA) in "Ecstasy" tablets by 13C solid state nuclear magnetic resonance (NMR) spectroscopy. Journal of Forensic Sciences 44(4):761–771.

19. Saindon PJ, Cauchon N, Sutton PA, Chang CJ, Peck GE, Byrn SR 1993. Solid-state nuclear magnetic resonance (NMR) spectra of pharmaceutical dosage forms. Pharm Res 10(2):197-203.

20. Gao P 1996. Determination of the composition of delavirdine mesylate polymorph and pseudopolymorph mixtures using 13C CP/MAS NMR. Pharm Res 13(7):1095-1104.

21. Offerdahl TJ, Salsbury JS, Dong Z, Grant DJW, Schroeder SA, Prakash I, Gorman EM, Barich DH, Munson EJ 2005. Quantitation of crystalline and amorphous forms of anhydrous neotame using 13C CPMAS NMR spectroscopy. J Pharm Sci 94(12):2591-2605.

22. Tozuka Y, Ito A, Seki H, Oguchi T, Yamamoto K 2002. Characterization and quantitation of clarithromycin polymorphs by powder X-ray diffractometry and solid-state NMR spectroscopy. Chem Pharm Bull 50(8):1128–1130.

23. Vickery R, Nemeth G, Maurin M 2002. Solid-state carbon NMR characterization of the polymorphs of roxifiban. J Pharm Biomed Anal 30(1):125–129.

24. Stephenson G, Forbes RA, Reutzel-Edens SM 2001. Characterization of the solid state: quantitative issues. Adv Drug Delivery Rev 48(1):67-90.

25. Suryanarayanan R, Wiedmann T 1990. Quantitation of the relative amounts of anhydrous carbamazepine (C15H12N2O) and carbamazepine dihydrate (C15H12N2O.2H2O) in a mixture by solid-state nuclear magnetic resonance (NMR). Pharm Res 7(2):184–187.

26. Lefort R, De Gusseme A, Willart J, Danede F, Descamps M 2004. Solid state NMR and DSC methods for quantifying the amorphous content in solid dosage forms: an application to ball-milling of trehalose. Int J Pharm 280(1-2):209–219.

27. Dybowski C 2006. Analytical aspects of solid-state NMR spectroscopy. Mod Magn Reson 1:385–390.

28. Zell MT, Padden BE, Grant DJW, Schroeder SA, Wachholder K, Prakash I, Munson EJ 2000. Investigation of polymorphism in aspartame and neotame using solid-state NMR spectroscopy. Tetrahedron 56(36):6603–6616.

29. Apperley DC, Harris RK, Larsson T, Malmstrom T 2003. Quantitative nuclear magnetic resonance analysis of solid formoterol fumarate and its dihydrate. J Pharm Sci 92(12):2487-2494.

30. Carless JE, Moustafa MA, Rapson HDC 1966. Cortisone acetate crystal forms. J Pharm Pharmacol 18(Supplement):190S-197S.

31. Harris RK, Kenwright A, Say B, Yeung R, Fletton R, Lancaster RW, Hardgrove G 1990. Cross-polarization/magic-angle spinning NMR studies of polymorphism: Cortisone acetate. Spectrochimica Acta Part A: Molecular Spectroscopy 46(6):927–935.

32. Torchia DA 1978. The measurement of proton-enhanced carbon-13 T1 values by a method which suppresses artifacts. J Mag Res 30:613-616.

33. Farrar TC 1970. Pulsed and Fourier transform NMR spectroscopy. Anal Chem 42(4):109A-112A.

34. Traficante DD 1991. Time averaging. Does the noise really average toward zero? Concepts in Magnetic Resonance 3(2):83-87.

35. Isbester PK, PhD Dissertation, *Development of an isolated flow variable-temperature magic-angle spinning (MAS) nuclear magnetic resonance (NMR) probe for hetereogeneous catalysis studies and high-temperature high-speed 19F MAS NMR techniques applied to fluoropolymers*. University of Minnesota, 1999, pp 179.

36. Lubach JW, Xu D, Segmuller BE, Munson EJ 2007. Investigation of the effects of pharmaceutical processing upon solid-state NMR relaxation times and implications to solid-state formulation stability. J Pharm Sci 96(4):777-787.

37. Wemmer DE, PhD Dissertation, *Some double resonance and multiple quantum NMR studies in solids*. University of California, Berkeley, 1979, pp 293.

38. Kolodziejski W, Klinowski J 2002. Kinetics of cross-polarization in solid-state NMR: a guide for chemists. Chem Rev 102(3):613-628.

Chapter 5

Comparison of Physical Form Quantitation by Solid-State Characterization Techniques

5.1 Introduction

The specific aim of this chapter is to utilize the quantitative SSNMR method that was developed in the previous chapter and compare its performance against other common techniques. This analysis will involve mixtures of physical forms of an API in both pure API and a 10% (w/w) formulation. The application of all of these common techniques to the same set of samples should allow a more direct comparison of the techniques than has typically been available for such characterization.

Various solid-state characterization techniques have been used to quantify polymorphs for both pure API and formulated products. Often times, these studies focus on the application of one or two methods to the system that is being investigated. In other cases, a model compound may be chosen to demonstrate a particular technique. Additionally, some studies have been able to demonstrate extremely low levels of detection and quantification by utilizing non-standard equipment, such as synchrotron sources for PXRD.[1]

There is also no universal method for reporting the quality of the models that are used to quantify physical forms of pharmaceuticals. In some cases, a limit-of-detection (LOD) and limit-of-quantification (LOQ) are reported. In other cases the statistics that are obtained from the generation of a multivariate model are reported. Also, unlike quantitative analysis in solution, where the samples are homogeneous, solids are inherently inhomogeneous and the quality of the samples will also impact the results.[2,3] Therefore, a broad comparison of the techniques across all of the studies is difficult. However, it has been possible to generally conclude that most techniques can be applied to the analysis of pure

API and generally yield LODs and LOQs of approximately 1–2% and 3–5%, respectively. Formulated materials are significantly more challenging due to the presence of the excipients which often overlap with signals from the API physical forms. Therefore, quantitative analysis of formulated materials is typically accomplished with PXRD or Raman spectroscopy and generally have LODs and LOQs of approximately 5 and 10%, respectively, and vary by physical form.

The approach here is to develop basic quantitative methods for the most common solid-state characterization techniques: DSC, TGA, PXRD, and Raman spectroscopy. In addition, the SSNMR quantitation method will be used in order to compare its performance against the other techniques. The methods will then be applied to two systems, one consisting of binary mixtures of a pure API and the other containing the same binary blends of API diluted in excipients to simulate a formulation.

Norfloxacin (Figure 5.1) was chosen as the model API because it could be readily obtained in sufficient quantities for the study. It was also possible to generate two relatively stable physical forms. The molecule also contains fluorine, which will allow the comparison of both ^{13}C and ^{19}F SSNMR, and a methyl group that should result in relatively short NMR relaxation times. Drug loadings in a formulation can range from a few percent for potent compounds, to >20% when large doses are required. Therefore a 10% (w/w) drug loading was selected and lactose, microcrystalline cellulose, sodium alginate, and magnesium stearate were chosen to compose the remainder of the formulation because they are routinely used as excipients. The relative amounts of each of the excipients were selected to simulate their typical levels within a formulation.

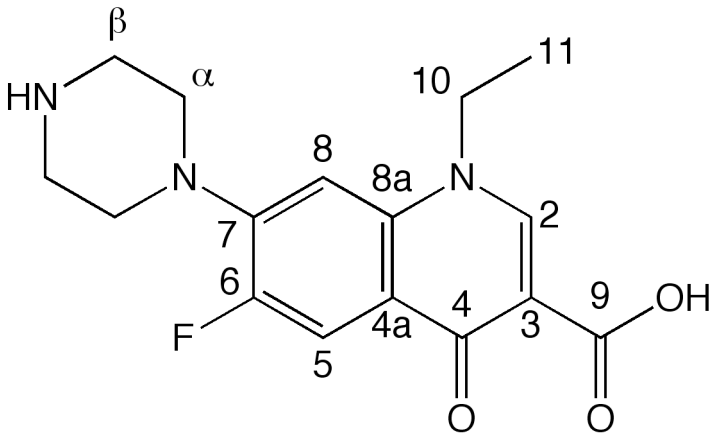

Figure 5.1. Chemical structure of norfloxacin with carbon numbering scheme from Barbas et al.[4,5]

5.2 Experimental

5.2.1 Materials

Norfloxacin, magnesium stearate, microcrystalline cellulose (Avicel ® PH-101, Fluka), and sodium alginate (alginic acid sodium salt, from brown algae, viscosity of 2% solution at 25 °C: 250 cps) were purchased from Sigma-Aldrich (St. Louis, MO). Foremost® #310 Regular NF Lactose monohydrate was obtained from Foremost Farms (Baraboo, WI).

Norfloxacin Form A was produced by drying stock material at 80 °C, under vacuum, for 4 hours after which the oven was turned off and left overnight to return to room temperature. Approximately 150 mL of N,N-dimethyl formamide (DMF) was added to 15.5 g of the norfloxacin Form A. Seed crystals of norfloxacin Form B, which were generated by suspending approximately 200 mg of norfloxacin in 10 mL of DMF for 6 months, were added to the DMF suspension and the mixture was stirred at room temperature for a week to convert all of the norfloxacin to Form B. The norfloxacin Form B was recovered by vacuum filtration and then was dried according to the same drying procedure outlined above (80 °C for 4 hours under vacuum), lightly ground in a mortar and pestle and then dried overnight at 40 °C, under vacuum.

Norfloxacin mixtures were produced in order to generate calibration curves and to test the calibrations. Each mixture had a total mass of approximately 1 g and consisted of either only norfloxacin or 10% (w/w) norfloxacin in placebo. The placebo consisted of α-lactose monohydrate, microcrystalline cellulose, sodium alginate, and magnesium stearate in sufficient

quantities such that when mixed with norfloxacin they would make up 75, 10, 4, and 1% (w/w), respectively. The samples consisting of only norfloxacin were generated by mixing norfloxacin Forms A and B such that the samples contained either 0, 1, 2.5, 5, 10, 20, 40, 60, 80, 90, 95, 97.5, 99, or 100% (w/w) Form A. The 10% norfloxacin formulations all contained the same relative concentration of norfloxacin, but it was present as different physical forms. In these formulations the relative Form A composition was the same as the previously described binary blends of Form A and B. In addition, five binary blends and five 10% (w/w) norfloxacin formulations were generated to act as "unknown" samples, in order to test the calibration curves.

5.2.2 DSC

A Q100 DSC from TA Instruments (New Castle, DE) with a refrigerated cooling system was utilized to characterize all of the materials and the quantitation mixtures. In all cases approximately 4 to 10 mg of material was placed in DSC pan for the analysis. The placebo blend and norfloxacin were analyzed by heating from -80 to 235 °C at a rate of 10 °C/min. All of the calibration mixtures and "unknowns" were analyzed in triplicate and were held at 150 °C for 2 min. and then were heated to 235 °C at 10 °C/min. All samples were analyzed in a dry nitrogen atmosphere (N_2 flow rate = 50 mL/min). Two processing methods, signal change and peak integration, were applied to the DSC thermographs. The signal change was the difference in the heat flow signal 190 and 200 °C. The peak integration method was performed by applying a sigmoidal horizontal integration from 190 to 227 °C. Divisions were then placed

at 214 and 216 °C to subdivide the integration into three peaks.

5.2.3 TGA

All of the materials and quantitation mixtures were analyzed by TGA (Q50 TGA from TA Instruments, New Castle, DE). Approximately 4 to 10 mg of each sample was placed in platinum pans under a dry nitrogen atmosphere (total N_2 flow rate = 100 mL/min). The placebo blend and norfloxacin were heated from room temperature to 300 °C at a rate of 10 °C/min. All of the calibration mixtures and "unknowns" were analyzed in triplicate and were held at 150 °C for 2 min. and then were heated to 250 °C at 10 °C/min. The TGA thermographs were analyzed by measuring the percent weight loss between 170 and 220 °C.

5.2.4 PXRD

PXRD patterns were collected on a Bruker D8a series XRD instrument where the sample was rotated at 30 times per min during data acquisition. Reference diffraction patterns of placebo and norfloxacin Forms A and B were collected from 3 to 40 °2θ with a step size of 0.020 °2θ/step and 4 sec/step. The calibration mixtures and the "unknowns" were analyzed in triplicate and the diffraction patterns were collected from 9 to 26 °2θ with a step size of 0.010 °2θ/step and 4 sec/step. The divergence, anti-scatter, absorbance, detector, and monochrometer slits were set to 1.0, 0.6, 6.0, 0.6, and 0.6 mm, respectively. Data processing and analysis was performed with The Unscrambler (see section 5.2.9).

5.2.5 FT-Raman Spectroscopy

FT-Raman spectra were collected on an NXR 9650 FT-Raman spectrometer (Nicolete 6700 FT-IR outfitted with an FT-Raman module) with a liquid nitrogen cooled germanium detector and a Nd:YVO_4 laser (1064 nm). All spectra were the result of 100 scans collected with 4 cm^{-1} resolution. The calibration mixtures and "unknowns" were collected in triplicate with a laser power at the sample of 0.5 and 1.0 W, respectively. Samples were loaded into NMR tubes and rotated during data acquisition. The NMR tubes were inverted multiple times between acquisitions to generate the replicates. Only one binary norfloxacin calibration mixture (20% Form A) was analyzed by preparing three independent NMR tubes. Data processing and analysis was performed with The Unscrambler (see section 5.2.9).

5.2.6 PhAT Probe Raman Spectroscopy

Dispersive Raman spectra were collected with a Raman Rxn System from Kaiser Optical Systems, Inc. The instrument consisted of a PhAT probe with a 6 mm spot size and a 785 nm laser set to 400 mW. The system was calibrated for both wavelength and intensity with the provided calibration accessory and cyclohexane. All spectra were collected with dark subtraction and intensity calibration, but no cosmic ray filtering was used. A total of 24 exposures, each with an exposure time of 5 sec, were collected and all 10 channels of the detector were summed together to yield each spectrum. The calibration mixtures and "unknowns" were each subjected to six replicates each and the sample was agitated between each replicate. Data processing and analysis was performed with The Unscrambler (see section 5.2.9).

5.2.7 ^{13}C SSNMR Spectroscopy

^{13}C SSNMR data was collected on a Tecmag (Houston, TX) 300 MHz (^{1}H resonance frequency) spectrometer with a custom built probe. The probe consisted of two spin modules and was designed to allow two samples to be analyzed simultaneously. Samples were packed into 7 mm zirconia rotors and held in place with Teflon® end caps (Revolution NMR, Fort Collins, CO). Packed rotors were spun with MAS at a rate of 4.9 kHz in 7 mm spin modules (Revolution NMR, Fort Collins, CO).

The FIDs were collected with ramped amplitude CP sequence with SPINAL-64 decoupling. Placebo and norfloxacin Form A and B FIDs consisted of 2,048, 7,168, and 7,168 transients, respectively, collected with a 6 sec pulse delay and 3 ms contact time. All of the calibration mixtures and unknown samples were analyzed with a pulse delay of 6 sec, a contact time of 6 msec, and utilized 16 "dummy" pulses to ensure steady state conditions. All of the FIDs consist of 1024 points and are the result of between 128 and 1,024 or 6,144 and 43,008 transients for pure norfloxacin and 10% formulations, respectively.

5.2.8 ^{19}F SSNMR Spectroscopy

^{19}F SSNMR studies were performed on the same Tecmag 300 MHz spectrometer, but utilized a traditional probe with only one spin module. Samples were packed into 4 mm zirconia rotors and held in place with Torlon® end caps (Revolution NMR, Fort Collins, CO). Packed rotors were spun with MAS at a rate of 11 kHz in a 4 mm spin module (Revolution NMR, Fort Collins, CO).

The FIDs were collected with ramped amplitude CP sequence with

SPINAL-64 decoupling. Placebo and norfloxacin Form A and B FIDs consisted of 512, 16, and 16 transients, respectively, collected with a pulse delay of 6 to 8 sec and a contact time of 0.5 to 4 ms. All of the calibration mixtures and unknown samples were analyzed with a pulse delay of 6 sec and utilized 16 "dummy" pulses to ensure steady state conditions. Each sample was analyzed with contact times of 4, 6, and 8 msec. All of the FIDs consist of 128 points with a dwell time of 20 μsec and are the result of between 512 and 2,048 or 512 and 4,096 transients for pure norfloxacin and 10% formulations, respectively.

5.2.9 Data Analysis (Multivariate Regression)

Multivariate methods were utilized to perform the quantitative analysis of the data from all of the analytical methods, with the exception of both ^{13}C and ^{19}F SSNMR results. The Unscrambler X version 10.1 from CAMO Software (Oslo, Norway) was utilized to perform both multiple linear regression (MLR) and partial least squares (PLS) analysis. MLR models were subjected to validation by leverage correction. PLS analysis was performed with cross validation in 20 random segments with the number of samples per segment being determined by the total number of samples in the calibration set. The PLS analysis utilized the non-linear iterative partial least squares (NIPALS) algorithm. The Savitzky-Golay (SG) algorithm was used for both smoothing and calculation of 2nd derivatives with 3rd order polynomials and a symmetrical kernel of ±5 points.

5.3 Results & Discussion

5.3.1 Characterization of Materials

Two anhydrous polymorphs of norfloxacin (Form A and Form B) and a placebo, or blend of excipients, were prepared. The DSC thermographs of the materials are shown in Figure 5.2. Form A of norfloxacin showed a single melting endotherm at 220 °C, which was consistent with previous observations.[4,5] However, Form B displays two endotherms at 211 and 221 °C, which correspond to melting of Forms B and A, respectively.[4,5] Additionally, an exothermic event is observed between the melting endotherms and is attributed to crystallization of Form A from the melted material. The thermograph of the placebo displays two prominent endotherms at 145 and 200 °C that are primarily from the α-lactose monohydrate component. The placebo's endotherm at 200 °C could significantly impact the ability to analyze the formulations due to signal overlap of the norfloxacin melting endotherms and placebo signal.

When TGA of the materials was performed (Figure 5.3) an interesting phenomenon was observed. Both Form A and B began to undergo significant mass loss above 220 °C, likely due to degradation. However, Form B exhibited a small but reproducible mass loss between 190 and 210 °C that was not associated with residual DMF. This mass loss was not observed with Form A, thus the measurement of the mass loss over this temperature range might provide quantitative information. The placebo showed mass loss in the same temperature range (mostly attributed to α-lactose monohydrate and sodium alginate), which would likely limit any quantitative information that could be

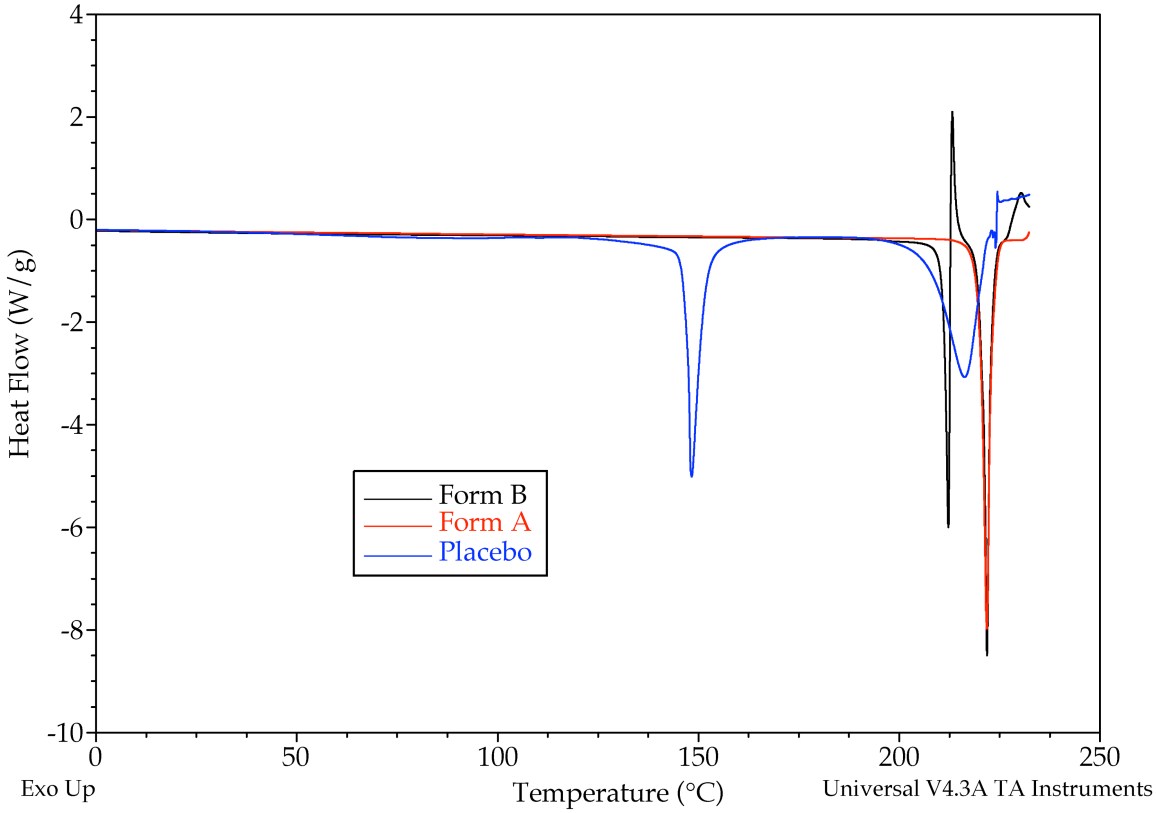

Figure 5.2. DSC thermographs of placebo and norfloxacin Forms A and B. The two endotherms of the placebo are primarily from the α-lactose monohydrate. Form A displays a single endotherm at 220.3 °C. Form B shows an endotherm at 211.0 °C, which was immediately followed by an exotherm and another endotherm at 220.7 °C.

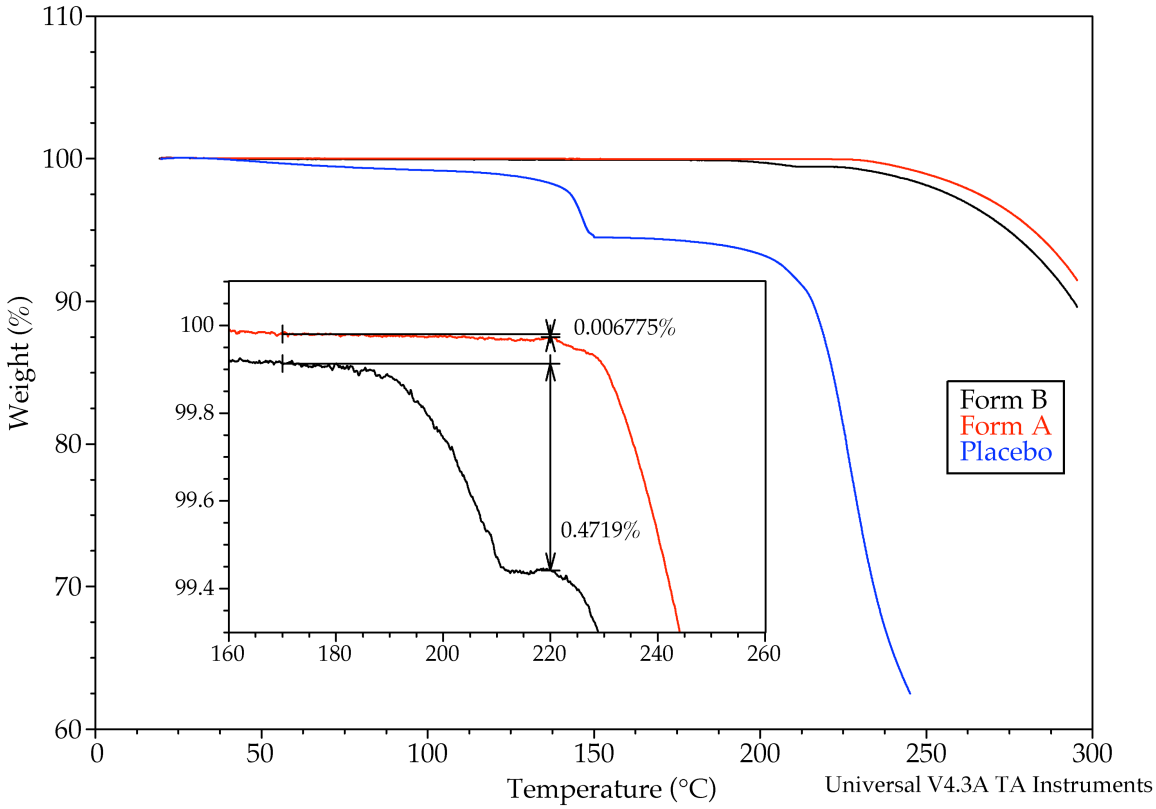

Figure 5.3. TGA thermographs of placebo and norfloxacin Forms A and B. The mass loss at 140–150 °C is from the α-lactose monohydrate, while the loss above 200 °C is due to the lactose and sodium alginate. Both forms of norfloxacin begin to degrade at about 250 °C, but Form B also showed a small mass loss from approximately 190 to 210 °C (see insert).

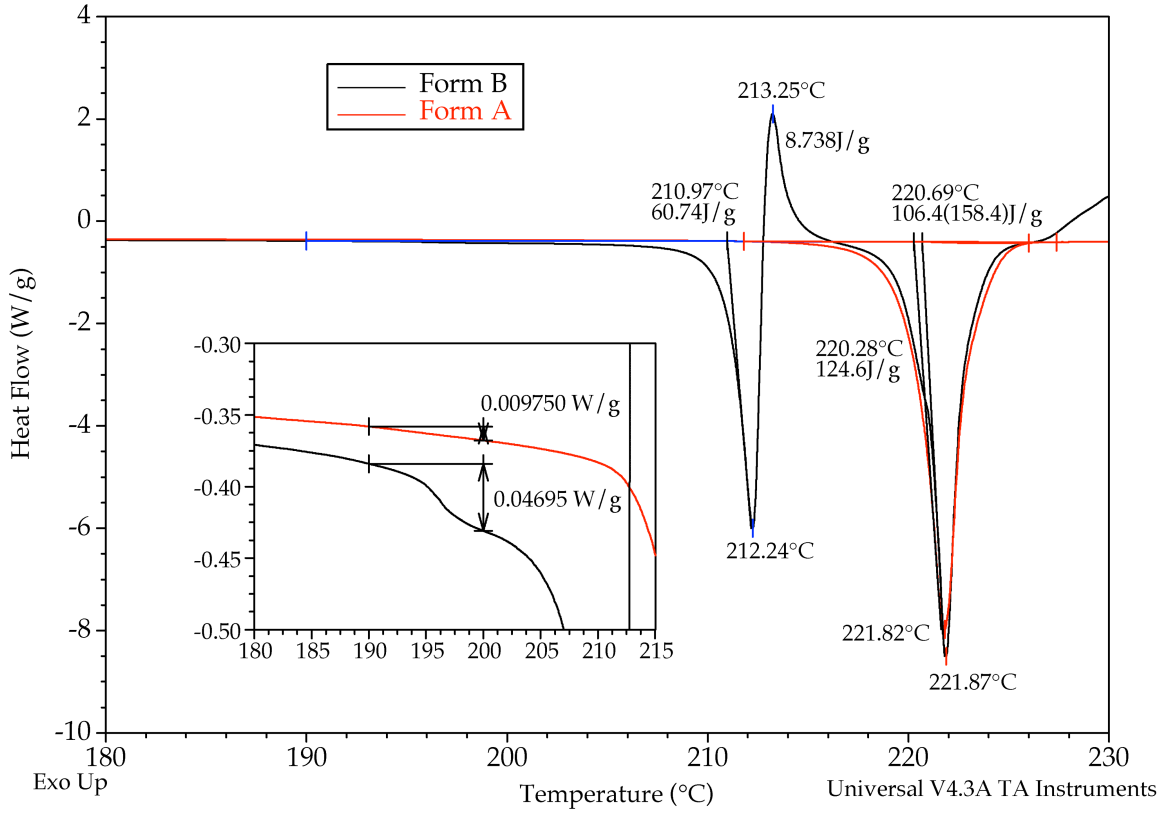

Figure 5.4. Illustration of DSC analysis for quantitation of norfloxacin Forms A and B. The insert shows the signal change method where the difference in the DSC heat flow is measured between 190 and 200 °C. Integration of the Form A melting endotherm resulted in a melting point of 220.3 °C and a heat of fusion of 124.6 J/g. For Form B the entire region from 190 to 227 °C was integrated, the integrated area (158.4 J/g) was then subdivided into three individual peaks. The peaks at 211.0 °C (60.74 J/g), 213.3 °C (8.738 J/g), and 220.7 (106.4 J/g) represented melting of Form B, crystallization of Form A, and melting of Form A, respectively.

obtained from TGA of formulated norfloxacin.

Closer inspection of the DSC thermographs of Forms A and B (Figure 5.4) revealed a small endothermic event just prior to the melting of Form B. This event has previously been attributed to solid-solid conversion of some of the Form B to Form A prior to melting of the remaining Form B.[4] This transition occurs over the same temperature range as the observed Form B mass loss in Figure 5.3. In addition to this event, the crystallization of Form A from the melt during the collection of the DSC thermographs significantly complicates the analysis of the data for quantitative measurements.

Two general approaches to quantitative analysis of the DSC data were adopted (Figure 5.4). The first is demonstrated in the insert of the figure and involves the measurement of the change in the heat flow over the temperature range from 190 to 200 °C. The second involved integration of the entire peak range (190 to 227 °C) which was then divided into three peaks (#1, #2, and #3) representing melting of Form B, crystallization of Form A, and melting of Form A, respectively. The results are demonstrated in Figure 5.4 and yielded integrated areas of 60.7, 8.7, and 106.4 J/g for Peaks #1, #2, and #3, respectively, and a total integrated area of 158.4 J/g. The melting of Form A in both samples occurs at the same temperature, but the heat of fusion is approximately 18 J/g lower for the material that crystallized from the melt of Form B. It is not clear why the two values differ by almost 15% but might indicate that the material did not completely crystallize to Form A.

The PXRD diffraction patterns of norfloxacin Forms A and B (Figure 5.5) are consistent with previous reports with some differences in the relative intensity of the peaks.[4,5] This may indicate that Form B is subject to preferred

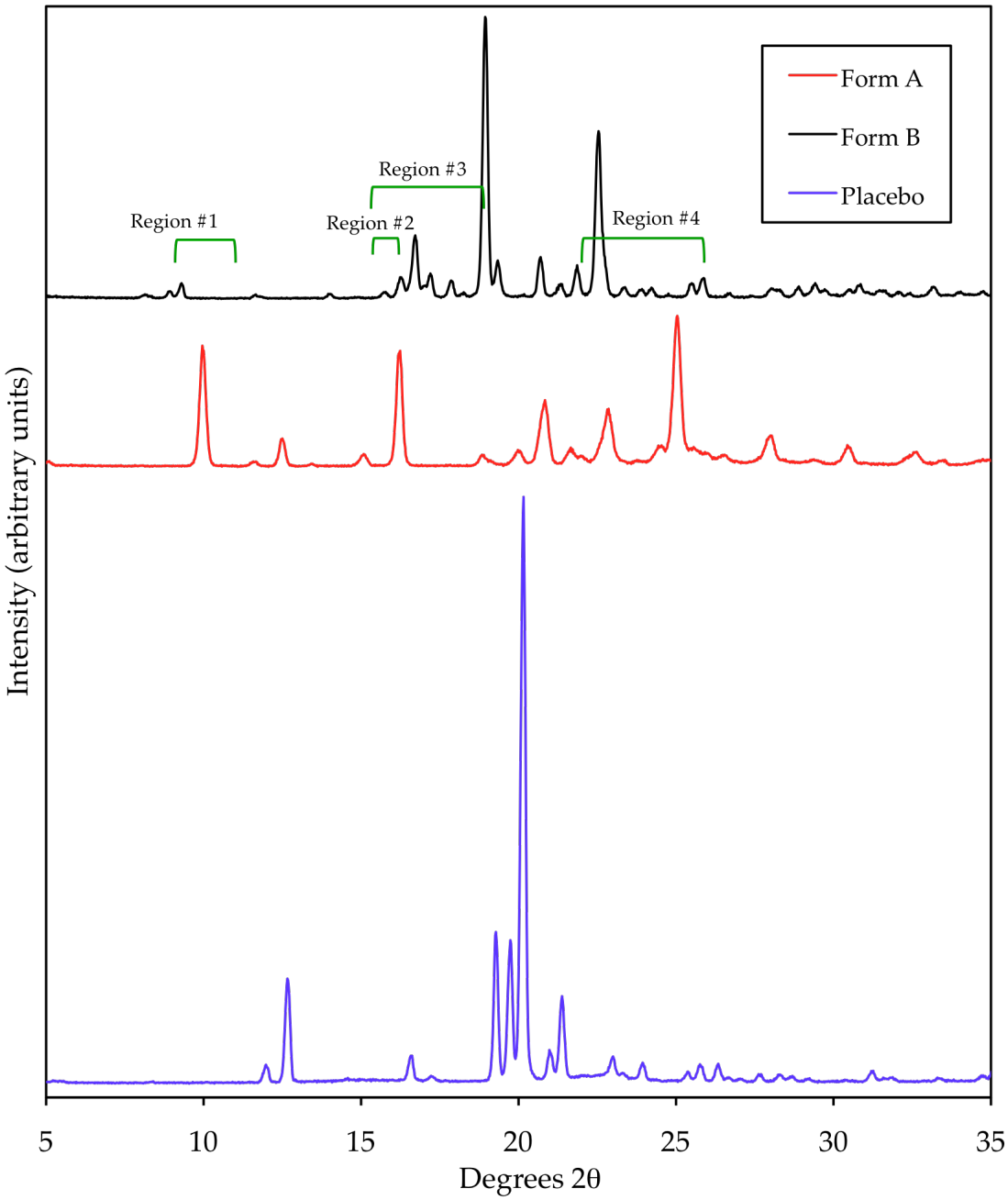

Figure 5.5. PXRD patterns of placebo and norfloxacin Forms A and B. The diffraction peaks of the placebo are primarily from the α-lactose monohydrate. Quantitative analysis was performed on the diffraction pattern from 9 to 26 °2θ or over one of the other regions shown above (#1 9–11 °2θ, #2 15.5–16.3 °2θ, #3 15.5–19 °2θ, and #4 22–26 °2θ).

orientation, but the samples were rotated during the acquisition of the powder patterns to minimize this effect. As with the DSC and TGA, the PXRD patterns are subject to significant overlap of the API and placebo peaks, particularly α-lactose monohydrate. This will likely frustrate the quantitative analysis of the formulations. To minimize the interference of the excipients on the analysis, four regions were selected for quantitative analysis (#1 9–11 °2θ, #2 15.5–16.3 °2θ, #3 15.5–19 °2θ, and #4 22–26 °2θ).

The Raman spectra of the materials are shown in Figure 5.6. The intensity of the Form A and B spectra relative to the placebo indicate that norfloxacin is a strong Raman scatterer compared to the placebo components, which should aid in detection of norfloxacin in the formulations. There is significant overlap of most of the norfloxacin and placebo peaks; however, three regions with no or limited signal overlap were identified. Region #1 is shown in Figure 5.7 (600 to 820 cm^{-1}), and does contain some relatively weak signals from the placebo. The other two regions are shown in Figure 5.8, where Region #2 (1500 to 1760 cm^{-1}) contains no placebo peaks and Region #3 extends over a wider range (1220 to 1760 cm^{-1}) and does contain some weak placebo signals.

The Raman spectra that were collected with the PhAT probe (Figure 5.9) showed very few differences from the FT-Raman spectra (Figure 5.6). The most significant difference is the elevated baseline at lower wavenumbers. This is due to differences in the wavelength of the lasers that are used with each instrument, the lower wavelength of the PhAT probe system (785 vs. 1064 nm) will tend to result in more background due to fluorescence.

The ^{13}C CPMAS spectra of the norfloxacin polymorphs and placebo are

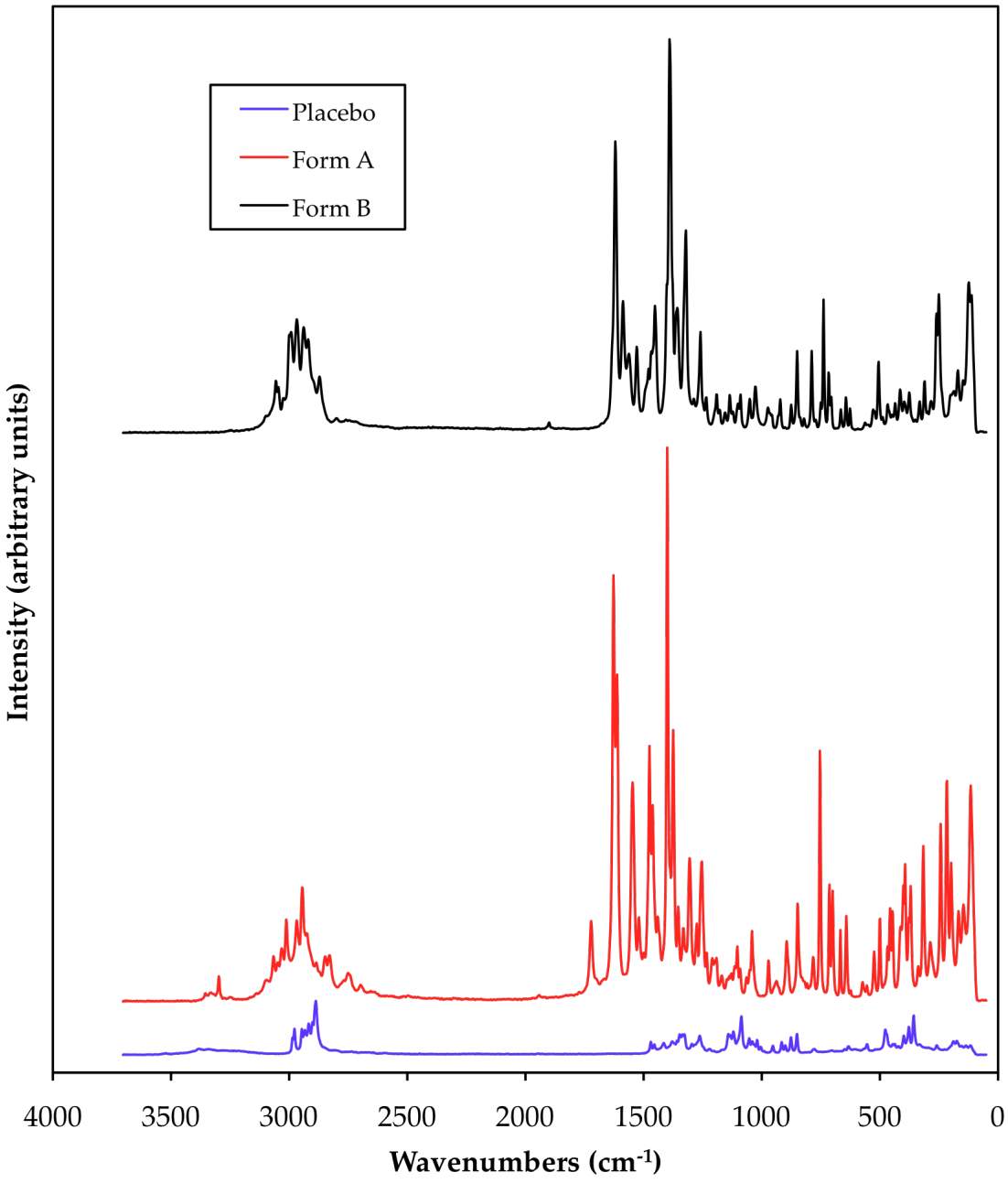

Figure 5.6. FT-Raman spectra of placebo and norfloxacin Forms A and B.

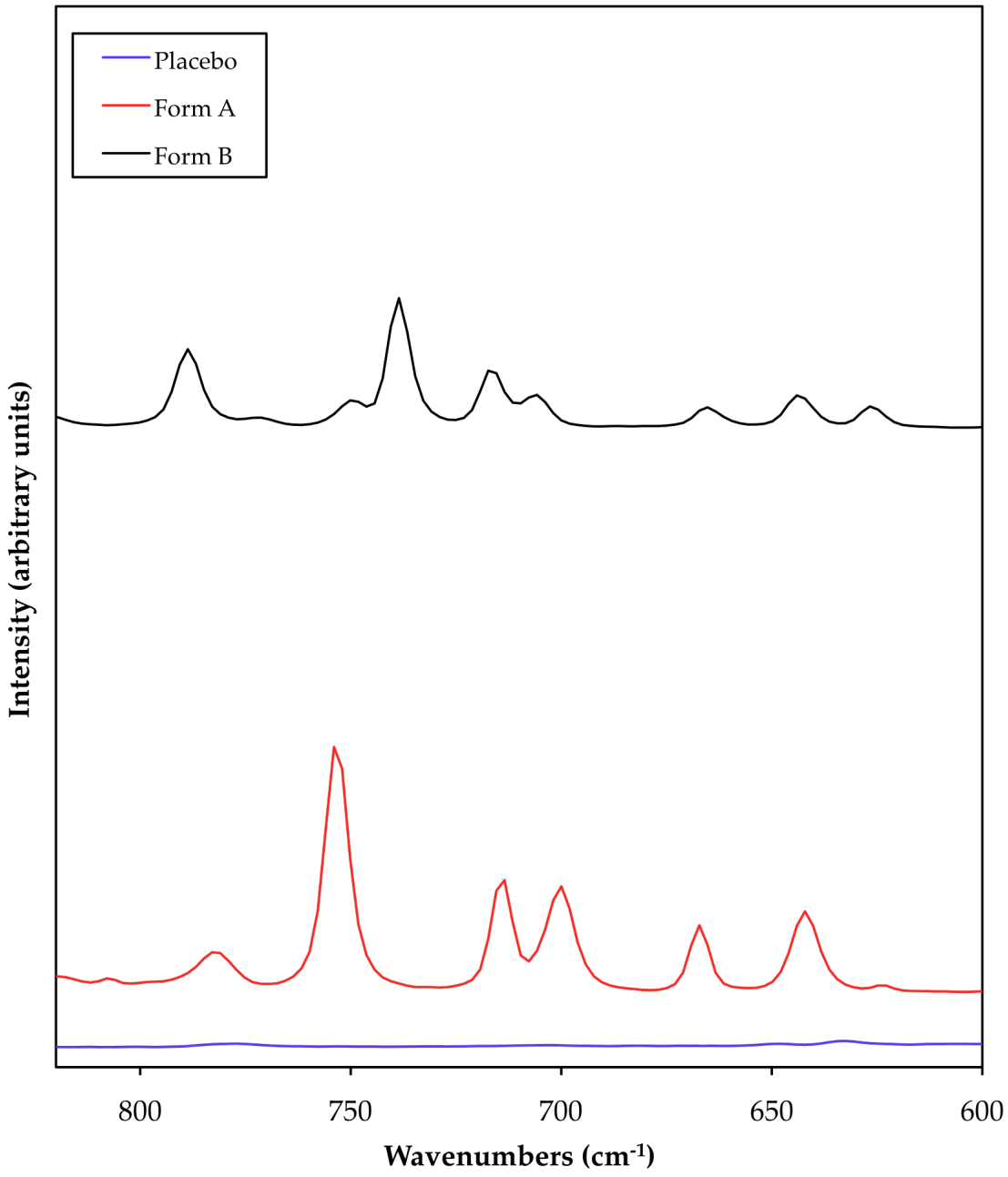

Figure 5.7. FT-Raman spectra of placebo and norfloxacin Forms A and B from Figure 5.6 expanded to show quantitation region #1 (600 to 820 cm^{-1}, region displayed).

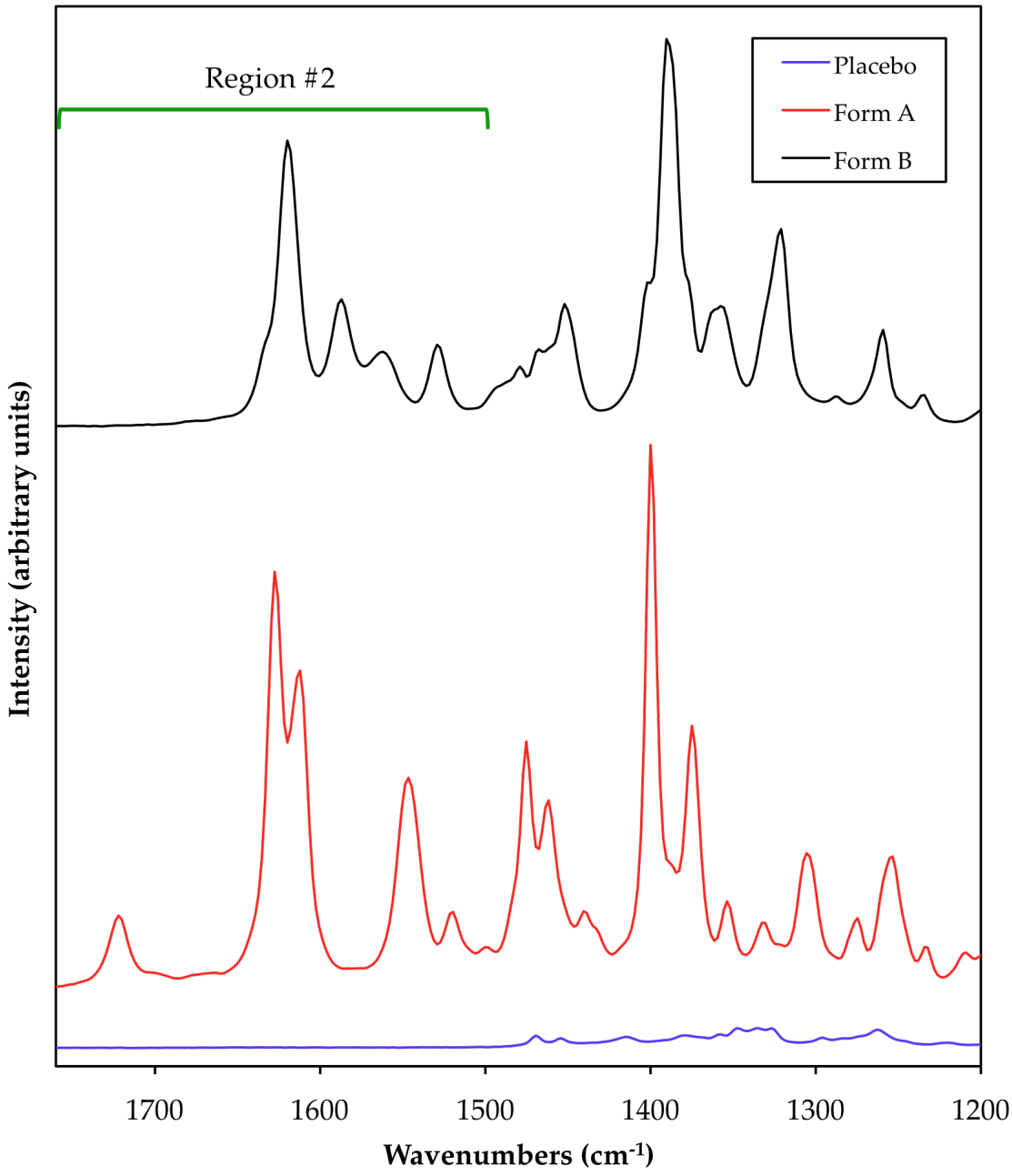

Figure 5.8. FT-Raman spectra of placebo and norfloxacin Forms A and B from Figure 5.6 expanded to show quantitation regions #2 (1500 to 1760 cm^{-1}, indicated on the figure) and #3 (1220 to 1760 cm^{-1}, region displayed).

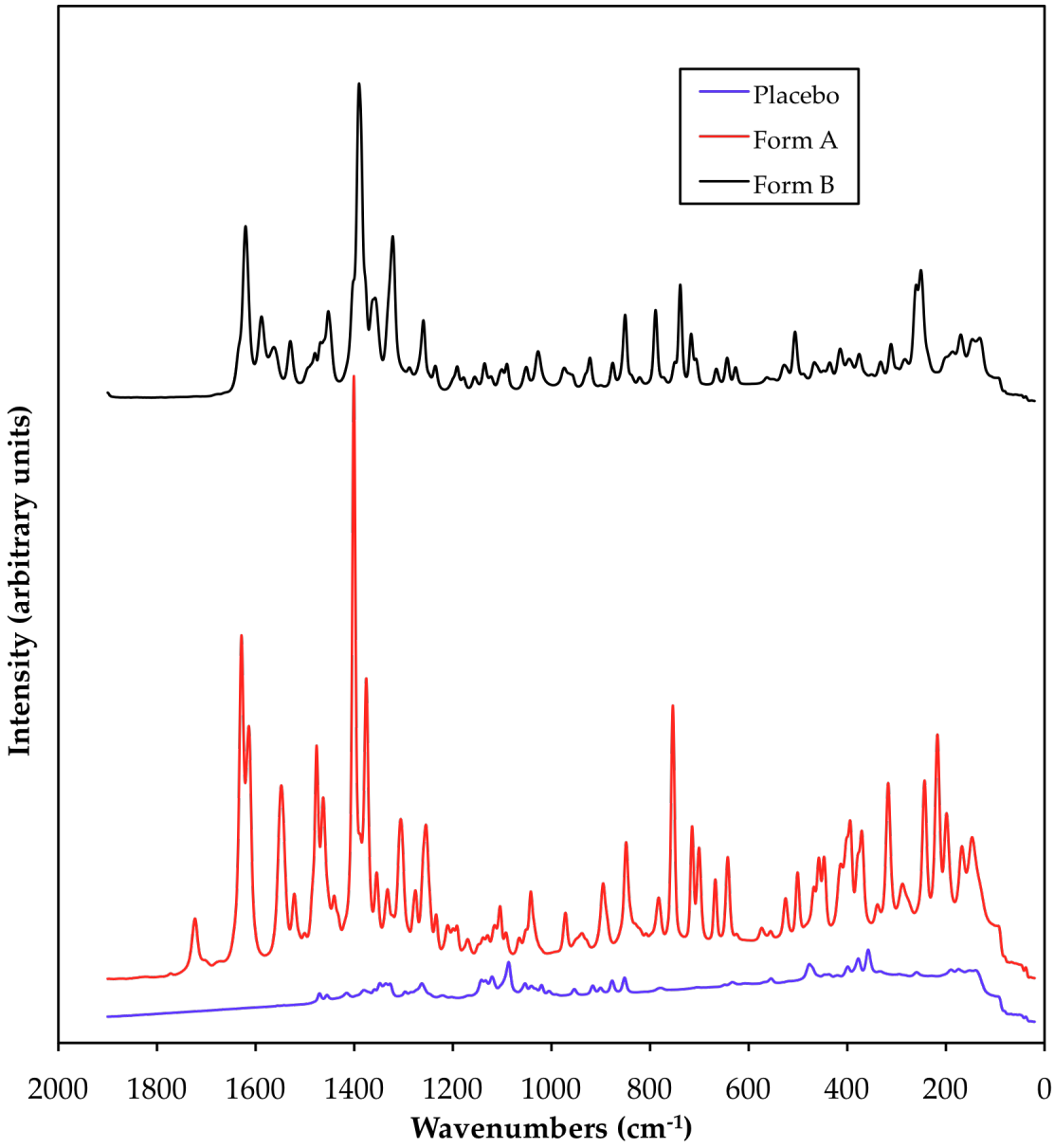

Figure 5.9. Raman spectra of placebo and norfloxacin Forms A and B, collected with a dispersive Raman spectrometer via a PhAT probe.

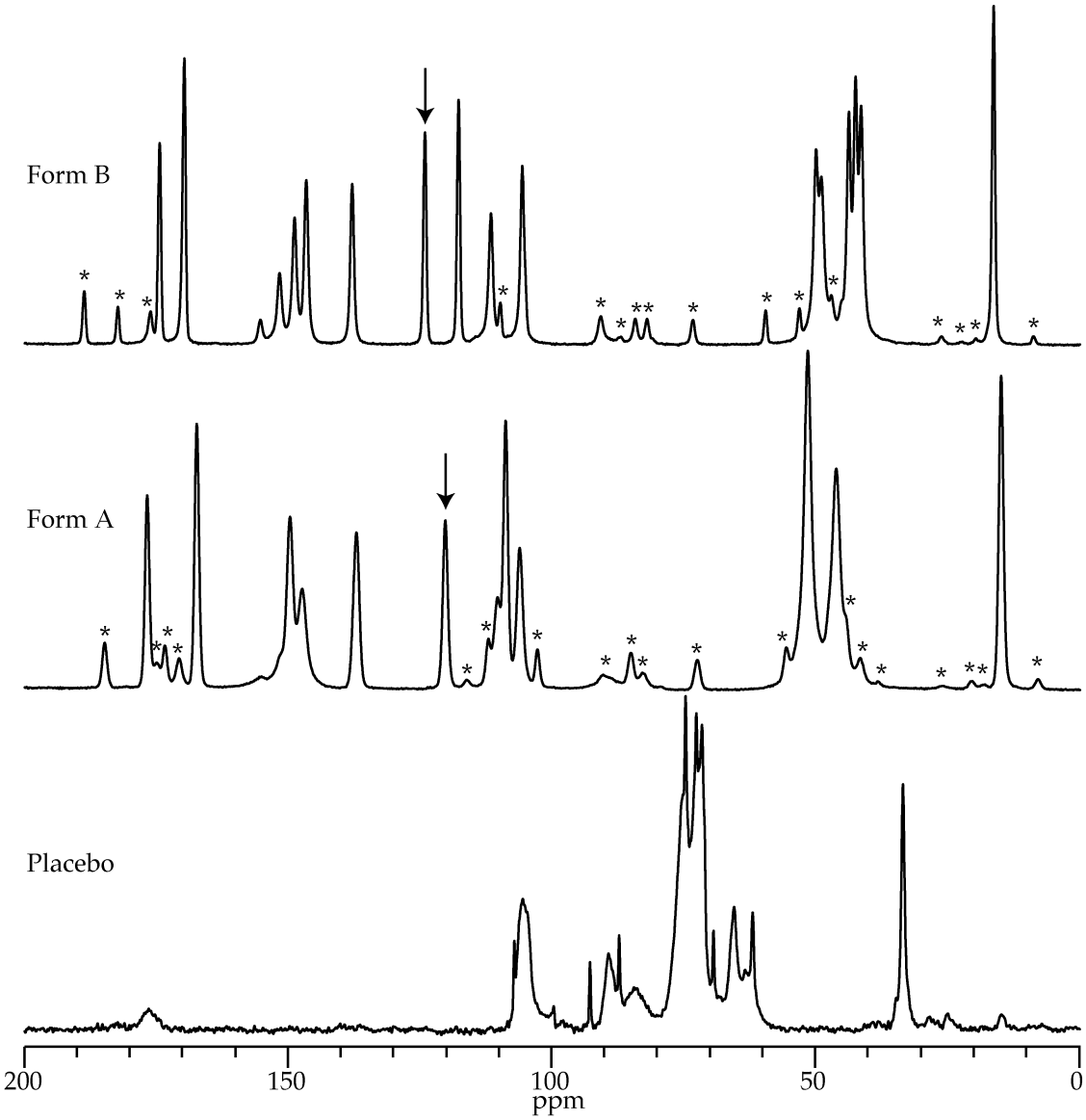

Figure 5.10. ^{13}C CPMAS spectra placebo and norfloxacin Forms A and B. Peaks that were selected for quantitation are marked with arrows (Form B at 124.1 ppm and Form A at 120.3 ppm). The narrow peaks between 60 and 110 ppm in the spectrum of the placebo are from the lactose, but are relatively small due to its long ^{1}H T_1 (~270 sec, Table 4.5) and the short delay between transients (6 sec). * = spinning sidebands

shown in Figure 5.10. The spectra of Forms A and B are consistent with the previously reported chemical shifts of both forms.[4,5] The spectrum of the placebo shows peaks from the different components. The peak at ~43 ppm is due to magnesium stearate while the broad peaks between 60 and 110 ppm are from microcrystalline cellulose and sodium alginate, which also results in the peak at 175 ppm. The relatively narrow peaks between 60 and 110 ppm are due to the α-lactose monohydrate, but while the lactose makes up the majority of the material the signals are relatively small. This demonstrates one of the benefits of SSNMR, depending upon the conditions used to collect the data signals can be suppressed or enhanced relative to one another. The α-lactose monohydrate takes a very long time to fully relax to its equilibrium magnetization (^{1}H T_1 ~270 sec) but the sample was only allowed to relax for approximately 6 sec between transients. In that relatively short amount of time only about 2% of the equilibrium magnetization has been recovered, which results in very weak signals from the lactose in the material. Upon inspection, the peaks for C-4a (Figrue 5.1 and 5.10 indicated by arrows) were selected for quantitation to avoid overlap of norfloxacin and placebo peaks.[4,5] Additionally, an MAS rate of 4.9 kHz was selected to avoid the overlap of spinning side bands with the C-4a peaks.

Since the chemical structure of norfloxacin (Figrue 5.1) contains fluorine, ^{19}F SSNMR can be used to study the norfloxacin forms (Figure 5.11). The spectra demonstrate the distinct advantages of ^{19}F, chiefly the lack of fluorine in most excipients and the dramatically higher sensitivity of ^{19}F as compared to ^{13}C SSNMR. Norfloxacin Form A and B each show one isotropic signal in their ^{19}F CPMAS spectra, due to the presence of only one fluorine atom in the molecule

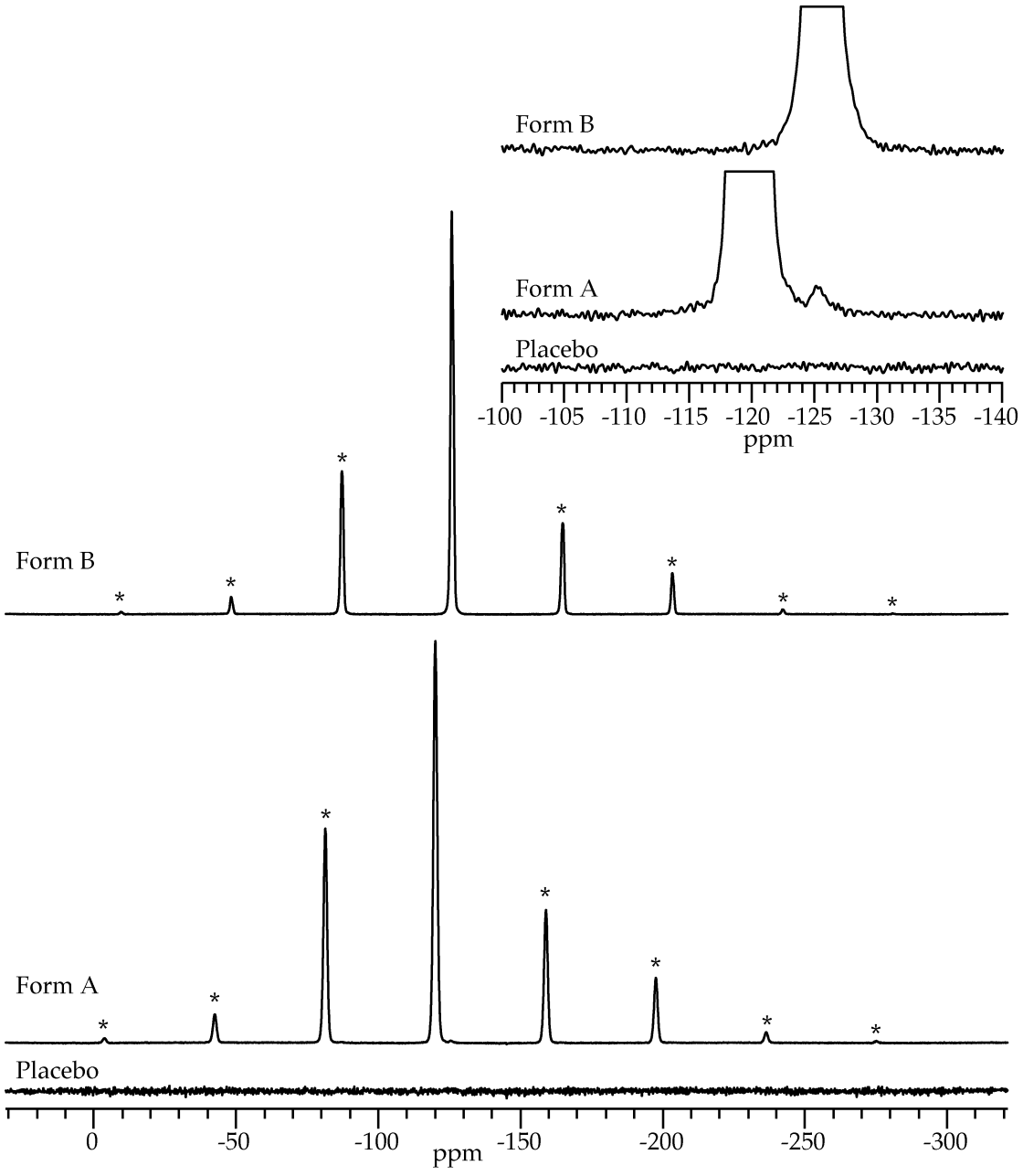

Figure 5.11. ^{19}F CPMAS spectra placebo and norfloxacin Forms A and B. The insert is an expansion of the spectra around the isotropic peaks to show the Form B impurity in the Form A sample, the impurity was estimated to be ~0.5% (w/w). * = spinning sidebands

and one molecule per asymmetric unit cell of the crystal structure (Z' = 1). Additionally, ^{19}F is 100% naturally abundant, which leads to significantly higher sensitivity when compared to ^{13}C. In fact the spectra in Figure 5.10 were the result of 7,168 transients collected over the period of 12 hrs while the spectra in Figure 5.11 only required 16 transients and a total collection time of less than 2 min. Additionally, the insert of Figure 5.11 shows that ^{19}F SSNMR was able to detect a small amount of Form B in the Form A sample, this impurity was estimated at ~0.5% (w/w)

5.3.2 Multivariate Regression

Quantitative measurements are typically performed with a univariate regression where it is assumed that the response (i.e., UV absorbance) is only influenced by a single factor (i.e., concentration of the analyte). This assumption is not always valid, especially for the quantitative analysis of solids. For example, the peaks in the Raman spectrum of an amorphous material are generally broad and poorly resolved from the peaks of the crystalline forms of the material. Thus, intensity of a Raman peak for a crystalline form may depend upon the amount of the corresponding crystalline form and the amorphous material that are present.

Multivariate regression takes several variables into account when performing the regression, and has the ability to differentiate independent factors, such as the concentrations of sample components. Therefore, multivariate regression has become popular within the field of solid form quantitation, particularly for spectroscopic techniques because it allows the use of the entire spectrum or spectral regions rather than the intensity at a single

point in the spectrum. Ideally, if the samples are a mixture of two physical forms then the multivariate regression will only depend upon a single factor, the relative concentrations of the two forms.

When performing multivariate regressions, cross validation is typically employed to test the robustness of the model. The entire calibration data set is initially used to build the model and the predicted sample compositions are determined from the model. In order to predict how the model will predict future results the calibration data set is validated by removing a small portion of the samples (test set), recreating the calibration model using the remaining training set, and then predicting the composition of the samples in the test set. This process is repeated until all of the samples have been used in a test set. The predicted compositions from the initial calibration and subsequent validation steps should be similar to one another. Additionally, the correlation of determination (R^2) will provide a measure of the correlation between the predicted and reference sample compositions in the model. The quality of a model is interpreted from the root mean square error (RMSE) and is given by Equation 5.1, where p is the predicted value, o is the observed value, and n is the

$$\mathrm{RMSE} = \sqrt{\frac{\sum_{i=1}^{n}\left(p_i - o_i\right)}{n}} \qquad \text{Equation 5.1}$$

number of samples. The RMSE is determined for both the calibration (RMSEC) and the validation (RMSEV) of the model. These values can be used to compare the error of two models, where the model with the lower RMSE values should

offer a more accurate and precise measurement.

5.3.3 Quantitation by DSC

In Section 5.3.1 it was shown that several DSC signals could be analyzed for Form A and B of norfloxacin, these included the change in the heat flow between 190 and 200 °C and the integration of various peaks (Figure 5.4). Melting of Form A was observed as Peak #3 and showed no correlation to the relative amount of Form A in the binary mixtures because Form A crystallized from the melted Form B during the experiment. Additionally, crystallization of Form A (Peak #2) showed only a very weak correlation due to variability in the crystallization behavior. A multiple linear regression (MLR) of the total integrated area resulted in a calibration model with an RMSEC and RMSEV of 9.4 and 9.9, respectively. When the MLR was performed with either Peak #1 (melting of Form B) or the change in heat flow measurement, the RMSEC and RMSEV values fell to 7.5 and 8.0 or 6.4 and 6.7 for each of the models, respectively.

A partial least squares (PLS) model was generated to utilize both the Peak #1 area and heat flow change, with each measurement weighted by 1/(standard deviation). The PLS model had the lowest RMSEC and RMSEV values (5.6 and 5.9, respectively) and the predicted versus reference plot from the model is shown in Figure 5.12. The calibration and validation sets are in good agreement, indicating that the model is a relatively good model. However, the DSC thermographs of the 10% formulations showed no signals from norfloxacin. Thus, the peaks could not be integrated, but the signal change was determined for some of the samples to see if there was any discernable correlation. The

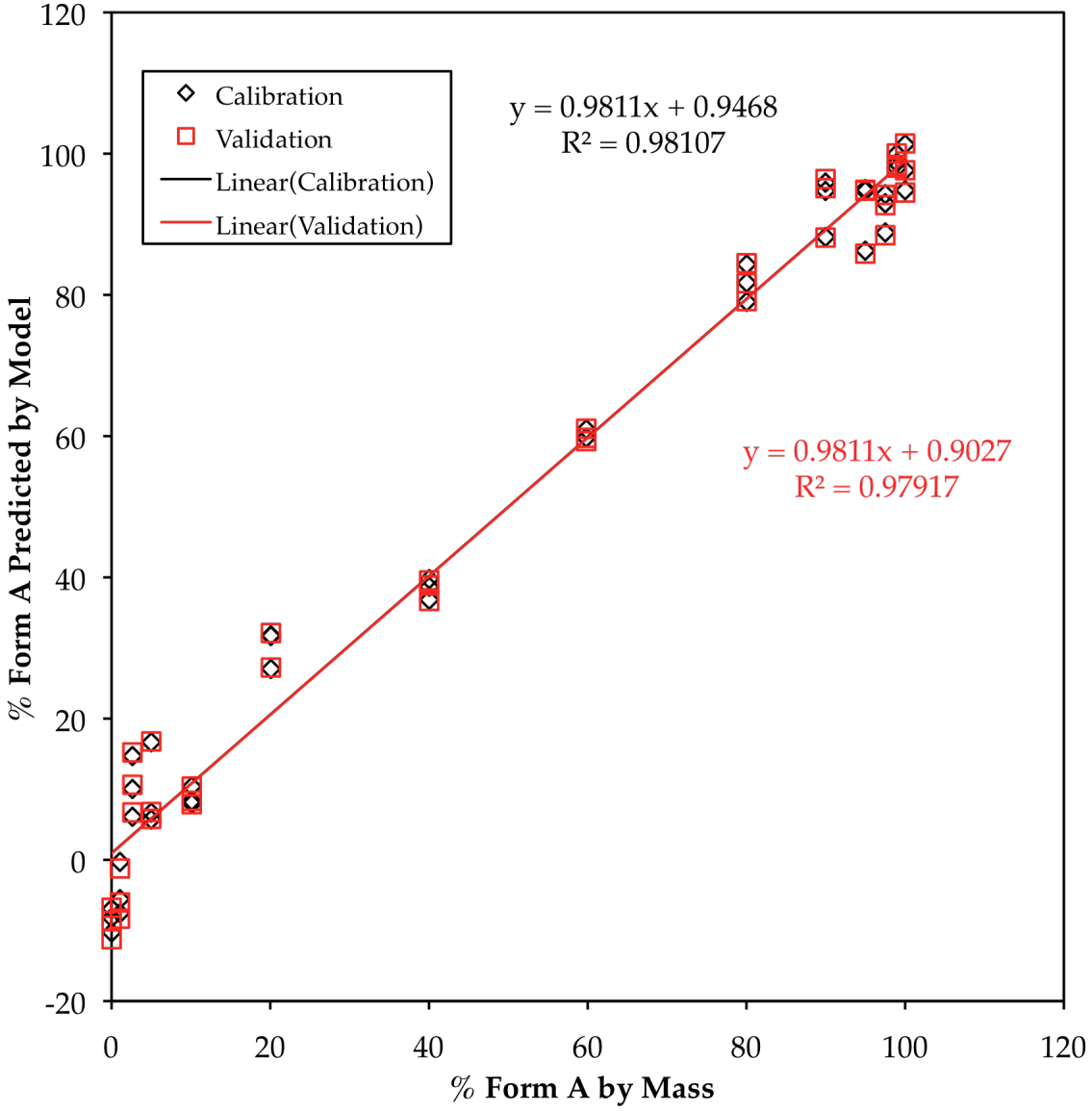

Figure 5.12. Predicted vs. reference plot for the PLS model of the DSC results from Peak #1 (Form B melting) and the heat flow change of the binary mixtures of Form A and B. The model was generated by weighting each of the DSC results by (1/Standard Deviation). The model has an RMSEC of 5.6 and an RMSEV of 5.9.

predicted versus reference plot from the resulting MLR model is shown in Figure 5.13, and the model had RMSEC and RMSEV values of 33 and 37, respectively. These results indicate that the MLR model for the signal change in the formulation was very poor and there was no correlation in the data to the percent Form A in the samples. This is not surprising considering the significant overlap of the placebo endotherm with the norfloxacin signals. Thus, DSC should allow quantification of the relative amounts of Form A and B in binary mixtures but not in the formulated materials.

5.3.4 Quantitation by TGA

When the calibration materials were analyzed by TGA the trends were similar to those observed with DSC. The MLR of the mass loss in the binary blends showed a good correlation with the percent Form A in the mixtures (Figure 5.14) and suggested that it was a better method than DSC (RMSEC = 2.5 and RMSEV = 2.6). However, the MLR of the 10% formulations is significantly worse (Figure 5.15) than the binary blends. A correlation was observed but there was a large amount of uncertainty with an RMSEC of 10 and an RMSEV of 11. It can be seen in Figure 5.3 that the noise in the data is relatively large, compared to the transition that is observed. Therefore, smoothing was applied over a 5 °C window prior to measuring the mass loss, but had no significant impact on the quality of the MLR of the binary mixtures or 10% formulations. Thus TGA model appears to be superior to DSC for the analysis of both the binary mixtures and 10% formulations, but the model for the formulations is still relatively weak.

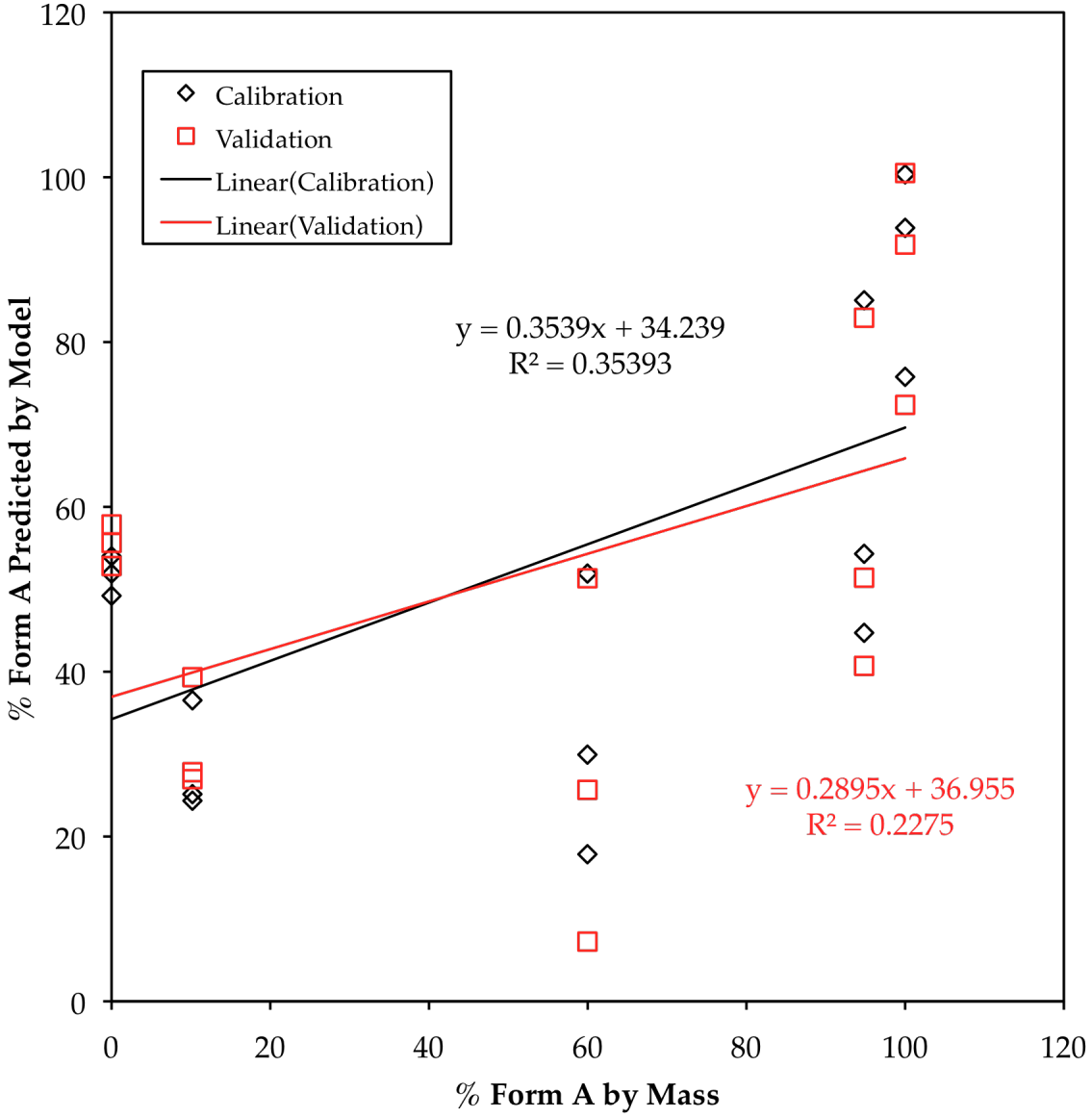

Figure 5.13. Predicted vs. reference plot for the MLR model of the DSC results from the heat flow change of the 10% (w/w) norfloxacin formulation. The model has an RMSEC of 33 and an RMSEV of 37.

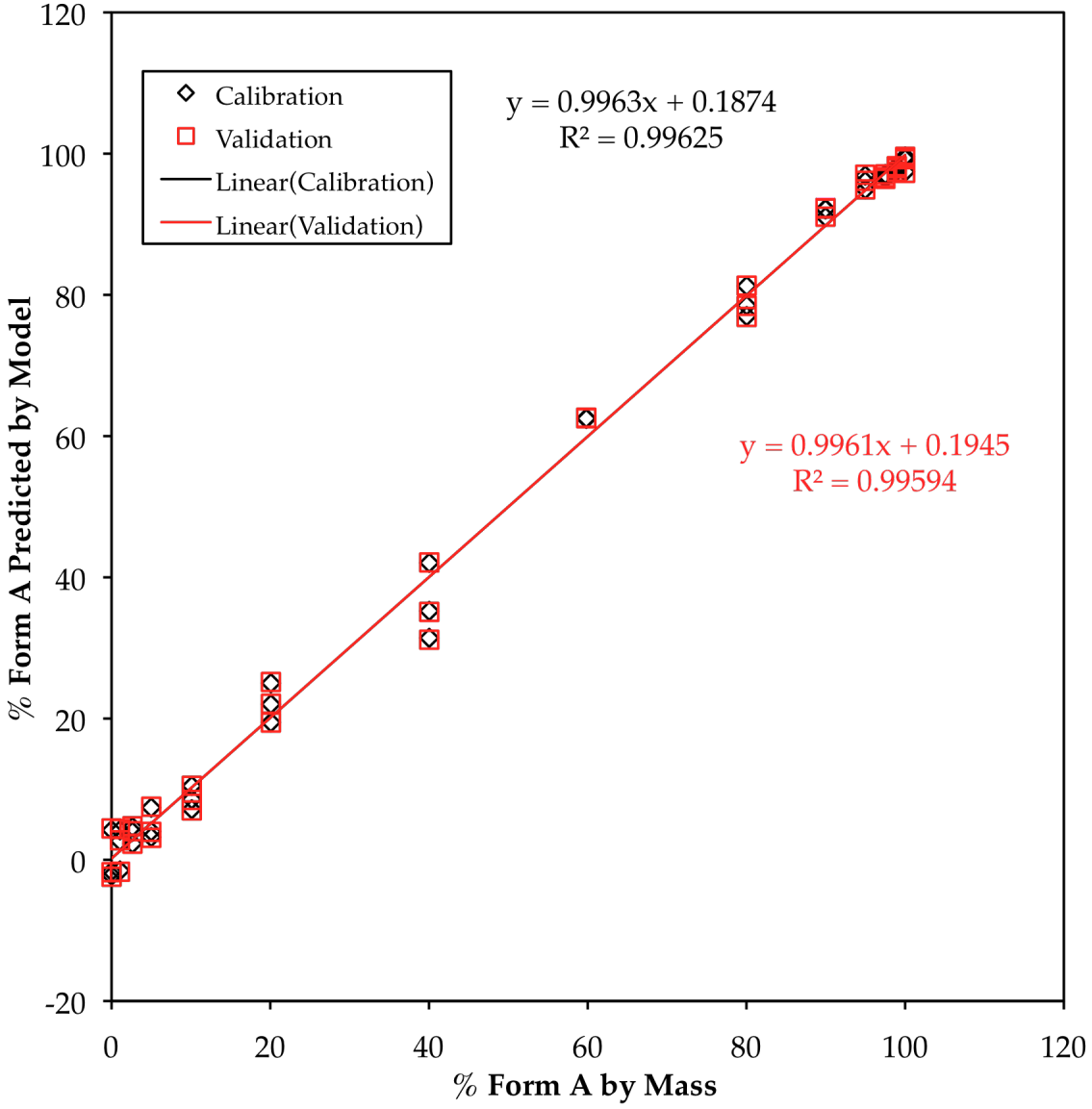

Figure 5.14. Predicted vs. reference plot for the MLR model of the TGA mass loss of the binary mixtures of Form A and Form B. The model has an RMSEC of 2.5 and an RMSEV of 2.6.

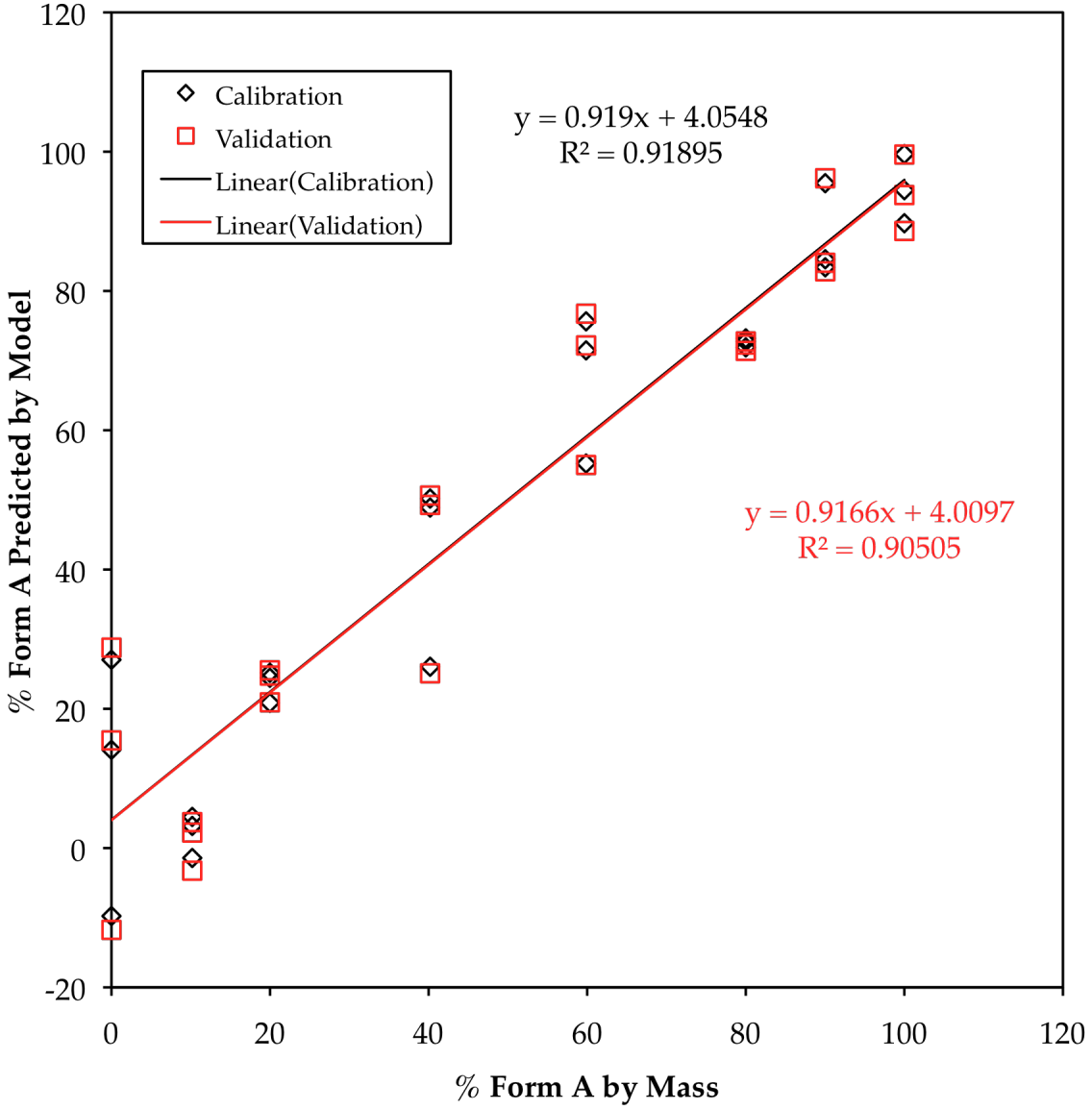

Figure 5.15. Predicted vs. reference plot for the MLR model of the TGA mass loss of the 10% (w/w) norfloxacin formulation. The model has an RMSEC of 10 and an RMSEV of 11.

5.3.5 Quantitation by PXRD

The PXRD patterns were subjected to various processing steps prior to generation of the calibration models. The diffraction patterns were used in their raw form, smoothed with Savitzky-Golay (SG) filtering, or smoothed with SG filtering and then normalized with either the standard normal variate (SNV) function or multiplicative scattering correction (MC). PLS models of raw data from the full diffraction patterns, Region #3, and Region 4 were significantly better than Regions #1 and #2 (Figure 5.5). Smoothing of the diffraction patterns had no significant impact on the quality of the models, but normalization did improve the results. The best results were obtained by smoothing the diffraction patterns and then normalizing them by the SNV function. The best model was obtained from the analysis of Region #4 (Figure 5.16) and had an RMSEC of 4.1 and an RMSEV of 4.2.

The results were similar for the effects of processing on the diffraction patterns of the 10% formulations, and the best model was again found to be of Region #4 with SG smoothing and SNV normalization. The predicted versus reference plot of the model is shown in 5.17, and clearly shows the same trend as the TGA results with a large amount of uncertainty (RMSEC = 14 and RMSEV = 16). Additionally, all of the data is clustered around the calibration and validation trend lines, with the exception of the 10% formulations where 60% of the norfloxacin is present as Form A. These data points are significantly skewing the quality of the model but it is not clear if this is due to the sample itself or the instrument. If the sample does not actually contain the reported amount of Forms A and B then it should be excluded from the model. However, if the sample composition is correct then the issue must be with the PXRD instrument

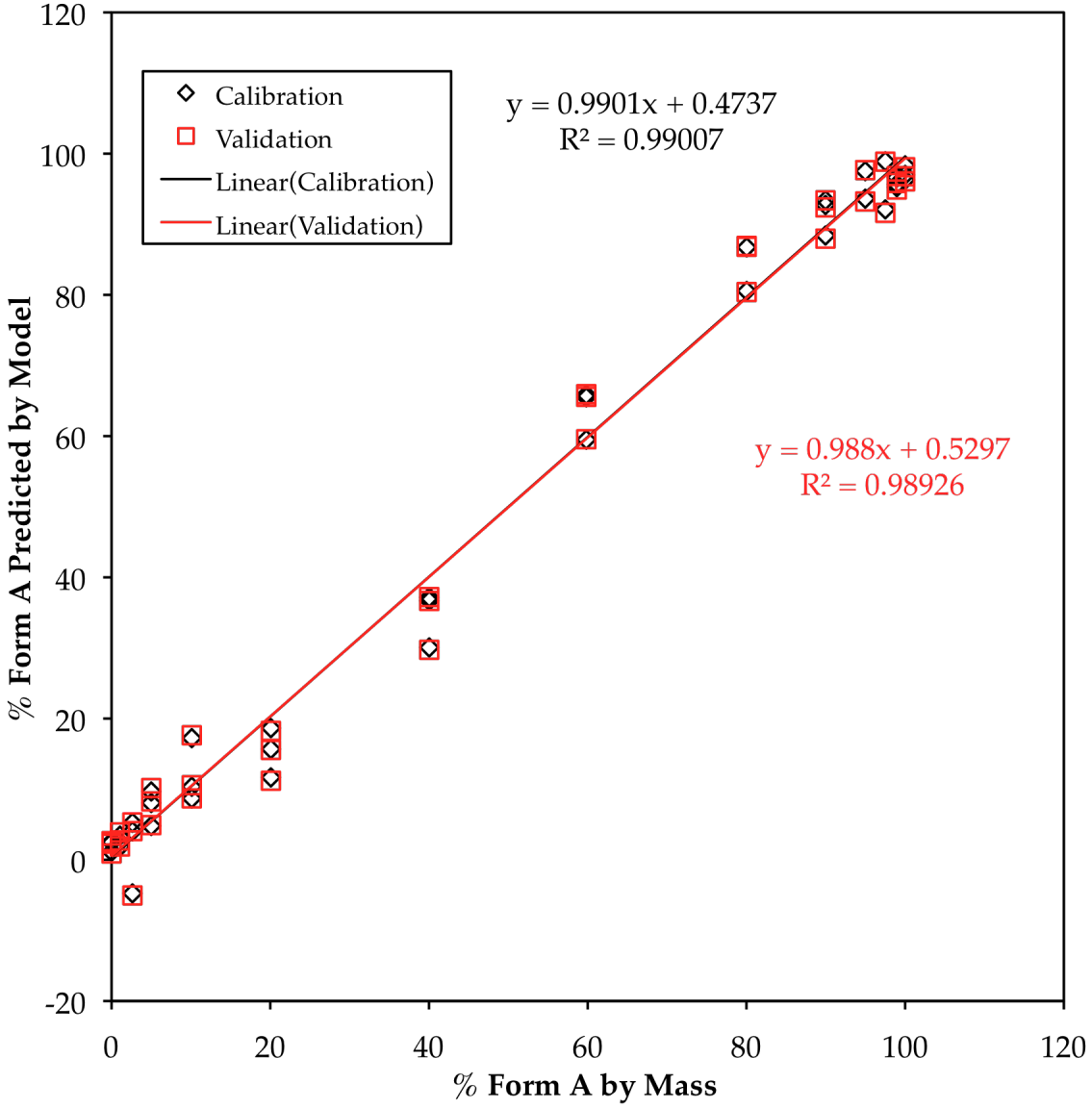

Figure 5.16. Predicted vs. reference plot for the PLS model of the PXRD signals from Region #4 of the diffraction patterns binary mixtures of Form A and Form B. The entire diffraction pattern was smoothed with the SG algorithm and normalized by SNV transformation prior to generating the model. of the. The model has an RMSEC of 4.1 and an RMSEV of 4.2.

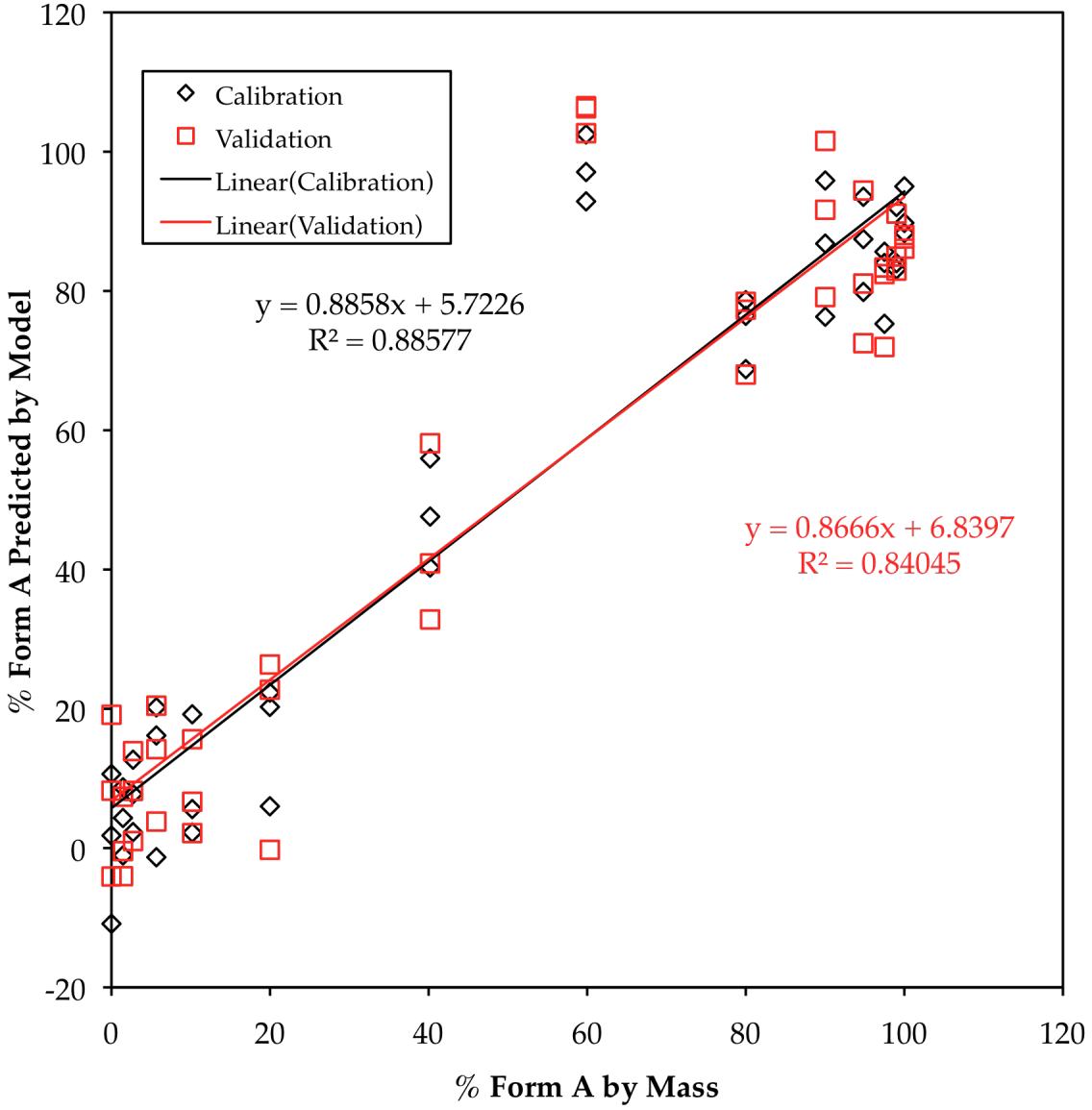

Figure 5.17. Predicted vs. reference plot for the PLS model of the PXRD signals from Region #4 of the 10% (w/w) norfloxacin formulation diffraction patterns. The entire diffraction pattern was smoothed with the SG algorithm and normalized by SNV transformation prior to generating the model. The model has an RMSEC of 14 and an RMSEV of 16.

or the method. Unfortunately, it is not possible from this data to clearly identify the source of the error. But, if the same sample shows similar results by other instrumental methods it should be possible to attribute the error to an inaccurate sample composition.

5.3.6 Quantitation by FT-Raman Spectroscopy

Several processing methods were applied to the FT-Raman spectra prior to generating the PLS models for the binary mixtures and 10% formulations. The spectra were used in their raw form, normalized by the SNV function, or normalized with SNV and then converted to 2nd derivatives with the SG filter. The various processing methods had little impact on the PLS models of the full spectra and subregions of the spectra. However, Region #2 (Figure 5.8) did show moderate improvement with processing and resulted in the best model when both SNV normalization was performed and the spectra were converted to 2nd derivatives. Figure 5.18 shows the predicted versus reference plot for the model, RMSEC = 2.0 and RMSEV = 2.0. The same behavior was seen with the 10% formulation, but as with the previous methods the model was significantly worse for the formulations (Figure 5.19) with an RMSEC of 9.9 and an RMSEV of 10.

These results suggest that FT-Raman spectroscopy is slightly better than TGA at quantifying Form A in the binary mixtures and both methods are approximately equivalent for the analysis of the formulations. However, Figure 5.19 shows that the 10% formulation with 60% of the norfloxacin as Form A is predicted to have more Form A than it actually contains, according to the sample preparation. This suggests that there is a problem with the sample that is skewing the error of the formulation models. There does not seem to be a

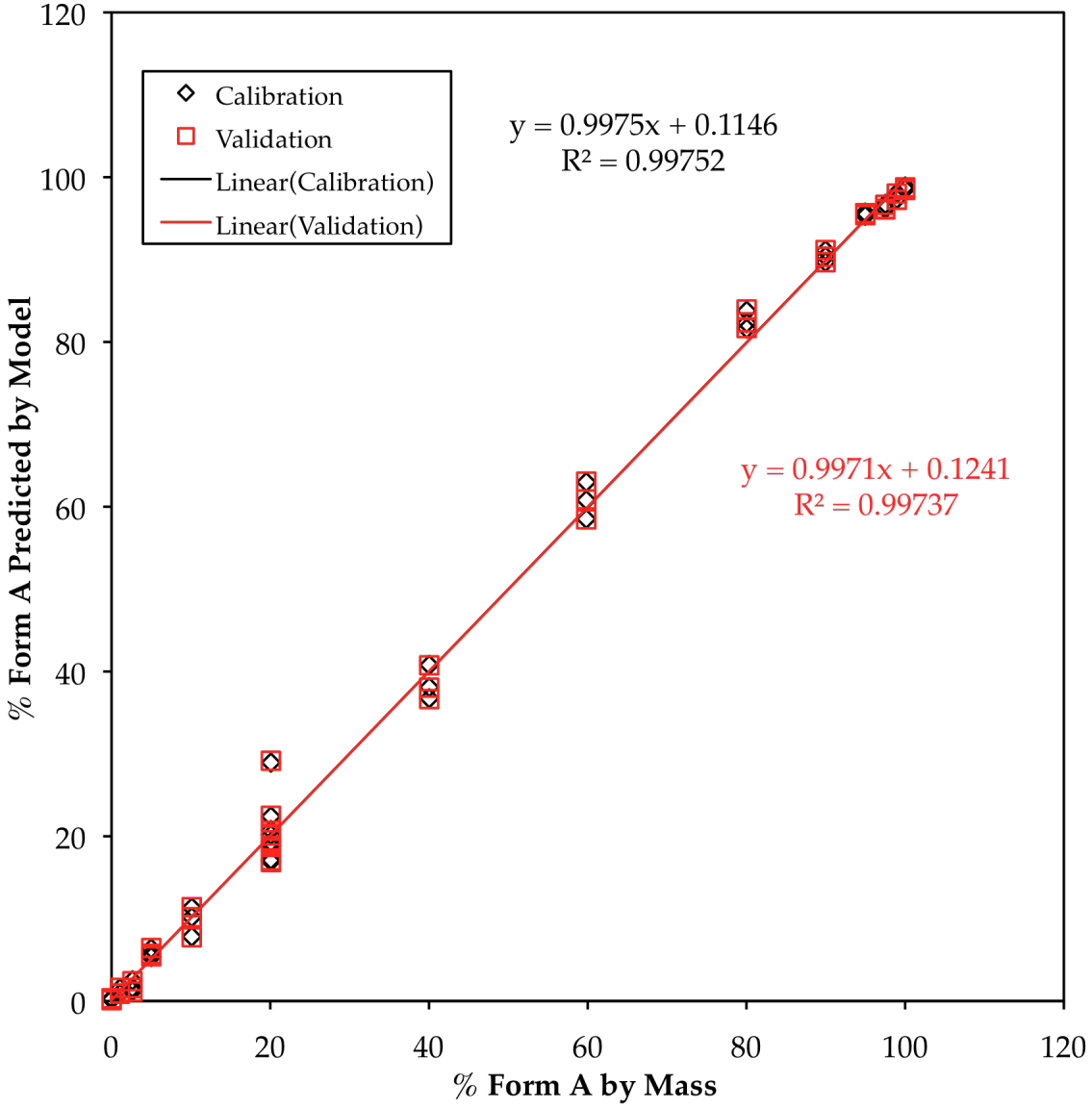

Figure 5.18. Predicted vs. reference plot for the PLS model of the FT-Raman signals from Region #2 of the spectra of binary mixtures of Form A and Form B. The entire spectra were normalized by SNV transformation and then converted to 2nd derivatives with the SG algorithm prior to generating the model. The model has an RMSEC of 2.0 and an RMSEV of 2.0.

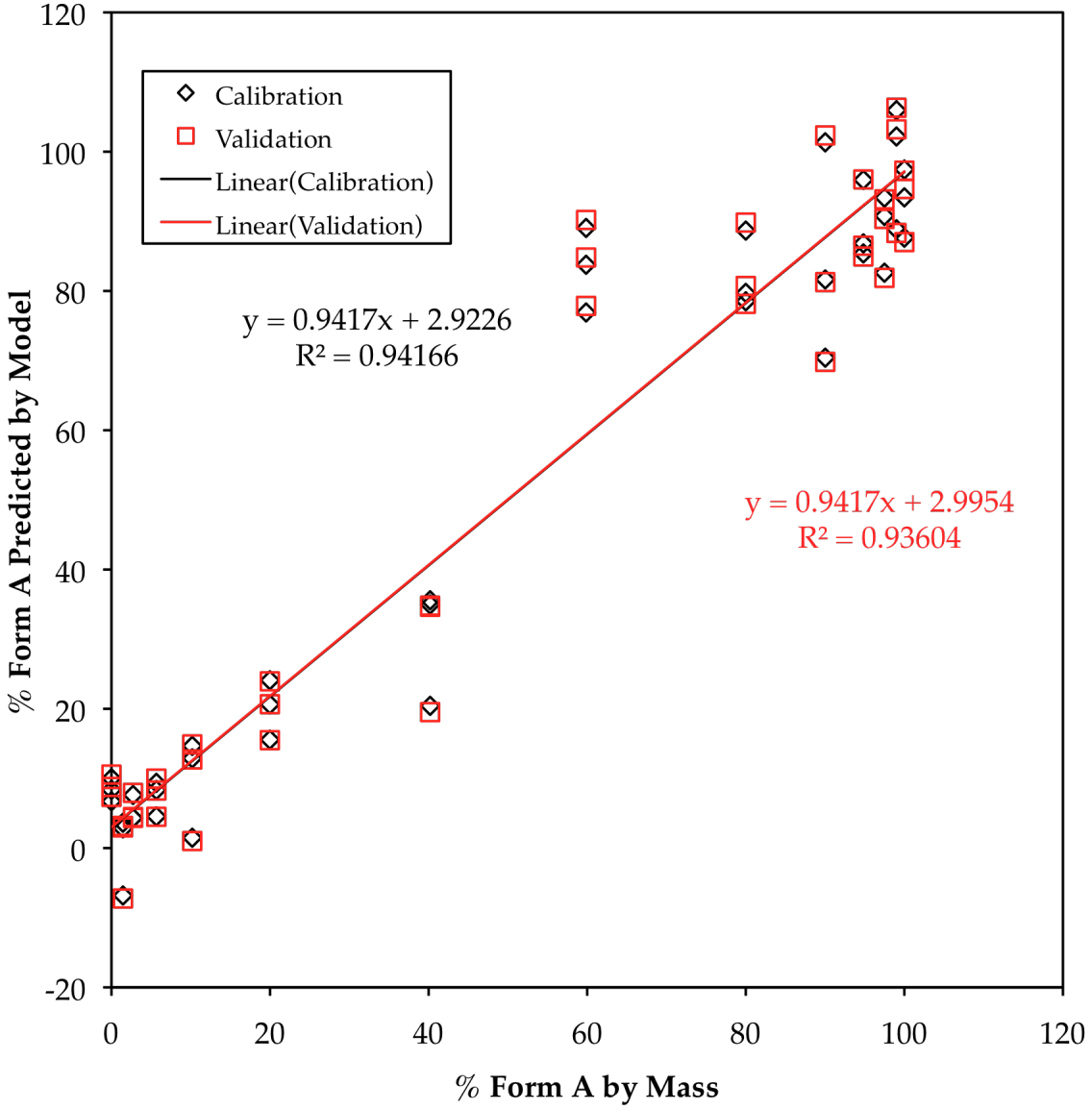

Figure 5.19. Predicted vs. reference plot for the PLS model of the FT-Raman signals from Region #2 of the 10% (w/w) norfloxacin formulation spectra. The entire spectra were normalized by SNV transformation and then converted to 2nd derivatives with the SG algorithm prior to generating the model. The model has an RMSEC of 9.9 and an RMSEV of 10.

noticeable trend in the other formulation samples, which indicates that the issue is with the sample preparation and not that the norfloxacin is undergoing a polymorphic form conversion. It is not entirely surprising that a sample could have been improperly prepared considering the relatively small masses of norfloxacin that were involved in preparing the sample (900 mg of placebo, 40 mg of Form B and 60 mg of Form A). The incorrect transfer of just 5 mg of one norfloxacin polymorph would result in about a 5% error in the Form A content. This is a common issue with the generation of calibration standards for solid-state quantitation studies, this issue will be addressed further in Section 5.3.9.

5.3.7 Quantitation by PhAT Probe

PhAT probe technology is very popular within the pharmaceutical industry because it samples a much larger area than FT-Raman, and it can easily be utilized to actively monitor many industrial-processing steps. This makes it a valuable tool for the monitoring of production lines. Not surprisingly the Raman spectra that were collected with the PhAT probe showed almost identical calibration model properties as the FT-Raman spectra. The same processing methods from the FT-Raman data were used, and again resulted in the best model when SNV normalization is used and the spectra are converted to 2nd derivatives with the SG filter. However, in this case the best model was obtained for Region #1 (Figure 5.7), RMSEC = 2.1 and RMSEV = 2.1 (Figure 5.20). And the quality of the 10% formulation model (Figure 5.21, RMSEC and RMSEV of 11) was slightly worse than the FT-Raman results. Also, the 10% formulation with 60% of the norfloxacin as Form A showed the same behavior, offering further proof that the reference composition of the sample is incorrect. The sample was

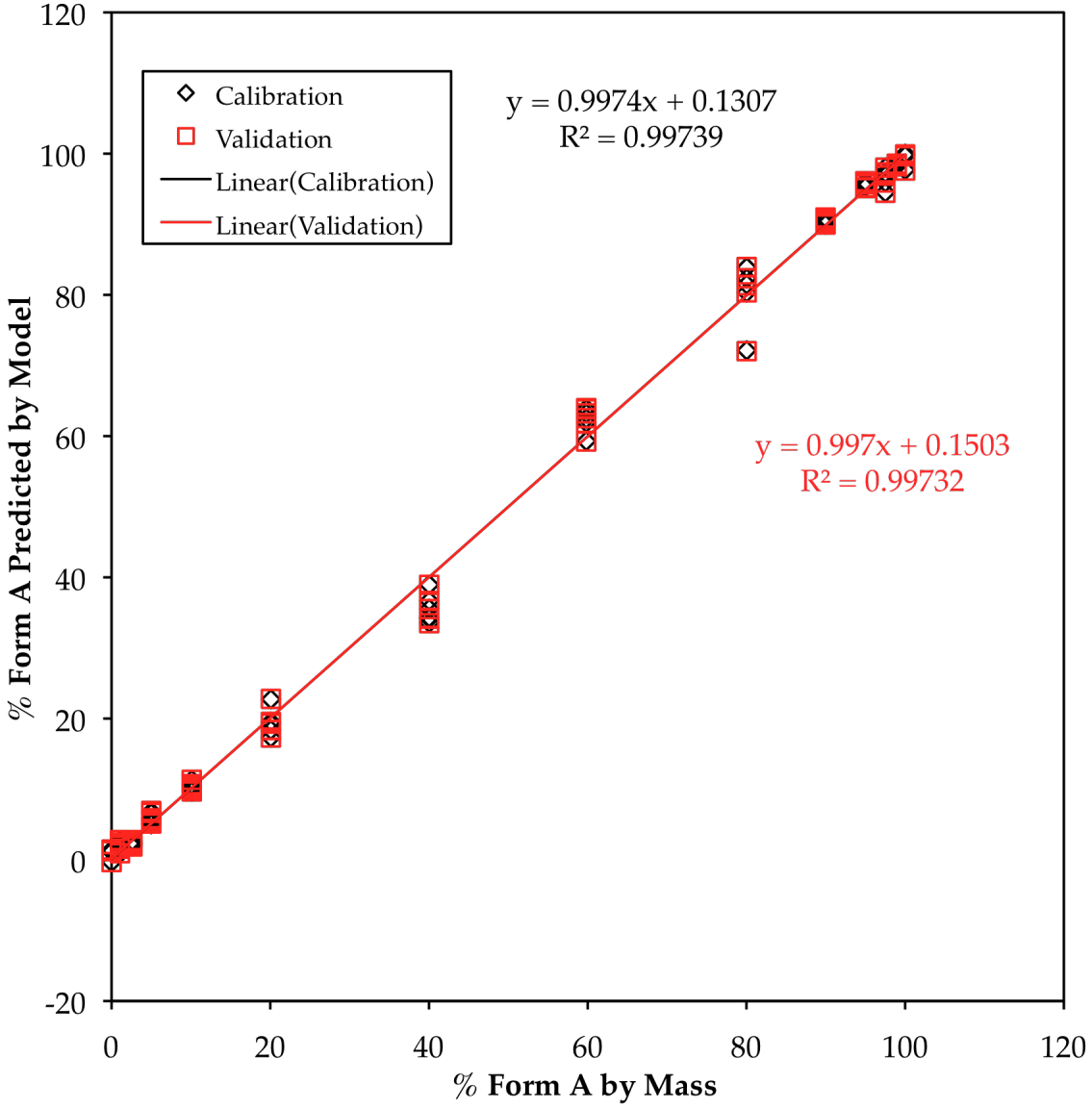

Figure 5.20. Predicted vs. reference plot for the PLS model of the PhAT probe Raman signals from Region #1 of the spectra of binary mixtures of Form A and Form B. The entire spectra were normalized by SNV transformation and then converted to 2nd derivatives with the SG algorithm prior to generating the model. The model has an RMSEC of 2.1 and an RMSEV of 2.1.

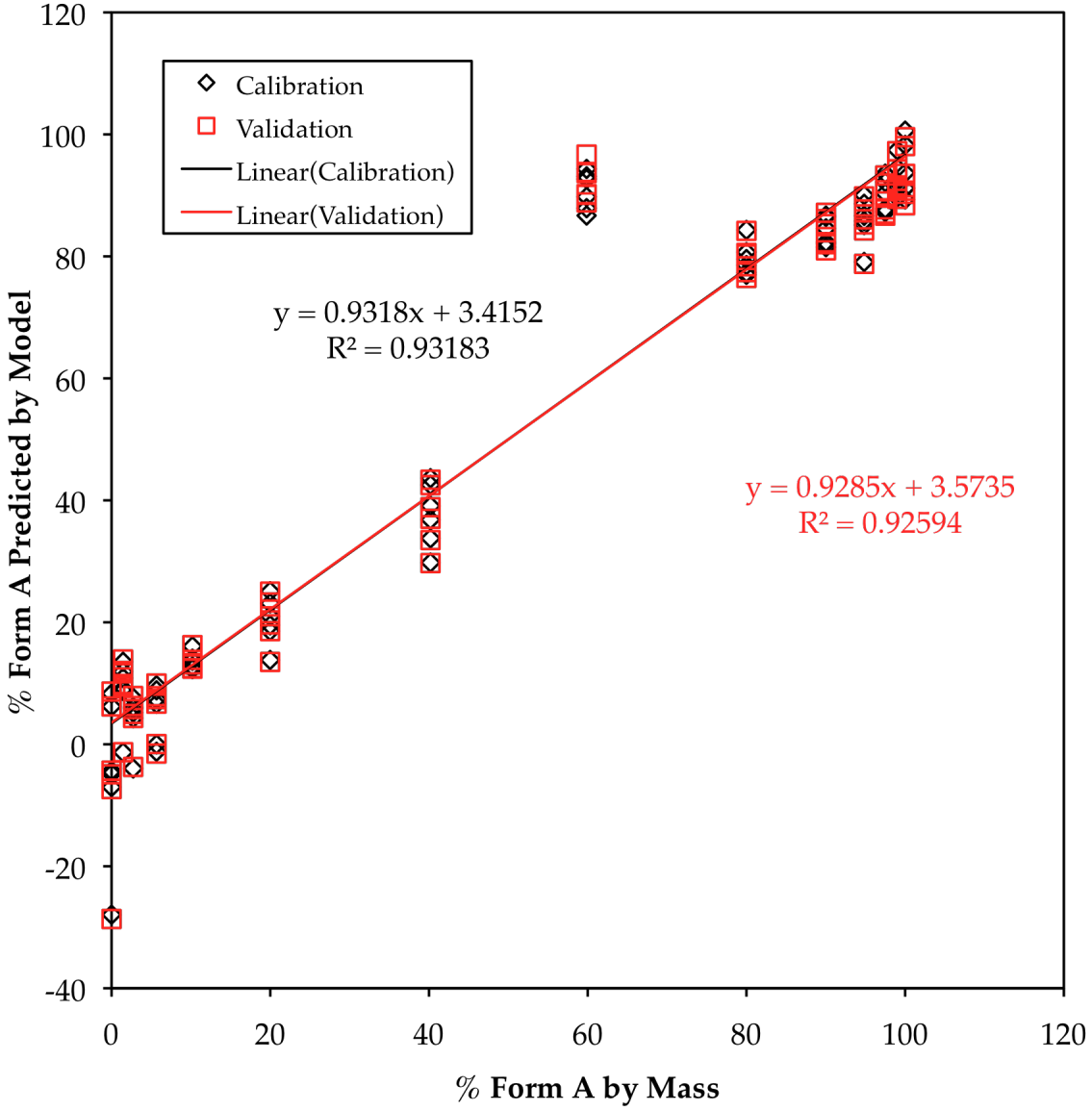

Figure 5.21. Predicted vs. reference plot for the PLS model of the PhAT probe Raman signals from Region #1 of the 10% (w/w) norfloxacin formulation spectra. The entire spectra were normalized by SNV transformation and then converted to 2nd derivatives with the SG algorithm prior to generating the model. The model has an RMSEC of 11 and an RMSEV of 11.

only included in the model to allow comparison of the RMSE values of the PhAT probe model to the other models.

5.3.8 Quantitation by ^{13}C SSNMR Spectroscopy

It was shown in the previous chapter of this dissertation, that the relative amounts of two physical forms could be determined by SSNMR without generating a calibration curve. Therefore, only two of the calibration samples were analyzed by ^{13}C SSNMR in order to provide a comparison with the analysis methods, apart from the analysis of the "unknowns". The same general approach as was developed in the previous chapter with one noticeable exception. An additional term, Z, needs to be added to account for differences that were observed due to the use of a custom built two-module probe.

The probe is able to simultaneously collect FIDs of two samples, by interleaving the periods of pulsing and delays of the two samples. This approach allows two samples to be analyzed without utilizing any more resources (another spectrometer) or time. However, it was discovered that when analyzed with the two-module probe, a particular amount of the signal was lost. If the effect was the same for all physical forms it could be ignored; however it was found that this value was not consistent for all physical forms. The amount of signal that was retained is referred to as Z and can be incorporated into Equation 4.10 of Chapter 4 to account for these effects. The Z of norfloxacin Form A and B were determined on the reference materials and are provided, along with the other relevant NMR properties in Table 5.1.

Two binary mixtures of norfloxacin Forms A and B were analyzed by SSNMR to determine the relative amount of Form A. The first sample consisted

Table 5.1 NMR properties for ^{13}C and ^{19}F SSNMR Quantitation Measurements

Parameter ± Error[‡]	Detected by	Form A	Form B
$^{1}H\ T_1$ (sec)	^{13}C	1.98 ± 0.03	4.29 ± 0.09
$^{1}H\ T_1$ (sec)	^{19}F	2.25 ± 0.02	4.37 ± 0.02
$^{19}F\ T_1$ (sec)	^{19}F	42.5 ± 0.4	8.3 ± 0.2
T_{CH} (msec)	^{13}C	0.94 ± 0.05	1.5 ± 0.1
$^{1}H\ T_{1\rho}$ (msec)	^{13}C	12 ± 1	---[‡]
T_{FH} (msec)	^{19}F	0.12 ± 0.01	0.3 ± 0.3
$^{1}H\ T_{1\rho}$ (msec)	^{19}F	12 ± 1	---[‡]
$f_{4.9\ kHz}$ (^{13}C)	^{13}C	0.673	0.679
$f_{11\ kHz}$ (^{19}F)	^{19}F	0.481	0.573
Z	^{13}C	0.825	0.665

[†] = Relevant NMR properties for Equation 4.10, with the multiple sample correction factor (Z) for each form incorporated in the equation below. The parameters are reported with their associated errors from nonlinear regression.

$$F_X = \frac{1}{1 + \left(\frac{A_Y}{A_X} \times \frac{f_X}{f_Y} \times \frac{e^{-t/T_{1\rho,H,X}}}{e^{-t/T_{1\rho,H,Y}}} \times \frac{\left[1 - e^{-d/T_{1,X}}\right]}{\left[1 - e^{-d/T_{1,Y}}\right]} \times \frac{Z_X}{Z_Y} \right)}$$

[‡] = The $^{1}H\ T_{1\rho}$ of Form B was too long to be determined from the data sets. For the purposes of quantitation it is assumed to be ~50 msec or longer.

of 40.0% Form A, according to the masses used to prepare the mixture. Two 7 mm zirconia rotors were packed with the material and both rotors were placed in the two-module probe for analysis. The relevant peaks of the spectra from both rotors were integrated and analyzed with the corrected equation. The samples gave Form A compositions of 35.8 and 37.0%, with an average and standard deviation of 36.4 and 0.9%, respectively. The results from the two samples agree very well with one another but are approximately 3.6% lower than the reference value. The other mixture had a reference Form A composition of 90.0% but the resulting ^{13}C CPMAS spectra resulted in values of 87.6 and 88.3 %. Again, the SSNMR results agree very well with each other (standard deviation ~0.5%) but are approximately 2.1% lower than the known value. This raises an important issue regarding the "known" composition of reference standards in quantitative solid-state analysis. These issues will be considered further in Section 5.3.9.

5.3.9 Quantitation by ^{19}F SSNMR Spectroscopy

The sensitivity of ^{19}F is significantly higher than that of ^{13}C, which results in much shorter experiments and allows the detection of components of a mixture at relatively low levels. This was demonstrated in Figure 5.11 where a very small amount of Form B was detected in the Form A with a spectrum that was collected in less than 2 min while no other technique detected its presence. When performing quantitation by ^{19}F SSNMR the considerations are largely the same as when using ^{13}C. Cross-polarization (CP) does not offer the same increase in sensitivity as is observed for ^{13}C but it can shorten the relaxation delay between transients. This is the primary reason that the ^{19}F data here was collected with the CP method, since the ^{19}F T_1 of Form A is 43 sec, a delay

between transients of at least 54 sec should be used to maximize the S/N of the data. But by using CP the delay can be shortened by almost an order of magnitude, and the results can be corrected with Equation 4.10 of Chapter 4 to account for the CP dynamics.

Since ^{19}F yield such high S/N data in very short time experiments the quantitation method was changed slightly. Rather than collecting data with a single CP duration and using Equation 4.10 of Chapter 4 to correct for the CP dynamics, data was collected with three different CP durations. The areas from the three spectra were then extrapolated back to the y-intercept and allowed an uncertainty in the intercept and ultimately the percent Form A that was measured.

When the binary blends of norfloxacin Forms A and B were analyzed by ^{19}F SSNMR the results were in good agreement with the percent Form A from the prepared masses. In most cases the ^{19}F SSNMR and Mass values were within 1.5%. These results were used to generate an MLR model (Figure 5.22) in order to see how the correlation of the values compared to the previous calibration models. The ^{19}F SSNMR MLR model was clearly the best model that was developed for the binary mixtures with an RMSEC of 1.3 and an RMSEV of 1.5. However, note that unlike the other models, the model in Figure 5.22 was only generated for comparison since the quantitation was actually performed by comparing the corrected peak areas.

As a measure of the uncertainty of the ^{19}F results, the uncertainty of the linear regressions for the CP dynamics were used to estimate the uncertainty in the percent Form A that was obtained from the same extrapolation. In every case the uncertainty was less than 0.5%, with the exception of one sample where the

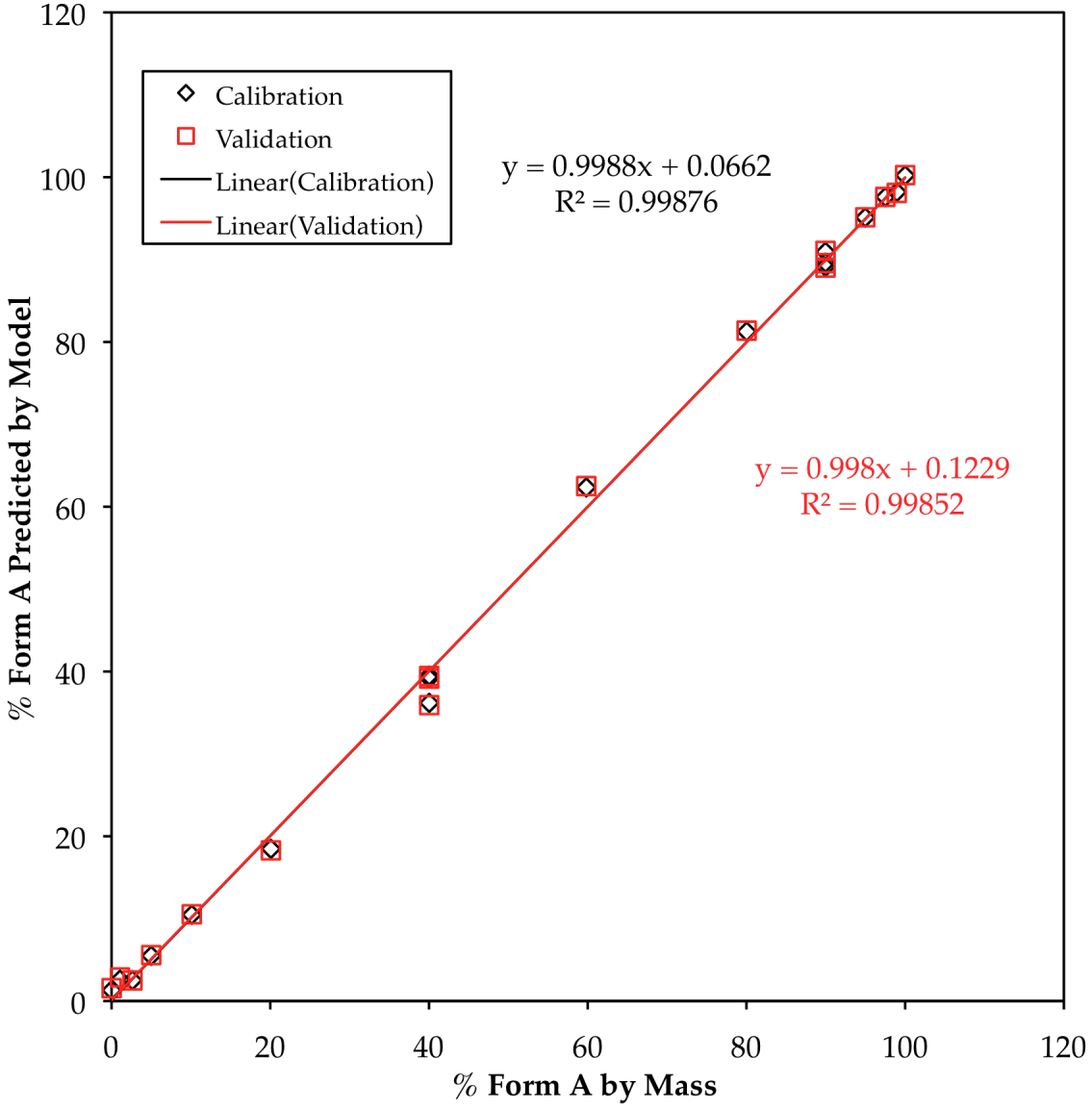

Figure 5.22. Predicted vs. reference plot for the MLR model of the ^{19}F SSNMR results of the binary mixtures of Form A and Form B. The model has an RMSEC of 1.3 and an RMSEV of 1.5.

value was 0.6%. In fact, most of the samples gave values of 0.2% or lower. This suggests that the percent Form A that is determined from each of these measurements is an accurate representation of the sample that is being analyzed. In order to test this, two samples (40.0 and 90.0% Form A) were analyzed by ^{19}F in triplicate. The 40.0% Form A sample gave values of 35.2 ± 0.6%, 38.3 ± 0.5%, and 38.6 ± 0.2% with an average of 37.3% and standard deviation of 1.8%. These results are interpreted as indicating that the sample is not completely homogeneous, thus when the material is placed in the 4 mm zirconia rotor the actual composition in the rotor may differ slightly. While the NMR is able to measure the relative composition of the sample in the rotor the sample in the rotor may not accurately reflect the composition of the sample. This is a well known issue with solid-state quantitation studies. The variability of the data is not only dependent upon the variability of the instrument and the user but also the homogeneity of the materials that are being analyzed. Analysis of the 90.0% Form A mixture resulted in values of 90.2 ± 0.1%, 88.8 ± 0.2%, and 88.3 ± 0.2% with an average of 89.1% and a standard deviation of 0.9%. These results were in line with what was observed for the 40.0% mixture.

The 10% formulations were also analyzed with the same CP extrapolation technique and the results were used to generate another MLR model for comparison against the other techniques. The predicted versus reference plot is shown in Figure 5.23 and shows a very good linear correlation with the exception of the 60% Form A sample, again, which was previously observed to be an outlier. However, the other data points in the plot do not show as much scatter as was observed for previous techniques, thus the 60% Form A data was removed and the new MLR model is shown in Figure 5.24. The model was

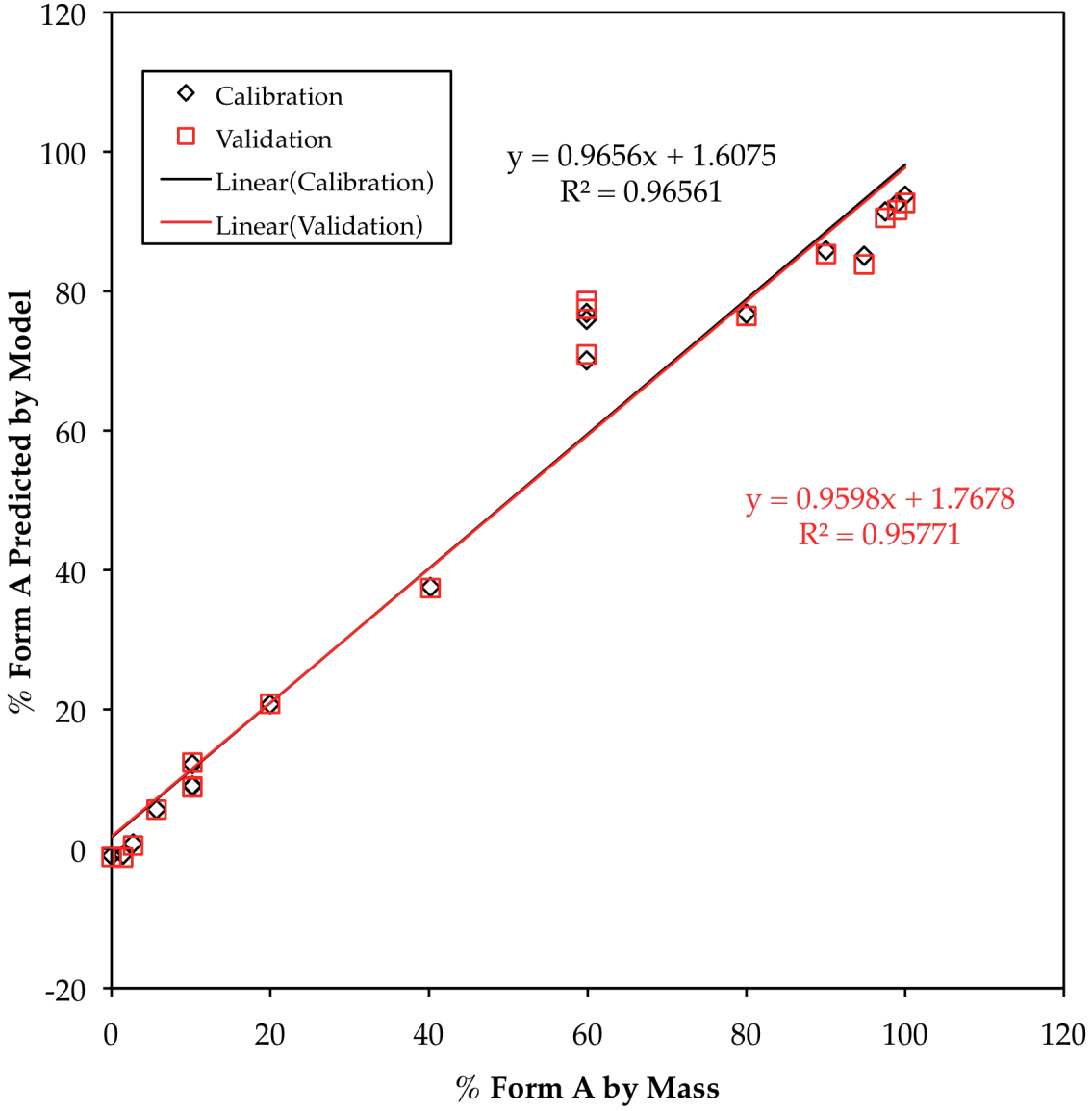

Figure 5.23. Predicted vs. reference plot for the MLR model of the ^{19}F SSNMR results of the 10% (w/w) norfloxacin formulation. The model has an RMSEC of 7.1 and an RMSEV of 7.9.

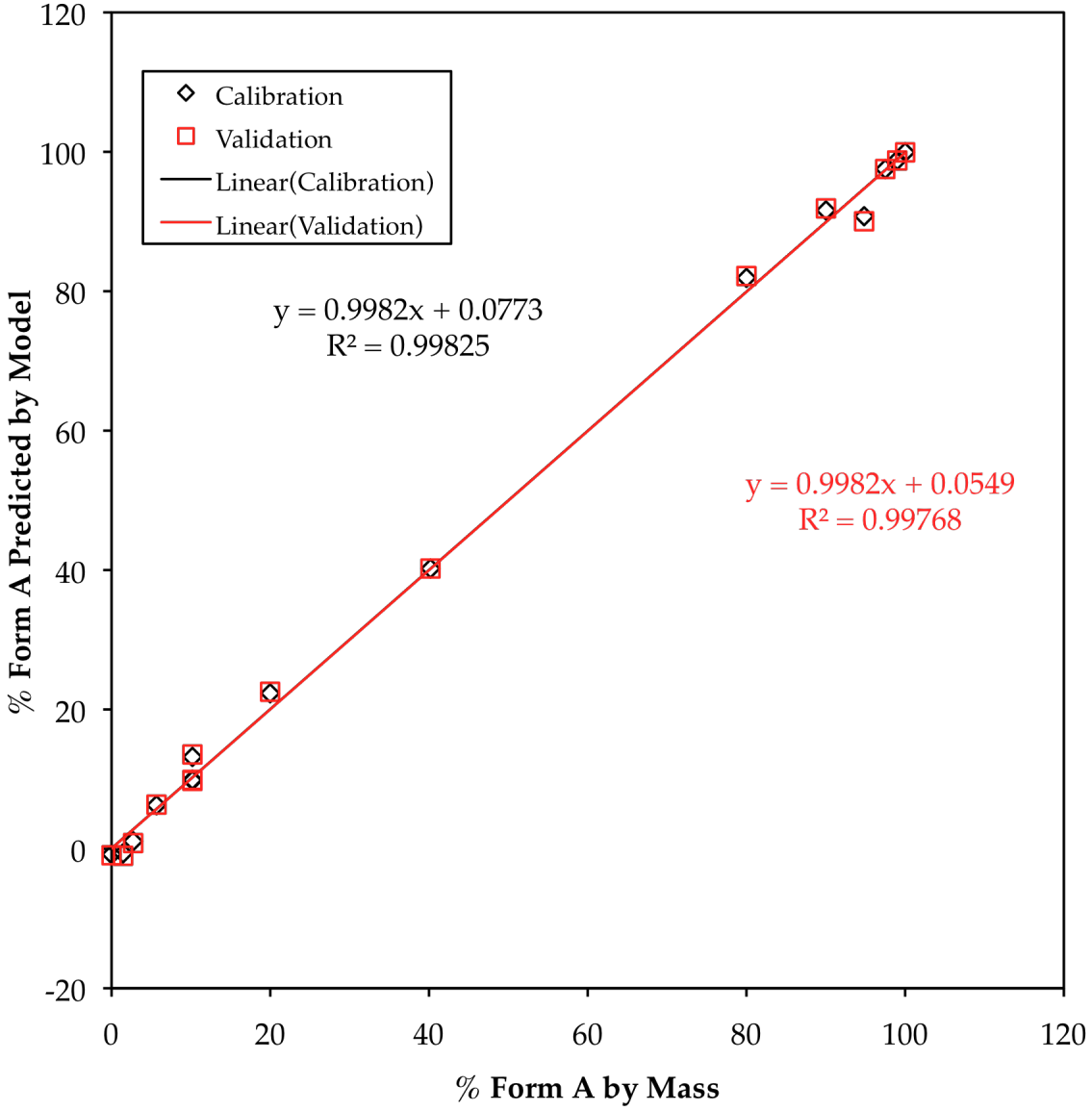

Figure 5.24. Predicted vs. reference plot for the MLR model of the ^{19}F SSNMR results of the 10% (w/w) norfloxacin formulation when the 60% Form A calibration formulation was excluded. The model has an RMSEC of 1.7 and an RMSEV of 2.0.

noticeably better and the RMSEC decreased from 7.1 to 1.7 and the RMSEV went from 7.9 to 2.0, so that the quality of the new model was similar to the ^{19}F model of the binary blends.

The previous observations regarding understanding sample homogeneity by ^{19}F measurements were tested with two of the 10% formulations that were selected for analysis in triplicate. The first was the 10.2% Form A and resulted in values of 11 ± 2%, 13 ± 2%, and 10.6 ± 0.6% with an average of 12% and a standard deviation of 2%. These uncertainties are considerably larger than those that were observed from the results from the binary mixtures, but are likely due to the reduced S/N of the data that is being analyzed here because approximately the same number of transients were collected for the binary mixtures and 10% formulations but the formulations contained an order of magnitude less norfloxacin. Thus the intensity of the signals that are being processed are approximately an order of magnitude lower and have a higher relative uncertainty. The 10% formulation that consists of 59.9% norfloxacin as Form A gave results of 80.8 ± 0.6%, 74.7 ± 0.5%, and 81.8 ± 0.1% with an average of 79% and a standard deviation of 4%.

Thus the ^{19}F SSNMR quantitation results appear to be relatively accurate for the material that was packed in the rotor and analyzed. Additionally, it appears that while the composition obtained by a single measurement may not accurately reflect the composition of the sample, this is really due to inhomogeneity of the material and not inaccuracy of the SSNMR method. These effects could be minimized by using a larger rotor for the analysis (4 mm rotors hold ~40 mg and 7 mm rotors hold ~350 mg) as with ^{13}C analysis, but for a variety of practical reasons ^{19}F data is typically not collected with rotors larger

than 4 mm. Thus, when using small rotors multiple replicates should be performed to limit the inaccuracy of the measurements due to inhomogeneity.

5.3.10 "Choice of Reference Composition Values"

When preparing standards for solid-state quantitation studies, the masses of all of the components are used to determine the known sample composition. One potential method to increase the accuracy of these known values is to use larger amounts of material. The relative uncertainty of weighing 1 g is smaller than the relative uncertainty of weighing 1 mg on the same balance. Additionally, the transfer of a larger mass will likely be prone to less relative loss compared to the transfer of a smaller mass. These concepts are routinely used to produce accurate calibration standards for solution studies. However, in solids it can be difficult to ensure that mixtures are adequately blended to minimize inhomogeneity. Also, it is often more difficult to ensure complete mixing of large samples of powders. Thus the preparation of calibrations for solid-state quantitative methods typically involves the generation of the smallest amount of material that can be used for the analysis and yet large enough so that the components can be accurately weighed.

In general none of the calibration standards in the binary blends appeared to be outliers in the predicted versus reference plots (Figures 5.12, 5.14, 5.16, 5.18, and 5.20). However, the 10% formulation the sample where 60% of the norfloxacin was present as Form A appeared to be an outlier in the PLS models of the PXRD, FT-Raman, and PhAT probe Raman methods (Figures 5.17, 5.19, and 5.21). When this sample was removed from the MLR of the ^{19}F model the quality of the model was improved significantly. This sample was probably

subject to an error in preparation and typically would just have to be thrown out of the analysis. Yet, the ^{19}F SSNMR allowed the actual composition of the mixture to be determined since the method does not require a calibration curve. So the PXRD, FT-Raman, and PhAT probe models were regenerated, but the percent Form A from the ^{19}F SSNMR measurements were used as the reference compositions, rather than the values from the prepared masses. The predicted versus reference plot of the PhAT probe method is shown in Figure 5.25, and shows a significant improvement in the model. Similar improvements were also observed for the PXRD and FT-Raman models. The RMSEC and RMSEV of the models changed from 14 and 16, 9.9 and 10, and 11 and 11 to 11 and 13, 7.5 and 7.9, and 7.1 and 7.2 for PXRD, FT-Raman, and the PhAT probe, respectively.

5.3.12 LOD and LOQ of Methods

There are several methods for determining the LOD and LOQ for an instrumental method, and are typically based on either the S/N of the signal or some measure of the standard deviation of the repsonce.[6] The LOD and LOQ are given by Equations 5.2 and 5.3, respectively, where σ is the standard deviation of

$$LOD = \frac{3.3\sigma}{S} \qquad \text{Equation 5.2}$$

$$LOQ = \frac{10\sigma}{S} \qquad \text{Equation 5.3}$$

regression models were determined from the standard deviations of the

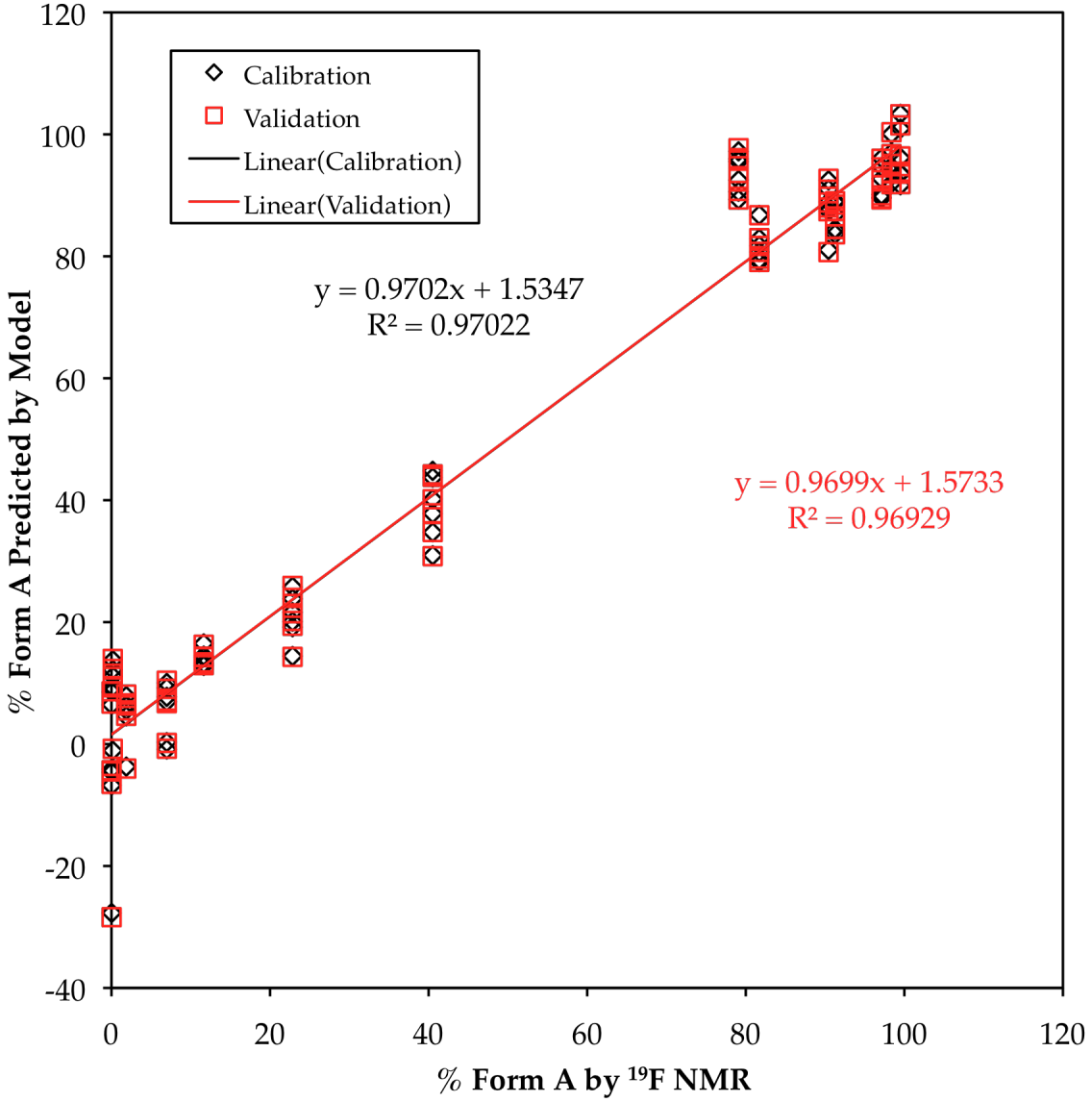

Figure 5.25. Predicted vs. reference plot for the PLS model of the PhAT probe Raman signals from Region #1 of the 10% (w/w) norfloxacin formulation spectra, with ^{19}F results as reference compositions. The entire diffraction pattern normalized by SNV transformation and then converted to 2nd derivatives with the SG algorithm prior to generating the model. The model has an RMSEC of 7.1 and an RMSEV of 7.2.

either the blank, the regression line, or the y-intercept of the regression line and S is the slope of the calibration curve.[6] The LOD and LOQ of the multivariate calibration regressions and are shown in Table 5.2. The LOD and LOQ values follow the same trends as the RMSE values, where ^{19}F SSNMR was the best model for both binary mixtures and the 10% formulations. For the binary mixtures, DSC and PXRD provided the least sensitive measurements, while TGA, and both Raman methods were of intermediate sensitivity. The 10% formulations have similar results but the TGA and PXRD had relatively similar sensitivity. It is important to note that the LOD and LOQ values shown in Table 5.2 for ^{19}F SSNMR are based upon the MLR models of Figures 5.22 and 5.24, which were only used for comparison and not for the actual quantitation measurements.

The LOD and LOQ of the SSNMR measurements would be better represented by the S/N of the spectra since they do not actually rely upon a calibration curve. It was possible to observe 0.5% of Form B within the Form A material when 2,048 transients were acquired (Figure 5.11) and the S/N of the peak was 6.2, which is well above the S/N limit of 2 to 3 for detection. Additionally, the 1% Form A binary mixture had a S/N of the Form A peak of 8.5. These two measurements indicate that for ^{19}F SSNMR of norfloxacin binary mixtures the LOD of Form A is ~0.5% and Form B is ~0.25% when 2,048 transients are collected with the appropriate spectrometer settings. These results also indicate that the LOQs should be ~1.5% and ~0.75% for Forms A and B, respectively. The analysis of the ^{19}F SSNMR of the 10% formulations indicates that with 4,096 transients the LODs of Forms A and B are ~1.5% and ~0.5%, respectively, with LOQs of ~4.5% and ~1.5%.

Table 5.2 LOD and LOQ of Quantitation Methods for Binary Mixtures and 10% Formulation from standard error of regression. The values represent the detection of Form A in the norfloxacin component of the mixtures.

	Binary		10% Formulation[a]	
Instrumentation	LOD[†]	LOQ[‡]	LOD[†]	LOQ[‡]
DSC	19%	58%	---	---
TGA	8.5%	26%	37%	110%
PXRD	14%	42%	40%	120%
FT-Raman	6.7%	20%	26%	78%
PhAT Probe	7.0%	21%	24%	73%
^{19}F SSNMR	4.8%	14%	6.2%	19%

[†] = LOD is 3.3 times the standard error of the regression divided by the slope of the regression.

[‡] = LOQ is 10 times the standard error of the regression divided by the slope of the regression.

[a] = Based on regressions with ^{19}F SSNMR results as reference composition. In the case of the ^{19}F SSNMR, the values are based on the compositions by mass, but the results of the 10% formulation with 60% Form A were excluded from the regression.

When LOD and LOQ are determined from the S/N they reflect the uncertainty in the intensity of the signals. However, as discussed in the previous chapter of this dissertation (Chapter 4) the intensity of peaks in the SSNMR spectra are not typically used for quantitative analysis, rather the peak areas are analyzed for these measurements. Therefore, the S/N of 2–3 and 10 for LOD LOQ may not be appropriate measures for SSNMR. This is also supported by the work in Chapter 4 where ^{13}C SSNMR was used to accurately quantitate a mixture of two cortisone 21-acetate polymorphs and one of the peaks had a S/N of only 5.5.

5.3.12 "Unknowns"

In order to test the calibration models five "unknown" binary blends of norfloxacin Forms A and B were analyzed. The results for each of the methods are given in Table 5.2, and appear to follow the same general trends that were observed with each of the calibration models. The DSC method tended to give highly variable results while the TGA method tended to be more reproducible. The PhAT probe and ^{19}F SSNMR results tended to be the most reproducible. In addition, as with the calibration samples the extrapolation of the peaks to account for the CP dynamics resulted in uncertainties of less than 0.5% for all but two of the samples which were 0.9 and 0.7% and were from the same mixture(72.2% Form A). Thus the data seems to suggest that as with the calibration samples, the $CI_{95\%}$ of the ^{19}F results is primarily due to inhomogeneity in the samples. This will also influence the outcome of the other methods. The ^{13}C results were shown as the raw results and show that for all of the mixtures where Form A was detected the two values agree very well with one another,

Table 5.2. Quantitation results for "unknown" binary mixtures of norfloxacin Forms A and B.

Mass	% Norfloxacin Form A by Indicated Method						
	DSC ± $CI_{95\%}$ [a]	TGA ± $CI_{95\%}$ [a]	PXRD ± $CI_{95\%}$ [a]	FT-Raman ± $CI_{95\%}$ [a]	PhAT Probe ± $CI_{95\%}$ [b]	^{19}F SSNMR ± $CI_{95\%}$ [c]	^{13}C SSNMR [d]
1.4	3 ± 10	4 ± 2	6 ± 6	1.6 ± 0.4	2.7 ± 0.6	2 ± 1	-----[†]
11.4	20 ± 10	11 ± 6	10 ± 6	10 ± 2	10.6 ± 0.7	8.2 ± 1	10.9 & 11.2
50.9	61 ± 5	56 ± 4	50 ± 7	51 ± 7	50 ± 3	49 ± 2	48.4 & 47.2
72.2	78 ± 3	68 ± 9	77 ± 6	70 ± 6	71 ± 1	69 ± 5	69.7 & 65.6
87.6	90 ± 10	88 ± 2	90 ± 3	87 ± 2	87 ± 1	86 ± 2	85.2 & 85.8

[a] = Each "unknown" sample was analyzed in triplicate and fit to the best, appropriate MLR or PLS model. The results are given as the average ± the $CI_{95\%}$ from the three replicates.

[b] = Each "unknown" sample was analyzed with six replicates and fit to the PLS model produced from SNV normalization and conversion to the 2nd derivative with the SG filter. The results are given as the average ± the $CI_{95\%}$ from the six replicates.

[c] = Each "unknown" sample was analyzed in triplicate with three contact times, see Section 5.3.8. The results are given as the average ± the $CI_{95\%}$ from the three replicates.

[d] = Each "unknown" sample was analyzed twice according to the method in Section 5.3.7. The two values are the % Form at from each of the replicates.

[†] = No peaks were observed in the spectra that were consistent with the presence of Form A.

except for the 72.2% Form A sample, which seems to be more inhomogeneous based on the ^{19}F SSNMR.

The "unknown" 10% formulations (Table 5.3) are also consistent with these observations. The TGA and PXRD models perform poorly when trying to predict the Form A component of the "unknowns." This is likely due to the significant overlap of the norfloxacin and excipient peaks. Unlike the binary mixtures, the FT-Raman seems to be slightly better than the PhAT probe, but both are very similar to each other and the ^{19}F SSNMR results. Again, the uncertainties from the extrapolations in the ^{19}F results were all at or below 1% but the $CI_{95\%}$ is significantly higher for all of the samples. Indicating that homogeneity may be an issue with all of the "unknown" 10% formulations, which would impact the uncertainty of the other methods as well. This is also reflected in the ^{13}C results where the values from the 92.6% Form A sample are in relatively good agreement (^{19}F $CI_{95\%}$ = 3%) but the others are centered around the percent Form A from the masses but are significantly different from one another, suggesting that material was split unevenly between the rotors, such that one appears to have a Form A content that is higher than the reference value and the other is lower than the reference value.

5.4 Summary

These results demonstrate the complications that are typically encountered with performing quantitation studies in the solid state. These observations are consistent with previous observations. Specifically, DSC suffered from conversion of the materials during analysis, which complicated the

Table 5.3. Quantitation results for "unknown" 10% (w/w) norfloxacin formulations.

	% Norfloxacin Form A by Indicated Method					
Mass	TGA ± $CI_{95\%}$ [a]	PXRD ± $CI_{95\%}$ [a]	FT-Raman ± $CI_{95\%}$ [a]	PhAT Probe ± $CI_{95\%}$ [b]	^{19}F SSNMR ± $CI_{95\%}$ [c]	^{13}C SSNMR [d]
1.6	4 ± 70	20 ± 60	3 ± 10	6 ± 2	2 ± 4	-----[†]
17.4	34 ± 3	20 ± 10	22 ± 2	10 ± 10	21 ± 7	19.9 & 12.3
48.8	50 ± 40	50 ± 10	46 ± 9	45 ± 4	50 ± 10	48.9 & 45.0
72.2	80 ± 23	80 ± 20	76 ± 3	60 ± 10	70 ± 10	68.0 & 73.3
92.6	80 ± 10	100 ± 20	90 ± 10	89 ± 4	93 ± 3	90.7 & 92.6

[a] = Each "unknown" sample was analyzed in triplicate and fit to the best, appropriate MLR or PLS model. The results are given as the average ± the $CI_{95\%}$ from the three replicates.

[b] = Each "unknown" sample was analyzed with six replicates and fit to the PLS model produced from SNV normalization and conversion to the 2nd derivative with the SG filter. The results are given as the average ± the $CI_{95\%}$ from the six replicates.

[c] = Each "unknown" sample was analyzed in triplicate with three contact times, see Section 5.3.8. The results are given as the average ± the $CI_{95\%}$ from the three replicates.

[d] = Each "unknown" sample was analyzed twice according to the method in Section 5.3.7. The two values are the % Form at from each of the replicates.

[†] = No peaks were observed in the spectra that were consistent with the presence of Form A.

analysis. TGA was able to quantify the binary mixtures, but apart from the detection of solvates, has limited applicability to quantitative measurements of mixtures of physical forms. PXRD also had limited success in the quantification of the mixtures. However, all three methods provided very poor quantitative data in the formulated materials. This is attributed to the overlap of API and excipient signals, and in the case of PXRD the relatively weak diffraction peaks that had to be used in order to avoid the relatively intense peaks from α-lactose monohydrate.

Conversely, Raman spectroscopy performed relatively well but suffered from inhomogeneity of the samples and a 10% formulation calibration standard did appear to contain a different amount of Form A than was determined from the masses of the materials that were used to generate the sample. However, SSNMR was able to give relatively accurate measurements of the Form A content of the sample that was currently being analyzed in the spectrometer, and could reflect the homogeneity of the samples by collection of several replicates. Typically, SSNMR is not utilized for quantitative studies either due to the long analysis times (especially for ^{13}C) or unfamiliarity with the technique. However, these results indicate that it could be a valuable tool to confirm the actual sample composition and provide reference compositions for the generation of calibration curves with other techniques.

5.5 References

1. Nunes C, Mahendrasingam A, Suryanarayanan R 2005. Quantification of crystallinity in substantially amorphous materials by synchrotron X-ray powder diffractometry. Pharmaceutical research 22(11):1942-1953.

2. Chieng N, Rehder S, Saville D, Rades T, Aaltonen J 2009. Quantitative solid-state analysis of three solid forms of ranitidine hydrochloride in ternary mixtures using Raman spectroscopy and X-ray powder diffraction. J Pharm Biomed Anal 49(1):18-25.

3. Campbell Roberts S, Williams A, Grimsey I, Booth S 2002. Quantitative analysis of mannitol polymorphs. X-ray powder diffractometry-exploring preferred orientation effects. J Pharm Biomed Anal 28(6):1149–1159.

4. Barbas R 2006. Polymorphism of norfloxacin: Evidence of the enantiotropic relationship between polymorphs A and B. Crystal Growth & Design 6(6):1463-1467.

5. Barbas R, Prohens R, Puigjaner C 2007. A new polymorph of norfloxacin: Complete characterization and relative stability of its trimorphic system. Journal of Thermal Analysis and Calorimetry 89(3):687-692.

6. ICH Guideline. Secondary Validation of analytical procedures: text and methodology Q2 (R1); IFPMA: Geneva, 2005.

Chapter 6

Conclusions and Future Work

6.1 General Conclusions

The primary objective of this dissertation has been to evaluate the ability of various solid-state characterization techniques, especially solid-state NMR (SSNMR), to detect and quantify physical forms of drugs within model formulations. This is critical to drug development because changes in the physical form of the drug can impact the dissolution and bioavailability of the drug from the formulation. Additionally, changes in the physical form of the drug can also lead to chemical instability of the drug.

The identification and characterization of a new physical form is not always straightforward. This was demonstrated in the second chapter of this dissertation with the dehydration of levofloxacin hemihydrate. Previous studies had concluded that dehydration of the material resulted in a collapse of the crystal structure and produced a mixture of physical forms.[1] However, through the use of SSNMR it was possible demonstrated that dehydration of levofloxacin actually does not result in collapse of the crystal structure. In fact, levofloxacin hemihydrate acts like a channel hydrate, which was supported by the crystal structure of the material that was determined by single-crystal X-ray diffraction. Additionally, with SSNMR and other solid-state characterization techniques it was possible to show that the anhydrous material undergoes a polymorphic change to a previously unreported δ form. Finally, analysis of the SSNMR results and examination of the crystal structure of levofloxacin was able to suggest the structural changes that occur between the δ and γ anhydrous forms of levofloxacin.

Incorporation of a drug into a formulation presents two major issues. First of all, the excipients often interfere with the analysis of the physical form of the drug either due to overlap of the excipient signals with those of the physical forms of the drug or altering the behavior of the drug. An example of the latter issue is the formation of a eutectic between the drug and an excipient during DSC analysis. The third chapter of this dissertation exemplified these issues with two nanoparticle formulations of budesonide and nifedipine. In both cases when DSC was used to analyze the materials there was no conclusive evidence to indicate the physical form of the drugs. However, SSNMR was able to unambiguously identify the budesonide as being in an amorphous state and nifedipine was present as crystalline Form I in the respective formulations that were analyzed.

In addition to signal overlap, the generation of a formulation can also result in physical form changes. This was also demonstrated in the third chapter of this dissertation with ciprofloxacin. When the material was processed to produce the nanoparticles for use in the formulation, new peaks were observed in the DSC thermographs and SSNMR spectra (^{13}C and ^{19}F) indicating that a physical form change had occurred. Additionally, it was noted that the physical form or forms were metastable and converted to the original physical form over the course of a month. These changes can have a significant impact on the behavior of the formulation, and may change over time if the drug converts to a more stable form with time. Therefore, it is critical to characterize materials throughout the manufacturing process and especially in the final drug product to ensure that no unanticipated physical form changes have occurred. Also, it is important to monitor the formulation for potential changes in the physical form

of the drug during storage.

When characterizing physical forms in formulations it is also important to understand the quantitative aspects of the instrumental method. If the technique is not sufficiently sensitive it may not detect small amounts of a physical form that may be present. Additionally, a final formulation may contain a mixture of physical forms and it may be necessary to determine if these forms are stable or are undergoing form conversions. Thus a quantitative SSNMR method was developed to allow the relative quantitation of physical forms of drugs within formulations. A major advantage of this method is that it does not require pure reference materials or the generation of a calibration curve, which is a significant issue with other solid-state characterization techniques. Additionally, in Chapter 4 of this dissertation it was demonstrated that the SSNMR data that is collected in the most efficient manner by optimization of the delay between transients and the use of cross polarization methods, can still provide quantitative results if the relaxation properties of the materials are known.

6.2 Future Work

Analysis of the ciprofloxacin materials in the third chapter of this dissertation suggests that during production of the nanoparticles several crystalline forms of ciprofloxacin were produced. There have been no reports of polymorphism of ciprofloxacin and thus it would be interesting to further characterize these new forms. Unfortunately, attempts to produce the forms have thus far been unsuccessful but it is believed that one of the sonication steps was the cause of the form conversion. Additionally, it would be interesting to

understand the rate of the form conversion back to the stable form and to characterize the impact of the form conversion on the release properties from the formulation.

The SSNMR approach to quantitation of physical forms in formulations was applied to the analysis of norfloxacin materials and its performance was compared against other commonly used solid-state characterization techniques such as DSC, PXRD, and Raman spectroscopy. The data followed the general trends that have been reported previously in that most of the techniques were able to quantitate the relative physical forms of norfloxacin within samples of pure drug but suffered significantly when the drug is present in a formulation, with the exception of SSNMR. The results indicated that the homogeneity of the samples was a significant issue, but that SSNMR could be used to characterize the homogeneity of samples. Therefore it would be interesting to study mixtures of various degrees of homogeneity with the above-mentioned techniques in an attempt to separate the influence of sample homogeneity and technique variations (fluctuations in signal and sample handling) on the quality of the quantitation methods. This has not previously been possible because most techniques, with the exception of SSNMR, require the generation of a calibration curve, which would also be influenced by the homogeneity and technique variations. Additionally, SSNMR could provide more accurate reference compositions for reference standards when preparing calibration curves, since inaccuracies in the preparation of the materials may not be readily detected by other techniques.

SSNMR has gradually gained a foothold in the analysis if pharmaceutical solids, and continues to prove that it can have a significant impact on the

development of pharmaceuticals. Its two major impediments have been the expertise required to utilize the instrumentation properly and the relatively long analysis times. The first issue has gradually decreased as SSNMR has gained prominence within the solid-state characterization community. The second issue has actually become more significant as the community has realized the potential impacts of utilizing SSNMR and has started to demand more use of the technique. Thus increased throughput is needed to help meet these increasing demands and efforts are currently underway to develop technology that would allow the simultaneous analysis of multiple samples with a single SSNMR spectrometer.[2]

6.3 References

1. Kitaoka H, Wada C, Moroi R, Hakusui H 1995. Effect of dehydration on the formation of levofloxacin pseudopolymorphs. Chem Pharm Bull 43(4):649-653.

2. Nelson BN, Schieber LJ, Barich DH, Lubach JW, Offerdahl TJ, Lewis DH, Heinrich JP, Munson EJ 2006. Multiple-sample probe for solid-state NMR studies of pharmaceuticals. Solid State Nucl Magn Reson 29(1-3):204-213.